UNIVERSITY OF CALIFORNIA,
IRVINE

Source apportionment of Arctic and remote marine carbonaceous aerosols

DISSERTATION

Submitted in partial satisfaction of the requirements
for the degree of

DOCTOR OF PHILOSOPHY

in Earth System Science

by

Blanca Teresa Rodríguez

Dissertation Committee:
Associate Professor, Claudia I. Czimczik, co-Chair
Associate Professor, Saewung Kim, co-Chair
Distinguished Professor, Ellen Druffel
Professor, Alex Gunther

2021

DEDICATION

Para mis papás, Blanca y Rafael. No estaría aquí sin sus inmensos sacrificios y perseverancia.

To my parents, Blanca and Rafael. I would not be here without their immense sacrifice and perseverance.

TABLE OF CONTENTS

LIST OF FIGURES

LIST OF TABLES

ACKNOWLEDGEMENTS

I owe a world of gratitude to my advisor, Dr. Claudia I. Czimczik, for persistently believing in me and always being the voice of hope during dark times. I am eternally grateful for her unfaltering mentorship, guidance, support, and for always pushing me to higher levels of critical thinking. She taught me the value of perseverance and turning the other cheek in the world of academia. I would like to thank my co-advisor, Dr. Saewung Kim, for also providing mentorship, supporting my ideas, and giving me the opportunity of a lifetime to reach the Arctic by icebreaker, not once, but twice. With the combined support of my advisers, I was able to pursue many creative outreach and research opportunities, which I will forever be thankful for.

My favorite times working on my PhD were doing fieldwork and working in the lab, for which I have many people to thank for. Specifically, I would like to thank Dr. Gergana Mouteva for being my inspiration to do isotopic measurements of aerosol, and Dr. Xiaomei Xu for her faith in me and for always pushing me to do better work in the lab. I am extremely thankful for Dr. Guaciara M. Santos, for her patience with me in the lab, for inspiring me to increase my level of understanding of radiocarbon measurement as it relates to atmospheric aerosol, for always catching my mistakes no matter how small, and for never failing to make me laugh. I would also like to thank Jennifer Walker, Drs. Elizabeth Wiggins, and Brett Walker for always being willing to help and teach me new laboratory techniques. Your efforts have truly made my time in the Earth System Science Department at UCI fulfilling. I am grateful to have had the opportunity to learn from you all.

I would like to acknowledge my dissertation committee, Drs. Ellen R.M. Druffel, and Alex Gunther for wholeheartedly supporting my research and providing helpful guidance throughout the years. I would also like to acknowledge Drs. Elizabeth Crook and Julie Ferguson for inspiring me to become a better educator through the strong examples they set and making the TA experience worthwhile and invigorating.

Finally, I am extremely grateful to my parents, Blanca H. and Rafael Rodríguez for their never-ending love, support, and patience. I am incredibly proud, as a first-generation Chicana, to submit this dissertation in their honor as proof that their biggest sacrifice to immigrate to the United States in search for a better life was worth it. ¡Sí se puede! (Yes we can!) has become ¡Sí se pudo! (Yes, we did!). Thank you to my partner, Evan Shaw, for the wonderful last two years full of support, love, and encouragement to pursue my hobby passions.

Funding for the first year of PhD was provided by the Jenkins Foundation Fellowship and the Earth System Science Department at the University of California, Irvine.

CURRICULUM VITAE

Blanca Teresa Rodríguez

Education

- 2016 – 2020: **PhD. in Earth System Science,** University of California, Irvine
  Thesis:
- 2015 – 2016: **M.S. in Earth System Science,** University of California, Irvine
  Concentrations: Isotope geochemistry, carbon cycling, and particle chemistry
- 2011 – 2015: **B.S. in Chemistry**, Arizona State University, Tempe, Arizona
  Concentration: Environmental Chemistry

Research Experience

Graduate Researcher (Fall 2015 – January 2021)

Advisers: Drs. C. I. Czimczik, S. Kim

- Obtained and analyzed environmental samples (aerosol, fog, snow, and sea ice) chemical and isotopic components and attributes
- Measured isotopes ($\Delta^{14}C$, $\delta^{13}C$, $\delta^{34}S$, $\delta^{18}O$) of aerosols and water to quantify the relative contributions of different sources to bulk aerosol, aerosol fractions, and waters
- Analyzed data
- Performed backward airmass trajectory analyses
- Mentored undergraduate and graduate students
- Trained and mentored undergraduate students during fieldwork and in the lab

Undergraduate Research Assistant (Spring 2013 – Spring 2015)

Advisor: Dr. P. Herckes

- Collected high volume aerosol samples for Haboob study during Arizona monsoon season
- Investigated the use of single particle inductively coupled mass spectrometry (sp-ICP-MS) for quantifying nanoparticles in environmental matrices
- Screened tap water for specific metal-containing nanoparticles using sp-ICP-MS
- Project involved screening surface water from the environment to determine possible atmospheric inputs

Teaching Experience

Instructor, Earth System Science, University of California, Irvine (Summer 2020)

- Class: EarthSS5: The Atmosphere

Teaching Assistant, Earth System Science, University of California, Irvine (2016-2020)

- General Education Classes: EarthSS 17: Catastrophes (2x), EarthSS 7: Physical Geology Lab (2x), EarthSS 5: The Atmosphere (4x), EarthSS 1: Intro to ESS, Chem 1LC: General Chemistry Lab, EarthSS: 23: Air Pollution (2x)
- Major Classes: EarthSS 114: Field Methods

Middle School Lead Tutor, Arizona State University America Reads, Tempe AZ (January 2015 – May 2015)

- Leadership role supervising and managing tutors at Heard Elementary

Middle School General Tutor (August 2011 – December 2014)

- Tutor for recently-immigrated and refugee middle school students at Heard Elementary

Honors and Awards

- Summer 2020: Division of Teaching Excellence and Innovation Fellowship
- October 2017: Associated Graduate Students (AGS) Travel Grant
- Fall 2011-Spring 2015: President Barack Obama Scholar's Program
- Fall 2012-Spring 2015: Alhambra Foundation for the Future Scholarship
- Fall 2012, Fall 2014: Hispanic Scholarship Foundation General Scholarship
- Summer 2013 - Spring 2014: Western Alliance to Expand Student Opportunities
- November, 2011; April, 2014: Tutor of the Month Award
- Fall 2011, Spring 2013, Spring 2014, Fall 2014, and Spring 2015: Dean's List Term Honor

Transferable Skills

- Microsoft Office (typing speed: 70 wpm)
- Data entry and graphic analysis (Igor PRO, Matplotlib)
- Python programming (Spyder GUI)
- HYSPLIT Trajectory Analysis
- Environmental sampling of water, fog, and aerosol for laboratory analysis
- Radiocarbon (AMS) and stable isotope analysis (EA/GB-IRMS)
- Elemental analysis
- Sunset OC/EC analyzer
- Optical analysis (UV-vis/fluorescence)
- Scientific writing

Professional Development Experience

Mentoring Excellence Program (April – May, 2019)

- Short course taken to develop mentorship skills
- Covered topics: ethics of mentorships, campus resources, mental health in mentorship, effective interpersonal communication strategies, conflict management strategies

Graduate Interconnect Program (April – December 2019)

- Peer mentorship program which trains and graduate student peer mentors with incoming graduate international students with the purpose of orienting new students during their first quarter
- Peer mentors provide mentorship, situate international students with campus resources as needed, and are the first line of communication between the student and Graduate Division

Science in Action Inaugural Member (November 2018 – November 2019)

- New professional development program targeting students in the sciences looking for jobs outside of academia
- Program included 100 hours of professional development participations, Mentoring Excellence Program, and the Foundations of Leadership workshop series provided by the Graduate Resource Center

Foundations of Graduate Health and Wellness Certificate Program (March – June 2017)

- 6-week course aimed at: developing an understanding of the connection between physical, mental, and professional health, recognizing signs of work-life imbalance, identifying and utilizing resources that promote health and well-being, developing the financial literacy needed to budget for the future, learning to pursue health and wellness beyond the graduate career
- Taught by Phong Luong Psy.D.

Outreach

KUCI Talk Show Host (October 2018 – June 2019)

- Talk show host of The Science Spiel (thesciencespiel.org)
- Communicates science news and complex scientific concepts to the general public
- Interviews faculty and graduate students to spread awareness of local research
- Regular postings on webpage (thesciencespiel.org) to improve scientific literacy among the general public

KUCI Volunteer/Assistant Librarian (March 2018 – June 2019)

- Management of the music library
- Assists lead librarian in:
  - Returning misplaced music
  - Integrating new releases into the library
  - Developing new ideas to improve library organization and ease of use

Office Assistant (May – August 2012)
Growing Together/Creciendo Unidos Organization, Phoenix, AZ

- Assisted in basic clerical tasks for the non-profit organization which seeks to better the community by strengthening Latino families.
- Tasks included but were not limited to: database entry, inventory, preparing materials for workshops, making calls, and translating.
- Provided logistical support to functions of the organization which include community workshops, cultural and community events.

Publications

- **Rodríguez BT**, Park KH, Santos GM, Xu X, Kim S, Czimczik CI. Characterization of summertime organic aerosol in the marine boundary layer of the Pacific and Arctic Ocean. In Prep.
- Huang L, Zhang W, Santos GM, **Rodríguez BT**, Holden SR, Vetro V & Czimczik CI. 2020. Application of the ECT9 protocol for radiocarbon-based source apportionment of carbonaceous aerosols. *Atmospheric Measurement Techniques Discussion*. https://doi.org/10.5194/amt-2020-201
- **Rodríguez BT**, Huang L, Santos GM, Zhang W, Vetro V, Xu X, Kim S, Czimczik CI. 2020. Seasonal cycle of isotope-based source apportionment of elemental carbon in airborne particulate matter and snow at Alert, Canada. *Journal of Geophysical Research: Atmospheres*. https://doi.org/10.1029/2020JD033125
- Kirpes, RM, **Rodríguez BT**, Kim S, China S, Laskin A, Park K, Jung J, Ault AP, Pratt KA. (2020) Emerging investigator series: influence of marine emissions and atmospheric processing on individual particle composition of summertime Arctic aerosol over the Bering Strait and Chukchi Sea. *Environmental Science: Processes Impacts.*, 2020, 22, 1201-1213. DOI: 10.1039/c9em00495e
- Jung J, Han B, **Rodríguez BT**, Miyazaki Y, Chung HY, Kim K, Choi JO, Park K, Kim IN, Kim S, Yang EJ, Kang SH. (2019) Atmospheric Dry Deposition of Water-Soluble Nitrogen to the Subarctic Western North Pacific Ocean during Summer. *Atmosphere*, *10*, 351. DOI: https://doi.org/10.3390/atmos10070351
- Venkatesan AK, **Rodríguez BT**, Marcotte AR, Bi X, Schoepf J, Ranville JF, Herckes P, Westerhoff P. (2018) Using single-particle ICP-MS for monitoring metal-containing particles in tap water. *Environmental Science: Water Research & Technology*., 2018, 4, 1923. DOI: 10.1039/c8ew00478a

Conference Presentations

- **Rodríguez BT**, Zhang W, Huang L, Santos GM, Xu X, Vetro V, Kim S, Czimczik, CI. Seasonal cycle of isotope-based source apportionment of elemental carbon in airborne particulate matter and snow at Alert, Canada. American Geophysical Union Fall Meeting; Dec. 1-17, 2020; Virtual Remote. *Poster Presentation.*
- **Rodríguez BT**, Park KH, Santos GM, Xu X, Czimczik CI, Kim S. Determining the process-dependent source contribution of marine arctic carbonaceous aerosols with

ultra-small radiocarbon isotopic analysis. American Geophysical Union Fall Meeting; Dec. 10-14, 2018; Washington D.C. *Oral Presentation*

- **Rodríguez BT**, Santos GM, Sanchez D, Jeong D, Czimczik CI, Kim S. Carbonaceous aerosol characterization during 2016 KOR-US 2016. American Geophysical Union Fall Meeting; Dec. 11-15, 2017; New Orleans, Louisiana. *Poster Presentation*
- **Rodríguez BT**, Huang L, Zhang W, Holden SR, Santos GM, Czimczik CI. Radiocarbon measurements of ultra-small samples with the EnCan-total-900 protocol for source apportionment of carbonaceous aerosols. International Radiocarbon in the Environment Conference; Jul. 3-7, 2017; Debrecen, Hungary. *Poster Presentation.*

ABSTRACT OF THE DISSERTATION

Source apportionment of Arctic and remote marine carbonaceous aerosols

By

Blanca Teresa Rodríguez

Doctor of Philosophy in Earth System Science

University of California, Irvine, 2020

Associate Professor Claudia I. Czimczik, Chair

Associate Professor, Saewung Kim, co-Chair

Carbonaceous aerosols are critical, short-lived climate forcers (SLCFs) that play complex roles in the climate system through their interaction with solar radiation, cloud nucleation, and are also a major contributor to air pollution. Globally and within the Arctic, changing aerosol burden associated with the decline of sea ice, shifts in the productivity of marine and terrestrial ecosystems, wildfire, and anthropogenic activities, remains an important uncertainty for projections of future climate change. To develop and evaluate effective air quality and climate change mitigation policy, we urgently need a better understanding of emissions sources.

An important step forward in unraveling the complexity of carbonaceous aerosols lies in the analysis of specific aerosol fractions that have different emissions sources, lifetimes, and climate- and health impacts. A minor component with significant climate and health implications is black carbon (BC), a light absorbing SLFC emitted directly through incomplete combustion that leads to increased air column temperatures, accelerated ice and snow melt, shifts in cloud formation, cover, and lifetime, and have adverse effects on human health. The vast majority are organic carbon (OC) aerosols, that are light-scattering, also emitted through combustion processes, and formed secondarily in the atmosphere. In this thesis, I combine OC/BC analysis with stable (^{12}C, ^{13}C) and radioactive (^{14}C) carbon isotope data to improve our understanding of BC and OC sources (fossil vs. modern and terrestrial vs. marine) and their spatiotemporal variations within the High Arctic, which are considered primarily marine. I also explore aerosol composition in currently understudied marine source regions.

Despite significant history of Arctic aerosol monitoring networks and power of isotopic (and specifically ^{14}C data) for source attribution, consistent ^{14}C observations of Arctic aerosol remain sparse. This is largely driven by the small sample sizes of aerosol collected in remote environments. To make such data more readily accessible for current and future monitoring networks, I evaluate the efficacy of the ECT9 protocol, a temperature protocol designed to physically separate and trap OC and BC microsamples (<100 µg C) for accurate $\delta^{13}C$ and ^{14}C analysis. This is done by measuring the ^{14}C content of individual and mixed OC and BC standards of varying sizes to quantify the extraneous carbon incorporated throughout the analytical process and the efficacy of OC/BC physical separation. The total modern and fossil extraneous carbon incorporated by the set-up was 0.9±0.45 and 0.4±0.2 µg C respectively. The ECT9 technique was found effective at physically separating exclusively non-refractory OC and highly refractory

BC and can be applied directly to monitoring networks using this protocol to quantify OC/BC concentrations.

I utilize the ECT9 protocol to quantify BC concentrations and fossil fuel contribution to BC in total suspended particulates (TSP) and snow collected at the Dr. Neil Trivett Global Atmosphere Watch Observatory at Alert, Nunavut Canada, a long-term monitoring facility, over the course of one year (2014-2015). I determine the seasonal cycle of fossil fuel source contributions to show that BC is primarily dominated by fossil sources throughout fall- spring (47-70% fossil) and have major geographical sources from the Russian Arctic sector, though long-range contributions from Asia cannot be excluded. Additionally, summer BC (20-52% fossil) is dominated by biomass burning in the North American Arctic sector as shown by GFED v4.1 Summer 2014 biomass burning emissions and enriched ^{14}C values. BC in snow was enriched relatively to BC in TSP, though this effect was not homogeneous (53-88% biomass). High biomass burning contributions in snow BC suggests wet deposition may be a key pathway for long-range transport of biomass burning emissions from the upper troposphere.

Furthermore, I explore the various marine and terrestrial sources to OC aerosol across the northern Pacific and the Arctic Ocean. I combine dual isotopes (^{13}C, and ^{14}C) in a multi-source model to calculate and quantify the contributions from surface marine refractory dissolved organic carbon (RDOC), fresh biomass, and liquid fossil to ambient aerosol. The data shows that remote marine aerosol is dominated by RDOC in the Pacific (90% RDOC) and to a lesser extent in the Bering Sea (47% RDOC). This work suggests marine RDOC and fresh biomass are important contributors to marine OC and may play an important role in future Arctic climate change.

Together, my dissertation research established new analytical capabilities, produced critical benchmark dataset, and advanced our understanding of carbonaceous aerosol in the rapidly changing Arctic.

Chapter 1: Introduction

1.1 The changing Arctic

The Arctic is a critical component of the Earth system that is warming twice as fast relative to global rates, a process known as "Arctic amplification" (Overland et al., 2019). The accelerated warming observed in the Arctic has had complex and profound impacts on the region that are expected to continue for the next few centuries (Koenigk et al., 2020). The incidence of persistent warm air temperatures since the mid-1990s (Jones et al., 1999, 2012) has led to a consistent decline of sea ice extent and thickness (Kwok, 2018; Ricker et al., 2017), significant pan-Arctic permafrost warming (Biskaborn et al., 2019; Chadburn et al., 2017; Slater & Lawrence, 2013), and increased freshwater discharge to the Arctic Ocean from melting terrestrial ice stocks and increased river runoff (Ahmed et al., 2020; Durocher et al., 2019; Rood et al., 2017). Diminishing sea ice has cascading impacts on marine and terrestrial ecosystems, radiative forcing, cloud cover, and precipitation patterns (Richter-Menge et al., 2019). Specifically, declining sea ice extent and thickness has significantly shifted the timing and intensity of phytoplankton blooms. Earlier break up and recession of sea ice has shifted phytoplankton blooms earlier, particularly in marginal sea ice regions (Frey et al., 2018), and marine pan-Arctic primary productivity has increased in the past two decades (Comiso, 2015). Additionally, trans-Arctic shipping is expected to increase with decreasing sea ice extent and therefore may contribute significantly to the future of Arctic climate (Gong et al., 2019; Stephenson et al., 2018). On land, tundra productivity is changing (Lara et al., 2018; Myers-Smith et al., 2020) and woody plants (shrubs) are becoming more abundant (Myers-Smith & Hik, 2018). The changing composition and productivity of marine and terrestrial ecosystems is also likely to affect Arctic aerosol concentrations as secondary organic

aerosol (SOA) emissions may change (Croft et al., 2019; Faubert et al., 2010; Lindwall et al., 2016).

While the Arctic atmosphere is pristine compared to other, more densely-populated regions, pollutants produced within the Arctic region and transported to the Arctic from lower latitudes accumulate under dry, cold conditions of the Arctic dome in winter and early Spring – resulting in a phenomenon known as "Arctic haze" (Law & Stohl, 2007; Quinn et al., 2007; Shaw et al., 1993). Arctic haze occurs during the winter and spring months due to long-range transport of accumulation mode particles (0.1-2.5 μm diameter) from the midlatitudes and Arctic emissions (Freud et al., 2017) (Fig. 1.1), when the polar front expands asymmetrically into Asia and eastern North America. Key components of Arctic haze are black carbon (BC) and organic carbon (OC). BC is a refractory, light absorbing aerosol emitted directly through combustion (Andreae & Gelencsér, 2006; Petzold et al., 2013), that has extensive implications for climate (Bond et al., 2013), air pollution, and public health (Pöschl, 2005).

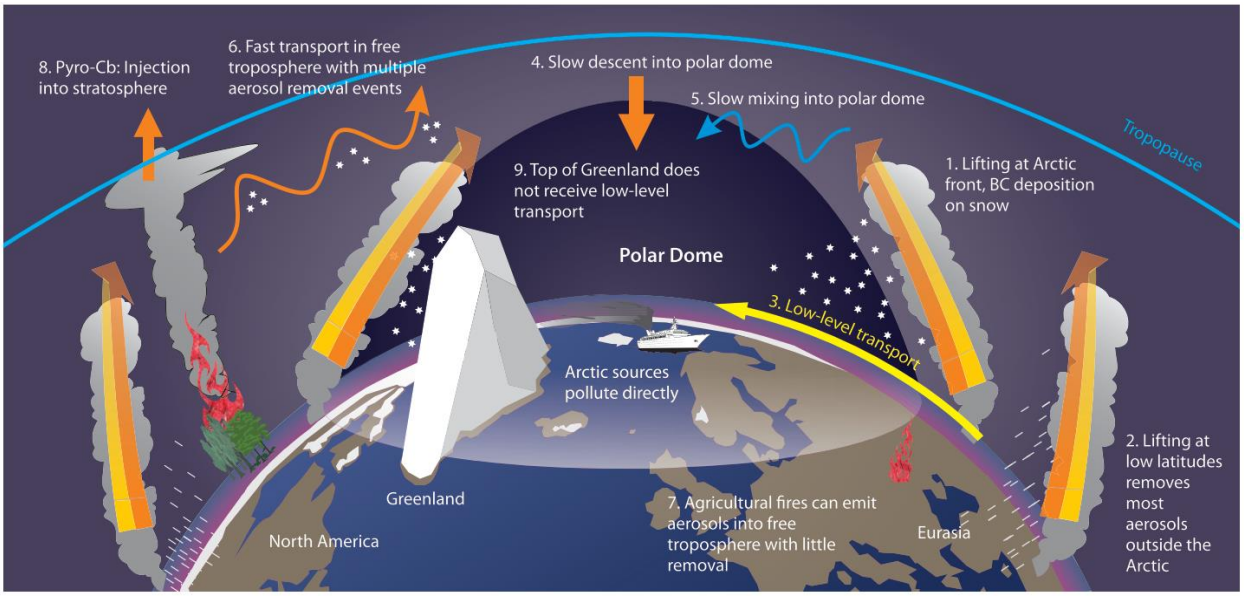

Figure 1.1 Summary of BC emissions, transport pathways, and atmospheric processing. From AMAP (2015).

The cold and dry conditions experienced within the polar dome limit the most effective removal mechanism for BC, wet scavenging. Since BC often develops sulfate and/or organic coatings after emission, the increased hydrophilicity allows BC to act as cloud condensation nuclei (CCN) or become scavenged by existing liquid droplets. However, exceedingly low temperatures within the polar dome in winter and spring, increase the lifetime of BC in the High Arctic (>70°N). The accumulation of BC within the polar dome is also exacerbated by the formation of strong temperature inversions that inhibit vertical air column movement. Instead, two distinct transport pathways are reflected in the vertical distribution of Arctic haze during springtime. Low-tropospheric Arctic pollution is attributed to emissions from Europe and north Asia (Siberia and Eurasia), and mid- and upper-tropospheric pollution to eastern and southern Asia (Xu et al., 2017) (Fig. 1.2).

The accumulation of light-absorbing particles, such as BC, during the spring plays a crucial role during polar sunrise in shifting the Arctic's radiation balance by trapping more heat and causing earlier melting of sea ice and/or snow (Flanner et al., 2009). During polar sunrise, strong temperature inversions are still prevalent, which limit vertical transport and exacerbate aerosol-radiation interactions. The end of the Arctic haze season is typically seen at the end of spring, when increased solar heating induces vertical mixing and along with it a sharp transition from ice-dominant clouds to warmer mixed-phase drizzling clouds (Browse et al., 2012). These interactions have cascading direct and indirect effects throughout the warm season that impact long-term climate.

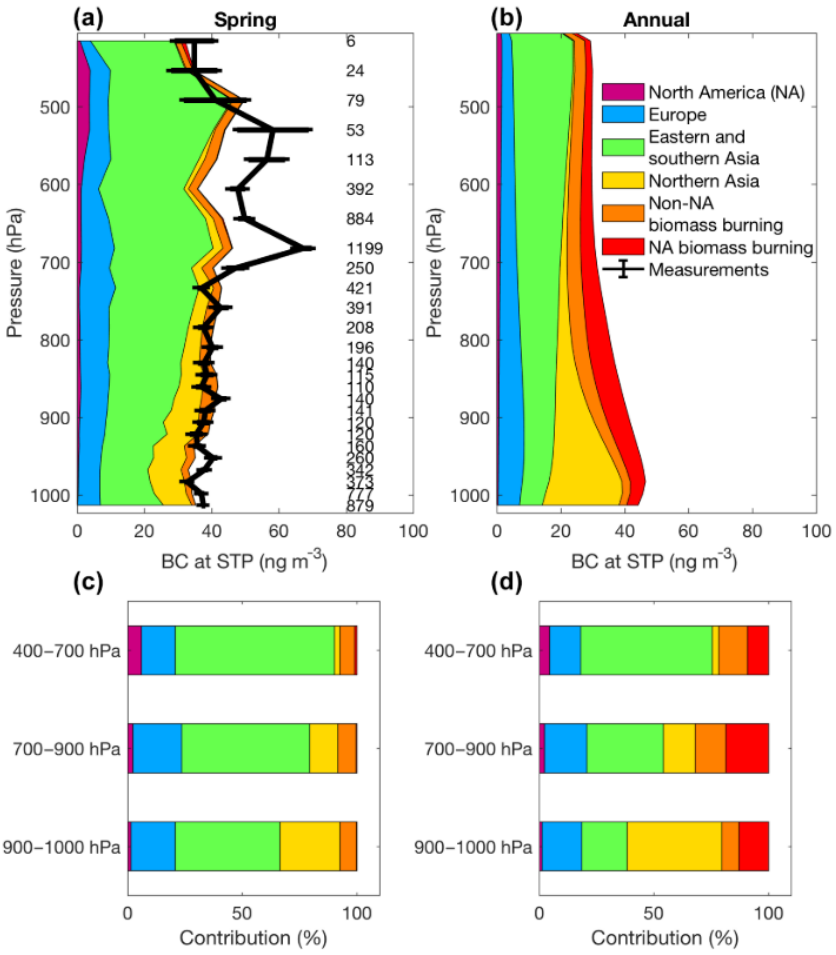

Figure 1.2 Spring and annual air column vertical distribution of BC sources from flight measurements. Average BC concentrations in (a) are shown in solid black line with number of measurements shown to the right. Simulated concentration contributions are color-coded in (a) and (b). Source contributions in percentages of 200 hPa pressure bins shown in (c) and (d). From Xu et al., (2017).

This changing aerosol burden contributes to the uncertainty for understanding future climate change in the Arctic because direct and indirect effects of aerosol on climate forcing remains poorly understood (Pierrehumbert, 2014). Direct effects of aerosol on climate stem from aerosol interactions with incoming and outgoing radiation. For example, sulfate and organic aerosol generally cause cooling through increased scattering of radiation while colored aerosol (i.e. black and brown carbon) causes warming by lowering surface albedo and enhancing surface snowmelt. The indirect effects of aerosol on climate originate from complex cloud-aerosol interactions which can affect cloud cover, the radiative and microphysical properties of the cloud for example. A key challenge is to understand the sources of these aerosols in the rapidly changing Arctic. These data are urgently needed to develop and monitor effective mitigation policies.

1.2 Black carbon aerosol in a changing Arctic

1.2.1 Arctic black carbon emission sources

Black carbon (BC) aerosol is directly emitted through high-temperature combustion of carbon-based material alongside longer-lived, climate-forcing greenhouse gases. As such, the primary source of BC in and to the Arctic is the combustion of fossil and biogenic fuels (e,g, coal, peat, and wood; anthropogenic processes) and biomass burning (wildfires). Historically, global anthropogenic BC emissions increased linearly from 1850 to 2000 as a result of steadily growing fuel demand (Lamarque et al., 2010). With the onset of industrialization, emissions were initially dominated by Europe and North America from 1750 to 1960 after which rapid economic growth and shifts in manufacturing expanded emissions from China and other Asian countries to (Skeie et al., 2011). 70-80% of BC emissions in North America, Europe, and Asia originate from a combination of surface and air transportation (i.e. gasoline, diesel, or kerosene combustion) and residential/commercial activities (i.e. domestic and commercial heating and cooking with wood, natural gas, or coal) (AMAP, 2015). Increasingly efficient combustion technology and stricter air pollution regulations have lowered emissions from Europe and North America since 1950. As a result, Arctic monitoring stations measuring properties of colored aerosols showed a decreasing trend in equivalent BC concentrations of 49% and 33% during winter at Alert and Barrow respectively (Hirdman et al., 2010; Sharma et al., 2006).

The lifetime of BC is highly dependent on the transportation pathway. Siberian and European emissions to the Arctic are transported in the low-troposphere, and is subject to increased wet and dry deposition (Bourgeois & Bey, 2011; Wang et al., 2014). As such, the lifetime of BC from Siberia and Europe is 7-9 days on average throughout the year but 10-16 during springtime (Qi et al., 2017). However, long-range transport of BC from Asia is lifted to the mid and upper

troposphere, which severely limits wet and dry deposition (Law & Stohl, 2007) (Fig. 1.1). Consequently, the lifetime of BC arriving from Asian anthropogenic and biomass burning can be as long as four months (Qi et al., 2017).

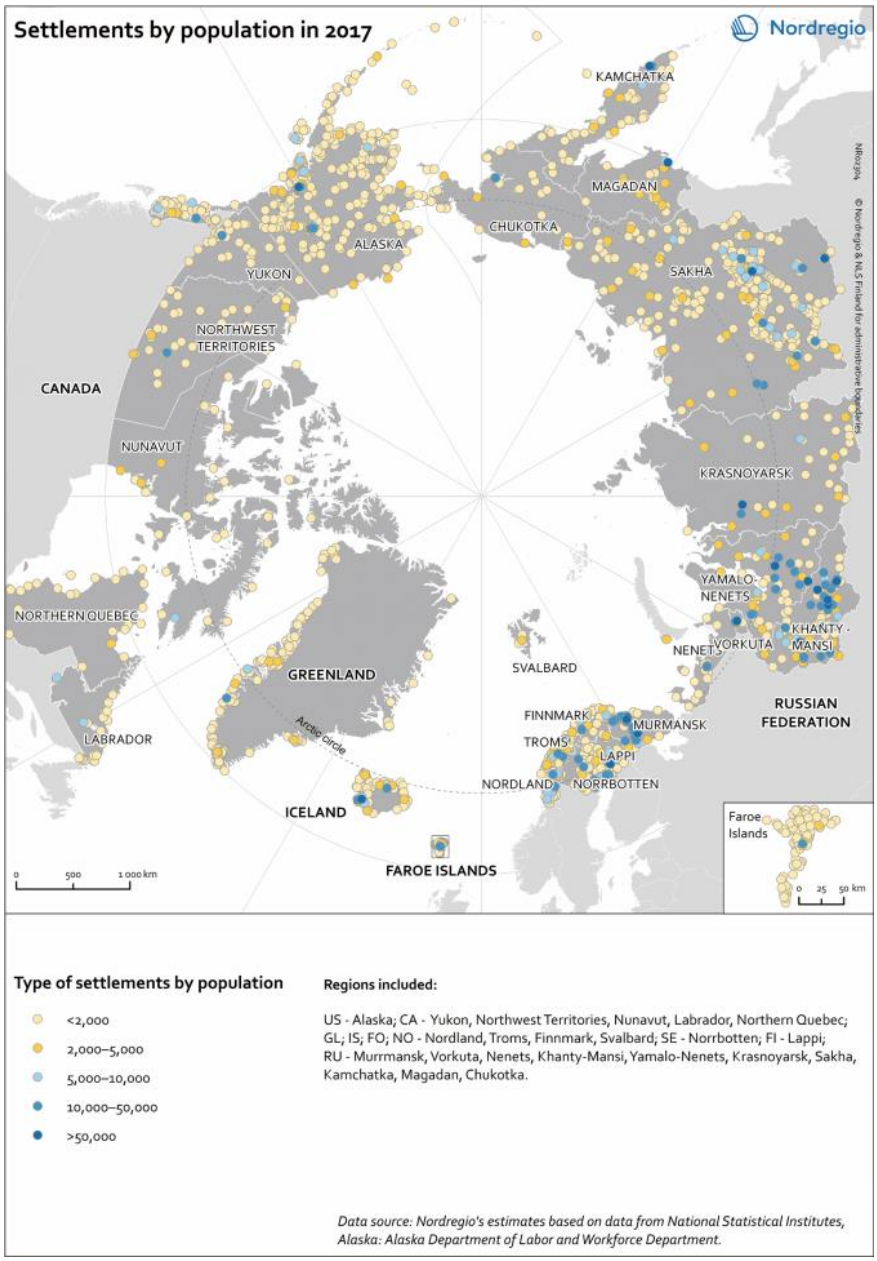

Figure 1.3. Circum-Arctic settlements distinguished by population size. From Jungsberg et al. (2019).

Within the Arctic, BC emissions are associated with residential activities and commercial gas and oil extraction and its infrastructure. This includes gas flaring, which consists of burning excess gaseous or liquid hydrocarbons at production sites. Quantifying gas flaring emissions into inventories in the Arctic is highly uncertain due to the lack of observations and BC emission factors associated with flaring. Stohl et al. (2013) has suggested that flaring is highly prevalent in the Rus-

sian sector of the Arctic (Fig. 1.3). Future shipping related to gas and oil production logging, and mining is also expected to increase (Gunnarsson, 2021; Peters et al., 2011) and thus getting a better understanding of how BC in the Arctic will impact future climate change is imperative.

1.2.2 Direct Arctic climate impacts

Black carbon directly impacts regional climate through BC-radiation interactions and their respective feedbacks (Table 1.1). The direct radiative forcing (DRF) associated with BC in the atmospheric column is another important climate forcing pathway, particularly in the spring when Arctic haze is prevalent. This is due to enhanced emission transportation from lower latitudes in conjunction with polar sunrise providing shortwave radiation. BC absorbs shortwave radiation in the atmospheric column and resulting radiation balance perturbations vertically dependent (Samset & Myhre, 2011).

Accurately modeling the DRF imparted from tropospheric BC requires accurate estimates of BC emissions, lifetimes, mass absorption cross section (MAC), and forcing efficiency. Consequently, estimates are highly variable as these four BC properties are represented differently in models. For example, estimates within the Arctic of DRF include co-emitted light-absorbing aerosols, such as OC aerosol. A multi-model mean from 15 AeroCom models (Samset et al., 2013) estimated +0.38±0.3 W m^{-2} and ranged from +0.07 to +1.19 W m^{-2}. Arctic DRF estimates are subject to the largest uncertainties due to the uncertainties in emission inventories, particularly in Russia and Eurasia. Hao et al. (2016) updated Eurasian emission estimates, reporting 3.2 times higher emissions than that reported by the Global Fire Emissions Database version 4 (GFED4). Huang et al. (2015) updated Russian anthropogenic emissions and included added gas flaring emissions greater than previously reported (Bond et al., 2007). Nonetheless, incorporating these

estimates with a GEOS-Chem model, Dong et al. (2019), calculated a DRF ranging from 0.25-0.35 W m^{-2} and DRF, which is within the previous range.

Another direct climate impact is the effect of BC deposition on snow and ice on surface albedo. This positive feedback results in radiative forcing ranging +0.03 to +0.28 W m^{-2} (AMAP, 2015; Flanner et al., 2009; Koch et al., 2009) and is characterized by significant reduction in surface albedo leading to earlier onset of melting. Furthermore, albedo reduction creates other feedback loops that interact. These include feedbacks related to resulting increased surface air temperatures which affects sublimation rates, deposition and transport pathways, and snow grain sizes (Bond et al., 2013) (Fig. 1.4). This emphasizes that the effect of BC deposition on snow and DRF associated with atmospheric BC alone do not account for the rapid climate warming occurring in the Arctic. Indirect and semi-direct effects must also be considered.

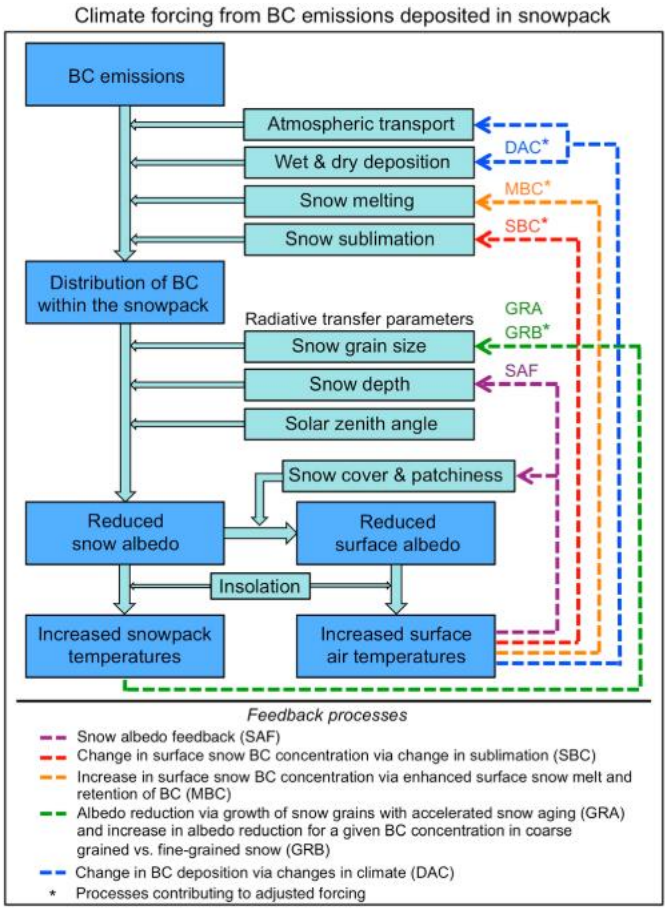

Figure 1.4 Summary of feedback loops associated with deposition of BC on snow and ice. From Bond et al. (2013).

1.2.3 Indirect Arctic climate impacts

The indirect climate impacts of BC in the Arctic are tied to aerosol-cloud interactions, which can affect cloud-cover, emissivity, and brightness. Modelling and accurately quantifying the forcing from these effects is challenging due to various cloud-aerosol feedbacks involved, which vary by region and meteorological conditions. Nonetheless, BC affects cloud properties consequently from shifting air-column temperatures and BC's role as CCN, which have cascading impacts on the cloud's macro and microphysical properties.

BC's light-absorbing properties serve to increase the temperature of the air column. BC, when aloft, increases atmospheric stability and leads to increased low-level cloud cover (Johnson et al., 2004). BC within or below cloud can increase convection, which may also enhance cloud cover. This impact is highly dependent on the amount of absorption. As such, weakly-absorbing aerosols, such as dust, decline cloud-cover (Johnson et al., 2004). The radiative impact of BC is estimated to range from -0.30 to +0.15 W m^{-2} (Cherian et al., 2017; Ghan et al., 2012; Hansen et al., 2005; Penner et al., 2003) but is subject to large uncertainties dependent on accurate representation of BC altitude.

BC readily becomes scavenged by existing liquid droplets within a cloud due to organic or sulfate coatings that increase the hydrophilicity. Upon incorporation the absorption effects are amplified, though the radiative impact of this effect has yet to be accurately modeled. The indirect effect of BC on clouds stems from the effect of BC on CCN number concentrations within a cloud. Increased CCN-activated BC aerosol increases the number of cloud droplets and limits droplet growth, therefore suppresses precipitation. This effect, however, is amplified in pristine

regions, such as summertime Arctic, where the formation and lifetime of low-level clouds are highly dependent on CCN concentrations (Burkart et al., 2017; Willis et al., 2016). The radiative forcing reported for indirect effect of BC ranges from -0.32 to +0.26 W m^{-2} and is also subject to high uncertainties (Bauer et al., 2010; Bond et al., 2013; Koch et al., 2011).

Despite significant contributions to the various feedbacks implicated in increasing Arctic temperatures, BC is only one component of the climate system contributing. OC aerosol is another important component that has massive potential climatic impacts.

Table 1.1 Overview of BC radiative forcing estimates

Effect	Radiative Forcing W m^{-2}	References
Direct Radiative Forcing	+0.07 to +1.19	Samset et al., 2013; Dong et al., 2019
Deposition on snow and ice	+0.03 to +0.28	Flanner et al., 2009; Koch et al., 2009; AMAP 2015
Indirect effect	-0.3 to +0.15	Cherian et al., 2017; Ghan et al., 2012; Hansen et al., 2005; Penner et al., 2003

1.3 Organic carbonaceous aerosol in the climate system

1.3.1 Sources to atmospheric OC aerosol

OC aerosol encompasses diverse sources that are emitted primarily and secondarily created in the atmosphere through condensation. OC constitutes a major fraction (20-90%) of aerosol burden globally (Jimenez et al., 2009).

Primary organic aerosol (POA) is emitted directly from anthropogenic and natural sources (Després et al., 2012). A significant fraction of fine-mode POA (<2.5μm) is semi-volatile and can partition between the gas and particle phase depending on background temperatures and OC concentrations (Grieshop et al., 2009; Robinson et al., 2007). These POA are co-emitted through combustion processes, much like BC. This includes combustion of fossil and biogenic fuels and

wildfires, global fluxes of which are estimated to be 55.4 Tg yr^{-1} (Pai et al., 2020). These emissions dominate OC in urban regions and are a main component of $PM_{2.5}$ pollution in urban regions (Donahue et al., 2009; Rivellini et al., 2019; Theodoritsi et al., 2020). In marine environments, natural sources of POA include mechanically generated sea spray, which may originate from the surfactant-rich sea-surface microlayer (SSML), biogenically-derived particulate organic matter (POM), and/or dissolved organic carbon (DOC). Current GEOS-CHEM parametrizations estimate marine POA emissions 15 Tg yr^{-1} and have an average lifetime of 3 days (Gantt et al., 2015; Pai et al., 2020).

Furthermore, semi-volatile volatile organic compounds (SMVOCs) co-emitted through combustion (natural or anthropogenic) or anthropogenic activities undergo further atmospheric chemical- (by O_3, OH, or NO_3) and photooxidation, which lowers the volatility to the point of forming secondary organic aerosol (SOA) through condensation. Natural biogenic volatile organic compounds (BVOCs), such as mono- and sesquiterpenes emitted by plants and trees, also undergo similar atmospheric aging prior to forming fine-mode SOA. The highest concentrations of SOA are observed in various peri-urban regions around the world, where BVOCs interact with urban SMVOCs and undergo photooxidation (Gentner et al., 2017; Kim et al., 2015; Nault et al., 2018). SOA formation is estimated to range between 12 and 70 Tg yr^{-1} (Kanakidou et al., 2005).

OC are incredibly challenging to model in the climate system due to the dynamic and uncertain nature of the OC life cycle, particularly in remote regions as observations remain sparse. Currently models underestimate OC contribution to total aerosol mass in remote regions (Hodzic et al., 2020), which leads to uncertainties in determining radiative forcing attributed to OC.

1.3.2 Climate impacts

Direct OC impacts on global radiative forcing are dependent on OC-shortwave radiation interactions that can vary significantly (Table 1.2). Uncolored OC scatters visible radiation, imparting a cooling effect. Nonetheless, the degree of scattering is dependent on the OC source (Lin et al., 2014). Vice versa, colored OC (i.e. brown carbon or BrC) absorbs a significant fraction of visible radiation and much like BC, can have a warming effect. BrC is generated during low-temperature combustion, such as biogenic fuel burning or wildfires. However, BrC has a limited lifespan due to efficient aging mechanisms that lower its absorptivity, such as photobleaching (Lee et al., 2014; Zhao et al., 2015). Estimates of the direct forcing of OC range from -0.12 to -0.43 W m^{-2} (Lin et al., 2014; Tilmes et al., 2019).

Characterizing the indirect radiative effect of OC is further challenging since OC can act as CCN to alter cloud micro- and macrophysical characteristics, such as rain output, cloud lifetime, and subsequent radiative impacts. For example, incorporating marine OC showed an increase in low-level in-cloud droplet number concentration, particularly in areas such as the Southern Ocean where OC is prevalent. This effect was attributed to an increased indirect forcing value from -1.38 to -1.29 W m^{-2} (Gantt et al., 2012).

Table 1.2 Overview of OC radiative forcing estimates

Effect	Radiative Forcing W m^{-2}	References
Direct Radiative Effect	-0.12 to -0.43	Lin et al., 2014; Tilmes et al., 2019
Indirect Effect	-1.38 to -1.29	Gantt et al., 2012

1.3.3 Implications for future Arctic climate

The role of OC in future Arctic climate is uncertain with available studies focusing on characterizing sources and atmospheric processing of marine emissions, less has been done to assess terrestrial BVOCs and their contribution to SOA formation in the Arctic. Terrestrial BVOC

studies (Faubert et al., 2010; Lindwall et al., 2016; Potosnak et al., 2013) are limited to the lower Arctic. Shifting productivity and ecosystem paradigms could provide a significant additional source of SOA in the high Arctic, which is currently unassessed.

The Arctic's OC burden depends on marine POA flux or condensable OC for SOA formation. These fluxes are expected to increase due to sea ice extent decline during the summer months (Browse et al., 2014). Still, prevalent summertime ultrafine SOA (5-50 nm) from particle forming events are an important component to OC because of their ability to act as CCN (Burkart et al., 2017; Collins et al., 2017). Furthermore, new ultrafine particles observed were in pristine ice-free boundary layer in productive regions where background particles are 100-150 cm^{-3}, suggesting that ultrafine SOA have a biogenic origin (Croft et al., 2019; Lange et al., 2019; Willis et al., 2016, 2017). This suggests that future Arctic marine productivity may play an important role in mitigating future Arctic warming since current estimates indicate that the direct and indirect effects of SOA are cooling in nature (-0.04 and -0.4 W m^{-2} respectively) (Croft et al., 2019).

1.4 Characterization of carbonaceous aerosol

1.4.1 Brief overview of common methods

Methods for characterizing carbonaceous aerosol fall into two main categories: *in-situ* and offline methods. *In-situ* methods offer short temporal resolutions, which is valuable in determining the evolution of an observed space but can be limited in the level of detail the analysis provides. Offline methods are limited in temporal resolution but can offer detailed chemical analysis.

Common *in-situ* analysis of carbonaceous aerosol characterizes its optical properties. For BC, this measures the aerosol's ability to absorb visible radiation by measuring the extinction of incident light due to the absorption. Common techniques include particle soot absorption photometer (PSAP), aethalometer, and the single-particle soot photometer (SP2), all of which differ in

sensitivity and type of BC measured (Sharma et al. 2017). For OC, measuring the scattering ability is not useful as sulfate and liquid droplets, other prevalent components of atmospheric aerosol, also scatter radiation. OC concentrations are instead determined via mass spectrometry, which provides detailed OC mass concentration and molecular composition information with high temporal resolution. The most popular technique is the time-of-flight aerosol mass spectrometer (ToF-AMS), which can size and provide mass spectra of individual particles (Drewnick et al., 2005). These *in-situ* techniques are also often coupled with particle counters and sizers, such as the Condensation Particle Counter (CPC), Scanning Mobility Particle Sizer (SMPS), and Aerodynamic Particle Sizer (APS).

Offline methods of carbonaceous aerosol require collection on an inert filter, such as quartz fiber, prior to analysis. Common techniques include thermo-evolution and chromatography in conjunction with mass spectrometry. Thermo-optical analysis, such as the OC/BC analyzer, utilizes a temperature protocol to induce thermally desorb OC and BC separately (Chan et al., 2019; Chow et al., 2004; Huang et al., 2006; Mouteva et al., 2015; Zencak et al., 2007; Zhang et al., 2012). The carbonaceous material is then oxidized to CO_2 and quantified with either a nondispersive infrared (NDIR) sensor or reduced methane and quantified with flame ionization detector (FID). A red laser focused on the collected filter indicates changes in transmission of the filter throughout the temperature protocol, which shows the evolution of light-absorbing colors and any pyrolization occurring on the filter. Gas chromatographic techniques (i.e GC) involve either dissolving or thermally desorbing aerosol on collected filters prior to chromatographic separation (Eglinton et al., 1996). The separated effluent is then chemically characterized with mass spectrometry, which can range in their ionization and mass spectrometry technique. The products often include detailed mass spectra with molecular compositions based on the effluent time and

mass to charge ratio measured. This technique is useful for detecting tracers for biomass burning and fossil combustion. Bridging compound-specific and thermal-evolution techniques is challenging due to differing method sensitivities but is necessary to integrate for powerful aerosol characterization.

1.4.2 Radiocarbon as a source apportionment tool

Characterizing the radiocarbon (^{14}C) content of bulk aerosol and its fractions offers a powerful tool for quantifying emissions sources. ^{14}C is a naturally occurring radioisotope (5,730-year half-life) produced in the atmosphere. Once oxidized to carbon dioxide ($^{14}CO_2$), ^{14}C enters the food chain through photosynthesis which labels living organisms with the same characteristic $^{14}C/^{12}C$ ratio as that of the atmosphere. Materials containing carbon older than about 50,000 years are described as "fossil" carbon as $^{14}C/^{12}C$ ratio approaches zero from beta-decay. Over the past centuries, the ^{14}C content of the atmosphere has undergone distinct changes (Graven, 2015; Levin et al., 2010). Nuclear weapons testing doubled the ^{14}C content of CO_2 in the Northern Hemisphere in the mid-20th century, followed by a rapid decline due to mixing of this bomb-derived ^{14}C-enriched carbon into the ocean and biosphere. Any materials containing this "bomb"-C (including all biomass produced since the 1950s) are referred to as "modern". Concurrently, emissions of ^{14}C-free carbon emitted through anthropogenic combustion of fossil fuels continue to dilute the proportion of ^{14}C relative to ^{12}C.

Aerosol ^{14}C content can be used to ascertain relative contributions from contemporary biomass and fossil sources (Heal, 2014). This technique utilizes the stark contrasts in ^{14}C content (*FM*) between the two sources and employs a simple 2-source mass balance model to quantify the contemporary (f_c) and fossil (f_f) fractions as described by Eq. 1 and Eq. 2.

$$1 = f_c + f_f \qquad \textit{Eq. 1}$$

$$FM_m = f_c FM_c + f_f FM_f \qquad \textit{Eq. 2}$$

Where FM_m is the measured radiocarbon content, FM_c is the ^{14}C content of contemporary source, and FM_f is the ^{14}C content of the fossil source. This source attribution can be done separately for OC and BC. However, contrasting sources to OC and BC require clear separation, which, as is discussed in Chapter 2, is operationally defined because carbonaceous aerosol exists as a spectrum when characterized by its thermal and optical properties (Zenker et al., 2017; Zhang et al., 2012). This, along with sample masses required for precise measurement, pose the main challenges to utilizing ^{14}C to quantify fossil and contemporary sources, particularly in the pristine Arctic atmosphere.

1.4.3 Multi-source characterization with multiple isotopes

Source apportionment of additional sources can be determined by measuring other isotopes (i.e. $\delta^{13}C$, $\delta^{15}N$) provided that each source has distinct isotopic profiles for each isotope and the source's variance in isotopic values is limited. For example, $^{13}C/^{12}C$ and $^{14}C/^{12}C$ ratios can be used in conjunction to quantify three sources with the mass balance approach. This adds a third term to *Eq. 1* and *Eq. 2* and a third linear equation delineating the sources and fractions of the ^{13}C isotope. To generate a single solution to the system of linear equations, each additional source must include an additional mass-balance equation characterizing another isotope. Characterizing the solution's uncertainty based off variance in the source's and measured isotopic value (i.e. from repeated measurements) is done with simple statistical models such as EPA's IsoError (Phillips & Gregg, 2001).

In the case that sources outnumber the number of isotopes measured, statistical methods, such as the IsoSource model (Phillips et al., 2005; Phillips & Gregg, 2003) can be used. This model calculates all feasible solutions within % tolerances provided. The statistics of the results

can then be used to interpret the likely ranges of potential contributions. This technique requires distinct isotopic profiles for the sources and limited variance of the isotopic values of the source to yield meaningful information. Source contributions of multiple sources (3+) can also be used in conjunction with chemical tracer measurements to verify multi-isotopic source attribution results.

1.5 Organization of dissertation

In my thesis, I combined method development, data collection in the field, and atmospheric modeling to improve our understanding of BC and OC sources in fine airborne particulate matter of diverse environments. By characterizing the isotopic composition of OC and BC, I was able to explore the shifting nature of source contribution in the long- and short-term. A major goal of this dissertation is to report a benchmark dataset for use in modelling efforts aiming to accurately model carbonaceous aerosol sources and lifecycle. This is urgently needed to mitigate current uncertainties about the current and future impact of OC and BC on climate, air quality, and the carbon cycle.

In an effort to constrain the differences in techniques that measure ^{14}C of OC and BC and make the data more accessible for current and future monitoring and modeling work, Chapter 2 evaluates the efficacy of the ECT9 protocol to physically separate and trap OC and BC microsamples (<100 µg C) for accurate ^{14}C analysis. The ECT9 protocol is a new temperature protocol developed by the carbonaceous aerosol & isotope research (CAIR) lab of Environment and Climate Change Canada (ECCC) whereby a modified thermal-optical OC/BC analyzer is attached to a vacuum line to cryogenically trap and purify desorbed OC and BC in the form of CO_2. Trapped CO_2 was then graphitized and analyzed via accelerator mass spectrometry (AMS) at the UC Irvine KCCAMS facility. The work was done by measuring the ^{14}C content of individual OC and BC standards of varying sizes and ^{14}C content to quantify the extraneous carbon incorporated

throughout the analytical process. Furthermore, OC and BC pure standards were mixed prior to ^{14}C analysis to evaluate the efficacy of OC/BC physical separation. Quantified extraneous carbon and optical observations were directly compared to the Swiss_4S thermal-optical protocol developed by University of Bern, Switzerland (Zhang et al., 2012) and evaluated by Mouteva et al. (2015). Finally, the results from a mixed particulate matter (SRM 1649a) standard were discussed in comparison to other ^{14}C measurements with other protocols to evaluate biases and limitations of the protocol. The ECT9 technique was found effective at physically separating exclusively non-refractory OC and highly refractory BC compared to the Swiss_4S protocol and can be applied directly to monitoring networks previously and currently using this protocol to quantify OC/BC concentrations.

Driven by quick Arctic climate warming and limited High Arctic aerosol source data, Chapter 3 utilizes the ECT9 protocol to quantify BC concentrations and the fossil fuel contribution to BC in total suspended particulates (TSP) and snow collected at the Dr. Neil Trivett Global Atmosphere Watch Observatory at Alert, Nunavut Canada, an important long-term monitoring facility, over the course of one year (2014-2015). I describe the seasonal cycle of BC due to synoptic-scale meteorology and air mass source regions as described by back trajectories. Furthermore, we quantified the fossil fuel source contributions and seasonal cycle to show that BC is primarily dominated by fossil sources throughout fall, winter, and spring and have major geographical sources from the Russian Arctic sector. Additionally, summer BC is dominated by biomass burning in the North American Arctic sector as shown by GFED v4.1 Summer 2014 biomass burning emissions and relatively enriched ^{14}C values. BC in snow was enriched relatively to BC in TSP, though this effect was not homogeneous. Finally, the chapter discusses the implications of these results in context of previous measurements and the major global sources of BC

within the Arctic currently and in the future. BC in PM at Alert is dominated by fossil fuel emissions year-round except during summer, where biomass burning from North America plays an important role. Prevalent air masses throughout Fall-Spring were from the Russian sector, though long-range contributions from Asia cannot be excluded. Finally, high biomass burning contributions in snow BC suggests wet deposition may be a key pathway for transporting long-range transport emissions from the upper troposphere.

Motivated by the uncertainties in sources to marine OC in the context of the carbon cycle (Barrett & Sheesley, 2017), Chapter 4 explores the various marine and terrestrial sources to OC aerosol across the northern Pacific and into the Arctic. I used dual-isotopes (^{13}C, and ^{14}C) in a multi-source model to quantify the contributions from refractory dissolved organic carbon (RDOC), fresh biomass, and liquid fossil combustion-related organics. This chapter reports that a significant portion of terrestrial air masses significantly contribute to aerosol in coastal regions, as was the case in air masses sampled over the East/Japan Sea and Nome, Alaska. Additionally, the contribution from surface biology to ambient OC aerosol was discussed using non-sea salt sulfate, active surface productivity, and aerosol MSA observations. This chapter found that remote marine aerosol was dominated by RDOC in the North Pacific and the Bering Sea. Marine aerosol in highly productive regions, such as the Bering Sea and Bering Strait, are influenced by biogenically-derived biomass. This work suggests marine RDOC and POC are important contributors to marine OC and may play an important role in future Arctic climate change.

Finally, Chapter 5 summarizes the main scientific findings of the dissertation and provides future research direction. The implications for each chapter are discussed and their contribution to understanding the sources to OC and BC aerosol in both remote and anthropogenically-influenced marine environments is highlighted. This chapter details the significance of the conclusions and

outlines important remaining questions that, when answered, provide a better understanding of the sources and sinks of OC and BC aerosol. My dissertation successfully evaluated a new method for ^{14}C observations that can be directly linked with an important long-term monitoring facility (Alert) in the High Arctic. With one year's observations at Alert, I demonstrated strong synoptic dependency for fossil contributions at Alert and showed the drastic seasonal shifts in combustion and geographical sources to BC. Furthermore, I was first to measure ^{14}C in snow BC and showed that snow BC contains higher biomass burning contributions, which may be linked to transport from the upper troposphere. Lastly, I explored the role of RDOC in atmospheric aerosol of remote, coastal, and Arctic regions, which offers important insights on the sources and fates of RDOC in the atmosphere.

1.6 References

Ahmed, R., Prowse, T., Dibike, Y., Bonsal, B., & O'Neil, H. (2020). Recent Trends in Freshwater Influx to the Arctic Ocean from Four Major Arctic-Draining Rivers. *Water, 12*(4), 1189. https://doi.org/10.3390/w12041189

AMAP. (2015). *AMAP assessment 2015: Black carbon and ozone as Arctic climate forcers*. *Arctic Monitoring and Assessment Programme (AMAP)*. Oslo, Norway. Retrieved from https://www.amap.no/documents/doc/amap-assessment-2015-black-carbon-and-ozone-as-arctic-climate-forcers/1299

Andreae, M. O., & Gelencsér, A. (2006). Black carbon or brown carbon? The nature of light-absorbing carbonaceous aerosols. *Atmospheric Chemistry and Physics*, *6*, 3131–3148. https://doi.org/10.5194/acp-6-3131-2006

Barrett, T. E., & Sheesley, R. J. (2017). Year-round optical properties and source characterization

of Arctic organic carbon aerosols on the North Slope Alaska. *Journal of Geophysical Research: Atmospheres*, *122*(17), 9319–9331. https://doi.org/10.1002/2016JD026194

Bauer, S. E., Menon, S., Koch, D., Bond, T. C., & Tsigaridis, K. (2010). A global modeling study on carbonaceous aerosol microphysical characteristics and radiative effects. *Atmospheric Chemistry and Physics*, *10*(15), 7439–7456. https://doi.org/10.5194/acp-10-7439-2010

Biskaborn, B. K., Smith, S. L., Noetzli, J., Matthes, H., Vieira, G., Streletskiy, D. A., et al. (2019). Permafrost is warming at a global scale. *Nature Communications*, *10*(1), 264. https://doi.org/10.1038/s41467-018-08240-4

Bond, T. C., Doherty, S. J., Fahey, D. W., Forster, P. M., Berntsen, T., Deangelo, B. J., et al. (2013). Bounding the role of black carbon in the climate system: A scientific assessment. *Journal of Geophysical Research Atmospheres*, *118*(11), 5380–5552. https://doi.org/10.1002/jgrd.50171

Bond, Tami C., Bhardwaj, E., Dong, R., Jogani, R., Jung, S., Roden, C., et al. (2007). Historical emissions of black and organic carbon aerosol from energy-related combustion, 1850-2000. *Global Biogeochemical Cycles*, *21*(2), n/a-n/a. https://doi.org/10.1029/2006GB002840

Bourgeois, Q., & Bey, I. (2011). Pollution transport efficiency toward the Arctic: Sensitivity to aerosol scavenging and source regions. *Journal of Geophysical Research*, *116*(D8), D08213. https://doi.org/10.1029/2010JD015096

Browse, J., Carslaw, K. S., Arnold, S. R., Pringle, K., & Boucher, O. (2012). The scavenging processes controlling the seasonal cycle in Arctic sulphate and black carbon aerosol. *Atmospheric Chemistry and Physics*, *12*(15), 6775–6798. https://doi.org/10.5194/acp-12-6775-2012

Browse, J., Carslaw, K. S., Mann, G. W., Birch, C. E., Arnold, S. R., & Leck, C. (2014). The complex response of Arctic aerosol to sea-ice retreat. *Atmospheric Chemistry and Physics*, *14*(14), 7543–7557. https://doi.org/10.5194/acp-14-7543-2014

Burkart, J., Hodshire, A. L., Mungall, E. L., Pierce, J. R., Collins, D. B., Ladino, L. A., et al. (2017). Organic Condensation and Particle Growth to CCN Sizes in the Summertime Marine Arctic Is Driven by Materials More Semivolatile Than at Continental Sites. *Geophysical Research Letters*, *44*(20), 10,725-10,734. https://doi.org/10.1002/2017GL075671

Chadburn, S. E., Burke, E. J., Cox, P. M., Friedlingstein, P., Hugelius, G., & Westermann, S. (2017). An observation-based constraint on permafrost loss as a function of global warming. *Nature Climate Change*, *7*(5), 340–344. https://doi.org/10.1038/nclimate3262

Chan, T. W., Huang, L., Banwait, K., Zhang, W., Ernst, D., Wang, X., et al. (2019). Inter-comparison of elemental and organic carbon mass measurements from three North American national long-term monitoring networks at a co-located site. *Atmospheric Measurement Techniques*, *12*(8), 4543–4560. https://doi.org/10.5194/amt-12-4543-2019

Cherian, R., Quaas, J., Salzmann, M., & Tomassini, L. (2017). Black carbon indirect radiative effects in a climate model. *Tellus, Series B: Chemical and Physical Meteorology*, *69*(1), 1–10. https://doi.org/10.1080/16000889.2017.1369342

Chow, J. C., Watson, J. G., Chen, L. W. A., Arnott, W. P., Moosmüller, H., & Fung, K. (2004). Equivalence of elemental carbon by thermal/optical reflectance and transmittance with different temperature protocols. *Environmental Science and Technology*, *38*(16), 4414–4422. https://doi.org/10.1021/es034936u

Collins, D. B., Burkart, J., Chang, R. Y.-W., Lizotte, M., Boivin-Rioux, A., Blais, M., et al.

(2017). Frequent ultrafine particle formation and growth in the Canadian Arctic marine and coastal environments. *Atmospheric Chemistry and Physics*, *17*(21), 13119-13138. https://doi.org/10.5194/acp-17-13119-2017

Comiso, J. C. (2015). 1. Variability and trends of global sea ice cover and sea level: effects on physicochemical parameters. *Climate Change and Marine and Freshwater Toxins*, 1–34. https://doi.org/10.1515/9783110333596-003

Croft, B., Martin, R. V., Richard Leaitch, W., Burkart, J., Chang, R. Y. W., Collins, D. B., et al. (2019). Arctic marine secondary organic aerosol contributes significantly to summertime particle size distributions in the Canadian Arctic Archipelago. *Atmospheric Chemistry and Physics*, *19*(5), 2787–2812. https://doi.org/10.5194/acp-19-2787-2019

Després, V. R., Alex Huffman, J., Burrows, S. M., Hoose, C., Safatov, A. S., Buryak, G., et al. (2012). Primary biological aerosol particles in the atmosphere: A review. *Tellus, Series B: Chemical and Physical Meteorology*, *64*(1). https://doi.org/10.3402/tellusb.v64i0.15598

Donahue, N. M., Robinson, A. L., & Pandis, S. N. (2009). Atmospheric organic particulate matter: From smoke to secondary organic aerosol. *Atmospheric Environment*, *43*(1), 94–106. https://doi.org/10.1016/j.atmosenv.2008.09.055

Dong, X., Zhu, Q., Fu, J. S., Huang, K., Tan, J., & Tipton, M. (2019). Evaluating Recent Updated Black Carbon Emissions and Revisiting the Direct Radiative Forcing in Arctic. *Geophysical Research Letters*, *46*(6), 3560–3570. https://doi.org/10.1029/2018GL081242

Drewnick, F., Hings, S. S., DeCarlo, P., Jayne, J. T., Gonin, M., Fuhrer, K., et al. (2005). A new time-of-flight aerosol mass spectrometer (TOF-AMS) - Instrument description and first field deployment. *Aerosol Science and Technology*, *39*(7), 637–658. https://doi.org/10.1080/02786820500182040

Durocher, M., Requena, A. I., Burn, D. H., & Pellerin, J. (2019). Analysis of trends in annual streamflow to the Arctic Ocean. *Hydrological Processes*, *33*(7), 1143–1151. https://doi.org/10.1002/hyp.13392

Eglinton, T. I., Aluwihare, L. I., Bauer, J. E., Druffel, E. R. M., & McNichol, A. P. (1996). Gas chromatographic isolation of individual compounds from complex matrices for radiocarbon dating. *Analytical Chemistry*, *68*(5), 904–912. https://doi.org/10.1021/ac9508513

Faubert, P., Tiiva, P., Rinnan, Å., Michelsen, A., Holopainen, J. K., & Rinnan, R. (2010). Doubled volatile organic compound emissions from subarctic tundra under simulated climate warming. *New Phytologist*, *187*(1), 199–208. https://doi.org/10.1111/j.1469-8137.2010.03270.x

Flanner, M. G., Zender, C. S., Hess, P. G., Mahowald, N. M., Painter, T. H., Ramanathan, V., & Rasch, P. J. (2009). Springtime warming and reduced snow cover from carbonaceous particles. *Atmospheric Chemistry and Physics*, *9*(7), 2481–2497. https://doi.org/10.5194/acp-9-2481-2009

Freud, E., Krejci, R., Tunved, P., Leaitch, R., Nguyen, Q. T., Massling, A., et al. (2017). Pan-Arctic aerosol number size distributions: Seasonality and transport patterns. *Atmospheric Chemistry and Physics*, *17*(13), 8101–8128. https://doi.org/10.5194/acp-17-8101-2017

Frey, K. E., Comiso, J. C., Cooper, L. W., Eisner, L. B., Gradinger, R. R., Grebmeier, J. M., & Tremblay, J. E. (2018). Arctic Ocean Primary Productivity: The Response of Marine Algae to Climate Warming and Sea Ice Decline. *Arctic Report Card: Update for 2011*, 1–17. Retrieved from http://www.arctic.noaa.gov/report11/primary_productivity.html

Gantt, B., Xu, J., Meskhidze, N., Zhang, Y., Nenes, A., Ghan, S. J., et al. (2012). Global

distribution and climate forcing of marine organic aerosol-Part 2: Effects on cloud properties and radiative forcing. *Atmospheric Chemistry and Physics*, *12*(14), 6555–6563. https://doi.org/10.5194/acp-12-6555-2012

Gantt, B., Johnson, M. S., Crippa, M., Prévôt, A. S. H., & Meskhidze, N. (2015). Implementing marine organic aerosols into the GEOS-Chem model. *Geoscientific Model Development*, *8*(3), 619–629. https://doi.org/10.5194/gmd-8-619-2015

Gentner, D. R., Jathar, S. H., Gordon, T. D., Bahreini, R., Day, D. A., El Haddad, I., et al. (2017). Review of Urban Secondary Organic Aerosol Formation from Gasoline and Diesel Motor Vehicle Emissions. *Environmental Science and Technology*, *51*(3), 1074–1093. https://doi.org/10.1021/acs.est.6b04509

Ghan, S. J., Liu, X., Easter, R. C., Zaveri, R., Rasch, P. J., Yoon, J. H., & Eaton, B. (2012). Toward a minimal representation of aerosols in climate models: Comparative decomposition of aerosol direct, semidirect, and indirect radiative forcing. *Journal of Climate*, *25*(19), 6461–6476. https://doi.org/10.1175/JCLI-D-11-00650.1

Gong, W., Beagley, S. R., Cousineau, S., Sassi, M., Munoz-Alpizar, R., Ménard, S., et al. (2019). Assessing the impact of shipping emissions on air pollution in the Canadian Arctic and northern regions: Current and future modelled scenarios. *Proceedings of the Air and Waste Management Association's Annual Conference and Exhibition, AWMA*, *2019-June*, 16653–16687. https://doi.org/10.5194/acp-2018-125

Graven, H. D. (2015). Impact of fossil fuel emissions on atmospheric radiocarbon and various applications of radiocarbon over this century. *Proceedings of the National Academy of Sciences*, *112*(31), 9542–9545. https://doi.org/10.1073/pnas.1504467112

Grieshop, A. P., Logue, J. M., Donahue, N. M., & Robinson, A. L. (2009). Laboratory

investigation of photochemical oxidation of organic aerosol from wood fires 1: Measurement and simulation of organic aerosol evolution. *Atmospheric Chemistry and Physics*, *9*(4), 1263–1277. https://doi.org/10.5194/acp-9-1263-2009

Gunnarsson, B. (2021). Recent ship traffic and developing shipping trends on the Northern Sea Route—Policy implications for future arctic shipping. *Marine Policy*, *124*, 104369. https://doi.org/10.1016/j.marpol.2020.104369

Hansen, J., Sato, M., Ruedy, R., Nazarenko, L., Lacis, A., Schmidt, G. A., et al. (2005). Efficacy of climate forcings. *Journal of Geophysical Research D: Atmospheres*, *110*(18), 1–45. https://doi.org/10.1029/2005JD005776

Hao, W. M., Petkov, A., Nordgren, B. L., Corley, R. E., Silverstein, R. P., Urbanski, S. P., et al. (2016). Daily black carbon emissions from fires in northern Eurasia for 2002–2015. *Geoscientific Model Development*, *9*(12), 4461–4474. https://doi.org/10.5194/gmd-9-4461-2016

Heal, M. R. (2014). The application of carbon-14 analyses to the source apportionment of atmospheric carbonaceous particulate matter: A review. *Analytical and Bioanalytical Chemistry*, *406*(1), 81–98. https://doi.org/10.1007/s00216-013-7404-1

Hirdman, D., Burkhart, J. F., Sodemann, H., Eckhardt, S., Jefferson, A., Quinn, P. K., et al. (2010). Long-term trends of black carbon and sulphate aerosol in the Arctic: changes in atmospheric transport and source region emissions. *Atmospheric Chemistry and Physics*, *10*(19), 9351–9368. https://doi.org/10.5194/acp-10-9351-2010

Hodzic, A., Campuzano-Jost, P., Bian, H., Chin, M., Colarco, P. R., Day, D. A., et al. (2020). Characterization of organic aerosol across the global remote troposphere: A comparison of ATom measurements and global chemistry models. *Atmospheric Chemistry and Physics*,

20(8), 4607–4635. https://doi.org/10.5194/acp-20-4607-2020

Huang, K., Fu, J. S., Prikhodko, V. Y., Storey, J. M., Romanov, A., Hodson, E. L., et al. (2015). Russian anthropogenic black carbon: Emission reconstruction and Arctic black carbon simulation. *Journal of Geophysical Research: Atmospheres*, *120*(21), 11306–11333. https://doi.org/10.1002/2015JD023358

Huang, L., Brook, J. R., Zhang, W., Li, S. M., Graham, L., Ernst, D., et al. (2006). Stable isotope measurements of carbon fractions (OC/EC) in airborne particulate: A new dimension for source characterization and apportionment. *Atmospheric Environment*, *40*(15), 2690–2705. https://doi.org/10.1016/j.atmosenv.2005.11.062

Jimenez, J. L., Canagaratna, M. R., Donahue, N. M., Prevot, A. S. H., Zhang, Q., Kroll, J. H., et al. (2009). Evolution of organic aerosols in the atmosphere. *Science*, *326*(February), 1526–1529.

Johnson, B. T., Shine, K. P., & Forster, P. M. (2004). The semi-direct aerosol effect: Impact of absorbing aerosols on marine stratocumulus. *Quarterly Journal of the Royal Meteorological Society*, *130*(599), 1407–1422. https://doi.org/10.1256/qj.03.61

Jones, P. D., New, M., Parker, D. E., Martin, S., & Rigor, I. G. (1999). Surface air temperature and its changes over the past 150 years. *Reviews of Geophysics*, *37*(2), 173–199. https://doi.org/10.1029/1999RG900002

Jones, P. D., Lister, D. H., Osborn, T. J., Harpham, C., Salmon, M., & Morice, C. P. (2012). Hemispheric and large-scale land-surface air temperature variations: An extensive revision and an update to 2010. *Journal of Geophysical Research: Atmospheres*, *117*(D5), n/a-n/a. https://doi.org/10.1029/2011JD017139

Jungsberg, L., Turunen, E., Heleniak, T., Wang, S., Ramage, J., & Roto, J. (2019). *Atlas of*

population, society and economy in the Arctic. Stockholm. https://doi.org/10.30689/WP2019:3.1403-2511

Kanakidou, M., Seinfeld, J. H., Pandis, S. N., Barnes, I., Dentener, F. J., Facchini, M. C., et al. (2005). Organic aerosol and global climate modelling: a review. *Atmospheric Chemistry and Physics*, *5*, 1053–1123. https://doi.org/10.5194/acp-5-1053-2005

Kim, P. S., Jacob, D. J., Fisher, J. A., Travis, K., Yu, K., Zhu, L., et al. (2015). Sources, seasonality, and trends of southeast US aerosol: An integrated analysis of surface, aircraft, and satellite observations with the GEOS-Chem chemical transport model. *Atmospheric Chemistry and Physics*, *15*(18), 10411–10433. https://doi.org/10.5194/acp-15-10411-2015

Koch, D., Menon, S., Del Genio, A., Ruedy, R., Alienov, I., & Schmidt, G. A. (2009). Distinguishing aerosol impacts on climate over the past century. *Journal of Climate*, *22*(10), 2659–2677. https://doi.org/10.1175/2008JCLI2573.1

Koch, D., Bauer, S. E., Del Genio, A., Faluvegi, G., McConnell, J. R., Menon, S., et al. (2011). Coupled aerosol-chemistry-climate twentieth-century transient model investigation: Trends in short-lived species and climate responses. *Journal of Climate*, *24*(11), 2693–2714. https://doi.org/10.1175/2011JCLI3582.1

Koenigk, T., Key, J., & Vihma, T. (2020). Climate Change in the Arctic. In A. Kokhanovsky & C. Tomasi (Eds.), *Physics and Chemistry of the Arctic Atmosphere* (pp. 673–705). Cham: Springer International Publishing. https://doi.org/10.1007/978-3-030-33566-3_11

Kwok, R. (2018). Arctic sea ice thickness, volume, and multiyear ice coverage: losses and coupled variability (1958–2018). *Environmental Research Letters*, *13*(10), 105005. https://doi.org/10.1088/1748-9326/aae3ec

Lamarque, J. F., Bond, T. C., Eyring, V., Granier, C., Heil, A., Klimont, Z., et al. (2010).

Historical (1850-2000) gridded anthropogenic and biomass burning emissions of reactive gases and aerosols: Methodology and application. *Atmospheric Chemistry and Physics*, *10*(15), 7017–7039. https://doi.org/10.5194/acp-10-7017-2010

Lange, R., Dall'Osto, M., Wex, H., Skov, H., & Massling, A. (2019). Large Summer Contribution of Organic Biogenic Aerosols to Arctic Cloud Condensation Nuclei. *Geophysical Research Letters*, *46*(20), 11500–11509. https://doi.org/10.1029/2019GL084142

Lara, M. J., Nitze, I., Grosse, G., Martin, P., & David McGuire, A. (2018). Reduced arctic tundra productivity linked with landform and climate change interactions. *Scientific Reports*, *8*(1), 1–10. https://doi.org/10.1038/s41598-018-20692-8

Law, K. S., & Stohl, A. (2007). Arctic air pollution: origins and impacts. *Science*, *315*(5818), 1537–40. https://doi.org/10.1126/science.1137695

Lee, H. J., Aiona, P. K., Laskin, A., Laskin, J., & Nizkorodov, S. A. (2014). Effect of solar radiation on the optical properties and molecular composition of laboratory proxies of atmospheric brown carbon. *Environmental Science and Technology*, *48*(17), 10217–10226. https://doi.org/10.1021/es502515r

Levin, I., Naegler, T., Kromer, B., Diehl, M., Francey, R., Gomez-Pelaez, A., et al. (2010). Observations and modelling of the global distribution and long-term trend of atmospheric 14 CO 2. *Tellus B: Chemical and Physical Meteorology*, *62*(1), 26–46. https://doi.org/10.1111/j.1600-0889.2009.00446.x

Lin, G., Penner, J. E., Flanner, M. G., Sillman, S., Xu, L., & Zhou, C. (2014). Radiative forcing of organic aerosol in the atmosphere and on snow: Effects of SOA and brown carbon. *Journal of Geophysical Research: Atmospheres*, *119*(12), 7453–7476. https://doi.org/10.1002/2013JD021186

Lindwall, F., Schollert, M., Michelsen, A., Blok, D., & Rinnan, R. (2016). Fourfold higher tundra volatile emissions due to arctic summer warming. *Journal of Geophysical Research G: Biogeosciences*, *121*(3), 895–902. https://doi.org/10.1002/2015JG003295

Mouteva, G. O., Fahrni, S. M., Santos, G. M., Randerson, J. T., Zhang, Y.-L., Szidat, S., & Czimczik, C. I. (2015). Accuracy and precision of ^{14}C-based source apportionment of organic and elemental carbon in aerosols using the Swiss_4S protocol. *Atmospheric Measurement Techniques*, *8*(9), 3729–3743. https://doi.org/10.5194/amt-8-3729-2015

Myers-Smith, I. H., & Hik, D. S. (2018). Climate warming as a driver of tundra shrubline advance. *Journal of Ecology*, *106*(2), 547–560. https://doi.org/10.1111/1365-2745.12817

Myers-Smith, I. H., Kerby, J. T., Phoenix, G. K., Bjerke, J. W., Epstein, H. E., Assmann, J. J., et al. (2020). Complexity revealed in the greening of the Arctic. *Nature Climate Change*, *10*(2), 106–117. https://doi.org/10.1038/s41558-019-0688-1

Nault, B. A., Campuzano-Jost, P., Day, D. A., Schroder, J. C., Anderson, B., Beyersdorf, A. J., et al. (2018). Secondary organic aerosol production from local emissions dominates the organic aerosol budget over Seoul, South Korea, during KORUS-AQ. *Atmospheric Chemistry and Physics*, *18*(24), 17769–17800. https://doi.org/10.5194/acp-18-17769-2018

Overland, J., Dunlea, E., Box, J. E., Corell, R., Forsius, M., Kattsov, V., et al. (2019). The urgency of Arctic change. *Polar Science*, *21*(July 2018), 6–13. https://doi.org/10.1016/j.polar.2018.11.008

Pai, S. J., Heald, C. L., Pierce, J. R., Farina, S. C., Marais, E. A., Jimenez, J. L., et al. (2020). An evaluation of global organic aerosol schemes using airborne observations. *Atmospheric Chemistry and Physics*, *20*(5), 2637–2665. https://doi.org/10.5194/acp-20-2637-2020

Penner, J. E., Zhang, S. Y., & Chuang, C. C. (2003). Soot and smoke aerosol may not warm

climate. *Journal of Geophysical Research: Atmospheres*, *108*(21), 1–9. https://doi.org/10.1029/2003jd003409

Peters, G. P., Nilssen, T. B., Lindholt, L., Eide, M. S., Glomsrød, S., Eide, L. I., & Fuglestvedt, J. S. (2011). Future emissions from shipping and petroleum activities in the Arctic. *Atmospheric Chemistry and Physics*, *11*(11), 5305–5320. https://doi.org/10.5194/acp-11-5305-2011

Petzold, A., Ogren, J. A., Fiebig, M., Laj, P., Li, S.-M., Baltensperger, U., et al. (2013). Recommendations for reporting "black carbon" measurements. *Atmospheric Chemistry and Physics*, *13*(16), 8365–8379. https://doi.org/10.5194/acp-13-8365-2013

Phillips, D. L., & Gregg, J. W. (2001). Uncertainty in source partitioning using stable isotopes. *Oecologia*, *127*(2), 171–179. https://doi.org/10.1007/s004420000578

Phillips, D. L., & Gregg, J. W. (2003). Source partitioning using stable isotopes: coping with too many sources. *Oecologia*, *136*(2), 261–269. https://doi.org/10.1007/s00442-003-1218-3

Phillips, D. L., Newsome, S. D., & Gregg, J. W. (2005). Combining sources in stable isotope mixing models: alternative methods. *Oecologia*, *144*(4), 520–527. https://doi.org/10.1007/s00442-004-1816-8

Pierrehumbert, R. T. (2014). Short-lived climate pollution. *Annual Review of Earth and Planetary Sciences*, *42*, 341–379. https://doi.org/10.1146/annurev-earth-060313-054843

Pöschl, U. (2005). Atmospheric aerosols: Composition, transformation, climate and health effects. *Angewandte Chemie - International Edition*, *44*(46), 7520–7540. https://doi.org/10.1002/anie.200501122

Potosnak, M. J., Baker, B. M., Lestourgeon, L., Disher, S. M., Griffin, K. L., Bret-Harte, M. S., & Starr, G. (2013). Isoprene emissions from a tundra ecosystem. *Biogeosciences*, *10*(2),

871–889. https://doi.org/10.5194/bg-10-871-2013

Qi, L., Li, Q., Henze, D. K., Tseng, H. L., & He, C. (2017). Sources of springtime surface black carbon in the Arctic: An adjoint analysis for April 2008. *Atmospheric Chemistry and Physics*, *17*(15), 9697–9716. https://doi.org/10.5194/acp-17-9697-2017

Quinn, P. K., Shaw, G., Andrews, E., Dutton, E. G., Ruoho-Airola, T., & Gong, S. L. (2007). Arctic haze: current trends and knowledge gaps. *Tellus B*, *59*(1), 115–129. https://doi.org/10.3402/tellusb.v59i1.16972

Richter-Menge, J., Druckenmiller, M. L., & Jeffries, M. (2019). Arctic Report Card 2019, 100. Retrieved from http://www.arctic.noaa.gov/Report-Card

Ricker, R., Hendricks, S., Kaleschke, L., Tian-Kunze, X., King, J., & Haas, C. (2017). A weekly Arctic sea-ice thickness data record from merged CryoSat-2 and SMOS satellite data. *The Cryosphere*, *11*(4), 1607-1623. https://doi.org/10.5194/tc-11-1607-2017

Rivellini, L.H., Adam, M., Kasthuriarachchi, N., & Lee, A.K.Y. (2020). Characterization of carbonaceous aerosols in Singapore: insight from black carbon fragments and trace metal ions detected by a soot-particle aerosol mass spectrometer. *Atmospheric Chemistry and Physics*, *20*(10), 5977-5993. https://doi.org/10.5194/acp-20-5977-2020

Robinson, A. L., Donahue, N. M., Shrivastava, M. K., Weitkamp, E. a, Sage, A. M., Grieshop, A. P., et al. (2007). Rethinking Organic Aerosols : *Science*, *315*, 1259–1262. https://doi.org/10.1126/science.1133061

Rood, S. B., Kaluthota, S., Philipsen, L. J., Rood, N. J., & Zanewich, K. P. (2017). Increasing discharge from the Mackenzie River system to the Arctic Ocean. *Hydrological Processes*, *31*(1), 150–160. https://doi.org/10.1002/hyp.10986

Samset, B. H., Myhre, G., Schulz, M., Balkanski, Y., Bauer, S., Berntsen, T. K., et al. (2013).

Black carbon vertical profiles strongly affect its radiative forcing uncertainty. *Atmospheric Chemistry and Physics*, *13*(5), 2423–2434. https://doi.org/10.5194/acp-13-2423-2013

Samset, Bjrn H., & Myhre, G. (2011). Vertical dependence of black carbon, sulphate and biomass burning aerosol radiative forcing. *Geophysical Research Letters*, *38*(24), 1–5. https://doi.org/10.1029/2011GL049697

Sharma, S., Andrews, E., Barrie, L. A., Ogren, J. A., & Lavoué, D. (2006). Variations and sources of the equivalent black carbon in the high Arctic revealed by long-term observations at Alert and Barrow: 1989-2003. *Journal of Geophysical Research Atmospheres*, *111*(14), 1989–2003. https://doi.org/10.1029/2005JD006581

Sharma, S., Richard Leaitch, W., Huang, L., Veber, D., Kolonjari, F., Zhang, W., et al. (2017). An evaluation of three methods for measuring black carbon in Alert, Canada. *Atmospheric Chemistry and Physics*, *17*(24), 15225–15243. https://doi.org/10.5194/acp-17-15225-2017

Shaw, G. E., Stamnes, K., & Hu, Y. X. (1993). Arctic haze: Perturbation to the radiation field. *Meteorology and Atmospheric Physics*, *51*(3–4), 227–235. https://doi.org/10.1007/BF01030496

Skeie, R. B., Berntsen, T., Myhre, G., Pedersen, C. A., Ström, J., Gerland, S., & Ogren, J. A. (2011). Black carbon in the atmosphere and snow, from pre-industrial times until present. *Atmospheric Chemistry and Physics*, *11*(14), 6809–6836. https://doi.org/10.5194/acp-11-6809-2011

Slater, A. G., & Lawrence, D. M. (2013). Diagnosing Present and Future Permafrost from Climate Models. *Journal of Climate*, *26*(15), 5608–5623. https://doi.org/10.1175/JCLI-D-12-00341.1

Stephenson, S. R., Wang, W., Zender, C. S., Wang, H., Davis, S. J., & Rasch, P. J. (2018).

Climatic Responses to Future Trans-Arctic Shipping. *Geophysical Research Letters*, *45*(18), 9898–9908. https://doi.org/10.1029/2018GL078969

Stohl, A., Klimont, Z., Eckhardt, S., Kupiainen, K., Shevchenko, V. P., Kopeikin, V. M., & Novigatsky, A. N. (2013). Black carbon in the Arctic: The underestimated role of gas flaring and residential combustion emissions. *Atmospheric Chemistry and Physics*, *13*(17), 8833–8855. https://doi.org/10.5194/acp-13-8833-2013

Theodoritsi, G. N., Posner, L. N., Robinson, A. L., Yarwood, G., Koo, B., Morris, R., et al. (2020). Biomass burning organic aerosol from prescribed burning and other activities in the United States. *Atmospheric Environment*, *241*(June), 117753. https://doi.org/10.1016/j.atmosenv.2020.117753

Tilmes, S., Hodzic, A., Emmons, L. K., Mills, M. J., Gettelman, A., Kinnison, D. E., et al. (2019). Climate Forcing and Trends of Organic Aerosols in the Community Earth System Model (CESM2). *Journal of Advances in Modeling Earth Systems*, *11*(12), 4323–4351. https://doi.org/10.1029/2019MS001827

Wang, H., Rasch, P. J., Easter, R. C., Singh, B., Zhang, R., Ma, P.-L., et al. (2014). Using an explicit emission tagging method in global modeling of source-receptor relationships for black carbon in the Arctic: Variations, sources, and transport pathways. *Journal of Geophysical Research: Atmospheres*, *119*(22), 12,888-12,909. https://doi.org/10.1002/2014JD022297

Willis, M. D., Burkart, J., Thomas, J. L., Köllner, F., Schneider, J., Bozem, H., et al. (2016). Growth of nucleation mode particles in the summertime Arctic: a case study. *Atmospheric Chemistry and Physics*, *16*(12), 7663–7679. https://doi.org/10.5194/acp-16-7663-2016

Willis, M. D., Köllner, F., Burkart, J., Bozem, H., Thomas, J. L., Schneider, J., et al. (2017).

Evidence for marine biogenic influence on summertime Arctic aerosol. *Geophysical Research Letters*, *44*(12), 6460–6470. https://doi.org/10.1002/2017GL073359

Xu, J. W., Martin, R. V., Morrow, A., Sharma, S., Huang, L., Richard Leaitch, W., et al. (2017). Source attribution of Arctic black carbon constrained by aircraft and surface measurements. *Atmospheric Chemistry and Physics*, *17*(19), 11971–11989. https://doi.org/10.5194/acp-17-11971-2017

Zencak, Z., Elmquist, M., & Gustafsson, Ö. (2007). Quantification and radiocarbon source apportionment of black carbon in atmospheric aerosols using the CTO-375 method. *Atmospheric Environment*, *41*, 7895–7906.

Zenker, K., Vonwiller, M., Szidat, S., Calzolai, G., Giannoni, M., Bernardoni, V., et al. (2017). Evaluation and inter-comparison of oxygen-based OC-EC separation methods for radiocarbon analysis of ambient aerosol particle samples. *Atmosphere*, *8*(11). https://doi.org/10.3390/atmos8110226

Zhang, Y. L., Perron, N., Ciobanu, V. G., Zotter, P., Minguillón, M. C., Wacker, L., et al. (2012). On the isolation of OC and EC and the optimal strategy of radiocarbon-based source apportionment of carbonaceous aerosols. *Atmospheric Chemistry and Physics*, *12*(22), 10841–10856. https://doi.org/10.5194/acp-12-10841-2012

Zhao, R., Lee, A. K. Y., Huang, L., Li, X., Yang, F., & Abbatt, J. P. D. (2015). Photochemical processing of aqueous atmospheric brown carbon. *Atmos. Chem. Phys*, *15*, 6087–6100. https://doi.org/10.5194/acp-15-6087-2015

Chapter 2

Application of the ECT9 protocol for radiocarbon-based source apportionment of carbonaceous aerosols

Adapted from:

Huang, L., Zhang, W., Santos, G.M., Rodríguez B.T., Holden S.R., and Czimczik C.I (2020) Application of the ECT9 protocol for radiocarbon-based source apportionment of carbonaceous aerosols, *Atmospheric Measurement Techniques Discussions*, 1-51.

2.1 Introduction

Carbonaceous aerosol is a major component (15-90%) of airborne particulate matter (PM) (Hand et al., 2013; Jimenez et al., 2009; Putaud et al., 2010; Ridley et al., 2017; Yang et al., 2011), and a complex mixture composed of light-scattering organic carbon (OC) and highly-refractory, light-absorbing black carbon (BC, also referred to as black carbon) (Pöschl, 2005). The OC and BC fractions play important and often distinct roles in climate (Bond et al., 2013; Hallquist et al., 2009; Kanakidou et al., 2005; Laskin et al., 2015), air pollution and human health (Cohen et al., 2017; Grahame et al., 2014; Janssen et al., 2012). Moreover, both OC and BC were identified as short-lived climate forcers (SLCFs) by the IPCC expert meeting (https://www.ipcc-nggip.iges.or.jp/public/mtdocs/1805_Geneva.html) in 2018. To develop and monitor the efficiency of mitigation strategies for both climate change and air pollution, it is required to have a better understanding of the temporal and spatial dynamics of OC and BC emission sources.

The majority (>50%) of carbonaceous aerosol is OC, which has a wide size range. Coarse OC (in PM_{10}) consists of plant debris, microorganisms, fungal spores, and pollen. Fine OC (in $PM_{2.5}$) is formed predominantly via the oxidation or nucleation/coagulation of volatile organic compounds, such as mono- and sesquiterpenes, from both biogenic and anthropogenic sources (Shrivastava et al., 2017), but can also be directly emitted from combustion sources (Fuzzi et al., 2015; Hallquist et al., 2009). In contrast, BC is found primarily in fine particles, e.g., $PM_{1.0}$ or smaller (Bond et al., 2013; Chan et al., 2013) as it is emitted through incomplete combustion of fossil fuels and biomass/biofuels (Bond et al., 2013; Evangeliou et al., 2016; Huang et al., 2010; Winiger et al., 2016, 2017, 2019).

Measuring the isotopic signature and composition, i.e. radiocarbon (^{14}C) content and stable isotope ratio ($^{13}C/^{12}C$) of aerosol, offers a powerful tool for quantifying the sources of bulk aerosol and its OC and BC fractions. Aerosol ^{14}C content can be used to quantify the relative contributions from contemporary biomass and fossil sources (Heal, 2014). ^{14}C is a naturally occurring radioisotope (5,730-year half-life) produced in the atmosphere. After its oxidation to carbon dioxide ($^{14}CO_2$), ^{14}C enters the food chain through photosynthesis so that all living organisms are labeled with a characteristic $^{14}C/^{12}C$ ratio and described as "modern" carbon. Materials containing carbon older than about 50,000 years ($^{14}C << ^{12}C$) are described as "fossil" carbon. Over the past centuries, the ^{14}C content of the atmosphere has undergone distinct changes (Graven, 2015; Levin et al., 2010): Anthropogenic combustion of fossil fuels emit ^{14}C-depleted carbon into the atmosphere (i.e. dilute the proportion of ^{14}C relative to ^{12}C). In contrast, nuclear weapons testing doubled the ^{14}C content of CO_2 in the Northern Hemisphere in the mid-20th century, followed by mixing of this bomb-derived ^{14}C-enriched carbon into the ocean and biosphere. Similarly, aerosol stable isotope ratios provide insight to different types of anthropogenic sources (e.g. combustion

of solid and liquid vs. gasesous fossil fuels). However, ^{13}C data cannot distinguish emissions from mixed fossil fuel combustion and live C3 plant biomass (Huang et al., 2006; Winiger et al., 2016). Thus, isotope-based source apportionment studies become particularly insightful when both ^{14}C and stable carbon isotopes are considered (Andersson et al., 2015; Winiger et al., 2016, 2017) or when combined with analyses of specific source tracers, such as levoglucosan or potassium for wood burning emissions (Sönke Szidat et al., 2006; Zhang et al., 2008) and/or remote sensing data and modeling analysis (Barrett et al., 2015; Mouteva, et al., 2015b; Wiggins et al., 2018).

The objective of this study is to evaluate the effectiveness of separating OC and BC via the ECT9 (EnCan-Total-900) protocol (Chan et al., 2010, 2019; Huang et al., 2006) for ^{14}C-based source apportionment studies of carbonaceous aerosols. The ECT9 technique was originally developed to physically separate OC and BC mass fractions for concentration quantification and stable carbon isotope analysis. This protocol has been used since 2006 to monitor carbonaceous aerosol mass concentrations and stable isotope composition over Canada, including in the Arctic at Alert, as part of the Canadian Aerosol Baseline Measurements (CABM) Network by Environment & Climate Change Canada (Chan et al., 2010, 2019; Eckhardt et al., 2015; Huang, 2018; Leaitch et al., 2018; Sharma et al., 2017; Xu et al., 2017). It has also been used to monitor carbonaceous aerosol over China (Yang et al., 2011). Furthermore, BC concentration measurements made with the ECT9 protocol correlate well with those derived from light absorption by an aethalometer as well as refractory black carbon (rBC) using a Single Particle Soot Photometer (SP2) (Chan et al., 2019; Sharma et al., 2017). It was demonstrated that the ECT9 protocol can be used to quantify OC/BC concentrations and provide source information at the same time.

The ECT9 protocol is a thermal evolution analysis (TEA) protocol which is different from commonly used thermal optical analysis (TOA) methods for monitoring air quality, such as the

Interagency Monitoring of Protected Visual Environments (IMPROVE) protocol (Chow et al., 2001, 2007), the National Institute for Occupational Safety and Health protocol (NIOSH method 5040, Birch, 2002), as well as the European Supersites for Atmospheric Aerosol Research (EUSAAR) protocol (Cavalli et al., 2010). In those protocols, the OC fraction is thermally desorbed from filter samples in an inert helium (He) atmosphere at relatively lower temperatures and the BC fraction is combusted at higher temperatures by introducing oxygen (O_2) in He stream while the filter reflectance or transmittance for a laser signal is continuously monitored. During the analysis, a fraction of the OC may char (forming pyrolyzed OC or POC), causing the transmittance or reflectance to decrease. While TOA methods use the changes in laser signal to mathematically correct for POC within the measured BC fraction, the ECT9 protocol aims to minimize or remove POC, together with carbonate carbon (CC), during an intermediate temperature step of 870°C in pure He via high temperature evaporation (Chan et al., 2019). With much longer retention times at each temperature step (see Methods) and without either reflectance or transmittance used, the ECT9 protocol effectively isolates OC, POC+CC, and BC.

It should be noted that other methods have been also developed mainly for ^{14}C analysis of OC and BC, such as the CTO-375 (Zencak et al., 2007), the Swiss_4S protocol (Mouteva, et al., 2015a; Zhang et al., 2012), or hydropyrolysis (Meredith et al., 2012; Zhang et al., 2019), which use distinct temperature protocols, gas mixture and/or remove water-soluble OC or inorganic carbon prior to BC analysis. In contrast to the ECT9 protocol, however, these approaches differ substantially from the protocols that are widely used for monitoring OC/BC mass concentrations in the field, which limits the relevance of this data for improving the representation of carbonaceous aerosols in chemical transport models.

Here we analyzed the ^{14}C content of OC and BC fractions (<100 μg C) isolated with the ECT9 protocol from four pure fossil and contemporary reference materials. These materials were analyzed on their own to quantify the amount and source (modern or fossil) of extraneous carbon introduced by the procedure as well as its reproducibility. Mixtures of two reference materials were measured to elucidate how efficiently the ECT9 protocol isolates OC from BC. In addition, we investigated the laser signals of three reference materials and three aerosol samples (tailpipe emissions, ambient aerosol from Alert, and SRM8785) to assess how efficiently the ECT9 protocol removes POC. Our evaluation of the ECT9 protocol on its ability to physically separate OC from BC for ^{14}C-based source apportionment studies significantly expands the existing opportunities for characterizing and monitoring sources of carbonaceous aerosol at regional or global scales at the same time providing solid base for BC and OC concentration measurements.

2.2 Methods

2.2.1 The ECT9 protocol for the physical separation of OC and BC

The ECT9 protocol was developed at the carbonaceous aerosol & isotope research (CAIR) lab of Environment and Climate Change Canada (ECCC) to quantify the amount of OC and BC in carbonaceous aerosol and their $\delta^{13}C$ values (Chan et al., 2010, 2019; Huang et al., 2006). Carbon fractions are isolated with an OC/BC analyzer (Sunset Laboratory Inc.) coupled to a custom-made gas handling and cryogenic trapping system for CO_2 collection from OC and BC fractions (Fig. 2.1a). The fractions are separated based on their thermal refractory. Specifically, carbon fractions are released by the ECT9 protocol in three steps (Fig. 2.1b): (1) OC at 550°C for 600 seconds in pure He; (2) POC and CC at 870°C for 600 seconds in pure He; and (3) BC at 900°C for 420 seconds in a mixture of 2% O_2 with 98% He (99.9999% purity). All fractions are fully oxidized to CO_2 by passing through a furnace containing MnO_2 maintained at 870°C. For concentration de-

termination, the CO_2 passes through a methanator at 500°C, is converted to CH_4, and quantified with a flame ionization detector. For isotope analysis, the CO_2 is cryo-trapped with liquid N_2 (-196°C) in a U-shaped glass trap, purified on a vacuum system (to remove He), sealed into a pyrex ampoule, and analyzed for its $\delta^{13}C$ ratio with an Isotopic Ratio Mass Spectrometer (IRMS), i.e., MAT2563 or FM^{14}C with an Accelerated Mass Spectrometer (AMS).

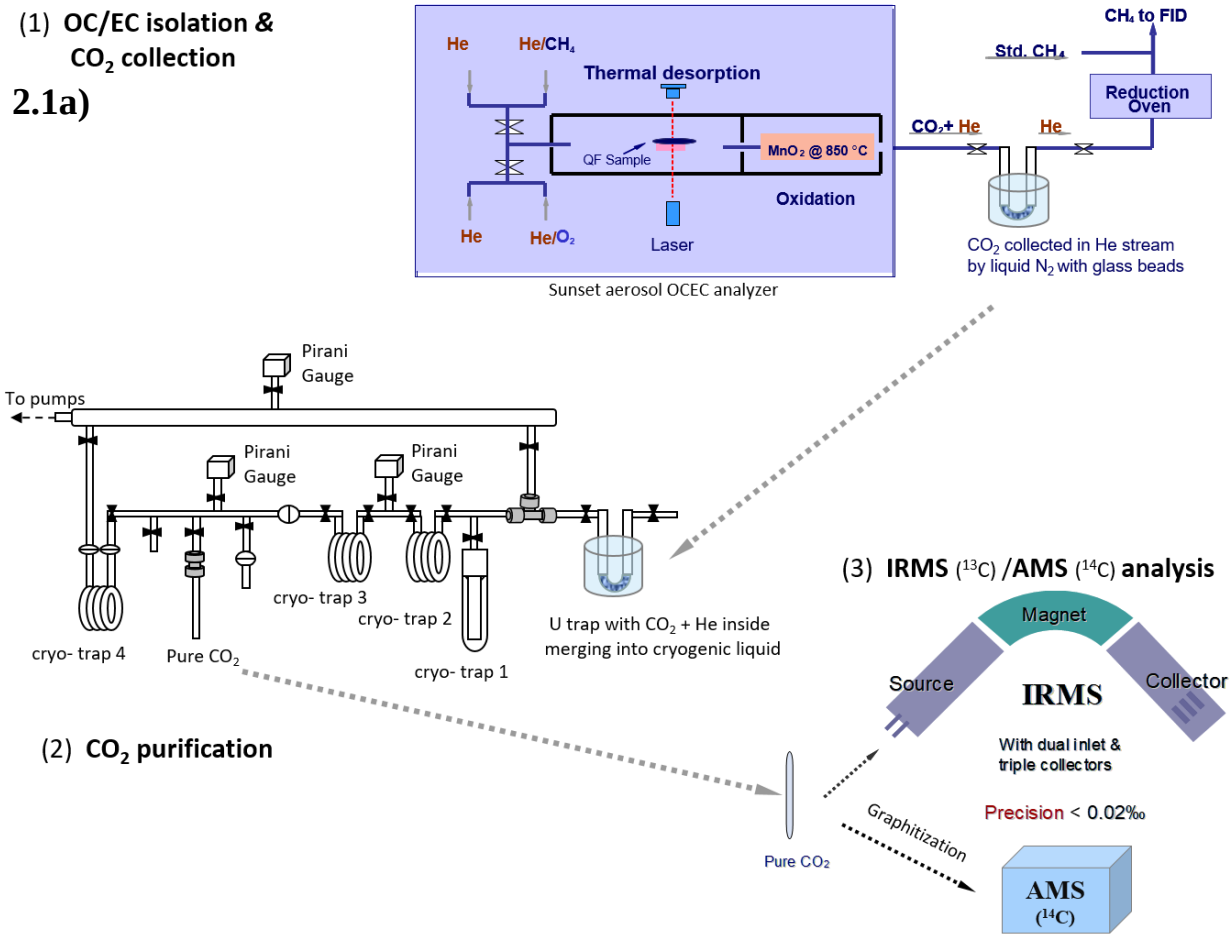

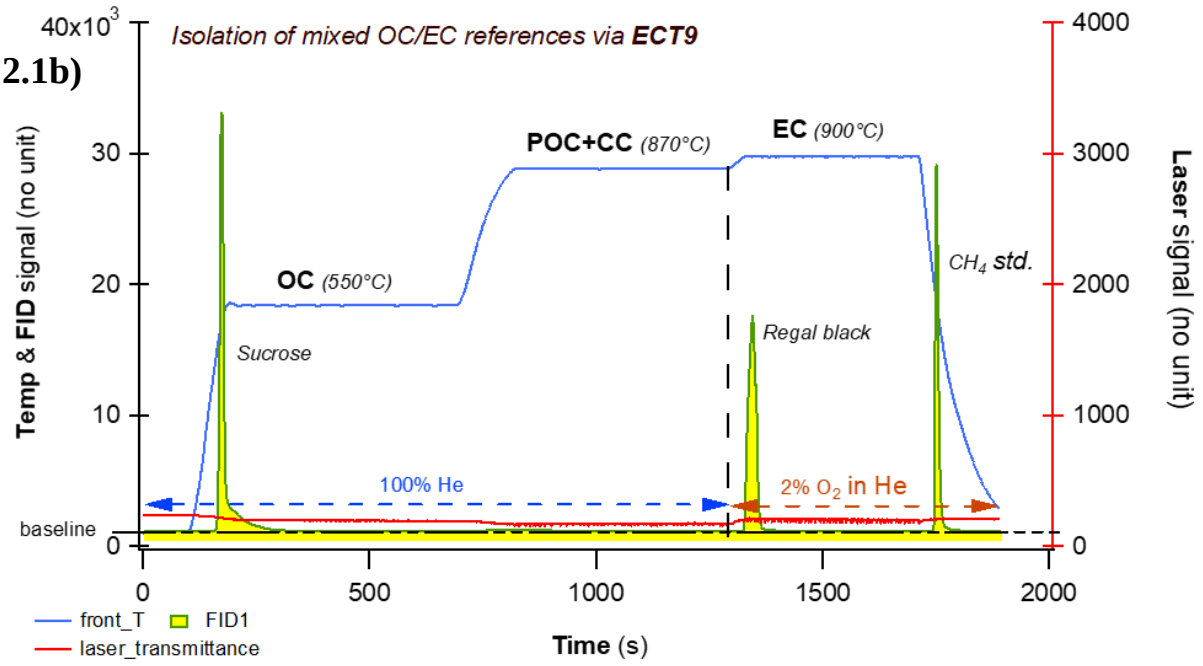

Figure 2.1 Overview of the carbonaceous aerosol analysis system at Environment and Climate Change Canada.
(a) Schematic flow chart for ^{13}C & ^{14}C measurements of OC/BC via ECT9, including 1) OC/BC isolation/CO_2 colletion via cryo-trapping, 2) CO_2 purification, and 3) isotope analysis with IRMS ($^{13}C/^{12}C$ of CO_2) or AMS ($^{13}C/^{12}C$ and $^{14}C/^{12}C$ of graphite targets).
(b) Thermogram of the ECT9 protocol on a Sunset OC/BC Analyzer. First, organic carbon (OC) is thermally desorbed at 550ºC for 600 seconds in 100% He, then any pyrolyzed OC (POC), refractory OC, and carbonate carbon (CC) is released at 870ºC in 100% He for 600 seconds. Finally, BC is combusted at 900ºC for 420 seconds by introducing 2% O_2 in He. All carbon fractions are oxidized to CO_2 followed by reduction to CH_4 and quantification via flame ionization detection (FID) for carbon content or purified and cryo-trapped in Pyrex ampoules for isotope analysis. Example FID signals are shown for a pure OC reference material (sucrose) mixed with a pure BC material (regal black) along with the internal standard (CH_4).

2.2.2 Reference materials and their composition

To evaluate the ECT9 method for separating OC and BC for ^{14}C analysis, we isolated and measured the ^{13}C and ^{14}C content of the OC or BC fraction or TC from 5-6 modern or fossil reference materials (Table 2.1), including two pure OC (adipic acid, sucrose), two BC (C1150, regal black), and two natural OC/BC-mixtures (rice char and urban dust SRM1649a).

Table 2.4 Overview of the bulk reference materials analyzed with the ETC9 method for their total carbon (TC), organic carbon (OC), and black carbon (BC) contents.

	BC		**OC**		**BC + OC mixture**	
Reference material	**Regal black**	**C1150**	**Sucrose**	**Adipic Acid**	**Rice Char**	**SRM-1649a**
	mean (s.d.)	mean (s.d.)	mean (s.d.)	mean (s.d.)	mean (s.d.)	mean (s.d.)
TC (%)	96 (9)	98 (12)	101 (4)[a]	43 (5)[b]	52 (1)[c]	17.9 (1.1)[d]
OC/TC (%)	**3 (1)**	**1 (2)**	**99 (2)**	**100 (0)**	**14 (1)**	**51.5 (0.8)**
BC/TC (%)	**97 (1)**	**98 (2)**	**1 (1)**	**0 (0)**	**86 (1)**	**48.5 (0.8)**
n	41	24	117	5	6	6
Bulk material / Loading Method	fine powder / gravimetric via balance (0.1 - 1 µg accuracy)		solution / volumetric inection	fine powder / gravimetric (0.1 - 1 µg accuracy)		
Loading range (µg)	20 - 100	4 - 100	20 - 80	30 - 250	70 - 210	440 - 1100
Analysis period	2015 – 2017	2006, 2013, 2015	2013 - 2018	2015, 2019	2018	2004 - 2005
Supplier	Aerodyne Research, MA, USA	McMaster Univ., ON, Canada	Sigma-Aldrich, MO, USA	Fisher-Scientific, NH, USA	Univ. of Zurich, Switzerland	NIST, MD, USA

[a]101% is obtained from the ratio of TC measured to TC calculated from the injected solution of sucrose; [b]49% of TC to bulk material in adipic acid based on its molecular mass; [c]58.6% of TC to bulk material in Rice char obtained from Hammes et al. (2006); [d]17% of TC to bulk material in SRM 1649a obtained from a critical evaluation of inter-laboratory data by Currie et al. (2002)

Some of the reference materials have previously been utilized to compare different protocols that quantify OC/BC fractions (Hammes et al., 2007; Willis et al., 2016) as well as determine the mass of extraneous carbon introduced during OC/BC isolation from carbonaceous aerosol (Mouteva, et al., 2015a). Table 2.1 provides an overview of their chemical compositions, i.e., total carbon contents and relative fraction of OC and BC, respectively. Primary methods (i.e., gravimetric or volumetric) are used for mass loading of the materials, whereas the mass of TC, OC, and BC are quantified via the ECT9 thermal protocol. Based on repeat injections of sucrose results (20-80 µg sucrose, n =117), the accuracy of the TC mass is about 5%. The reproducibilities of both OC/TC and BC/TC percentages are 2% or better. Although uncertainties of weighing pure

BC mass (i.e., regal black and C1150) via microbalances are relatively large (due to static electricity and variable relative humidity), the BC/TC and OC/TC ratios for all reference materials are highly reproducible (1 s.d. <2%). The results show that the two BC materials (i.e., regal black and C1150) contain 97% and 98% BC, with only 3% and 2% OC, respectively. The two OC materials (i.e., sucrose and adipic acid) are 99% and 100% OC, and less than 1% BC, respectively. Thus, the materials are suitable for the purpose of this study.

Table 2.5 Overview of the isotopic composition of the reference materials used in this study. Radiocarbon ($^{14}C/^{12}C$, reported as fraction modern ($FM^{14}C$)) was measured at the KCCAMS facility and $\delta^{13}C$ at the CAIR lab.

Reference Material	TC FM ^{14}C			$\delta^{13}C_{VPDB}$ (‰)		
	n	mean (s.d.)	Loading Range (µg)	n	mean (s.d.)	Loading Range (µg or µg C*)
BC						
Regal Black	2	-0.0001 (0.0006)	700 – 750	5	-27.61 (0.08)	15 – 70
C1150	3	0.0027 (0.0008)	60 - 560	5	23.06 (0.08)	20 – 50
OC						
Sucrose	2	1.0586 (0.0016)	730 – 770	9	-12.22 (0.16)	10 – 20
Adipic Acid	5	0.00000 (0.0002)	740 - 1050	n/a	n/a	n/a
BC + OC Mixture						
Rice Char	3	1.0675 (0.0007)	900 – 960	1	-26.74	160
SRM-1649a	1	0.512 (0.001)	760	2	-25.84	130 - 200

*Sucrose was loaded as a solution (µg C), Regal Black, C1150, Adipic acid, Rice char, and SRM-1649a as a fine powder (µg dry mass); n/a = not applicable

We also analyzed the ^{13}C and ^{14}C isotopic composition of each reference material, using off-line combustions and ECT9 coupled with cryo-purification to convert them into CO_2. The results are summarized in Table 2.2 (for individual results see Tables A2.1 & A2.2). The ^{14}C analysis of µg C-sized carbonaceous aerosol samples requires the assessment of extraneous carbon (Santos et al., 2010). This is achieved by measuring multiple smaller-sized materials with known ^{14}C content. Consequently, the results in Table 2.2 are critical, as those ^{14}C values provide the reference for quantifying the extraneous carbon introduced during the isotope analysis procedures.

2.2.3 Isolation of OC, BC or TC with the ECT9 protocol and purification of CO_2

The isotopic analysis of carbonaceous aerosol via the ECT9 system involves three steps (Fig. 2.1a): 1) OC and BC isolation/CO_2 collection and 2) CO_2 purification, followed by 3) isotope analysis for either $^{13}C/^{12}C$ by IRMS or ^{14}C by AMS (coupled measurements of $^{13}C/^{12}C$ and $^{14}C/^{12}C$ of μg C- sized graphite targets), as desired.

The initial masses of the pure reference materials ranged from 5 to 46 μg C (n=3-13; Table A2.5), whereas those for the mixed materials ranged from 5-30 μg C for OC and 7-59 μg C for BC (n=5-6; Table A2.6). The loaded mass of each material was determined via a microbalance (MX5, Mettler Toledo or CCE6, Sartorius) with the lowest reading to 1 μg C or 0.1 μg C, respectively. OC materials were dissolved in MQ-water with known volumes and volumetrically loaded onto a pre-cleaned quartz filter punch (1.5 cm^2, Pall Canada Limited). BC (i.e., Regal black and C1150) and mixed materials (rice char or SRM 1649a), which cannot be completely dissolved in water, were directly weighed onto pre-cleaned quartz filter punches. These filters were pre-combusted at 900°C in a muffle furnace overnight and wrapped into aluminum foil before cooling below 200°C. A filter punch with the loaded mass was put into the Sunset analyzer and analyzed with the ECT9 protocol. OC and BC were separated and the combusted OC or BC fractions as CO_2 were cryo-collected in a U-shaped flask submerged in liquid N_2 (Fig. 2.1a, step 1). Then, this flask containing CO_2 and He was connected to a vacuum line with 4 cryo-traps and several open ports (Fig. 2.1a, step 2), where the CO_2 is purified by sequential distillation when passing cryo-traps 1 through 3. Finally the pure CO_2 is transferred and sealed into a 6 mm glass ampoule for ^{13}C or ^{14}C analysis. Pressure is read by a Pirani gauge before sealing the ampoule for an estimation of the amount of gas, and consequentely, sample size determination as μg C.

2.2.4 ^{14}C measurements

At the KCCAMS facility, the OC and BC fractions or TC (in form of CO_2) were reduced to graphite on iron powder via hydrogen (H_2) reduction using equipment and protocols specifically developed for smaller-sized (≤15 μg C) samples (Santos et al., 2007a, 2007b). Briefly, sample-CO_2 was introduced into a vacuum line, cryogenically isolated from any water vapor, manometrically quantified, and then transferred to a heated reaction chamber, where it was mixed with H_2 and reduced to filamentous graphite. To characterize the graphitization, handling and AMS analysis, two relevant standandards (Oxalic Acid II as modern carbon and Adipic acid as fossil carbon), with similar size ranges of the samples prepared via ECT9, were also processed into graphite. The graphite was then pressed into aluminum holders and loaded into the AMS unit alongside measurement standards (Table A2.5) and blanks for ^{14}C measurement (Beverly et al., 2010). The data are reported in fraction modern carbon ($FM^{14}C$), following the conventions established by Stuiver & Polach (1977) and also described elsewhere (Trumbore et al., 2016).

To establish consensus values (Table 2.2), we also analyzed the ^{14}C content of the bulk reference materials ranging in size from 0.06 to 1 mg C, using our standard combustion and graphitization methods. Larger aliquots of material were weighed into pre-combusted quartz tube with 80 mg CuO, evacuated, and combusted at 900°C for 3 hours. The resulting CO_2 was cryogenically purified on a vacuum line, reduced to graphite using a closed-tube zinc-reduction method (Xu et al., 2007), and analyzed as described above.

2.2.5 Quantification of extraneous carbon

Any type of sample processing and analysis introduces extraneous carbon (C_{ex}). Therefore, the measured mass of any sample will include the mass of this sample and of any C_{ex} incorporated throughout the analysis [Eq. 1]:

$$m_{spl\_meas} = m_{spl} + m_{ex} \quad \text{[Eq. 1]},$$

where m_{spl_meas}, m_{spl}, and m_{ex} are the measured and theoretical mass of the sample and of C_{ex}, respectively. For small samples (with a mass of a few μg C), the mass of C_{ex} can compete with or overwhelm the sample mass and cause the measured $FM^{14}C$ value of a sample to deviate from its consensus value.

Here, we estimated the mass of C_{ex} introduced during the ECT9 protocol and the ^{14}C analysis following (Santos et al., 2010), where C_{ex} is understood to consist of a modern and of fossil component [Eq. 2]:

$$m_{ex} = m_{mex} + m_{fex} \quad \text{[Eq. 2]},$$

where m_{ex} and m_{fex} is the mass of the modern and fossil C_{ex}, respectively.

Following an isotope mass balance approach, the measured isotopic ratio ($^{14}C/^{12}C$) of a sample (R_{spl_meas}) can be expressed as [Eq. 3].

$$R_{spl\_meas} = \frac{m_{spl}R_{spl} + m_{mex}R_m + m_{fex}R_f}{m_{spl\_meas}} \quad \text{[Eq. 3]},$$

where R_{spl} is the theoretical isotopic ratio of the sample, and R_m and R_f are the consensus isotopic ratios of a modern and fossil standard, respectively. This equation can be further simplified because R_f is 0. R_m is determined by measuring regular-sized aliquots of this reference material. In

addition, all $^{14}C/^{12}C$ ratios are corrected for isotope fractionation using their $\delta^{13}C$ measured alongside ^{14}C on the AMS (Beverly et al., 2010).

The mass of modern C_{ex} can be quantified by analyzing fossil reference materials, which are highly sensitive to modern and insensitive to fossil pollutants. Based on [Eq. 3] the measured isotopic ratio of the fossil reference (R_{f_meas}) can be expressed as [Eq. 4]:

$$R_{f\_meas} = \frac{m_{mex}R_m}{m_{spl\_meas}} \qquad \text{[Eq. 4]}$$

The smaller the mass of the fossil reference material, the greater the effect of the constant mass of modern C_{ex} on the isotope ratio of the fossil reference material, i.e. R_{f_meas} deviates toward R_m.

Similarly, the mass of fossil C_{ex} can be quantified by analyzing modern reference materials. With decreasing mass, the measured isotopic ratio of the modern reference (R_{m_meas}) will deviate more strongly from R_m (toward R_f). Based on [Eq. 1-3] and assuming $m_{spl} \gg m_{mex}$, the R_{m_meas} can be expressed as [Eq. 5]:

$$R_{m\_meas} = \frac{m_{spl}R_m + m_{mex}R_m}{m_{spl\_meas}} \approx \frac{(m_{spl_{meas}} - m_{fex})R_m}{m_{spl\_meas}} \qquad \text{[Eq. 5]}$$

Finally, we can calculate the C_{ex}-corrected isotope ratio of an unknown sample (FM_{spl_corr}). This value reported as the ratio between the theoretical isotopic ratio of this sample and the accepted value of a modern standard (R/R_m) also known as Fraction Modern (FM; with all R corrected for stable isotope fractionation). This data is reported as [Eq. 6]:

$$FM_{spl\_cor} = \frac{R_{spl}}{R_m} \approx \frac{R_{spl\_meas} - R_{f\_meas}}{R_{m\_meas} - R_{f\_meas}} \approx FM_{m^*} \times \frac{\left[\frac{R_{spl\_meas}}{R_m} - \frac{m_{mex}}{m_{spl\_meas}}\right]}{\left[1 - \frac{m_{mex}}{m_{spl\_meas}} - \frac{m_{fex}}{m_{spl\_meas}}\right]} \qquad \text{[Eq. 6],}$$

where FM_{m^*} is determined from the direct measurement of the modern primary reference material (OX1) used to produce six time-bracketed graphite targets measured in a single batch, after iso-

topic fractionation correction and normalization (Santos et al., 2007a, 2007b). The individual uncertainty of FM_{spl_cor} is determined from counting statistics and by propagating the quantified blanks using a mass balance approach. Long-term and continuous measurements of various types of blanks indicate that the mass of C_{ex} within one analytical method or system can vary as much as 50% (see Santos et al., 2010; Fig. 2.1). Therefore, we applied a 50% error in m_{fex} and m_{mex} from long-term measurements of variance in m_{ex} of small samples (Santos et al., 2007a).

In this study, we used a multi-step approach to quantify m_{ex} introduced by the ECT9 protocol and ^{14}C analysis. First, we quantified m_{ex} introduced during ^{14}C analysis by analyzing different masses of our bulk reference materials. Extraneous carbon is introduced during sealed tube combustion and graphitization followed by graphite target handling and measurement. Typically, ^{14}C analysis contributes a small portion to m_{ex} (Mouteva et al., 2015a; Santos et al., 2010). Second, we quantified the portion of m_{ex} added during the isolation of OC and BC with the ECT9 protocol. This portion of m_{ex} allows us to determine the practical minimum sample size limit for the entire method, including m_{ex} contributions from filter handling before OC/BC analysis, instrument separation, and transfer to cryo-collection system and Pyrex ampoules. To isolate this portion, we quantified m_{ex} of the entire procedure (ECT9 protocol plus ^{14}C analysis) by analysing the ^{14}C signature of OC and BC from different masses of a large set of reference materials, and then subtracted the portion of m_{ex} introduced during ^{14}C analysis.

2.3 Results and Discussion

2.3.1 Recovery estimation

The reference materials used in this study, including the modern and fossil endmembers (i.e., the major carbon sources) found in carbonaceous aerosol, and their TC, OC, and BC concen-

trations are shown in Table 2.1. Reference materials were separated into OC, BC, or TC using the ECT9 method at ECCC's CAIR lab (Fig. 2.1) and analyzed for their ^{14}C content at UC Irvine's KCCAMS facility.

Fig. 2.2 shows the cross-validation of carbon-mass between the mass determined at ECCC's CAIR lab and the mass quantified at UC Irvine's KCCAMS lab indicating a very good positive correlation ($R^2 = 0.93$ for pure materials and $R^2 = 0.95$ for two-material-mixtures in Fig. 2.2a and 2.2b, respectively). This suggests that no major losses or gains of carbon occurred during the entire analytical process and the overall recovery was close to 100%, with a 5% uncertainty for samples ranging in size from about 5 to 60 µg C.

2.3.2 Quantification of extraneous carbon and its sources

All types of samples, regardless of size, show deviations in their measured $FM^{14}C$ value from their consensus values to certain degree due to C_{ex} introduced during sample analysis. In µg C-sized samples (mass <15 µg C), significant bias from any C_{ex} can be observed, because C_{ex} constitutes a large fraction of the total sample. Previous work (using solvent-free analytical protocols) has shown that modern C_{ex} is introduced mostly through instrumentation and sample handling techniques, while fossil C_{ex} originates from iron oxide used as a catalyst for the reduction of CO_2 to graphite prior to AMS analysis (Santos et al., 2007a, 2007b).

The $FM^{14}C$ values of the pure modern or fossil reference materials generally agreed with their accepted $FM^{14}C$ values for both OC and BC fractions (within approximately 5% uncertainty, Fig. 2.3 and Table A2.5) after applying a constant amount C_{ex} correction in $FM^{14}C$ determination. This constant C_{ex} is a critical prerequisite for accurately correcting the $FM^{14}C$ value of unknown samples. Hence, the data demonstrated that the ECT9 method (and subsequent ^{14}C analysis) introduces a small, reproducible amount of C_{ex}.

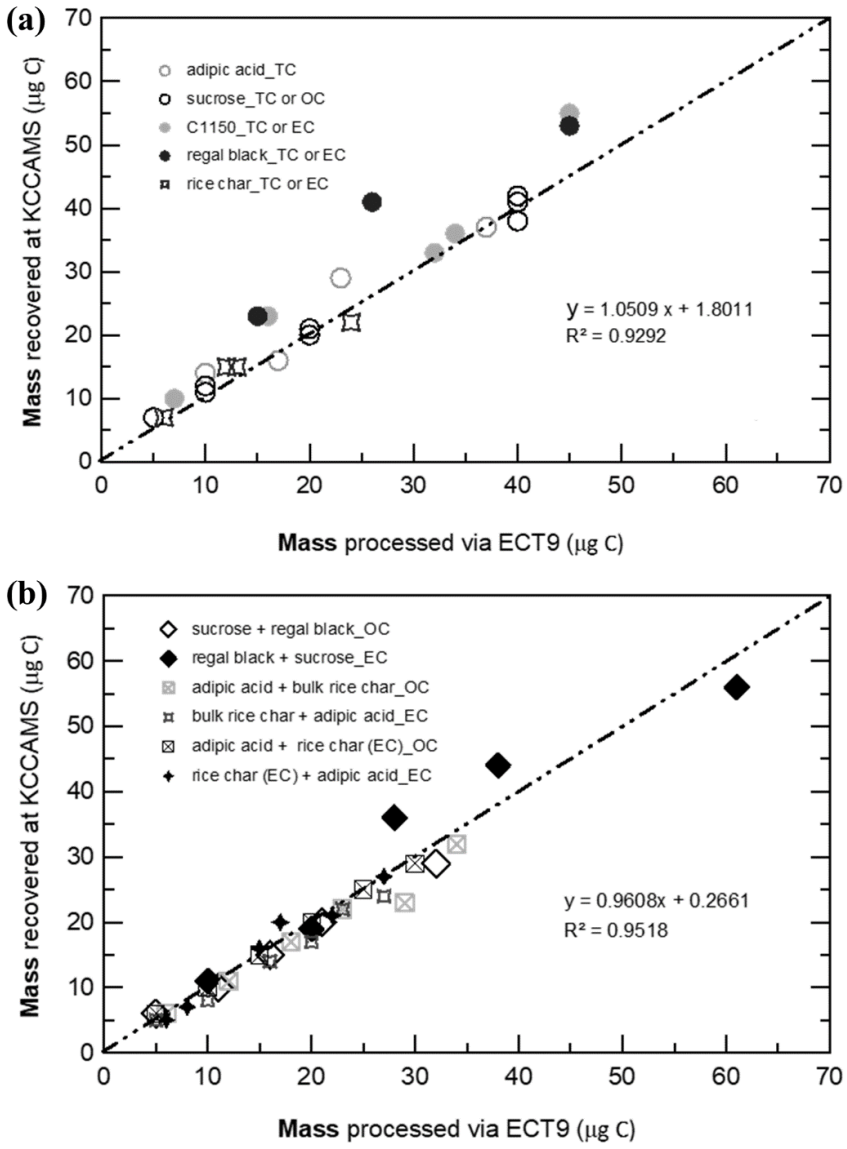

Figure 2.2 Cross-validation of carbon-mass prepared, isolated by the ECT9 protocol and collected via cryo-trapping at ECCC and then, retrieved during the purification and graphitization on a KCCAMS vacuum line. Carbon fractions (organic carbon (OC), black carbon (BC), or total carbon (TC)) were isolated from two reference materials for OC (sucrose, adipic acid), BC (regal black, C1150), and one OC & BC mixture (rice char). Most of the points deviating from the 1:1 line are carbon-rich reference materials, e.g., Regal black and C1150 (>90% TC), which usually there are greater uncertainties in initial mass determination via weighing using microbalance, because their sample sizes aimed were very small.

According to equations [4]-[5] in section 2.5, C_{ex} can be quantified by measuring $FM^{14}C$ of pure modern or fossil materias with different sizes. Fig. 2.3 demonstrates that regardless what

^{14}C content are in carbon fractions isolated from the reference materials and what sizes they are, the corrected $FM^{14}C$ values match with consensus value within propagated uncertainty.

Table 2.6. Comparison of the OC and BC ECT9 and Swiss_4S isolation protocols.

Carrier gas	Carbon fraction	Temperature	Duration	Comments
		°C	s	
ETC9[a]				
He-purge		20 – 50	90	Purging of volatile and semi-volatile OC
He	OC	550	600	
He	POC + CC	870	600	Minimizing charred OC contribution to BC
O_2/He[b]	BC	900	420	
Swiss_4S[c]				
O_2-purge		20 – 50	90	Purging of volatile and semi-volatile OC
O_2	S1_OC	375	240	Fraction captured for ^{14}C analysis
O_2	S2_OC	475	120	
He	S3_OC	650	180	
O_2	S4_BC	760	160	Water-soluble OC is removed by water extraction prior to thermal analysis.

[a]POC + CC = pyrolysis OC + carbonate carbon; [b]The flow of 10% O_2 + 90% He mixing with the flow of 100% He resulting in 2% O_2 + 98%He. in [c]The BC punch is flushed with Milli-Q water prior the analysis to remove the water-soluble OC and minimize charring (Zhang et al., 2012; Mouteva et al., 2015a).

To evaluate the suitability of ECT9 for ^{14}C analysis of aerosol samples, a comparison is made between the results of a published method (i.e., Swiss_4S) and those of ECT9. The two protocols are listed in Table 2.3 and their C_{ex} distribution is shown in Table 2.4. The total amount of C_{ex} introduced by the complete procedure through ECT9, and determined based on all reference materials, was 1.3±0.6 µg C, with 70% originating from contamination with modern carbon (Table 2.4). The isolation of OC and BC with the ECT9 protocol introduced 65% of total C_{ex} (0.85 out of 1.35 µg C), with 65% derived from modern carbon. Overall, the total amount of C_{ex} introduced during OC/BC isolation with the ECT9 protocol is comparable to that for the Swiss_4S protocol established at UC Irvine within uncertainties (Table 2.3, Mouteva et al. (2015a)). This

demonstrates that the ECT9 protocol serves as a suitable alternative for the ^{14}C analysis of aerosol samples with masses >2 μg C.

Table 2.4 Comparison of the procedural contamination with extraneous carbon for aerosol reference materials partitioned into organic carbon (OC) and black carbon (BC) with the ECT9 or Swiss_4S protocols based on their ^{14}C contents. We assume a measurement uncertainty of 50% (see Methods).

Contamination Source	ECT9	Swiss_4S[a]
	μg C	
OC/EC isolation + trapping		
Modern	0.55	0.37
Fossil	0.3	0.13
Total	0.85	0.5
^{14}C analysis[b]		
Modern	0.35	0.43
Fossil	0.1	0.53
Total	0.45	0.97
Full set-up		
Modern	0.9	0.8
Fossil	*0.4*	*0.67*
Total	*1.3*	*1.47*

[a]From Mouteva et al. (2015a), [b]Carbon introduced during sample combustion, CO_2 purification and graphitization, and measurement with ^{14}C-AMS.

2.3.3 Effectiveness of OC/BC separation

To investigate the effectiveness of the ECT9 to separate OC from BC in more complex mixtures with minimizing OC into the BC fraction via pyrolysis, mixtures of the modern and fossil reference materials (Table 2.2) were used for measuring $\delta^{13}C$ (Table A2.3 - A2.4) and $FM^{14}C$ (Table A2.6).

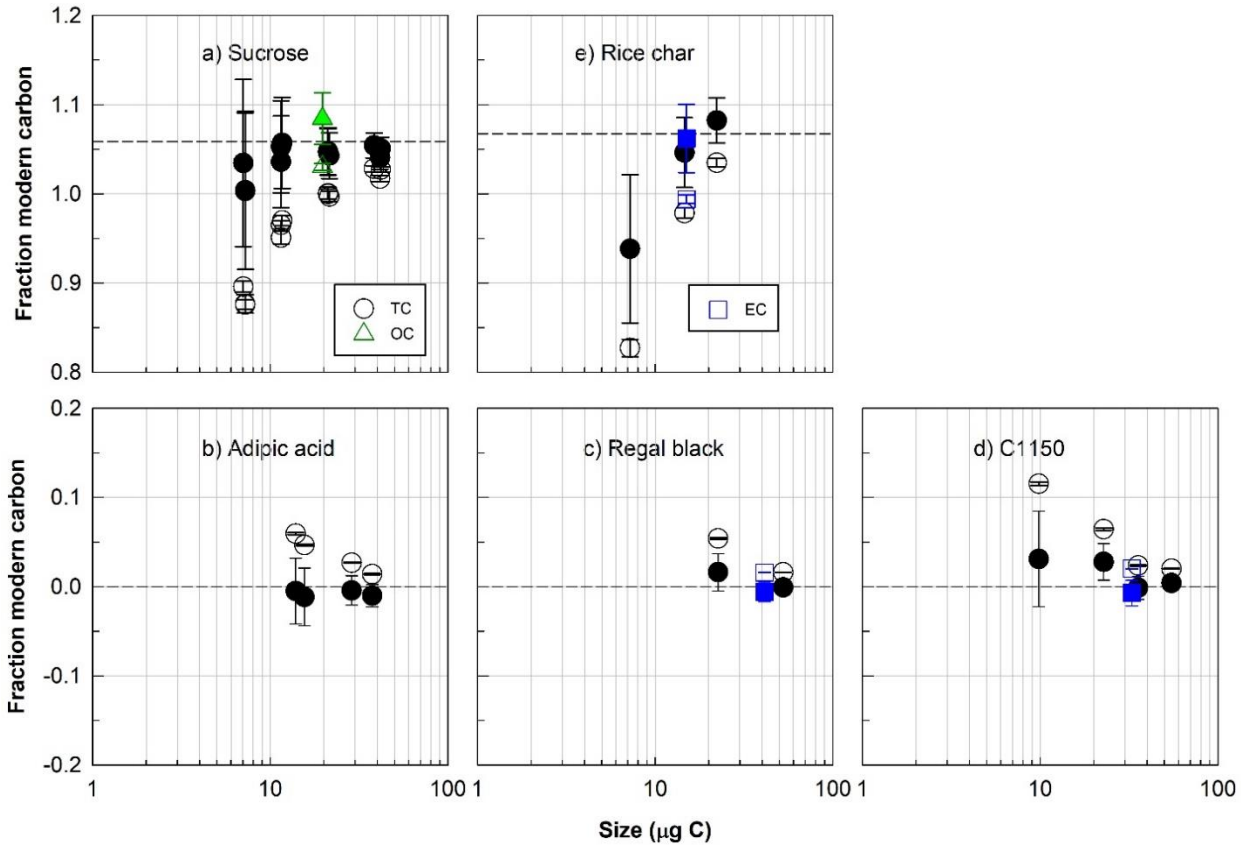

Figure 2.3 Radiocarbon (^{14}C) compositions, expressed as Fraction Modern Carbon, of total carbon (TC, circles), organic carbon (OC, triangles) and black carbon (BC, squares) fractions isolated with the ECT9 protocol from modern or fossil individual reference materials. a) Sucrose and b) adipic acid are modern and fossil OC, respectively, c) regal black and d) C1150 are fossil BC, and e) rice char is a mixture of modern OC and BC. Open and solid symbols represent ^{14}C data before and after correction for extraneous carbon introduced during OC/BC isolation and subsequent ^{14}C analysis, respectively. The dashed line indicates the consensus value determined from regular-sized bulk samples of these materials undergoing off-line combustions (see Table 2.2).

FM^{14}C values of OC and BC fractions isolated from mixtures of pure sucrose (modern OC) and pure regal black (fossil BC) were within the measurement uncertainty of their accepted FM^{14}C values, after correction for a constant amount of C_{ex} (Fig. 2.4) for samples with 5 – 34 μg OC carbon and 10 – 60 μg BC carbon, showing a good separation of OC from BC. This amount of C_{ex} was identical to that applied to the pure reference materials above, further corroborating the constant background introduced by the ECT9 protocol and ^{14}C analysis.

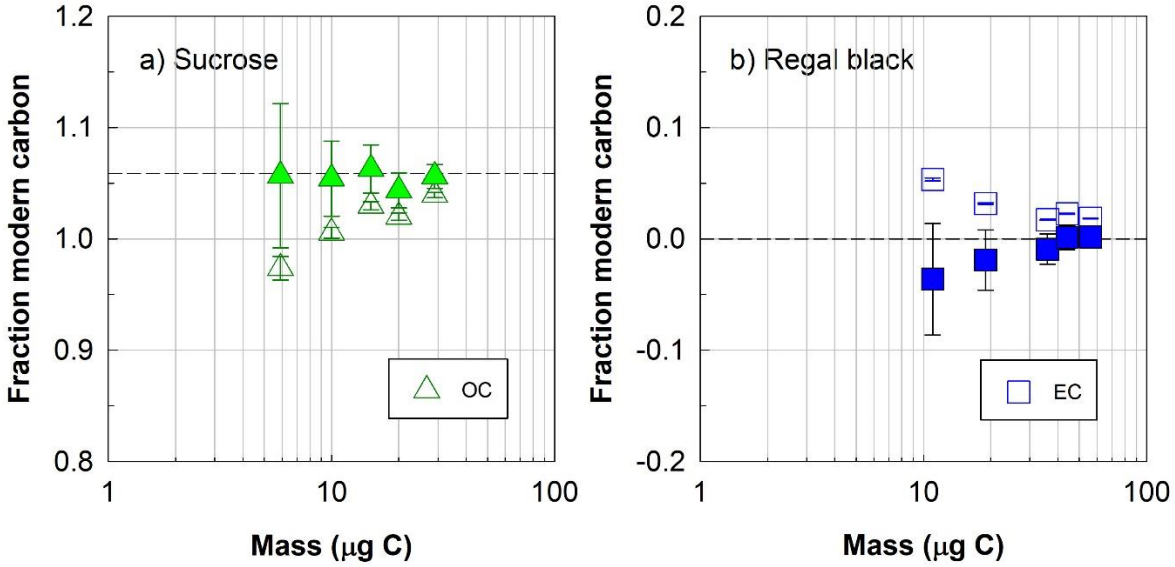

Figure 2.4 Radiocarbon (^{14}C) composition, expressed as Fraction Modern Carbon, of **a)** organic (OC, triangles) or **b)** black (BC, squares) carbon fractions isolated with the ECT9 protocol from mixtures of pure modern OC (sucrose) with fossil BC (regal black). Open and solid symbols represent ^{14}C data before and after correction for extraneous carbon introduced during OC/BC isolation via ECT9 and subsequent ^{14}C analysis via AMS, respectively (see Table A2.6). The dashed line indicates the consensus value (see Table 2.2).

Next, the mixtures of fossil adipic acid (pure OC) and modern rice char (mixture of OC and BC) were isolated and analyzed. After correction for C_{ex}, the $FM^{14}C$ values of the OC (from the mixture) were systematically greater than the consensus value of the pure adipic acid, i.e., a $FM^{14}C$ of zero (Fig. 2.5a), indicating that there was certain level of modern fraction contributed to the measured OC from the modern rice char. This was because rice char contains about 14% of modern OC (Table 2.1).

To confirm that ECT9 could remove OC contained in rice char, an additional step was taken before mixing modern rice char's BC with the fossil OC (adipic acid). Specifically, we stripped the OC fraction of rice char by running rice char (on a filter) through the ECT9 protocol. Adipic acid (fossil OC) was then injected onto the filter with the remaining rice char-BC. The results show that the $FM^{14}C$ of OC values of this mixture lie well within the expected range of the

consensus value (Fig. 2.5b) after a C_{ex} correction as described above, demonstrating an efficient removal of rice char OC.

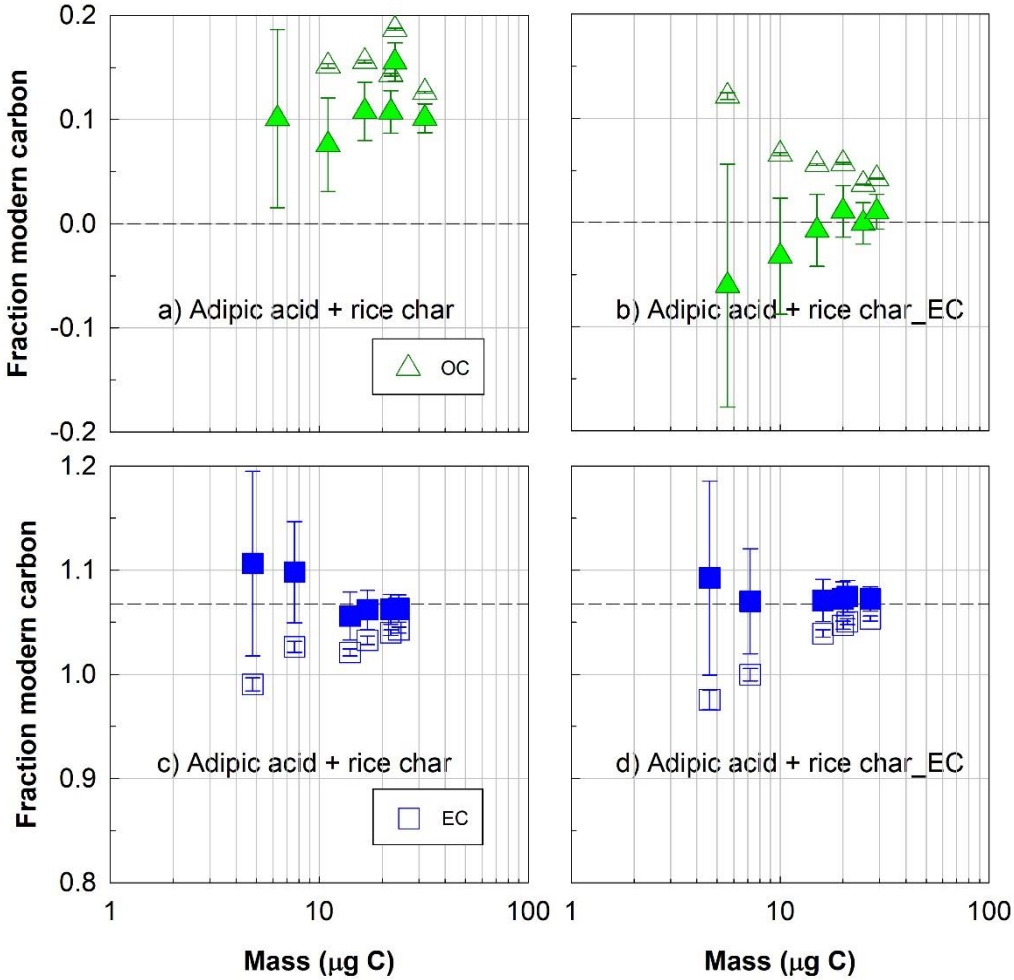

Figure 2.5 Radiocarbon (^{14}C) compositions, expressed in fraction modern carbon, of organic (OC, triangles) and black (BC, squares) carbon fractions isolated with the ECT9 protocol from the mixtures of reference materials. Fraction of modern carbon **a)** OC and **c)** BC isolated from mixtures of pure fossil OC (adipic acid) with modern bulk rice char (made of 14% OC and 86 % BC), and of **b)** OC and **d)** BC isolated from mixtures of pure fossil OC (adipic acid) with modern BC from rice char_BC (rice char OC has been removed before mixing). Open and solid symbols represent data before and after correction for extraneous carbon introduced during OC/BC isolation via ECT9 and subsequent ^{14}C analysis via AMS respectively (Table A2.6). The dashed line indicates the consensus value (see Table 2.2).

In both mixtures (fossil adipic acid with modern bulk rice char or rice char-BC), the corrected $FM^{14}C$ values of the isolated BC fractions were within the expected range for the rice char reference material (Fig. 2.5c, d). This provides further evidence that the ECT9 protocol isolates

modern BC from fossil OC with no obvious evidence of transferring fossil OC into the BC fraction. Together, the three sets of mixing experiments (Figs. 2.4 & 2.5) provide strong evidence for the effectiveness of separating OC from BC via ECT9 protocol.

In addition to $FM^{14}C$ measurements, $\delta^{13}C$ measurements in mixtures of OC and BC can also provide quantitative information on the effectiveness of OC and BC separation via ECT9. Various amounts of sucrose (pure OC, 10 – 30 μg C) were first mixed with varying amounts of Regal black (pure BC, 20 – 66 μg C). The mixtures were then physically separated into OC and BC fractions by ECT9 for $\delta^{13}C$ measurements. The measured $\delta^{13}C$ values of OC and BC from these mixing experiments are listed in Table A2.3. Based on the $\delta^{13}C$ values of individual pure reference materials (Table A2.2) and a two-end-member mixing mass balance, the average fraction contributed into each other in the mixtures (i.e., sucrose fraction into Regal black or vice versa) were estimated to be less than 3% (Table A2.4).

2.3.4 Charring evaluation & POC removal using the ECT9 protocol

Charring of OC (e.g., oxygenated OC or water-soluble OC) is a known phenomenon where some OC forms pyrolyzed organic carbon (POC) when heated in an inert He atmosphere, darkening the filter (Chow et al., 2004, 2007) and causes decreased laser signals due to light-absorption of charred OC. In most TOA protocols, this POC would combust and contribute to BC when O_2 is added. However, POC can also be gasified and released as CO at high temperatures (>700°C) with limited O_2 supply, e.g., oxygenated OC at 870°C (Chan et al., 2010, 2019; Huang et al., 2006). Most TOA protocols estimate POC by quantifying the mass associated with reflectance/transmittance changes, i.e., the mass released between the time when O_2 is introduced and the OC/BC split point (where the reflectance/transmittance returns to the initial value). In contrast to other TOA protocols, ECT9 defines POC as the mass released at the temperature step of 870°C

(during a period of 600 seconds). This includes charred OC, calcium carbonate ($CaCO_3$) that decomposes at 830°C, and any refractory OC not thermally released at 550°C (Chan et al., 2010, 2019; Huang et al., 2006).

Although ECT9 do not use laser signals to quantify POC, the changes of laser signals during the stage of 870°C can provide useful information about POC. Thus, four sets of samples were selected, including those of pure reference materials and ambient aerosol samples from different sources with heavy or light mass loading (e.g., Arctic sample filters from different seasons) to evaluate the possible charring via ECT9. Their thermograms are shown in Figures 2.6 to 2.9.

Figure 2.6 shows thermograms of pure or bulk references for Regal black, sucrose, and rice char, respectively. It is observed in all three that the laser transmittance signals first decrease and then increases again during the 870°C step, and that they return to their initial values just before BC is released at the next step of 900°C. This demonstrates that the ECT9 method minimizes POC-contributions to the BC fraction.

The thermograms of aerosol (on filters) collected directly from tailpipe exhaust of a diesel engine vehicle and a gasoline engine passage car, respectively are shown in Figure 2.7. These data suggest that the amount of POC generated during analysis are sample/matrix dependent. Specifically, the mass fraction during the 870°C temperature is larger for the gasoline than the diesel engine. This finding supports previous work showing that POC is proportional to the amount of oxygenated OC (Chan et al., 2010). It is noticed that the laser signal reaches the initial value before the BC step, further demonstrating that the charring contribution to BC is minimized.

Another set of thermograms of two total suspended particle filter samples collected during the summer (August) and winter (December) of 2015 at an Arctic site (i.e., Alert) is shown in

Figure 2.8. More details about these samples can be found in Wex et al. (2019). The laser signal patterns are similar to those shown in Figures 2.6 & 2.7, yet more pronounced. During the 550°C step, the laser signals decrease. During the 870°C step, the signals further decrease, then increase, and finally increase to their initial point before BC is released at 900°C. These thermograms further demonstrate ECT9 is able to minimize POC by gasification.

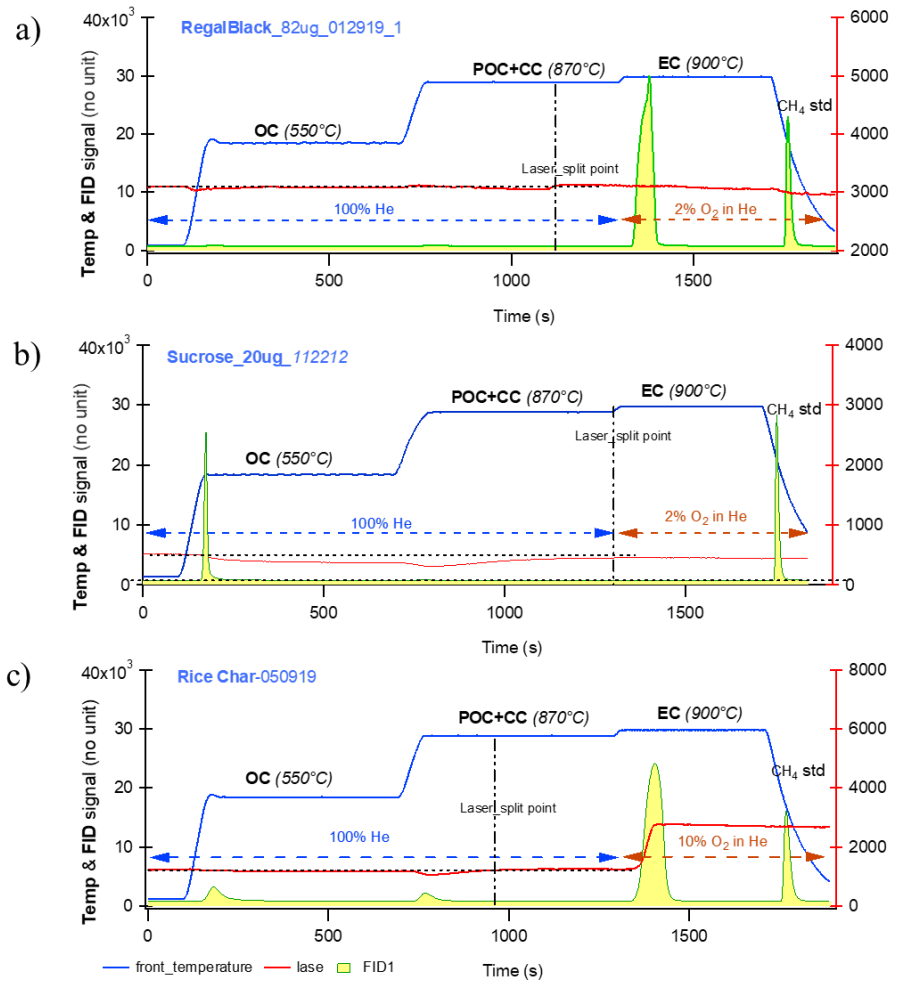

Figure 2.6 Thermograms of pure or bulk references. a) Regal black and b) Sucrose and c) Rice char. Temperature (blue solid line) and FID signals (integrated yellow area with green line) on the left axes and laser (red solid line) on the right axis. On the three thermograms during the temperature stage of 870°C, the laser transmittance signals decrease first and increases again before the next temperatures stage, minimizing POC fraction, i.e., possible charred OC contribution to BC.

Finally, the thermographs of NIST urban dust reference material SRM 8785 (the re-suspended SRM 1649a urban dust with a fine fraction <2.5 μm collected on quartz filter) analyzed with ECT9 and Swiss_4S are shown in Figure 2.9. Both thermograms obtained with the

ECT9 method (Fig. 2.9 a, b) show the similar patterns as those in Figs. 2.6-2.8, i.e., the laser signals reaching the initial value just before the BC release at 900°, suggesting that the charring contribution to BC is minimized during the stage of 870°C even though some POC might remain.

In comparison to previous ^{14}C assessments of BC in SRM1649a, the ECT9-separated BC fraction contained significantly more ^{14}C. Previous assessments (Table 2.5) either quantified the residual C content after extended periods of exposure to 375ºC (4-24 hrs) in air to evolve the OC (Currie et al., 2002; NIST, 2007; Reddy et al., 2002; Szidat et al., 2004) or evolved the BC at high temperatures (850ºC 4hr) after evolving the OC for a relatively short time (20 min 340ºC) (Heal et al., 2011; Szidat et al., 2004). The high oxygen atmosphere and extended period of evolution ensures that any pyrolyzable OC is removed prior to analysis and as a result, the BC quantified includes the most thermally refractory material, which in an urban environment results from fossil combustion. A combination of chemically complex material and a short OC removal step, relative to previous assessments of BC in SRM1649a, resulted in higher ^{14}C values in SRM1649a BC quantified by the ECT9 protocol. It is important to note that no thermal-evolution protocol is best suited for all sample types and thermograms with laser information can be very helpful to indicate charring extent.

In the thermogram obtained with the Swiss_4S protocol (Fig. 2.9c), the laser signal increases from the beginning of the run while the first two stages (375°C and 475°C) are under the conditions of pure O_2 stream, inferring that light absorbing carbon is released during the first two OC stages. The laser signal continues to increase while the temperature increases up to 650°C (the third stage) under the pure He gas stream, indicating that no charred OC is formed. However, when the temperature starts decreasing from 650°C, the laser signal decreases, indicating POC formation below that temperature. This signal decrease continues until the beginning of the next

pure O_2 stage. It is important to note that to obtain BC fraction, the Swiss_4S (Table 2.3) method calls for filter sample pre-treatment, i.e., extraction with water before the thermal separation of OC/BC to minimize the contribution of charred OC from the 3rd stage to BC at the 4th stage. While it is difficult to make direct comparisons between OC and BC from b) and c) in Figure 2.9, laser profiles from those thermograms indicate that in both cases charred OC is negligible or minimal.

Table 2.5 Values of fraction modern carbon of total organic carbon (TOC) and black carbon (BC) isolated from the urban dust NIST SRM1649a obtained by the EnCan-total-900 protocol coupled with the Sunset Analyzer.

Fraction Modern carbon ± s.d. (n)			OC Isolation Technique	BC Isolation Technique	Reference
TC	**TOC**	**BC**			
0.517±*0.004*	n.m	0.153±*0.002*	n.a	375°C in air / 24h Residual	Currie et al., 2002
n.m	n.m	0.065± 0.014 (3)	n.a	375°C in air / 24h Residual	Reddy et al., 2002
0.522±0.018 (5)	0.70±0.05 (3)	0.066±0.020 (4)	340ºC in O_2 / 20 min	375°C in air / 4hr Residual	Szidat et al., 2004
0.505±0.003 (5)	n.m	0.099±0.150 (9)*	n.a	375°C in air / 4hr Residual	Santos, unpublished
0.570±0.014	0.66±0.02	0.15±0.08	340ºC in O_2 / 20 min	850°C in O_2 / 4hr	Heal et al., 2011
0.61±0.08	n.m	0.065± 0.014 (3)**	n.a	375°C in air / 24h Residual	NIST, 2007
0.5126 (1)	0.6336±0.0004 (3)	0.35±0.03 (3)	550ºC in He / 600s	900ºC 2% O_2 in He / 600s	This Study

Average ±SD (n); Average±*Poisson uncertainty*; *Target sizes averaged: 2.5 to 400μgC
**Also reported in Reddy et al. (2002).

Together, the thermograms (Figs. 2.6-2.9) elucidate that the ECT9 protocol can effectively remove or minimize charred OC (POC) to achieve good physical separation of OC and BC. Another great advantage of using ECT9 to separate OC from BC for isotope analysis (both ^{13}C & ^{14}C) is its consistency with the protocol used for OC and BC concentration measurements. Moreover, the ECT9 method does not require filter samples to be pre-extracted with water before BC analysis (to reduce POC).

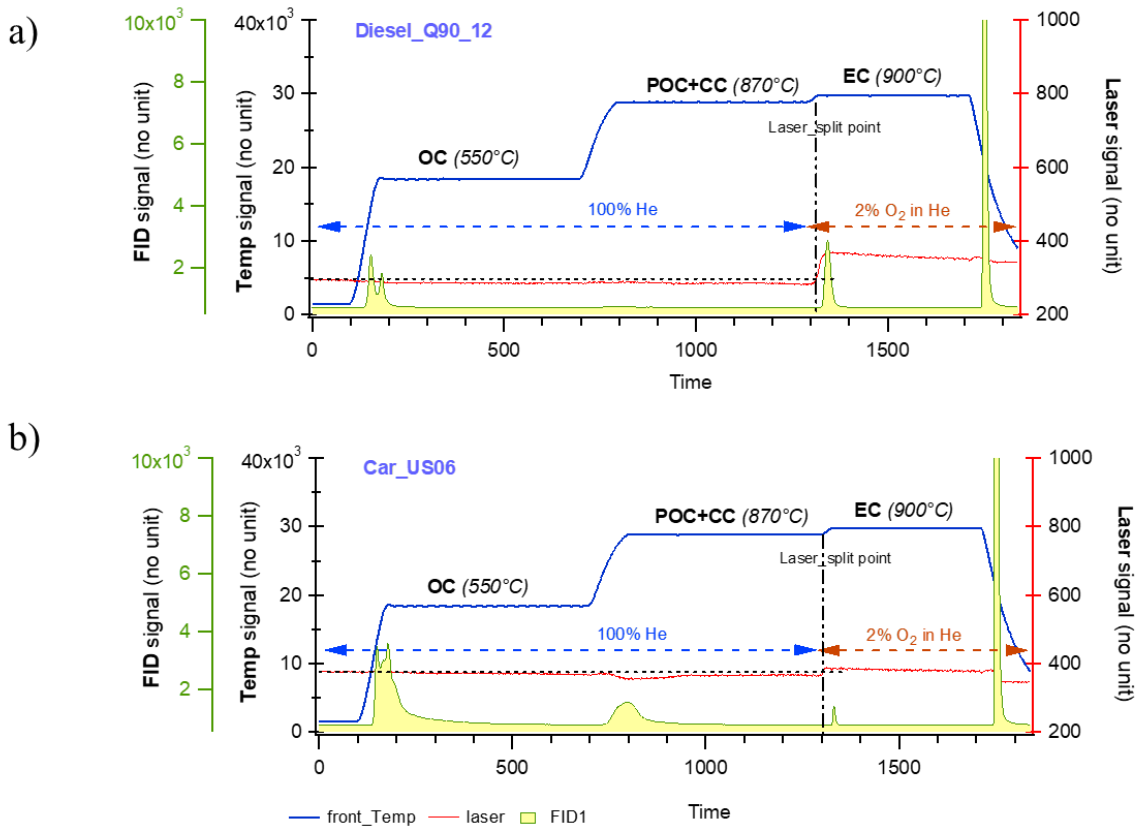

Figure 2.7 Thermograms of the filters directly collected from tailpipe exhaust of a diesel engine vehicle in a) and a gasoline engine passenger car in b). The legends are the same as Fig 2.6. It is noticed that the mass fraction from the temperature stage of 870°C in b) is obviously larger than that in a). The latter is negligible indicating that the amount of POC is sample-matrix dependent. The amount of POC from gasoline vehicle emissions is likely larger than that from diesel vehicle emissions. The laser signal reaches the initial value before the 900°C stage for BC releasing, demonstrating that the charring contribution to BC is minimized.

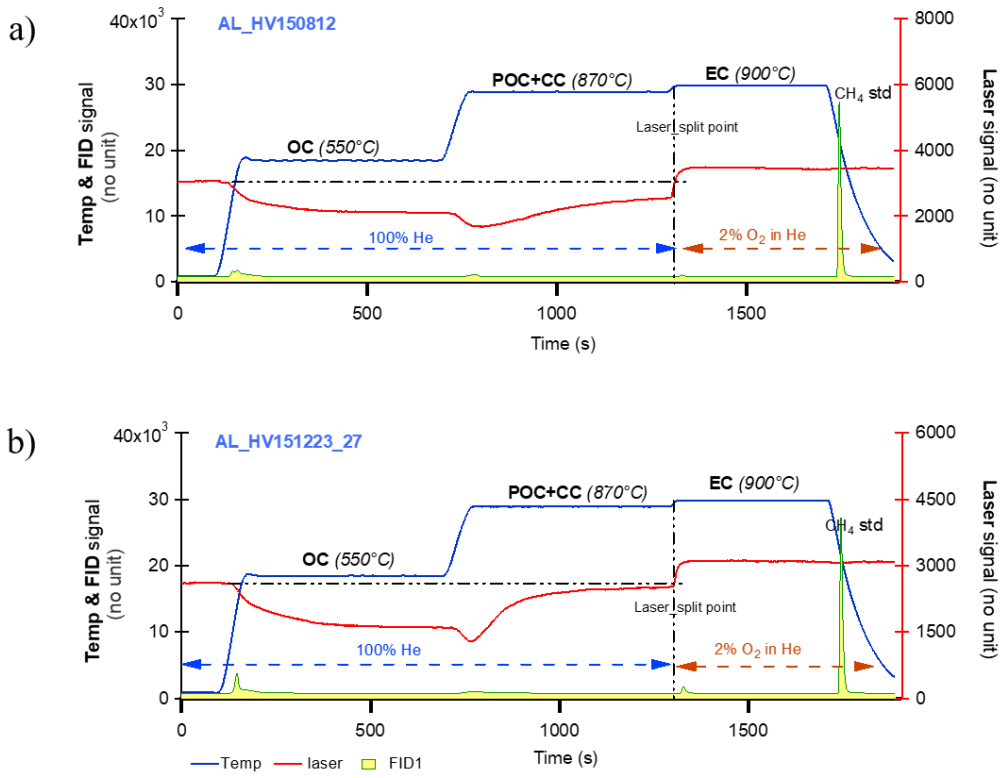

Figure 2.8 Thermograms of fine particles (PM1.0 μm) from the filter samples collected at an Arctic site, i.e., Alert, NU, Canada in summer **a)** and in winter **b)** of 2015. The legends are the same as Fig 2.6. Both thermograms clearly show that during 550°C stage, the laser signal starts decreasing (implying charred OC formation) and begins increasing during 870°C and reaches the initial value before the BC stage (indicating the contribution to BC by charred OC is minimized or removed).

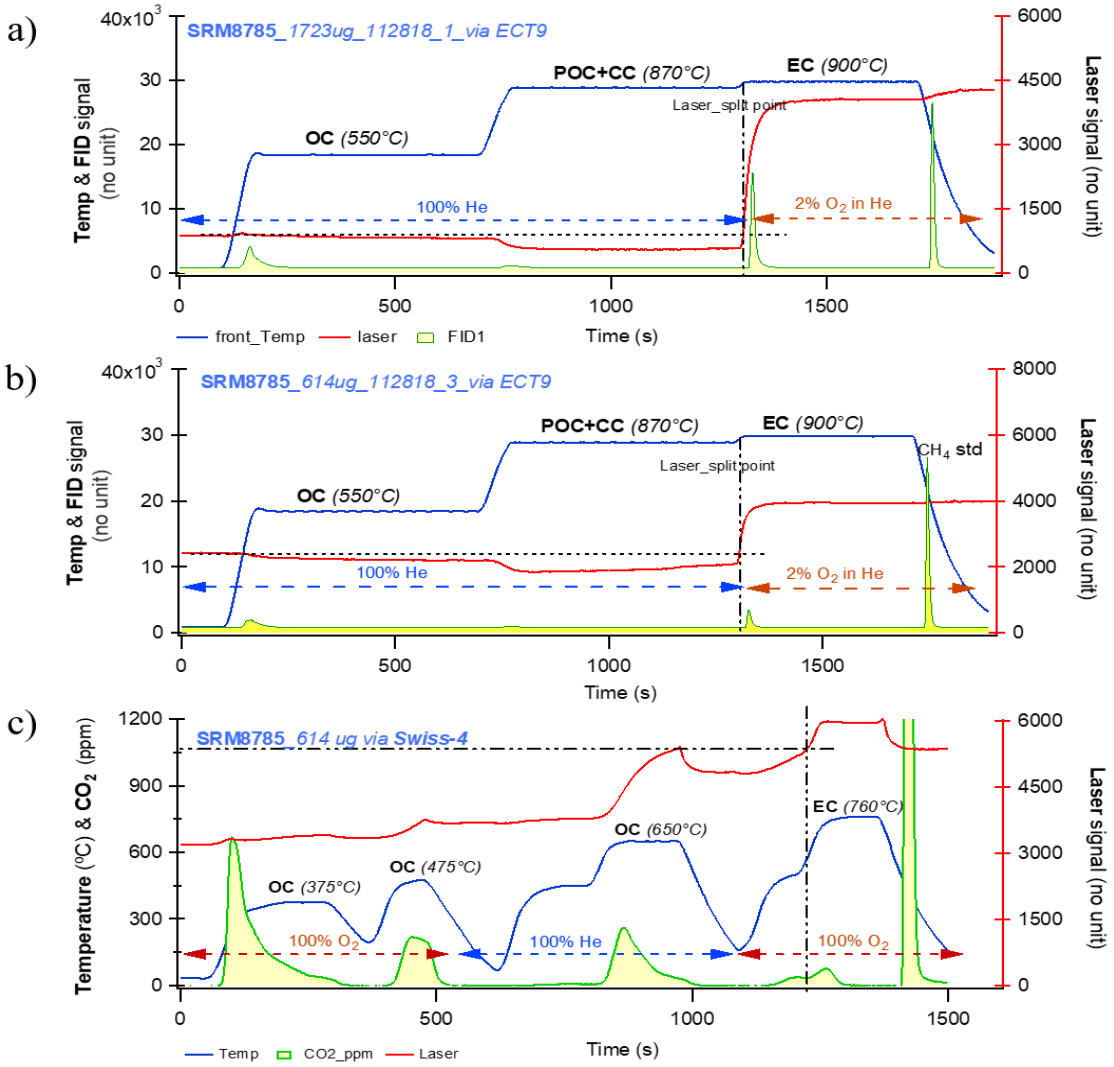

Figure 2.9 Thermograms of the SRM 8785 filters (the fine fraction ($PM_{2.5}$) of re-suspended urban dust particles from SRM 1649a and collected on quartz filters). **a)** and **b)** were obtained by ECT9. The legends are the same as Fig 2.6. Both thermograms in a) and b) show the similar patterns as in Fig. 2.6, 2.7, 2.8. that the laser signals reaching the initial value are just before the temperature stage of BC, suggesting that the charred OC contribution to BC is minimized. The thermogram in **c)** is obtained from the same filter in b) but by Swiss_4S protocol for comparison. The legends are similar except for the integrated area with green line, which stands for CO_2 in ppm (by NDIR) instead of FID signals.

2.4 Conclusions

We demonstrate the effectiveness of the ECT9 protocol to physically isolate OC and BC from aerosol samples for ^{14}C and ^{13}C analysis by using OC and BC reference materials on their own and as mixtures. The ECT9 protocol successfully separates OC and BC fractions with a low (but largely modern) total carbon blank of 1.3±0.6 μg C. The majority (65%) of this extraneous carbon originates from the isolation with the ECT9 protocol, with 35% contributed from graphitization and ^{14}C measurement of the samples at the KCCAMS facility. After mass balance background corrections, the $FM^{14}C$ results from both bulk pure materials and mixtures (with sample size as small as 5 μgC) can reach the consensus values (Table 2.2) with an average uncertainty of about 5%.

In addition, we evaluated potential POC formation during ECT9 by investigating thermograms of a variety of reference materials and ambient filter samples and demonstrated that the ECT9 provides a good alternative for carbonaceous aerosol source apportionment studies, including ultra small sized (5-15 μg C) samples obtained from Arctic regions. To increase the application of isotope data (^{14}C or ^{13}C) in atmospheric research, future efforts should be focused on the comparison on OC/BC separation via different methods/protocols using the same sets of reference materials. At the same time, the isolation results should be also compared among those methods/protocols widely used in long-term national monitoring network for OC/BC contents, ensuring a consistency in measurements between OC/BC concentrations and their corresponding isotopic compositions.

Acknowledgements

This research was supported by base funding from Environment and Climate Change Canada and the KCCAMS Facility at the University of California, Irvine through G.M.S. We thank V. Vetro (Environment and Climate Change Canada) for assisting with CO_2 extraction and J. Southon (KCCAMS) for supporting ^{14}C-AMS analyses.

2.5 References

Andersson, A., Deng, J., Du, K., Zheng, M., Yan, C., Sköld, M., & Gustafsson, Ö. (2015). Regionally-Varying Combustion Sources of the January 2013 Severe Haze Events over Eastern China. *Environmental Science & Technology*, *49*(4), 2038–2043. https://doi.org/10.1021/es503855e

Barrett, T. E., Robinson, E. M., Usenko, S., & Sheesley, R. J. (2015). Source Contributions to Wintertime Elemental and Organic Carbon in the Western Arctic Based on Radiocarbon and Tracer Apportionment. *Environmental Science and Technology*, *49*(19), 11631–11639. https://doi.org/10.1021/acs.est.5b03081

Beverly, R. K., Beaumont, W., Tauz, D., Ormsby, K. M., Reden, K. F. Von, Santos, G. M., & Southon, J. R. (2010). The Keck Carbon Cycle AMS laboraoty, University of California, Irvine: Status report. *Radiocarbon*, *52*(2), 301–309.

Birch, M. E. (2002). Applied Occupational and Environmental Hygiene Occupational Monitoring of Particulate Diesel Exhaust by NIOSH Method 5040. *Applied Occupational and Environmental Hygiene*, *17*(6), 400–405. https://doi.org/10.1080/10473220290035390 To

Bond, T. C., Doherty, S. J., Fahey, D. W., Forster, P. M., Berntsen, T., Deangelo, B. J., et al.

(2013). Bounding the role of black carbon in the climate system: A scientific assessment. *Journal of Geophysical Research Atmospheres*, *118*(11), 5380–5552. https://doi.org/10.1002/jgrd.50171

Cavalli, F., Viana, M., Yttri, K. E., Genberg, J., & Putaud, J. (2010). Toward a standardised thermal-optical protocol for measuring atmospheric organic and elemental carbon : the EUSAAR protocol, 79–89.

Chan, T. W., Huang, L., Leaitch, W. R., Sharma, S., Brook, J. R., Slowik, J. G., et al. (2010). Observations of OM/OC and specific attenuation coefficients (SAC) in ambient fine PM at a rural site in central Ontario, Canada. *Atmospheric Chemistry and Physics*, *10*(5), 2393–2411. https://doi.org/10.5194/acp-10-2393-2010

Chan, Tak W., Meloche, E., Kubsh, J., Brezny, R., Rosenblatt, D., & Rideout, G. (2013). Impact of ambient temperature on gaseous and particle emissions from a direct injection gasoline vehicle and its implications on particle filtration. *SAE Technical Papers*, *2*. https://doi.org/10.4271/2013-01-0527

Chan, Tak W., Huang, L., Banwait, K., Zhang, W., Ernst, D., Wang, X., et al. (2019). Inter-comparison of elemental and organic carbon mass measurements from three North American national long-term monitoring networks at a co-located site. *Atmospheric Measurement Techniques*, *12*(8), 4543–4560. https://doi.org/10.5194/amt-12-4543-2019

Chow, J. C., Watson, J. G., Crow, D., Lowenthal, D. H., & Merrifield, T. (2001). Comparison of IMPROVE and NIOSH Carbon Measurements. *Aerosol Science and Technology*, *34*(1), 23–34. https://doi.org/10.1080/02786820119073

Chow, J. C., Watson, J. G., Chen, L. W. A., Arnott, W. P., Moosmüller, H., & Fung, K. (2004).

Equivalence of elemental carbon by thermal/optical reflectance and transmittance with different temperature protocols. *Environmental Science and Technology*, *38*(16), 4414–4422. https://doi.org/10.1021/es034936u

Chow, J. C., Watson, J. G., Chen, L.-W. A., Chang, M. C. O., Robinson, N. F., Trimble, D., & Kohl, S. (2007). The IMPROVE_A Temperature Protocol for Thermal/Optical Carbon Analysis: Maintaining Consistency with a Long-Term Database. *Journal of the Air & Waste Management Association*, *57*(9), 1014–1023. https://doi.org/10.3155/1047-3289.57.9.1014

Cohen, A. J., Brauer, M., Burnett, R., Anderson, H. R., Frostad, J., Estep, K., et al. (2017). Estimates and 25-year trends of the global burden of disease attributable to ambient air pollution: an analysis of data from the Global Burden of Diseases Study 2015. *The Lancet*, *389*(10082), 1907–1918. https://doi.org/10.1016/S0140-6736(17)30505-6

Currie, L. A., Benner, B. A., Kessler, J. D., Klinedinst, D. B., Klouda, G. A., Marolf, J. V., et al. (2002). A critical evaluation of interlaboratory data on total, elemental, and isotopic carbon in the carbonaceous particle reference material, NIST SRM 1649a. *Journal of Research of the National Institute of Standards and Technology*, *107*(3), 279–298. https://doi.org/10.6028/jres.107.022

Eckhardt, S., Quennehen, B., Olivié, D. J. L., Berntsen, T. K., Cherian, R., Christensen, J. H., et al. (2015). Current model capabilities for simulating black carbon and sulfate concentrations in the Arctic atmosphere: A multi-model evaluation using a comprehensive measurement data set. *Atmospheric Chemistry and Physics*, *15*(16), 9413–9433. https://doi.org/10.5194/acp-15-9413-2015

Evangeliou, N., Balkanski, Y., Hao, W. M., Petkov, A., Silverstein, R. P., Corley, R., et al. (2016). Wildfires in northern Eurasia affect the budget of black carbon in the Arctic-a 12-year retrospective synopsis (2002-2013). *Atmospheric Chemistry and Physics*, *16*(12), 7587–7604. https://doi.org/10.5194/acp-16-7587-2016

Fuzzi, S., Baltensperger, U., Carslaw, K., Decesari, S., Denier Van Der Gon, H., Facchini, M. C., et al. (2015). Particulate matter, air quality and climate: Lessons learned and future needs. *Atmospheric Chemistry and Physics*, *15*(14), 8217–8299. https://doi.org/10.5194/acp-15-8217-2015

Grahame, T. J., Klemm, R., & Schlesinger, R. B. (2014). Public health and components of particulate matter: The changing assessment of black carbon. *Journal of the Air & Waste Management Association*, *64*(6), 620–660. https://doi.org/10.1080/10962247.2014.912692

Graven, H. D. (2015). Impact of fossil fuel emissions on atmospheric radiocarbon and various applications of radiocarbon over this century. *Proceedings of the National Academy of Sciences*, *112*(31), 9542–9545. https://doi.org/10.1073/pnas.1504467112

Hallquist, M., Wenger, J. C., Baltensperger, U., Rudich, Y., Simpson, D., Claeys, M., et al. (2009). The formation, properties and impact of secondary organic aerosol: current and emerging issues. *Atmospheric Chemistry and Physics*, *9*(14), 5155–5236. https://doi.org/10.5194/acp-9-5155-2009

Hammes, K., Smernik, R. J., Skjemstad, J. O., Herzog, A., Vogt, U. F., & Schmidt, M. W. I. (2006). Synthesis and characterisation of laboratory-charred grass straw (Oryza sativa) and chestnut wood (Castanea sativa) as reference materials for black carbon quantification. *Organic Geochemistry*, *37*(11), 1629–1633.

https://doi.org/10.1016/j.orggeochem.2006.07.003

Hammes, K., Schmidt, M. W. I., Smernik, R. J., Currie, L. A., Ball, W. P., Nguyen, T. H., et al. (2007). Comparison of quantification methods to measure fire-derived (black / elemental) carbon in soils and sediments using reference materials from soil , water , sediment and the atmosphere, *21*. https://doi.org/10.1029/2006GB002914

Hand, J. L., Schichtel, B. A., Malm, W. C., & Frank, N. H. (2013). Spatial and temporal trends in PM2.5 organic and elemental carbon across the United States. *Advances in Meteorology*, *2013*. https://doi.org/10.1155/2013/367674

Heal, M. R. (2014). The application of carbon-14 analyses to the source apportionment of atmospheric carbonaceous particulate matter: A review. *Analytical and Bioanalytical Chemistry*, *406*(1), 81–98. https://doi.org/10.1007/s00216-013-7404-1

Heal, M. R., Naysmith, P., Cook, G. T., Xu, S., Duran, T. R., & Harrison, R. M. (2011). Application of 14C analyses to source apportionment of carbonaceous PM2.5 in the UK. *Atmospheric Environment*, *45*(14), 2341–2348. https://doi.org/10.1016/j.atmosenv.2011.02.029

Huang, L. (2018). The issue of harmonizing the methodologies for emission inventories of GHGs with those of SLCFs Constraining Uncertainties of BC in the Climate Forcing Via robust and traceable measurements. In *IPCC Expert Meeting on SLCFs*. Geneva. Retrieved from https://www.ipcc-nggip.iges.or.jp/public/mtdocs/1805_Geneva.html

Huang, L., Brook, J. R., Zhang, W., Li, S. M., Graham, L., Ernst, D., et al. (2006). Stable isotope measurements of carbon fractions (OC/EC) in airborne particulate: A new dimension for source characterization and apportionment. *Atmospheric Environment*, *40*(15), 2690–

2705. https://doi.org/10.1016/j.atmosenv.2005.11.062

Huang, L., Gong, S. L., Sharma, S., Lavoué, D., & Jia, C. Q. (2010). A trajectory analysis of atmospheric transport of black carbon aerosols to Canadian high Arctic in winter and spring (1990–2005). *Atmospheric Chemistry and Physics*, *10*(11), 5065–5073. https://doi.org/10.5194/acp-10-5065-2010

Janssen, N. A., Gerlofs-Nijland, M. E., Lanki, T., O Salonen, R., Cassee, F., Hoek, G., et al. (2012). *Health effects of black carbon*. *World Health Organization Regional Office for Europe*. https://doi.org/10.1016/j.atmosenv.2007.03.042

Jimenez, J. L., Canagaratna, M. R., Donahue, N. M., Prevot, A. S. H., Zhang, Q., Kroll, J. H., et al. (2009). Evolution of organic aerosols in the atmosphere. *Science*, *326*(February), 1526–1529.

Kanakidou, M., Seinfeld, J. H., Pandis, S. N., Barnes, I., Dentener, F. J., Facchini, M. C., et al. (2005). Organic aerosol and global climate modelling: a review. *Atmospheric Chemistry and Physics*, *5*, 1053–1123. https://doi.org/10.5194/acp-5-1053-2005

Laskin, A., Laskin, J., & Nizkorodov, S. a. (2015). Chemistry of Atmospheric Brown Carbon. *Chemical Reviews*, *115*(10), 4335–4382. https://doi.org/10.1021/cr5006167

Leaitch, W. R., Russell, L. M., Liu, J., Kolonjari, F., Toom, D., Huang, L., et al. (2018). Organic functional groups in the submicron aerosol at 82.5° N, 62.5° W from 2012 to 2014. *Atmospheric Chemistry and Physics*, *18*(5), 3269–3287. https://doi.org/10.5194/acp-18-3269-2018

Levin, I., Naegler, T., Kromer, B., Diehl, M., Francey, R., Gomez-Pelaez, A., et al. (2010). Observations and modelling of the global distribution and long-term trend of atmospheric

14CO2. *Tellus B: Chemical and Physical Meteorology*, *62*(1), 26–46. https://doi.org/10.1111/j.1600-0889.2009.00446.x

Meredith, W., Ascough, P. L., Bird, M. I., Large, D. J., Snape, C. E., Sun, Y., & Tilston, E. L. (2012). Assessment of hydropyrolysis as a method for the quantification of black carbon using standard reference materials. *Geochimica et Cosmochimica Acta*, *97*, 131–147. https://doi.org/10.1016/j.gca.2012.08.037

Mouteva, G. O., Fahrni, S. M., Santos, G. M., Randerson, J. T., Zhang, Y.-L., Szidat, S., & Czimczik, C. I. (2015a). Accuracy and precision of ^{14}C-based source apportionment of organic and elemental carbon in aerosols using the Swiss_4S protocol. *Atmospheric Measurement Techniques*, *8*(9), 3729–3743. https://doi.org/10.5194/amt-8-3729-2015

Mouteva, G. O., Czimczik, C. I., Fahrni, S. M., Wiggins, E. B., Rogers, B. M., Veraverbeke, S., et al. (2015b). Black carbon aerosol dynamics and isotopic composition in Alaska linked with boreal fire emissions and depth of burn in organic soils. *Global Biogeochemical Cycles*, *29*(11), 1977–2000. https://doi.org/10.1002/2015GB005247

NIST. (2007). *Certificate of Analysis for Standard Reference Material 1649a, Urban Dust. Revised Certificate*. *National Institute of Standards and Technology*. Gaithersburg, MD. Retrieved from https://www-s.nist.gov/srmors/certificates/archive/1649a.pdf

Pöschl, U. (2005). Atmospheric aerosols: Composition, transformation, climate and health effects. *Angewandte Chemie - International Edition*, *44*(46), 7520–7540. https://doi.org/10.1002/anie.200501122

Putaud, J. P., Van Dingenen, R., Alastuey, A., Bauer, H., Birmili, W., Cyrys, J., et al. (2010). A European aerosol phenomenology - 3: Physical and chemical characteristics of particulate

matter from 60 rural, urban, and kerbside sites across Europe. *Atmospheric Environment*, *44*(10), 1308–1320. https://doi.org/10.1016/j.atmosenv.2009.12.011

Reddy, C. M., Pearson, A., Xu, L., McNichol, A. P., Benner, B. A., Wise, S. A., et al. (2002). Radiocarbon as a tool to apportion the sources of polycyclic aromatic hydrocarbons and black carbon in environmental samples. *Environmental Science and Technology*, *36*(8), 1774–1782. https://doi.org/10.1021/es011343f

Ridley, D. A., Heald, C. L., Ridley, K. J., & Kroll, J. H. (2017). Causes and consequences of decreasing atmospheric organic aerosol in the United States. *Proceedings of the National Academy of Sciences of the United States of America*, *115*(2), 290–295. https://doi.org/10.1073/pnas.1700387115

Santos, G.M., Moore, R. B., Southon, J. R., Griffin, S., Hinger, E., & Zhang, D. (2007a). AMS 14C sample preparation at the KCCAMS/UCI facility:status report and performance of small samples. *Radiocarbon*, *49*(2), 255–269.

Santos, G.M., Southon, J. R., Griffin, S., Beaupre, S. R., & Druffel, E. R. M. (2007b). Ultra small-mass AMS 14C sample preparation and analyses at KCCAMS/UCI Facility. *Nuclear Instruments and Methods in Physics Research Section B: Beam Interactions with Materials and Atoms*, *259*(1), 293–302. https://doi.org/10.1016/j.nimb.2007.01.172

Santos, Guaciara M., Southon, J. R., Drenzek, N. J., Ziolkowski, L. A., Druffel, E., Xu, X., et al. (2010). Blank Assessment for Ultra-Small Radiocarbon Samples: Chemical Extraction and Separation Versus AMS. *Radiocarbon*, *52*(03), 1322–1335. https://doi.org/10.1017/S0033822200046415

Sharma, S., Richard Leaitch, W., Huang, L., Veber, D., Kolonjari, F., Zhang, W., et al. (2017).

An evaluation of three methods for measuring black carbon in Alert, Canada. *Atmospheric Chemistry and Physics*, *17*(24), 15225–15243. https://doi.org/10.5194/acp-17-15225-2017

Shrivastava, M., Cappa, C. D., Fan, J., Goldstein, A. H., Guenther, A. B., Jimenez, J. L., et al. (2017). Recent advances in understanding secondary organic aerosol: Implications for global climate forcing. *Reviews of Geophysics*, *55*(2), 509–559. https://doi.org/10.1002/2016RG000540

Stuiver, M., & Polach, H. A. (1977). Discussion Reporting of 14C Data. *Radiocarbon*, *19*(03), 355–363. https://doi.org/10.1017/S0033822200003672

Szidat, S., Jenk, T. M., Gäggeler, H. W., Synal, H. A., Hajdas, I., Bonani, G., & Saurer, M. (2004). THEODORE, a two-step heating system for the EC/OC determination of radiocarbon (14C) in the environment. *Nuclear Instruments and Methods in Physics Research, Section B: Beam Interactions with Materials and Atoms*, *223–224*(SPEC. ISS.), 829–836. https://doi.org/10.1016/j.nimb.2004.04.153

Szidat, Sönke, Jenk, T. M., Synal, H.-A., Kalberer, M., Wacker, L., Hajdas, I., et al. (2006). Contributions of fossil fuel, biomass-burning, and biogenic emissions to carbonaceous aerosols in Zurich as traced by 14C. *Journal of Geophysical Research*, *111*(D7), D07206.

Trumbore, S. E., Sierra, C. A., & Hicks Pries, C. E. (2016). Radiocarbon Nomenclature, Theory, Models, and Interpretation: Measuring Age, Determining Cycling Rates, and Tracing Source Pools. In E. A. G. Schuur, E. Druffel, & S. E. Trumbore (Eds.), *Radiocarbon and Climate Change: Mechanisms, Applications and Laboratory Techniques* (pp. 45–82). Cham: Springer International Publishing. https://doi.org/10.1007/978-3-319-25643-6_3

Wex, H., Huang, L., Zhang, W., Hung, H., Traversi, R., Becagli, S., et al. (2019). Annual

variability of ice-nucleating particle concentrations at different Arctic locations. *Atmospheric Chemistry and Physics*, *19*(7), 5293–5311. https://doi.org/10.5194/acp-19-5293-2019

Wiggins, E. B., Czimczik, C. I., Santos, G. M., Chen, Y., Xu, X., Holden, S. R., et al. (2018). Smoke radiocarbon measurements from Indonesian fires provide evidence for burning of millennia-aged peat. *Proceedings of the National Academy of Sciences*, *115*(49), 12419–12424. https://doi.org/10.1073/pnas.1806003115

Willis, M. D., Healy, R. M., Riemer, N., West, M., Wang, J. M., Jeong, C., et al. (2016). Quantification of black carbon mixing state from traffic : implications for aerosol optical properties, 4693–4706. https://doi.org/10.5194/acp-16-4693-2016

Winiger, P., Andersson, A., Eckhardt, S., Stohl, A., & Gustafsson, O. (2016). The sources of atmospheric black carbon at a European gateway to the Arctic. *Nature Communications*, *7*. https://doi.org/10.1038/ncomms12776

Winiger, P., Andersson, A., Eckhardt, S., Stohl, A., Semiletov, I. P., Dudarev, O. V., et al. (2017). Siberian Arctic black carbon sources constrained by model and observation. *Proceedings of the National Academy of Sciences*, *114*(7), E1054–E1061. https://doi.org/10.1073/pnas.1613401114

Winiger, P., Barrett, T. E., Sheesley, R. J., Huang, L., Sharma, S., Barrie, L. A., et al. (2019). Source apportionment of circum-Arctic atmospheric black carbon from isotopes and modeling. *Science Advances*, *5*(2), eaau8052. https://doi.org/10.1126/sciadv.aau8052

Xu, J. W., Martin, R. V., Morrow, A., Sharma, S., Huang, L., Richard Leaitch, W., et al. (2017). Source attribution of Arctic black carbon constrained by aircraft and surface

measurements. *Atmospheric Chemistry and Physics*, *17*(19), 11971–11989. https://doi.org/10.5194/acp-17-11971-2017

Xu, X., Trumbore, S. E., Zheng, S., Southon, J. R., McDuffee, K. E., Luttgen, M., & Liu, J. C. (2007). Modifying a sealed tube zinc reduction method for preparation of AMS graphite targets: Reducing background and attaining high precision. *Nuclear Instruments and Methods in Physics Research, Section B: Beam Interactions with Materials and Atoms*, *259*(1), 320–329. https://doi.org/10.1016/j.nimb.2007.01.175

Yang, F., Huang, L., Duan, F., Zhang, W., He, K., Ma, Y., et al. (2011). Carbonaceous species in PM2.5 at a pair of rural/urban sites in Beijing, 2005-2008. *Atmospheric Chemistry and Physics*, *11*(15), 7893–7903. https://doi.org/10.5194/acp-11-7893-2011

Zencak, Z., Elmquist, M., & Gustafsson, Ö. (2007). Quantification and radiocarbon source apportionment of black carbon in atmospheric aerosols using the CTO-375 method. *Atmospheric Environment*, *41*, 7895–7906.

Zhang, X., Li, J., Mo, Y., Shen, C., Ding, P., Wang, N., et al. (2019). Isolation and radiocarbon analysis of elemental carbon in atmospheric aerosols using hydropyrolysis. *Atmospheric Environment*, *198*(August 2018), 381–386. https://doi.org/10.1016/j.atmosenv.2018.11.005

Zhang, X. Y., Wang, Y. Q., Zhang, X. C., Guo, W., & Gong, S. L. (2008). Carbonaceous aerosol composition over various regions of China during 2006. *Journal of Geophysical Research*, *113*, D14111.

Zhang, Y. L., Perron, N., Ciobanu, V. G., Zotter, P., Minguillón, M. C., Wacker, L., et al. (2012). On the isolation of OC and EC and the optimal strategy of radiocarbon-based source

apportionment of carbonaceous aerosols. *Atmospheric Chemistry and Physics*, *12*(22), 10841–10856. https://doi.org/10.5194/acp-12-10841-2012

2.6 Appendix

Table A2.1 Radiocarbon content of bulk reference materials, expressed as fraction modern carbon (FM) with and without background correction. CO_2 isolation and $^{14}C/^{12}C$ analysis were carried out at KCCAMS, UCI (the method is described in Table 2).

UCI AMS #	Size	Corrected FM		Uncorrected FM	
	µg C		±		±
Sucrose					
150230	735	1.0597	0.0021	1.0597	0.0021
150231	769	1.0575	0.0017	1.0574	0.0017
Adipic Acid					
123428	876	0.0002	0.0005	0.002	0.0001
123430	851	0.0001	0.0005	0.0019	0.0001
123431	934	-0.0001	0.0005	0.0016	0.0001
123432	1053	-0.0003	0.0005	0.0015	0.0001
123433	740	-0.0001	0.0005	0.0016	0.0001
Regal Black					
150228	717	0.0004	0.0005	0.0019	0.0001
150229	752	-0.0005	0.0005	0.0011	0
C1150					
150232	88	0.0026	0.0005	0.0042	0.0001
150233	64	0.0035	0.0005	0.005	0.0002
150234	560	0.0019	0.0005	0.0035	0.0001
Rice Char					
123434	924	1.0683	0.0023	1.0683	0.0023
123435	913	1.067	0.0018	1.067	0.0018
123436	961	1.0673	0.0019	1.0672	0.0019

Table A2.2 Stable isotopic composition ($^{13}C/^{12}C$) of OC and BC fractions or bulk materials. CO_2 isolation and $^{13}C/^{12}C$ analysis were carried out at the CAIR lab, CRD, ASTD/ECCC (the method is described in Table 2).

Reference material	Lab ID	Date	Fraction	Loaded mass on filter µg or µg C[a]	$\delta^{13}C_{VPDB}$ ‰
Regal Black	16-036-04	5-Feb-16	BC	16	-27.67
(n = 5)	16-036-05	5-Feb-16	BC	27	-27.49
	16-036-06	5-Feb-16	BC	22	-27.67
	16-036-08	5-Feb-16	BC	59	-27.62
	16-036-09	5-Feb-16	BC	68	-27.57
				mean	**-27.61**
				s.d.	**0.08**
C1150	13-013-05	13-Jan-13	BC	50	-23.01
(n = 5)	13-013-07	13-Jan-13	BC	22	-23.16
	13-013-08	13-Jan-13	BC	48	-22.96
	16-036-06	5-Feb-16	BC	30	-23.14
	16-036-07	5-Feb-16	BC	46	-23.05
				mean	**-23.06**
				s.d.	**0.08**
Sucrose[b]	15-146-07	26-May-15	OC	20	-12.08
(n = 9)	15-148-03	27-May-15	OC	20	-12.4
	15-148-04	27-May-15	OC	20	-12.31
		5-Oct-17	OC	20	-12.44
		18-Apr-18	OC	20	-12.04
		18-Apr-18	OC	20	-12.3
		26-Feb-19	OC	20	-12.21
		26-Feb-19	OC	20	-12.16
		26-Feb-19	OC	20	-12.04
				mean	**-12.22**
				s.d.	**0.15**
Rice Char	04-328-06	23-Nov-04	OC	n/m	-24.42
(n = 1)	04-328-07	23-Nov-04	POC	n/m	-26.67
	04-328-05	23-Nov-04	BC	n/m	-26.94
		fraction-weighted composition	TC	160	**-26.74**
SRM-1649a					
(n = 2)	04-330-03	25-Nov-04	OC	n/m	-26.38
	04-338-08	3-Dec-04	OC	n/m	-26.29

04-330-05	25-Nov-04	POC	n/m	-25.51
04-338-07	3-Dec-04	POC	n/m	-25.66
04-330-06	25-Nov-04	BC	n/m	-25.56
04-338-09	3-Dec-04	BC	n/m	-25.43
	fraction-weighted composition[c]	TC	~ 600	**-25.84 ± 0.07**

[a]Sucrose was loaded as a solution (µg C), Regal Black, C1150, Rice char, and SRM-1649a as a powder (µg dry mass);[b]$\delta^{13}C_{VPDB}$ of bulk material (sucrose) via off-line method: -12.0 ± 0.2‰ (Satoshi, 2008); [c]Mean fraction (of two measurements) weighted isotopic composition of TC; n/m = not measured.

Table A2.3 Stable isotopic compositions of 13C/12C in OC and BC fractions from mixtures of reference materials. OC and BC fractions were isolated with the ECT9 protocol (Huang et al., 2006), purified in a vacuum system and analyzed on a MAT253 at the CAIR lab, CRD, ASTD/ECCC.

Reference material	Lab ID	Date	Initial mass		Measured fraction	$\delta^{13}C_{VPDB}$
			Sucrose	Regal Black		
			µg C	µg		(‰)
Regal Black	15-148-08	28-May-15	10	22	BC	-27.49
n = 9	15-148-05	28-May-15	15	26	BC	-27.73
	15-149-07	29-May-15	20	50.4	BC	-27.34
	15-148-09	28-May-15	30	66	BC	-27.32
	16-224-04	11-Aug-16	20	57	BC	-27.31
	16-224-07	11-Aug-16	20	53	BC	-27.27
	16-224-08	11-Aug-16	20	58	BC	-27.37
	16-225-07	12-Aug-16	10	20	BC	-27.57
	17-248-08	30-Aug-17	20	53	BC	-27.47
					mean	**-27.43**
					s.d.	**0.15**
Sucrose	15-149-04	29-May-15	10	22	OC	-12.82
n = 9	15-148-06	28-May-15	15	26	OC	-12.54
	15-149-05	29-May-15	20	50.4	OC	-12.54
	15-149-06	29-May-15	30	66	OC	-12.29
	16-224-05	11-Aug-16	20	57	OC	-13.04
	16-224-06	11-Aug-16	20	53	OC	-12.36
	16-225-03	12-Aug-16	20	58	OC	-12.72
	16-225-04	12-Aug-16	10	20	OC	-12.86
	17-242-06	30-Aug-17	20	53	OC	-12.34
					mean	**-12.61**
					s.d.	**0.26**

Table A2.4 Calculated stable isotopic composition ($^{13}C/^{12}C$) in a two-end-member-mixing system with endmember #1 being Sucrose ($\delta^{13}CV_{PDB}$ =-12.22‰) and end member #2 being Regal black ($\delta^{13}CV_{PDB}$=-27.61‰) and where endmember #1 is mixed into endmember #2.

Sucrose fraction in mixture (Sucrose + Regal black)	**Caluclated $\delta^{13}C_{VPDB}$**
%	‰
0	-27.61
1	-27.456
2	-27.302
3	-27.148
4	-26.994
5	-26.841
10	-26.071
20	-24.532
30	-22.993
40	-21.454
50	-19.915
60	-18.376
70	-16.837
80	-15.298
90	-13.759
91	-13.605
92	-13.451
93	-13.297
94	-13.143
95	-12.99
96	-12.836
97	-12.682
98	-12.528
99	-12.374
100	-12.22

Table A2.5 Radiocarbon content, expressed as fraction modern carbon (FM), of total (TC), organic (OC), and black (BC) carbon fractions with and without background correction following Santos et al. (2010). OC and BC fractions were isolated with the ECT9 protocol (Huang et al., 2006) from pure reference materials (into the form of CO_2), then purified cryogenically and sealed in ampoules at the CAIR lab, ECCC. CO_2 is reduced to graphite (Santos et al., 2007a, 2007b) and analyzed at the KCCAMS facility.

UCIAMS#	Fraction	ECT9 Mass	KCCAMS Mass	Corrected FM		Uncorrected FM	
		µgC	µgC		±		±
			Adipic Acid				
153279	TC	10	14	-0.005	0.0367	0.0593	0.001
153280	TC	17	16	-0.0116	0.0325	0.0465	0.0009
153281	TC	23	29	-0.0043	0.0165	0.0268	0.0005
153282	TC	37	37	-0.0102	0.0125	0.014	0.0006
mean				-0.0078			
s.d.				0.0037			
			Sucrose				
153283	TC	5	7	1.0041	0.0885	0.8766	0.0101
153284	TC	5	7	1.0031	0.0878	0.8759	0.0051
153285	TC	5	7	1.0346	0.0938	0.896	0.0064
153286	TC	10	11	1.0529	0.0516	0.9652	0.0045
153287	TC	10	11	1.036	0.0511	0.951	0.007
153288	TC	10	12	1.0571	0.051	0.9702	0.0056
153289	TC	20	21	1.0477	0.0265	1.0006	0.0069
153290	TC	20	21	1.0429	0.0257	0.9971	0.0058
153291	TC	20	21	1.047	0.0262	1	0.0056
153292	TC	40	41	1.0405	0.0127	1.017	0.0034
153293	TC	40	38	1.0543	0.0139	1.0282	0.0034
153294	TC	40	42	1.0509	0.0125	1.0272	0.0026
153295	OC	20	20	1.0844	0.029	1.0305	0.0041
mean				1.0427			
s.d.				0.0213			
C1150							
153303	TC	7	10	0.031	0.0535	0.1154	0.002
153304	TC	16	23	0.0278	0.0205	0.0644	0.0012
153305	TC	34	36	-0.0012	0.0131	0.0237	0.0006
153306	TC	45	55	0.0041	0.0083	0.0201	0.0003
153307	BC	32	33	-0.0072	0.0144	0.0202	0.0004
mean				0.0109			
s.d.				0.0174			
			Regal Black				
153308	TC	16	23	0.0161	0.0209	0.054	0.0008

153309	TC	47	53	-0.0008	0.0087	0.016	0.0004
153310	BC	28	41	-0.0057	0.0112	0.0159	0.0004
mean				0.0032			
s.d.				0.0114			
Rice Char							
153299	TC	6	7	0.9383	0.083	0.8272	0.0097
153300	TC	12	15	1.0463	0.039	0.9784	0.0057
153301	TC	24	22	1.0823	0.0254	1.0348	0.0046
153302	BC	13	15	1.0621	0.0383	0.994	0.0046
mean				1.0323			
s.d.				0.0643			
Oxalic Acid-II[a]							
153316	TC	n/a	7	1.3141	0.0398	1.2411	0.0203
153315	TC	n/a	17	1.3365	0.0137	1.308	0.0063
153314	TC	n/a	45	1.3342	0.0051	1.3235	0.0027
mean				1.3283			
s.d.				0.0123			
Adipic Acid[a]							
153318	TC	n/a	6	-0.002	0.0313	0.0544	0.0031
153317	TC	n/a	16	-0.0016	0.0115	0.0205	0.0011
153278	TC	n/a	56	-0.0014	0.0033	0.0051	0.0003
mean				-0.0017			
s.d.				0.0003			

[a]Reference standards that underwent combustion and graphitization process only for blank determination at KCCAMS (without ECT9); n/a. = not applicable

Table A2.6 Radiocarbon content, expressed as fraction modern carbon (FM), of total (TC), organic (OC), and black (BC) carbon fractions with and without background correction following Santos et al. (2010). OC and BC fractions were isolated with the ECT9 protocol (Huang et al., 2006) from mixtures of reference materials (into the form of CO_2), then purified cryogenically and sealed in ampoules at ECCC. CO_2 is reduced to graphite (Santos et al., 2007a, 2007b) and analyzed at KCCAMS facility.

UCI AMS #	Fraction measured	Initial loaded mass		ECT9 Mass	KCCAMS Mass	Corrected FM		Uncorrected FM	
		µg C	µg	µg C		±		±	
Sucrose + Regal black		Sucrose	Regal black						
159800	OC	5	10	5	6	1.0568	0.0648	0.9738	0.0107
159802	OC	10	21	11	10	1.0542	0.0337	1.0057	0.0049
159804	OC	15	29	16	15	1.0629	0.0216	1.0298	0.0037
159806	OC	20	39	21	20	1.0436	0.0156	1.0201	0.0034
159808	OC	30	63	32	29	1.0563	0.0107	1.0395	0.0025
159801	BC	5	10	10	11	-0.0361	-0.0502	0.0535	0.0014
159803	BC	10	21	20	19	-0.0189	-0.027	0.0317	0.0007
159805	BC	15	29	28	36	-0.0091	-0.0136	0.0172	0.0005
159807	BC	20	39	38	44	0.0014	0.011	0.0226	0.0004
159809	BC	30	63	61	56	0.0019	0.0085	0.0186	0.0003
Adipic acid + Bulk rice char		Adipic acid	Bulk rice char[a]						
159822	OC	5	11	6	6	0.1009	0.0856	0.2279	0.0027
159824	OC	10	22	12	11	0.0759	0.045	0.1516	0.0021
159826	OC	15	35	18	17	0.1078	0.0278	0.1558	0.0013
159828	OC	20	44	23	22	0.1072	0.0204	0.1432	0.0014
159830	OC	25	51	29	23	0.1552	0.0185	0.1868	0.0011
159832	OC	30	60	34	32	0.1013	0.0138	0.1263	0.0009
159823	BC	5	11	5	5	1.1063	0.0887	0.9903	0.0063
159825	BC	10	22	10	8	1.0981	0.0486	1.0263	0.0052
159827	BC	15	35	16	14	1.0559	0.0231	1.0211	0.0034
159829	BC	20	44	20	17	1.0619	0.019	1.0328	0.004
159831	BC	25	51	23	22	1.0625	0.0143	1.04	0.0027
159833	BC	30	60	27	24	1.0633	0.0131	1.0426	0.0028
Adipic acid + Rice char BC[b]		Adipic acid	Rice char BC						
159810	OC	5	13	5	6	-0.0605	-0.1166	0.1212	0.0032
159812	OC	10	19	10	10	-0.0324	-0.0558	0.0655	0.0015
159814	OC	15	34	15	15	-0.0075	-0.0345	0.0556	0.0008
159816	OC	20	38	20	20	0.0107	0.0248	0.0568	0.0011
159818	OC	25	49	25	25	-0.0009	-0.0198	0.0366	0.0005

159820	OC	30	60	30	29	0.0103	0.0168	0.0421	0.0006
159811	BC	5	13	6	5	1.0926	0.0931	0.9755	0.0094
159813	BC	10	19	8	7	1.0702	0.0506	0.9997	0.0058
159815	BC	15	34	15	16	1.0709	0.0203	1.0392	0.0037
159817	BC	20	38	17	20	1.0726	0.0162	1.0471	0.0038
159819	BC	25	49	22	21	1.0749	0.0152	1.0505	0.0029
159821	BC	30	60	27	27	1.0723	0.0116	1.0535	0.0024

[a]The bulk rice char contains 52% of TC, on which 14% is OC and 86% BC, respectively; [b]Adipic acid was injected after the OC of rice char is removed through combustion at 870°C via ECT9. Thus, adipic acid was mixed only with rice char-BC, and the OC of the mixture is only from Adipic acid and BC of the mixture is only from Rice char.

Chapter 3

Seasonal cycle of isotope-based source apportionment of elemental carbon in airborne particulate matter and snow at Alert, Canada

Adapted from:

Rodríguez, B. T., Huang, L., Santos, G. M., Zhang, W., Vetro, V., Xu, X., et al. (2020). Seasonal cycle of isotope-based source apportionment of elemental carbon in airborne particulate matter and snow at Alert, Canada. *Journal of Geophysical Research: Atmospheres*, 125, e2020JD033125. https://doi.org/10.1029/2020JD033125

3.1 Introduction

Aerosol influences Arctic climate via aerosol-radiation and -cloud interactions (Willis et al., 2018). A major contributor is carbonaceous aerosol that mostly consists of weakly refractory, light-scattering organic carbon (OC) and a smaller fraction of strongly refractory, light-absorbing black carbon (BC) (Andreae & Gelencsér, 2006; Petzold et al., 2013; Pöschl, 2005). OC can be emitted during combustion processes as primary aerosols and also as secondary aerosols from the oxidation and condensation of volatile organic compounds (Hallquist et al., 2009), whereas most BC is directly emitted during combustion processes. Suspended within the atmosphere and deposited on snow- and ice-covered surfaces, BC impacts climate directly and indirectly (Bond et al., 2013).

Arctic aerosols arise from the long-range transport of pollutants into the Arctic from lower latitudes and emissions within the Arctic (Willis et al., 2018). Their concentrations, composition, life-time, sources, and climate impacts vary seasonally due to shifts in available solar radia-

tion, temperature, and precipitation (Law & Stohl, 2007). The aerosol burden is greatest in winter and spring, known as "Arctic haze" (Law & Stohl, 2007; Shaw et al., 1993). Its vertical distribution within the atmosphere is bimodal (Hansen & Rosen, 1984) and satellite observations show that regionally-emitted pollutants accumulate below strong inversions within the polar dome in winter, while pollutants from lower latitudes reach the free troposphere in spring (Qi & Wang, 2019; Thomas et al., 2019). Surface pollution episodes arise from stagnant conditions caused by high-pressure systems and inefficient scavenging of particles within the polar dome (Browse et al., 2012; Qi, et al., 2017a; Shen et al., 2017).

Concentrations of air pollutants such as BC have been decreasing at various Arctic monitoring stations due to an overall decrease in emissions (Dutkiewicz et al., 2014; Hirdman et al., 2010). However, we anticipate changes in the concentration and composition of Arctic aerosol (Willis et al., 2018) as a consequence of rapid climate change (Box et al., 2019), diminishing sea ice (Comiso, 2012), changes in the productivity and disturbance regimes of marine and terrestrial ecosystems (Post et al., 2013; Wang et al., 2020), and increasing anthropogenic activities (Stephenson et al., 2018). Thus, major uncertainties remain in our understanding of regional and global aerosol sources, their precursors, and their relative importance to depositional efficiency (Willis et al., 2018).

To minimize these uncertainties, aerosol monitoring efforts within the Arctic rely on continuous observations at long-term monitoring stations (Willis et al., 2018), ship and aircraft campaigns (Ancellet et al., 2014; Fisher et al., 2010; Roiger et al., 2015), and source analyses using emission inventories (Giglio et al., 2013; Huang et al., 2015; Randerson et al., 2012; Stohl et al., 2015). These data suggest that 70% of BC emissions within the Arctic are of anthropogenic origin (AMAP, 2015), while globally only about 40% are anthropogenic. In the High Arctic, coal

and diesel remain the primary fuels for transportation and heating, respectively. Another poorly constrained source of BC is gas flaring in the power sector (Stohl et al., 2013). Emission inventories indicate that gas flaring contributes 3% to global BC, but 60-70% to Arctic BC, yet ground observations do not corroborate significant gas flaring emissions (Winiger et al., 2019). In addition, volcanic activity might contribute to the fossil BC burden (Leaitch et al., 2018).

Biomass burning, including wildfires, crop residue burning, and biofuel usage, also contributes to the Arctic's BC burden (Barrett et al., 2015; Mouteva et al., 2015; Warneke et al., 2010; Winiger et al., 2017; Winiger et al., 2019). Biomass burning can inject significant amounts of BC into the free troposphere and stratosphere, which increases the lifetime of BC, particularly when the atmosphere is strongly stratified in winter and spring (Fromm et al., 2010; Qi & Wang, 2019; Stohl et al., 2006). Biomass emissions are greatest between March and October; yet transport to and within the Arctic is limited during the summer by increased wet-scavenging efficiency under warmer and more humid conditions (Browse et al., 2012; Garrett et al., 2011).

During the past three decades, peak concentrations of BC during winter have declined at most Arctic monitoring stations, including Alert (-49%), Barrow (-33%), and Zeppelin (-40%) due to improvements in combustion technology, the use of low emission fuels, and declines in former Soviet Union emissions (AMAP, 2015; Sharma et al., 2013; Sharma et al., 2006). Additionally, changes in transport and deposition pathways are expected to reduce Arctic BC by 14% by the end of the 21st century (Jiao & Flanner, 2016) in response to shifts in climate, large-scale weather patterns, increased atmospheric temperatures, and sea-ice regime shifts from thick multi-year ice to thinner first-year ice (Komatsu et al., 2018; Pozzoli et al., 2017; Woods & Caballero, 2016). Nonetheless, major uncertainties remain in respect to quantifying current BC emissions,

the rise of ship emissions, and modeling future aerosol-cloud interactions (Willis et al., 2018; Winiger et al., 2019).

Estimating geographical and sector contributions to Arctic BC load usually involves matching observationally based concentrations of BC to modelled outputs derived from emission inventories and meteorology-driven chemical transport models (Qi et al., 2017a; Qi et al., 2017b). These modeling studies depend on meteorology and a proper description of chemical processing with the current state of knowledge on BC aging and deposition rates. For the Alert monitoring station, modeling efforts continue to capture the observed seasonal cycle but either over- or underestimate BC concentrations year-round (Browse et al., 2012; Qi et al., 2017a; Qi et al., 2017b) due to uncertainties in emission inventories (AMAP, 2015) and shifting seasonal depositional processes (Browse et al., 2012, 2014).

Another approach for quantifying the sources of carbonaceous aerosol is to measure their stable ($\delta^{13}C$) and radiocarbon ($\Delta^{14}C$) compositions (Heal, 2014; Martinelli et al., 2002). $\delta^{13}C$ signatures reflect mass-dependent fractionation of ^{13}C vs. ^{12}C during biogeochemical processes and can be used to differentiate fossil fuels (gaseous vs. liquid/solid). $\Delta^{14}C$ data is corrected for mass-dependent isotopic fractionation, represents a measure of age (or source), and can be used to separate fossil fuel-derived from biomass carbon.

Specifically, ^{14}C is a radioisotope produced in the upper atmosphere with a half-life of 5730 years. It is oxidized to carbon dioxide (CO_2) and enters the food chain via photosynthesis so that living biomass (and any BC emitted during its combustion) is labeled with the ^{14}C content of the atmospheric CO_2 at growth. When the organism ceases carbon uptake upon death, its $\Delta^{14}C$ declines due to radioactive decay. Consequently, ancient fossil fuels (and their BC emissions) are ^{14}C-free ($\Delta^{14}C$ = -1000‰). While BC emissions from annual biomass have the same $\Delta^{14}C$ as cur-

rent atmospheric CO_2, BC from perennial plants reflect the integrated $\Delta^{14}C$ of the atmosphere over their lifetime. This atmospheric $\Delta^{14}C$ has been changing dramatically since 1950, because thermo-nuclear weapon's testing in the mid-20th century doubled the atmosphere's ^{14}C content; biomass formed after 1950 contains additional ^{14}C (bomb- or modern-^{14}C, $\Delta^{14}C > 0‰$). The amount of ^{14}C in the atmosphere (and biomass) has been declining over the past 70 years due to mixing of bomb-^{14}C with the ocean and biosphere reservoirs in the global carbon cycle and by dilution with fossil fuel-derived CO_2 (Graven, 2015; Levin et al., 2010).

Measurements of $\Delta^{14}C$ of BC across the Arctic by Winiger et al. (2015, 2016, 2017, 2019) generally support the predictions of BC emission inventories and modeling. Yet, low carbon concentrations posed a challenge that in the past have forced these studies to integrate samples for as long as three months, particularly during the summer. Here, we present the first time series of $\Delta^{14}C$ of µg-sized BC samples (5-20 µg C) at higher time resolution (13 to 41 days) from aerosol suspended in surface air and scavenged in snow. Specifically, we quantified the composition of carbonaceous aerosols in airborne particulate matter (PM) and snow at Alert, Canada between March 2014 and June 2015. To elucidate the chemical properties of the aerosol composition, we isolated OC and BC fractions with the ECT9 protocol (Huang et al., 2006, 2020). We also combined $\delta^{13}C$ and $\Delta^{14}C$ mass balance analyses of the BC fraction with backward trajectory modeling (HYSPLIT) to identify aerosol source sectors and regions.

3.2 Materials and methods

3.2.1 Sample collection

Total suspended particles

A custom-built high-volume aerosol sampler was used at the Dr. Neil Trivett Global Atmosphere Watch Observatory at Alert, Canada (83.2°N, 62.5°W, 210 m above sea level, Fig.

3.1) to collect weekly or biweekly samples as part of long-term carbonaceous aerosol observation program. The PM samples used in this study represent total suspended particles and were collected between March 5, 2014 and June 3, 2015. The sampler is installed at a walk-up deck, about 5 meters above the ground. Flow rate is approximately 1.4 m^3 min^{-1} at STP conditions. Quartz filters (QFF, Millipore, 8 x 10 in, USA) were sampled continuously with 7-days sampling time from Dec-Apr and 14-days from May-Nov. A total of 8 field blanks were measured. After sampling, filters were stored (at room temperature ~ 20°C) in their sampling cartridges (inside sealed plastic bags) at the Alert station and shipped in aluminum boxes (containing 5 sampling cartridges each) to Toronto, where they were wrapped in pre-combusted Al-foil and stored at -30°C until analysis. Air temperatures and pressures were recorded and averaged over the integrated sampling time and both are used for final flow rate and total air volume calculation.

Figure 3.1 Image of the Dr. Neil Trivett Global Atmosphere Watch Observatory at Alert, Nunavut Canada (83.2°N, 62.5°W, 210 m above sea level).

Snow

Fresh snow was collected from the ground at a fixed location (GPS coordinate: 82.45°N; 62.51°W) about 100 m south of the laboratory throughout a period of eight months (Oct. 2014 – May 2015). The sampling strategy was designed to capture fresh snow after snow fall events. Snow was collected into a stainless steel (SS) Dewar (750 ml) using a SS scooper. Each collection was 7-10 days apart. Ideally, three fresh snow samples were collected throughout one month evenly distributed in time. If there were no events, however, the collection would capture the same snow as the previous sample. Therefore, it is likely that dry deposition particles and wind-driven drifted snow was also captured. The collected samples in SS dewars were stored in coolers, which were placed outside of the lab until transporting them back to Toronto for BC analysis at the Carbonaceous Aerosol & Isotope Research (CAIR) laboratory within the Climate Research Division (CRD) of Environment and Climate Change Canada (ECCC).

The snow samples were melted individually in a microwave in a glass beaker. The snow water was sonicated and deposited onto quartz filters through filtration. After drying, the filters were analyzed for BC mass concentrations via the ECT9 protocol (see Supporting Information for more details).

3.2.2 Carbonaceous aerosol analysis

To determine the concentration and composition of the carbonaceous aerosol, all filters were analyzed with the EnCan-Total-900 (ECT9) protocol on an OC/BC analyzer (Sunset Laboratory Inc.) at CAIR (Chan et al., 2019; Huang et al., 2006). The ECT9 protocol and its application to isotope measurements are discussed in detail in Huang et al. (2020). Briefly: (1) OC is released in pure helium (He) at 550°C for 600 seconds, (2) pyrolyzed OC (POC) and carbonate carbon (CC) are released in He stream at 870°C for 600 seconds, and (3) BC is combusted at 900°C in 98% He and 2% oxygen (O_2) for 420 seconds. CO_2 oxidized from all carbon fractions

are then converted to methane, and carbon contents were quantified with a flame ionization detector. Each sample is internally calibrated with a known amount of CH_4 gas at the end of each analysis. The analytical accuracy, precision, and linearity range of the ECT9 method are 0.2, 0.1, and 1–17 μg cm^{-2}, respectively (Huang et al., 2006). The reproducibility of BC/TC ratio is less than 2% (Huang et al., 2020). The concentration of OC was calculated as the sum of OC and POC+CC, while total carbon (TC) was calculated as the sum of the OC, POC+CC, and BC fractions.

In addition, individual BC fractions were analyzed for their $\delta^{13}C$ and $\Delta^{14}C$. To quantify $\delta^{13}C$, the BC fraction was isolated from an additional aliquot of the individual aerosol filters or snow filters with the ECT9 protocol, cryogenically trapped, and measured with the cold-finger mode in an IRMS (MAT 253). The uncertainty of this measurement is about 0.3‰ (Huang et al., 2006, 2020).

For ^{14}C analysis, BC fractions were isolated from additional filter aliquots with the ECT9 protocol, cryogenically trapped, and combined to yield biweekly- or monthly-integrated samples (Table A3.1). Similarly, the BC fractions from individual snow events were pooled into monthly-integrated samples. Subsequently, the BC fraction (in the form of CO_2) was sent for ^{14}C analysis to the W. M. Keck Carbon Cycle Accelerator Mass Spectrometer (KCCAMS) facility at the University of California, Irvine, USA. Here, the BC-CO_2 samples were purified on a vacuum line and converted to graphite using a sealed-tube zinc reduction protocol for ultra-small samples (Walker & Xu, 2019) and measured alongside a suite of size-matched (7-34 μg C) and regular-sized (1 mg C) standards (materials with known ^{14}C content). The corresponding processing standards (^{14}C-free and modern carbon) were determined and their ^{14}C contents were corrected for contributions of extraneous carbon (Santos et al., 2007). The total extraneous carbon intro-

duced by BC separation, graphitization, and analysis with accelerator mass spectrometry (AMS) in this study was 1.85±0.62 µg C. BC separation through the ECT9 protocol incorporated on average 0.95±0.47 µg C, while 0.90±0.65 µg C was incorporated through the combustion, graphitization and AMS analysis (Table A3.3). Sample sizes ranged from 3.2 to 19.5 µg C and corrected using a mass balance approach, resulting in larger uncertainties for smaller samples (Figures 3.5, 3.6; Table A3.1). The details of ^{14}C analysis for ultra-small samples in conjunction with the ECT9 protocol can be found in Huang et al. (2020).

3.2.3 BC source apportionment

BC is a by-product of incomplete combustion processes. Major BC emission sources include biomass burning and fossil fuels. Therefore, we used two independent approaches to estimate the relative contribution of potential emission sources to the seasonal BC fraction in PM and snow.

First, we used an isotope-mixing model to estimate the relative contributions (f) of fossil ($_{FF}$) vs. biomass burning ($_{BB}$) fuel sources to the BC fraction in each sample ($_{SPL}$) of PM and snow [Eq. 1]. We considered BC emission sources with the following $\Delta^{14}C$ values (mean±SD): Combustion of fossil fuels ($\Delta^{14}C$ = -1000‰) and (a) annual biomass, which has the same $\Delta^{14}C$ as ambient atmospheric CO_2 ($\Delta^{14}C$ = 18.2±3.3‰ at Pt. Barrow, AK, USA between February 2014 and June 2015 (Xu, Pers. Comm. 2019) or (b) boreal forests in North America, which in previous years incorporated ^{14}C-enriched CO_2 (bomb-C) into their wood ($\Delta^{14}C$ = 131±52‰, Mouteva et al. (2015).

$$f_{FF} = (\Delta^{14}C_{SPL} - \Delta^{14}C_{BB}) / (\Delta^{14}C_{FF} - \Delta^{14}C_{BB}) \quad [1]$$

Second, we estimated $\delta^{13}C$ of fossil BC emissions [Eq. 2].

$$\delta^{13}C_{FF} = (\delta^{13}C_{SPL} - (1 - f_{FF}) \cdot \delta^{13}C_{BB}) / f_{FF} \quad [2]$$

Third, we apportioned the fossil fuel-derived BC into gaseous ($_{GAS}$) vs. solid or liquid ($_{SOLI}$) fuel sources [Eq. 3].

$$f_{GAS} = (\delta^{13}C_{FF} - \delta^{13}C_{SOLI}) / (\delta^{13}C_{GAS} - \delta^{13}C_{SOLI}) \quad [3]$$

We assume a $\delta^{13}C$ of -40±5‰ for gaseous sources, based on the combustion of natural gas (Deines, 1980) and gas flaring (-36 to -40‰, Winiger et al., 2016). For non-gaseous sources, we estimate a $\delta^{13}C$ of -27±4‰. These include the combustion of coal with a $\delta^{13}C$ of -23.4±1.3‰ and of liquid fuels (gasoline, diesel, and kerosene) with estimated ranges from -23.8 to -31.3‰ (Andersson et al., 2015; Mašalaitė et al., 2012; Pugliese et al., 2017).

3.2.4 HYSPLIT back trajectory modeling

We estimated the origin of the air masses at Alert using the HYSPLIT backward trajectory model (Stein et al., 2015) using daily files archived meteorological forecasts containing 3-hourly data from the Global Data Assimilation System (GDAS) at a 0.5º-resolution grid (https://www.ready.noaa.gov/archives.php). While the estimate lifetime of BC in the Arctic ranges from 7-23 days (Qi et al., 2017b), we initialized simulations every 12 hours and calculated air mass geographical position and height back to 240 hours before initialization. Backward trajectories were then pooled to match isotope sampling dates (Table A3.1) and segregated by meteorological season. Air masses were further distinguished into six geographical source regions (Arctic Ocean, Greenland, North America, Russia, Europe, and Asia; Fig. 3.2, Table A3.2) by counting the frequency of trajectory intersections over the geographical grids of 1º×1º-resolution. These frequencies were then normalized by the total number of trajectories and mapped (Fig. 3.3).

Arctic geographical and height sectors were analyzed by separating HYSPLIT output endpoints by major Arctic sector and calculating the percentage of each sector in each sample.

The planetary boundary layer height was obtained for each endpoint location and time from the GDAS 0.5º meteorology data. The endpoints were binned by height layer in each sector. The height layers include: (1) within boundary layer, (2) below 1 km, and (3) 1 to <2 km.

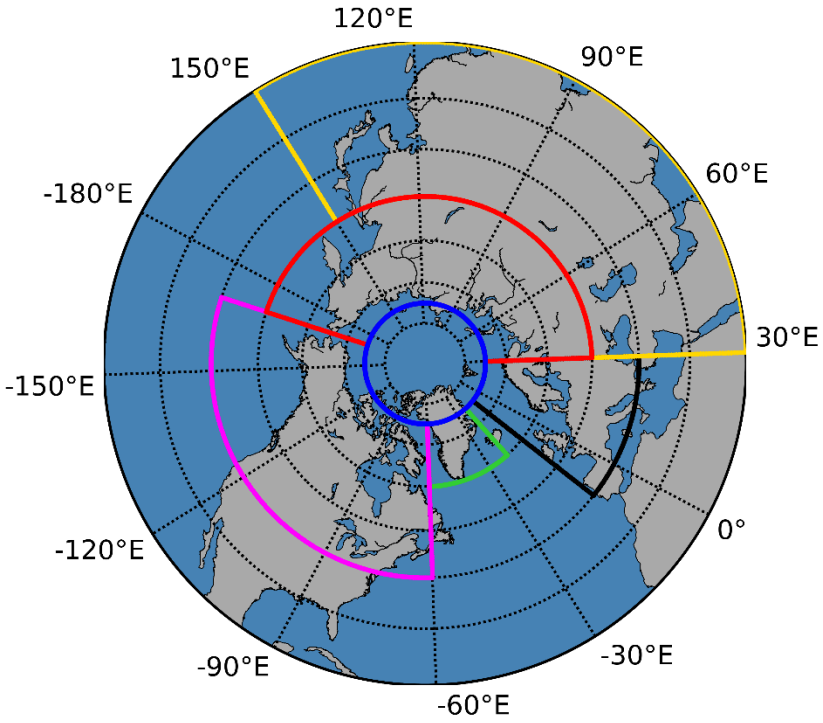

Figure 3.2 Map of geographical boundaries of six black carbon (BC) source regions (Arctic Ocean, Greenland, North America, Russia, Europe, and Asia).

3.3 Results and discussion

3.3.1 Air mass origin

Our 10-day backward trajectories indicate that BC in PM and snow was transported to Alert primarily from within the Arctic (>60°N) (Fig. 3.3). This is consistent with previous studies (Schulz et al., 2019; Sobhani et al., 2018; Thomas et al., 2019) showing that, due to the highly stratified nature of the Arctic atmosphere, most air masses at the surface level are contained within the boundary layer and are primarily influenced laterally by air masses with cyclonic flow around the pole.

Seasonally-integrated trajectories (Fig. 3.3) also show the contraction of the polar dome during the summer and its expansion during the winter, when there is a greater incidence of air masses within the Arctic and northern mid-latitudes (50-70ºN). The polar dome expands asymmetrically into the Russian and Eurasian sectors and to a lesser extent into the European sector. As a result, the air masses simulated for 10 days may not encapsulate all mid-latitude sources where the polar dome extends further south, such as in the Asian section. Winter and spring air masses arriving at Alert appear to originate predominantly from the Russian sector as far as 10 days back, but more southern sources cannot be ruled out (Xu et al., 2017). Summer air masses arrive from the North American sector, and predominant wind patterns isolate Alert from direct European emissions year-round.

Monthly composite means of sea level pressure (Fig. A3.1) further indicate that asymmetric synoptic-scale meteorology isolates Alert from European emissions and enhances air mass incidences from Russia during winter, spring, and fall while North America air masses were enhanced in summer. Our observations are consistent with previous synoptic-scale patterns described for the Arctic (Cassano et al., 2006; Serreze et al., 1993; Serreze & Barry, 1988) and at Alert (Leaitch et al., 2018; Sharma et al., 2006).

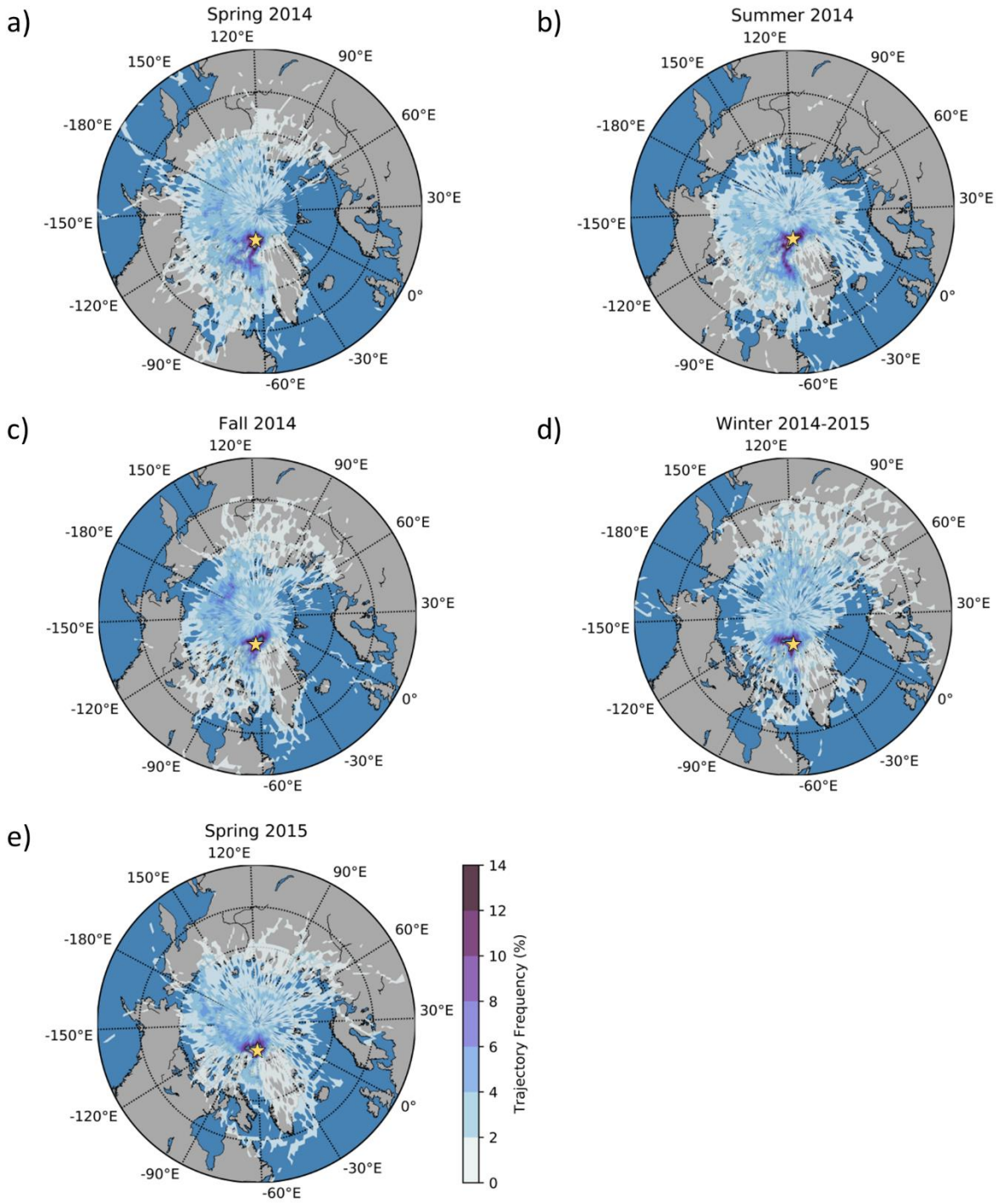

Figure 3.3 Seasonal (a-e) HYSPLIT backward trajectory frequency maps (see section 2.4) normalized by total trajectory endpoints. Frequency normalized for each 1º×1º grid cell and initialized every 12 hours for 240 hours (10 days) during sampling at Alert, Canada (82.499ºN, 62.342ºW).

3.3.2 Concentrations of TC, BC, and OC in PM

Concentrations of TC, BC, and OC in PM ranged from 35.3 to 697.9, 1.8 to 135.3, and 22.6 to 590.6 ng C m^{-3} air, respectively (Table A3.4). As such, BC/TC ratios ranged from 0.02 to 0.41 and OC/BC ratios ranged from 1.4 to 50.5 (Table A3.4). TC was mostly comprised of OC (58.8-98.1% TC), with BC accounting for 1.9-41.2% TC. These data are consistent with previous measurements at Alert (Croft et al., 2016; Evangeliou et al., 2016; Qi, et al., 2017b; Sharma et al., 2017; Sobhani et al., 2018; Winiger et al., 2019).

BC and OC concentrations varied seasonally, with maxima in late winter and early spring (February-April) and minima in early summer (Table 3.1, Fig. 3.4 & 3.5a). BC concentrations for winter 2014/2015 were 1.8-2.2 times greater than in spring, 4.8 times greater than in summer, and 2.8 times greater than in fall (Fig. 3.4) ($p<0.05$). This seasonal cycle is consistent with previous observations (Gong et al., 2010; Sharma et al., 2006). Greater BC concentrations in winter have been shown to arise from increases in emissions within the Arctic as a result of greater anthropogenic demand for heating (Huang et al., 2015; Stohl et al., 2013; Yttri et al., 2014), the southward expansion of the Arctic front (Bozem et al., 2019), and an increase in BC atmospheric lifetime due to inefficient scavenging and cool and stagnant atmospheric conditions (Mouteva et al., 2017; Thomas et al., 2019).

OC concentrations followed similar seasonal trends, but differences were not statistically significant (ANOVA, Tukey HSD Post-Hoc Test) because the maxima and minima occurred over more than one season. For example, post-arctic haze OC minima occurred mid-summer of 2014, but late spring the following year (Fig. 3.4). These sudden declines in total carbonaceous aerosol concentration have been described as a product of increasing insulation and warmer temperatures that yield increased wet scavenging efficiencies of organics and water-soluble OC and

BC resulting from a shift to a warmer mixed-phase and liquid-phase scavenging regime from inefficient ice-phase cloud particle scavenging (Browse et al., 2012).

TC and BC/TC varied greatly throughout the sampling period without statistically significant seasonal trends. Samples measured in summer had greater OC/BC ratios because BC concentrations were lowest in summer on average. The summer average OC/BC ratio was 3.1 times greater than the winter average.

Table 3.1. Seasonal[1] averages of measured TC, OC, and BC concentrations and isotopes (mean±SD)

	n	**OC[2]**	**BC**	**TC**	**OC/BC**	**BC/TC**	**n**	**$\delta^{13}C$**	**$\Delta^{14}C$**
		ng C m^{-3} air			%			‰	
PM									
Spring	23	259.2 (163.0)	40.8 (27.8)	300.1 (180.8)	7.1 (2.9)	15.1 (8.8)	7	-27.2 (0.4)	-581 (78.7)
Summer	9	172.1 (100.2)	14.4 (13.3)	169.7 (103.3)	13.0 (9.2)	8.9 (6.5)	3	-26.2 (0.8)	-361.8 (162.7)
Fall	6	156.0 (78.7)	29.8 (30.5)	185.8 (102.0)	6.8 (3.4)	15.0 (6.5)	5	-27.9 (0.5)	-593.5 (63.6)
Winter	10	324.0 (110.4)	82.3 (29.8)	406.2 (135.6)	4.1 (1.0)	20.2 (3.6)	5	-27.2 (0.3)	-591.4 (100.1)
Snow									
Spring	n.m.	n.m.	n.m.	n.m.	n.m.	n.m.	3	-27.4 (0.8)	-323.2 (115.5)
Summer	n.m.	n.m.	n.m.	n.m.	n.m.	n.m.	n.m.	n.m.	n.m.
Fall	n.m.	n.m.	n.m.	n.m.	n.m.	n.m.	1	-28.3	-106.2
Winter	n.m.	n.m.	n.m.	n.m.	n.m.	n.m.	3	-27.1 (1.1)	-341.7 (149.8)

[1]Seasons are defined meteorologically, with spring (March-May), summer (June-August), fall (September-November), and winter (December-February); n.m. = not measured (no samples available)
[2]OC concentrations are reported as OC_{total}, the sum of OC and pyrolized organic carbon (POC) (Huang et al., 2020)

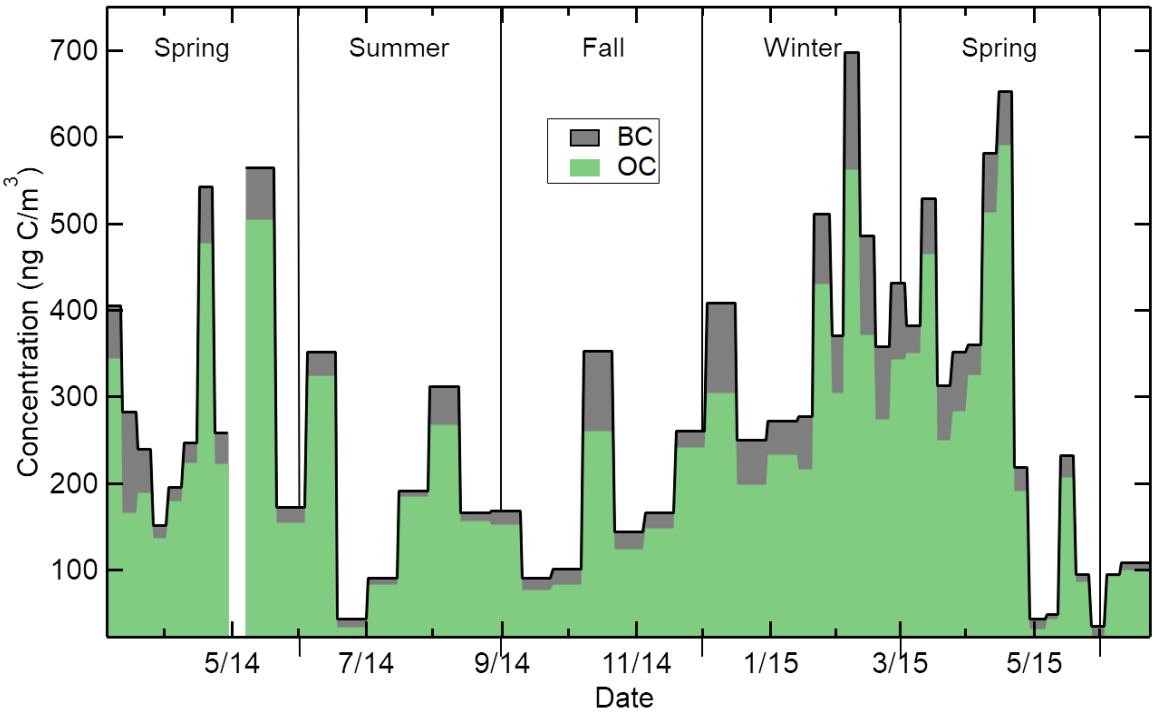

Figure 3.4 Weekly-integrated mass of total organic carbon in PM (bars) at Alert, Canada), composed of the sum of organic carbon (OC), pyrolyzed and carbonate carbon (POC+CC), and elemental carbon (BC). The sum of the OC, POC+CC, and BC fractions equals the mass of total carbon (TC) in each sample.

We also observed three periods of elevated EC concentrations throughout the observation period (Fig. 3.4, Fig. A3.3), which we defined as BC concentrations ≥2σ from the seasonal average (Table 3.1). The first occurred in spring 2014 (March 12-19 2014, 2.2σ), the second in summer 2014 (July 30 to August 13 2014, 2.0σ), and the third in fall 2014 (October 8-22 2014, 2.0σ).

We observed the highest overall BC concentrations in winter 2015 (135.8 ng C m^{-3} and 114.7 ng m^{-3} during February 4-11 and 11-18 2015, respectively), but they were only 1.8 and 1.1σ greater than the seasonal average. Both periods coincided with the development of persistent large high-pressure systems, the center of which oscillated between the east Russian and North American regions throughout winter and spring, that enveloped the entirety of east Russia and west North America (Fig. A3.1). Additionally, an opposing large low-pressure system cen-

tered over the Barents and Greenland seas created a sharp pressure gradient at the center of the Arctic Ocean and fueled trans-Arctic Ocean winds from east Russia to Alert (Fig. A3.1n). Similar sea level pressure patterns were observed during periods with elevated BC concentrations throughout winter and spring 2014/2015 (Fig. A3.1k-q). These conditions describe typical Arctic winter and springtime temperature inversion events, which are characterized by minimized vertical mixing and stable atmospheric conditions near the surface which drives BC accumulation in the polar dome at the surface (Qi, et al., 2017a; Shen et al., 2017; Thomas et al., 2019).

Surface BC concentrations at Alert closely followed expected seasonal variations of air mass origin as described by backward trajectory modeling and predominant synoptic-scale meteorology in the polar dome. In addition, our sampling approach captured air masses with elevated BC concentrations, each affecting Alert for up to 2 weeks, which suggests either anomalous flow not captured in the means or sudden increases in emissions from respective air mass sources.

3.3.3 Isotopes of BC in PM

$\Delta^{14}C$ of BC in PM ranged from -698.3 to -187.7‰, indicating that overall fossil fuel combustion was the largest contributor to the BC burden at Alert in winter (Table A3.1, Fig. 3.5c). BC was more enriched in ^{14}C during the summer (Table 3.1).

The relative contribution from fossil fuel combustion to BC ranged from 20-70% and was significantly lower in summer (Fig. 3.6a) (summer: 20-52% fossil, fall-spring: 47-70% fossil). This indicates a greater contribution from biomass burning, which is expected during the boreal region wildfire season (May-September) (Warneke et al., 2010). Throughout spring and winter, the Russian sector was a significant contributor to the BC load at Alert (Fig. 3.6b), because large persistent anti-cyclonic systems (Fig. A3.1) envelop the western Arctic in contrast with large cy-

clonic systems over the eastern Arctic. These conditions present frigid and dry conditions (Fig. A3.2) that limit wet scavenging and drive trans-Arctic ocean winds from Siberia to Alert.

Our BC source apportionment calculations assume that modern carbon emission originated primarily from the burning of annual biomass. As a sensitivity test for the calculated fuel-type contributions expressed in Fig. 3.6a, we calculated the fuel fractions with boreal forest fire endmember ($\Delta^{14}C$=131±52‰) (Mouteva et al., 2015) as the biogenic modern carbon source. We found that using a boreal forest fire endmember only reduced our estimate of biogenic contributions by 4±1% (avg±sd) on average and by up to 8% for samples with more enriched ^{14}C signatures (collected in summer). These differences in biogenic contributions were within the propagated uncertainty (Fig. 3.6a) and did not significantly affect the calculated fuel type.

Regarding the three elevated BC periods described in section 3.2, $\Delta^{14}C$ BC during the spring and fall events were consistent with that of BC during the respective season (Fig. 3.5c). In spring (March 2014), influent sectors, mean winds, and sea level pressures indicate a steep pressure gradient between a high pressure centered over the Chukchi and Beaufort seas and a low pressure settled over the Kara and Barents seas that drove winds to Alert from the Russian sector via the Arctic Ocean (Fig. A3.1a). A similar pattern was observed in fall (October 2014), but mean sea level pressure gradients were not as steep, the high pressure was contained to the Arctic Ocean, and the low pressure was shifted towards the Norwegian Sea (Fig. A3.1h). Therefore, Alert was affected less by the Russian Sector. Backward trajectories also indicate less Russian influence and less overall influence from air masses within 2 km (Fig. 3.6). This could be due to subsidence occurring at the high-pressure system therefore descending pollution, if any, from aloft (Willis et al., 2019).

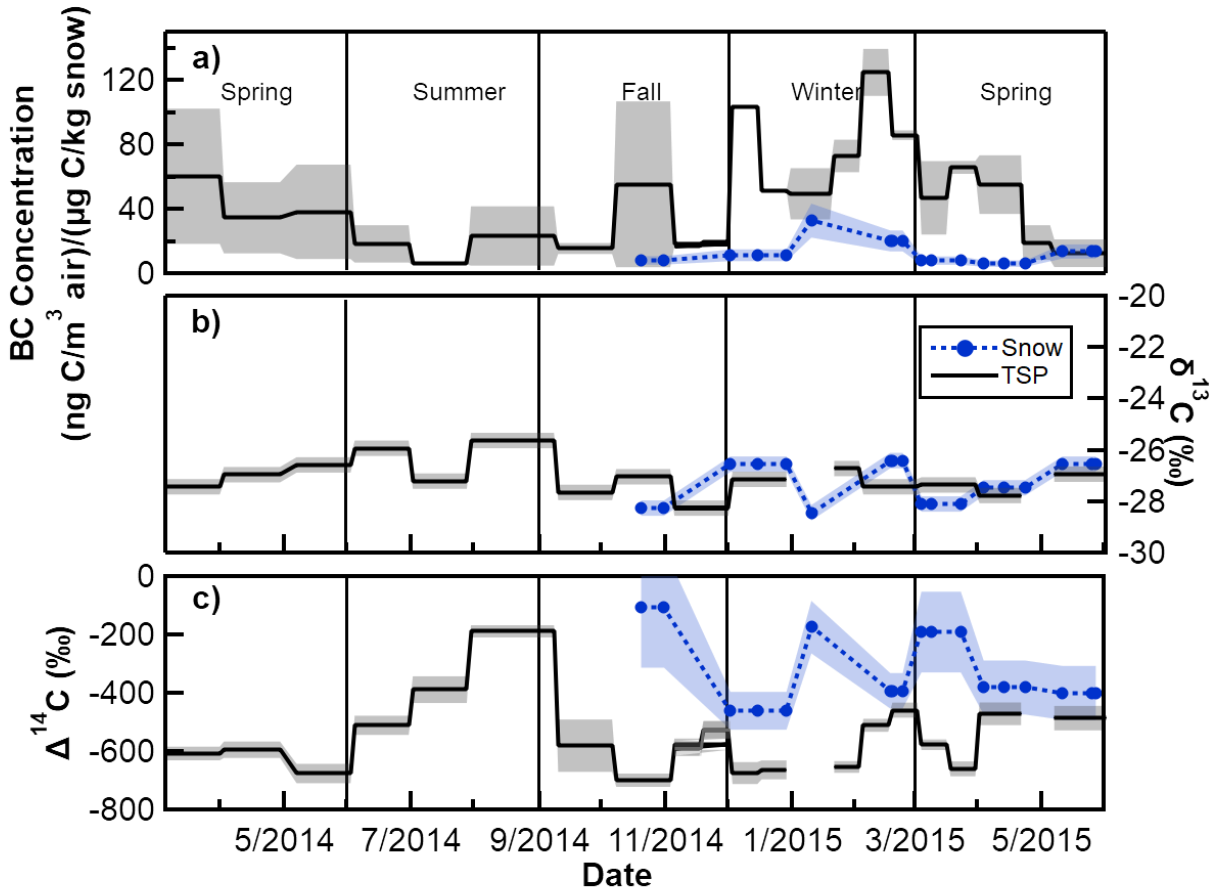

Figure 3.5 Concentration, stable isotope composition ($\delta^{13}C$), and radiocarbon content ($\Delta^{14}C$) of black carbon (BC) from PM (black solid lines) or snow (blue dotted lines) collected at Alert, Canada and isolated by the ECT9 method. PM concentrations were measured on weekly-integrated samples (Fig. 3.4), but pooled for isotope analysis (1-4 weeks/sample). (a) Average BC concentrations and standard deviations (shading) of the pooled samples. Measured (b) $\delta^{13}C$ and (c) $\Delta^{14}C$ of BC with $\pm 1\sigma$ analytical error (shading). Blue dots indicate snow sampling dates.

In contrast, $\Delta^{14}C$ during the elevated BC event in summer (August 2014) was enriched relative to the seasonal average (Fig. 3.5c). During the event, a regional and weak low-pressure system developed over the Canadian Archipelago (Fig. A3.1f) which drove southwesterly winds from the North American boreal zones, resulting in elevated BC concentrations with relatively high ^{14}C contents (Fig. 3.5a,c). This was further evident by increased incidences of back trajectories from North America in in July and August (Fig. 3.6b).

Biomass burning contributed 43.8±11.9% (avg±1σ) to BC (n=17) on average for the entire study period. This estimate is within the range of values reported for Alert by Winiger et al. (2019), who estimated an average fraction biomass for BC of 39.6±4.0% (12/02/14 to 18/03/2015, n=9). Winiger et al. (2019) utilizes more enriched ^{14}C values (+225±60‰) for their biomass burning endmember to represent the ^{14}C content of northern tree species that are 3-4 decades old and contain a significant fraction of bomb-^{14}C, while our approach assumes that fire consumes only the most recently-formed wood on the outer stems and carbon from the forest floor that is more depleted in bomb-^{14}C (Mouteva et al., 2015). However, since most BC emissions originate from fossil fuels, the apportionment is not very sensitive to the choice of biomass $\Delta^{14}C$.

The $\delta^{13}C$ of BC in PM ranged from -25.6 to -28.3‰ (Table A3.1, Fig. 3.5b). We observed the most depleted values during the fall, but seasonal differences were not significant (single-factor ANOVA, Tukey HSD test, $p>0.05$). Our data was similar to $\delta^{13}C$ of BC in PM previously reported for Alert (-27.9±0.8‰, 05/03/14 to 18/03/2015) (Winiger et al., 2019). Additionally, this data falls within the range of reported $\delta^{13}C$ values of particles produced by fossil fuel combustion (-24 to -28‰) (Andersson et al., 2015; Mašalaitė et al., 2012; Pugliese et al., 2017; Widory, 2006) and overlaps with $\delta^{13}C$ values found in biomass burning aerosols (-21 to -29‰) (Agnihotri et al., 2011; Garbaras et al., 2015; Mouteva et al., 2015; Sang et al., 2012).

The calculated $\delta^{13}C$ of fossil fuel-derived BC in PM showed little variation throughout the observation period and was not significantly different from the measured $\delta^{13}C$ of bulk BC (Fig. 3.5b, Table A3.1). Our stable isotope mass balance analysis indicated that the dominant source of fossil BC year-round was the combustion of liquid and solid fuels (82% to 100% of fossil BC). Consequently, gas flaring contributed 0 to 18% to fossil BC; with uncertainties in the

isotopic composition of sources and error propagation (Table A3.1). Our estimates are lower than those by Stohl et al. (2013), who suggested that flaring accounts for as much as 33% to the annual mean BC surface concentrations at Alert in January. However, our gas flaring estimate is greater than that reported by Winiger et al. (2017, 2019), who estimated only 6% contribution from gas flaring in East Siberia to the Tiksi Hydrometeorological Research Observatory and no discernable contribution to Alert.

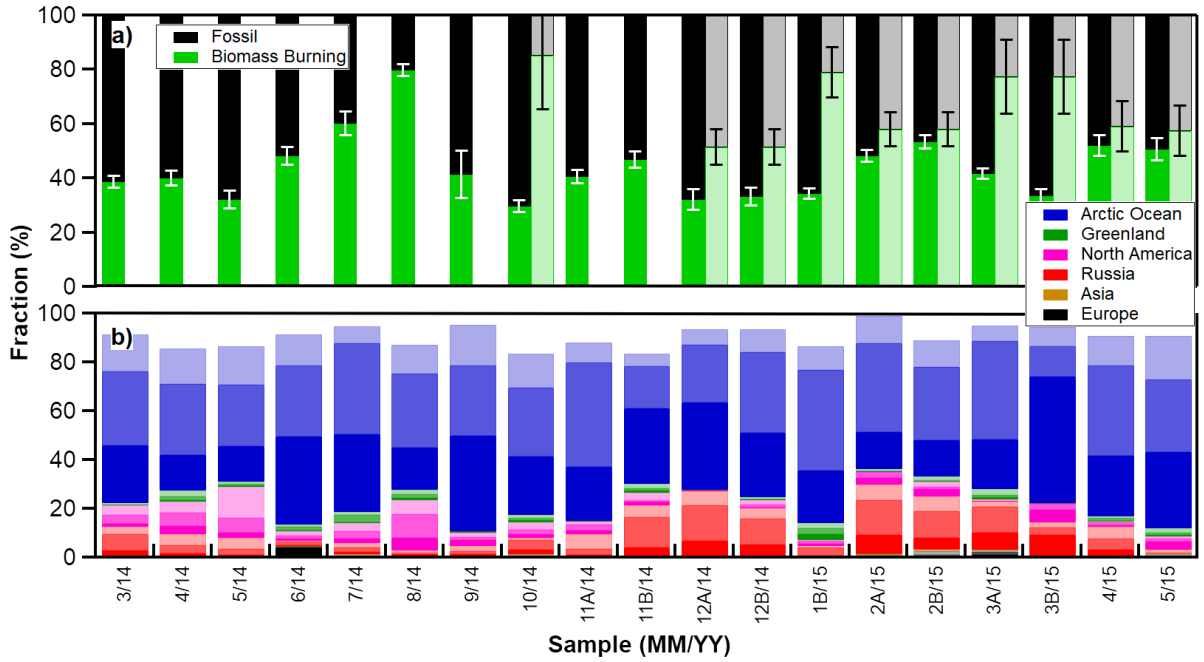

Figure 3.6 (a) Time series of calculated fuel type of BC in PM (non-opaque) and snow (opaque) based on ^{14}C measurements; (b) sector and height contributions based off 10-day HYSPLIT back trajectory results. Solid colors in (b) represent percentage of back trajectories within the meteorologically defined planetary boundary level height. Less opaque colors indicate back trajectories above boundary level height but are lower than 1km. The least opaque colors show back trajectories between 1-2km in height. From November 2014 to March 2015, two isotopic measurements were made in the same month. A and B in sample dates distinguish samples taken in the first half from the second half of the month.

3.3.4 Isotopes of BC in snow

BC in snow was consistently enriched in ^{14}C relative to that of BC in PM (Fig. 3.5c) (ANOVA single factor, $p<0.01$). This suggests that BC in snow was dominated by biomass burn-

ing (53-88%), with $\Delta^{14}C$ ranging from -106.2 to -460.2‰ with no significant differences between seasons.

Excluding samples with a fossil BC mass of less than 0.2 µg C, the calculated $\delta^{13}C$ data of fossil fuel-derived BC in snow was relatively constant and not significantly different from the measured $\delta^{13}C$ of bulk BC (Fig. 3.5b, Table A3.1). $\delta^{13}C$ values are typical for combustion either from solid or liquid fossil fuels, which accounted for 91 to 100% of fossil BC (avg. ± SD).

The relative enrichment of biomass burning-derived BC in snow compared to that in surface PM likely results from differences in the source region between the BC present aloft and near the surface. BC aloft may be derived from air masses that were directly affected by biomass burning at lower latitudes and uplifted during their northward transport (Bozem et al. 2019; Stohl et al., 2006; 2007), while BC near the surface is dominated by fossil BC emissions within the polar dome.

Biomass burning-derived BC aloft is also likely to be more efficiently scavenged by precipitation. BC scavenging may occur in ice clouds or in liquid and mixed-phase clouds that persist throughout the year in the Alert region as demonstrated at Eureka, Nunavut (de Boer et al., 2011; Coopman et al., 2018; Cox et al., 2014; Morrison et al., 2012).

Current field measurements and laboratory experiments (Bond et al., 2013; Kanji et al., 2017) have shown that BC aerosols are only moderately effective ice nuclei (IN) and easily outcompeted by other IN (Cziczo et al., 2013; Irish et al., 2019; Lupi et al., 2014). However, the lower temperature origin of biomass burning BC and atmospheric aging during transport promote the development of amorphous organic and/or sulfate coatings that increase the solubility of BC in the liquid phase, and its effectiveness as cloud condensation nuclei (CCN) (Henning et al., 2012; Pósfai et al., 2004; Sharma et al., 2013; Zhang et al., 2008).

In mixed-phase clouds, BC may thus act as CCN or become incorporated into existing liquid or super-cooled droplets through direct collisions (Ding et al., 2019). Further, the collision of droplets with snow grains ("rimming") can incorporate BC into snow within and below the cloud (Magono et al., 1979). Similarly, aged fossil particles with coatings accumulated through atmospheric processing (China et al., 2015; Weingartner et al., 1997; Zhang et al., 2008; Zuberi, 2005) may be incorporated into snow alongside the biomass burning-derived BC aloft.

We observed the largest differences between the ^{14}C of BC in PM and snow in October 2014, January, and March 2015 (Fig. 3.6a), while the ^{14}C of BC in snow in February, April, and May of 2015 were within the uncertainty range of ^{14}C of BC in PM. Assuming that the majority of snow samples represents fresh snow, the temporal variation in the difference between ^{14}C of BC in PM and snow may suggest a greater layer of complexity that is a function of the atmospheric column conditions. Besides difference in IN capacity, it is also possible that the discrepancy in biomass burning BC particles in snow and PM are due to variability in the extent of contact-freezing. Extensive contact-freezing of ambient BC-containing particles into existing ice crystals might incorporate more local PM particles, which would yield similar fraction fossil values to ambient PM as was observed in February, April, and May 2015 (Fig. 3.6a).

Our results imply that biomass burning BC is preferentially incorporated into snow. However, this effect is inconsistent across the study period and is likely a function of the specific meteorological and microphysical properties of the precipitating cloud. This study highlights the need for in-depth studies of BC in-cloud behavior as CCN and/or subsequent IN in mixed-phase clouds and measurements of additional biomass burning tracers (i.e. potassium) in snow to assess BC sources. This is particularly important in the Arctic as BC in snow significantly affects the

optical properties in snow and yields current uncertainties of the secondary effects of BC in snow (AMAP, 2015; Bond et al., 2013; Schwarz et al., 2013).

3.4 Conclusions

In this study, we quantified the concentration and sources of BC in PM and snow at Alert, Canada from March 2014 to May 2015. We found that BC concentrations in PM followed typical seasonal patterns. Throughout the winter, BC accumulated within the polar dome and was predominantly derived from liquid or solid fossil fuels. As far as 10 days back, BC was transported to Alert from the Russian Arctic, but more southern sources may also be important. During late spring and summer, BC concentrations were lower, with greater contributions from biomass burning in North America.

A comparison of BC in PM and snow showed that biomass burning BC was preferentially incorporated into snow. Since BC surface observing networks monitor BC in PM, but not snow, our findings also suggest that BC contributions from biomass burning might be underestimated in models and BC mitigation efforts due to complexity in transport patterns. Given the effect of BC trapped in snow on Arctic climate, future studies are needed to resolve the relative significant of BC scavenging by dry vs. wet deposition and the role of BC in cloud and ice nucleation.

Acknowledgments

We thank the KCCAMS staff for supporting isotope analyses, A. Platt, M. Fraser & D. Veber at ECCC for supporting aerosols and snow sampling and maintenance at Alert GAW station, and P. Winiger from Stockholm University for filter preparation.

3.5 References

Agnihotri, R., Mandal, T. K., Karapurkar, S. G., Naja, M., Gadi, R., Ahammmed, Y. N., et al. (2011). Stable carbon and nitrogen isotopic composition of bulk aerosols over India and northern Indian Ocean. *Atmospheric Environment*, *45*(17), 2828–2835. https://doi.org/10.1016/j.atmosenv.2011.03.003

AMAP. (2015). *AMAP assessment 2015: Black carbon and ozone as Arctic climate forcers*. *Arctic Monitoring and Assessment Programme (AMAP)*. Oslo, Norway. Retrieved from https://www.amap.no/documents/doc/amap-assessment-2015-black-carbon-and-ozone-as-arctic-climate-forcers/1299

Ancellet, G., Pelon, J., Blanchard, Y., Quennehen, B., Bazureau, A., Law, K. S., & Schwarzenboeck, A. (2014). Transport of aerosol to the Arctic: analysis of CALIOP and French aircraft data during the spring 2008 POLARCAT campaign. *Atmospheric Chemistry and Physics*, *14*(16), 8235–8254. https://doi.org/10.5194/acp-14-8235-2014

Andersson, A., Deng, J., Du, K., Zheng, M., Yan, C., Sköld, M., & Gustafsson, Ö. (2015). Regionally-Varying Combustion Sources of the January 2013 Severe Haze Events over Eastern China. *Environmental Science & Technology*, *49*(4), 2038–2043. https://doi.org/10.1021/es503855e

Andreae, M. O., & Gelencsér, A. (2006). Black carbon or brown carbon? The nature of light-absorbing carbonaceous aerosols. *Atmospheric Chemistry and Physics*, *6*, 3131–3148. https://doi.org/10.5194/acp-6-3131-2006

Barrett, T. E., Robinson, E. M., Usenko, S., & Sheesley, R. J. (2015). Source Contributions to Wintertime Elemental and Organic Carbon in the Western Arctic Based on Radiocarbon and Tracer Apportionment. *Environmental Science and Technology*, *49*(19), 11631–11639. https://doi.org/10.1021/acs.est.5b03081

de Boer, G., Morrison, H., Shupe, M. D., & Hildner, R. (2011). Evidence of liquid dependent ice nucleation in high-latitude stratiform clouds from surface remote sensors. *Geophysical Research Letters*, *38*, L01803. https://doi.org/10.1029/2010GL046016

Bond, T. C., Doherty, S. J., Fahey, D. W., Forster, P. M., Berntsen, T., Deangelo, B. J., et al. (2013). Bounding the role of black carbon in the climate system: A scientific assessment. *Journal of Geophysical Research Atmospheres*, *118*(11), 5380–5552. https://doi.org/10.1002/jgrd.50171

Box, J. E., Colgan, W. T., Christensen, T. R., Schmidt, N. M., Lund, M., Parmentier, F.-J. W., et al. (2019). Key indicators of Arctic climate change: 1971–2017. *Environmental Research Letters*, *14*(4), 045010. https://doi.org/10.1088/1748-9326/aafc1b

Bozem, H., Hoor, P., Kunkel, D., Köllner, F., Schneider, J., Herber, A., et al. (2019). Characterization of transport regimes and the polar dome during Arctic spring and summer using in situ aircraft measurements. *Atmospheric Chemistry and Physics*, *19*, 15049–15071. https://doi.org/10.5194/acp-19-15049-2019

Browse, J., Carslaw, K. S., Arnold, S. R., Pringle, K., & Boucher, O. (2012). The scavenging processes controlling the seasonal cycle in Arctic sulphate and black carbon aerosol. *Atmospheric Chemistry and Physics*, *12*(15), 6775–6798. https://doi.org/10.5194/acp-12-

6775-2012

Browse, J., Carslaw, K. S., Mann, G. W., Birch, C. E., Arnold, S. R., & Leck, C. (2014). The complex response of Arctic aerosol to sea-ice retreat. *Atmospheric Chemistry and Physics*, *14*(14), 7543–7557. https://doi.org/10.5194/acp-14-7543-2014

Cassano, J. J., Uotila, P., & Lynch, A. (2006). Changes in synoptic weather patterns in the polar regions in the twentieth and twenty-first centuries, Part 1: Arctic. *International Journal of Climatology*, *26*(8), 1027–1049. https://doi.org/10.1002/joc.1306

Chan, T. W., Huang, L., Banwait, K., Zhang, W., Ernst, D., Wang, X., et al. (2019). Inter-comparison of elemental and organic carbon mass measurements from three North American national long-term monitoring networks at a co-located site. *Atmospheric Measurement Techniques*, *12*(8), 4543–4560. https://doi.org/10.5194/amt-12-4543-2019

China, S., Scarnato, B., Owen, R. C., Zhang, B., Ampadu, M. T., Kumar, S., et al. (2015). Morphology and mixing state of aged soot particles at a remote marine free troposphere site: Implications for optical properties. *Geophysical Research Letters*, *42*(4), 1243–1250. https://doi.org/10.1002/2014GL062404

Comiso, J. C. (2012). Large Decadal Decline of the Arctic Multiyear Ice Cover. *Journal of Climate*, *25*(4), 1176–1193. https://doi.org/10.1175/JCLI-D-11-00113.1

Coopman, Q., Garrett, T. J., Finch, D. P., & Riedi, J. (2018). High Sensitivity of Arctic Liquid Clouds to Long-Range Anthropogenic Aerosol Transport. *Geophysical Research Letters*, *45*(1), 372–381. https://doi.org/10.1002/2017GL075795

Cox, C. J., Turner, D. D., Rowe, P. M., Shupe, M. D., & Walden, V. P. (2014). Cloud microphysical properties retrieved from downwelling infrared radiance measurements made at Eureka, Nunavut, Canada (2006-09). *Journal of Applied Meteorology and Climatology*, *53*(3), 772–791. https://doi.org/10.1175/JAMC-D-13-0113.1

Croft, B., Martin, R. V., Richard Leaitch, W., Tunved, P., Breider, T. J., D'Andrea, S. D., & Pierce, J. R. (2016). Processes controlling the annual cycle of Arctic aerosol number and size distributions. *Atmospheric Chemistry and Physics*, *16*(6), 3665–3682. https://doi.org/10.5194/acp-16-3665-2016

Cziczo, D. J., Froyd, K. D., Hoose, C., Jensen, E. J., Diao, M., Zondlo, M. A., et al. (2013). Clarifying the Dominant Sources and Mechanisms of Cirrus Cloud Formation. *Science*, *340*(6138), 1320–1324. https://doi.org/10.1126/science.1234145

Deines, P. (1980). The Isotopic Composition of Reduced Organic Carbon. In P. Fritz & J. C. Fontes (Eds.), *Handbook of Environmental Isotope Geochemistry* (Vol. 1, p. 329). Amsterdam: Elsevier.

Ding, S., Zhao, D., He, C., Huang, M., He, H., Tian, P., et al. (2019). Observed Interactions Between Black Carbon and Hydrometeor During Wet Scavenging in Mixed-Phase Clouds. *Geophysical Research Letters*, *46*(14), 8453–8463. https://doi.org/10.1029/2019GL083171

Dutkiewicz, V. A., DeJulio, A. M., Ahmed, T., Laing, J., Hopke, P. K., Skeie, R. B., et al. (2014). Forty-seven years of weekly atmospheric black carbon measurements in the Finnish Arctic: Decrease in black carbon with declining emissions. *Journal of Geophysical Research: Atmospheres*, *119*(12), 7667–7683. https://doi.org/10.1002/2014JD021790

Evangeliou, N., Balkanski, Y., Hao, W. M., Petkov, A., Silverstein, R. P., Corley, R., et al. (2016). Wildfires in northern Eurasia affect the budget of black carbon in the Arctic-a 12-year retrospective synopsis (2002-2013). *Atmospheric Chemistry and Physics*, *16*(12), 7587–7604. https://doi.org/10.5194/acp-16-7587-2016

Fisher, J. A., Jacob, D. J., Purdy, M. T., Kopacz, M., Le Sager, P., Carouge, C., et al. (2010). Source attribution and interannual variability of Arctic pollution in spring constrained by aircraft (ARCTAS, ARCPAC) and satellite (AIRS) observations of carbon monoxide. *Atmospheric Chemistry and Physics*, *10*(3), 977–996. https://doi.org/10.5194/acp-10-977-2010

Freud, E., Krejci, R., Tunved, P., Leaitch, R., Nguyen, Q. T., Massling, A., et al. (2017). Pan-Arctic aerosol number size distributions: Seasonality and transport patterns. *Atmospheric Chemistry and Physics*, *17*(13), 8101–8128. https://doi.org/10.5194/acp-17-8101-2017

Fromm, M., Lindsey, D. T., Servranckx, R., Yue, G., Trickl, T., Sica, R., et al. (2010). The Untold Story of Pyrocumulonimbus. *Bulletin of the American Meteorological Society*, *91*(9), 1193–1210. https://doi.org/10.1175/2010BAMS3004.1

Garbaras, A., Masalaite, A., Garbariene, I., Ceburnis, D., Krugly, E., Remeikis, V., et al. (2015). Stable carbon fractionation in size-segregated aerosol particles produced by controlled biomass burning. *Journal of Aerosol Science*, *79*, 86–96. https://doi.org/10.1016/j.jaerosci.2014.10.005

Garrett, T. J., Brattström, S., Sharma, S., Worthy, D. E. J., & Novelli, P. (2011). The role of scavenging in the seasonal transport of black carbon and sulfate to the Arctic. *Geophysical*

Research Letters, *38*(16), LI6805. https://doi.org/10.1029/2011GL048221

Giglio, L., Randerson, J. T., & van der Werf, G. R. (2013). Analysis of daily, monthly, and annual burned area using the fourth-generation global fire emissions database (GFED4). *Journal of Geophysical Research: Biogeosciences*, *118*(1), 317–328. https://doi.org/10.1002/jgrg.20042

Gong, S. L., Zhao, T. L., Sharma, S., Toom-Sauntry, D., Lavoué, D., Zhang, X. B., et al. (2010). Identification of trends and interannual variability of sulfate and black carbon in the Canadian High Arctic: 1981–2007. *Journal of Geophysical Research*, *115*(D7), D07305. https://doi.org/10.1029/2009JD012943

Graven, H. D. (2015). Impact of fossil fuel emissions on atmospheric radiocarbon and various applications of radiocarbon over this century. *Proceedings of the National Academy of Sciences*, *112*(31), 9542–9545. https://doi.org/10.1073/pnas.1504467112

Hallquist, M., Wenger, J. C., Baltensperger, U., Rudich, Y., Simpson, D., Claeys, M., et al. (2009). The formation, properties and impact of secondary organic aerosol: current and emerging issues. *Atmospheric Chemistry and Physics*, *9*(14), 5155–5236. https://doi.org/10.5194/acp-9-5155-2009

Hansen, A. D. A., & Rosen, H. (1984). Vertical distributions of particulate carbon, sulfur, and bromine in the Arctic haze and comparison with ground-level measurements at Barrow, Alaska. *Geophysical Research Letters*, *11*(5), 381–384. https://doi.org/10.1029/GL011i005p00381

Heal, M. R. (2014). The application of carbon-14 analyses to the source apportionment of

atmospheric carbonaceous particulate matter: A review. *Analytical and Bioanalytical Chemistry*, *406*(1), 81–98. https://doi.org/10.1007/s00216-013-7404-1

Henning, S., Ziese, M., Kiselev, A., Saathoff, H., Möhler, O., Mentel, T. F., et al. (2012). Hygroscopic growth and droplet activation of soot particles: uncoated, succinic or sulfuric acid coated. *Atmospheric Chemistry and Physics*, *12*(10), 4525–4537. https://doi.org/10.5194/acp-12-4525-2012

Hirdman, D., Burkhart, J. F., Sodemann, H., Eckhardt, S., Jefferson, A., Quinn, P. K., et al. (2010). Long-term trends of black carbon and sulphate aerosol in the Arctic: changes in atmospheric transport and source region emissions. *Atmospheric Chemistry and Physics*, *10*(19), 9351–9368. https://doi.org/10.5194/acp-10-9351-2010

Huang, K., Fu, J. S., Prikhodko, V. Y., Storey, J. M., Romanov, A., Hodson, E. L., et al. (2015). Russian anthropogenic black carbon: Emission reconstruction and Arctic black carbon simulation. *Journal of Geophysical Research: Atmospheres*, *120*(21), 11306–11333. https://doi.org/10.1002/2015JD023358

Huang, L., Brook, J. R., Zhang, W., Li, S. M., Graham, L., Ernst, D., et al. (2006). Stable isotope measurements of carbon fractions (OC/EC) in airborne particulate: A new dimension for source characterization and apportionment. *Atmospheric Environment*, *40*(15), 2690–2705. https://doi.org/10.1016/j.atmosenv.2005.11.062

Huang, Lin, Zhang, W., Santos, G. M., Rodríguez, B. T., Holden, S. R., & Czimczik, C. I. (2020). Application of the ECT9 protocol for radiocarbon-based source apportionment of carbonaceous aerosols. *Atmospheric Measurement Techniques Discussion*.

https://doi.org/https://doi.org/10.5194/amt-2020-201

Irish, V. E., Hanna, S. J., Willis, M. D., China, S., Thomas, J. L., Wentzell, J. J. B., et al. (2019). Ice nucleating particles in the marine boundary layer in the Canadian Arctic during summer 2014. *Atmospheric Chemistry and Physics*, *19*(2), 1027–1039. https://doi.org/10.5194/acp-19-1027-2019

Jiao, C., & Flanner, M. G. (2016). Changing black carbon transport to the Arctic from present day to the end of 21st century. *Journal of Geophysical Research: Atmospheres*, *121*(9), 4734–4750. https://doi.org/10.1002/2015JD023964

Kanji, Z. A., Ladino, L. A., Wex, H., Boose, Y., Burkert-Kohn, M., Cziczo, D. J., & Krämer, M. (2017). Overview of Ice Nucleating Particles. *Meteorological Monographs*, *58*, 1.1-1.33. https://doi.org/10.1175/AMSMONOGRAPHS-D-16-0006.1

Komatsu, K. K., Alexeev, V. A., Repina, I. A., & Tachibana, Y. (2018). Poleward upgliding Siberian atmospheric rivers over sea ice heat up Arctic upper air. *Scientific Reports*, *8*(1), 1–15. https://doi.org/10.1038/s41598-018-21159-6

Law, K. S., & Stohl, A. (2007). Arctic air pollution: origins and impacts. *Science*, *315*(5818), 1537–40. https://doi.org/10.1126/science.1137695

Leaitch, W. R., Russell, L. M., Liu, J., Kolonjari, F., Toom, D., Huang, L., et al. (2018). Organic functional groups in the submicron aerosol at 82.5° N, 62.5° W from 2012 to 2014. *Atmospheric Chemistry and Physics*, *18*(5), 3269–3287. https://doi.org/10.5194/acp-18-3269-2018

Levin, I., Naegler, T., Kromer, B., Diehl, M., Francey, R., Gomez-Pelaez, A., et al. (2010). Observations and modelling of the global distribution and long-term trend of atmospheric 14CO2. *Tellus B: Chemical and Physical Meteorology*, *62*(1), 26–46. https://doi.org/10.1111/j.1600-0889.2009.00446.x

Lupi, L., Hudait, A., & Molinero, V. (2014). Heterogeneous Nucleation of Ice on Carbon Surfaces. *Journal of the American Chemical Society*, *136*(8), 3156–3164. https://doi.org/10.1021/ja411507a

Magono, C., Endoh, T., Ueno, F., Kubota, S., & Itasaka, M. (1979). Direct observations of aerosols attached to falling snow crystals. *Tellus*, *31*(2), 102–114. https://doi.org/10.3402/tellusa.v31i2.10415

Martinelli, L. A., Camargo, P. B., Lara, L. B. L. S., Victoria, R. L., & Artaxo, P. (2002). Stable carbon and nitrogen isotopic composition of bulk aerosol particles in a C4 plant landscape of southeast Brazil. *Atmospheric Environment*, *36*(14), 2427–2432. https://doi.org/10.1016/S1352-2310(01)00454-X

Mašalaitė, A., Garbaras, A., & Remeikis, V. (2012). Stable isotopes in environmental investigations. *Lithuanian Journal of Physics*, *52*(3), 261–268. https://doi.org/10.3952/physics.v52i3.2478

Morrison, H., De Boer, G., Feingold, G., Harrington, J., Shupe, M. D., & Sulia, K. (2012). Resilience of persistent Arctic mixed-phase clouds. *Nature Geoscience*, *5*(1), 11–17. https://doi.org/10.1038/ngeo1332

Mouteva, G. O., Czimczik, C. I., Fahrni, S. M., Wiggins, E. B., Rogers, B. M., Veraverbeke, S.,

et al. (2015). Black carbon aerosol dynamics and isotopic composition in Alaska linked with boreal fire emissions and depth of burn in organic soils. *Global Biogeochemical Cycles*, *29*(11), 1977–2000. https://doi.org/10.1002/2015GB005247

Mouteva, Gergana O., Randerson, J. T., Fahrni, S. M., Bush, S. E., Ehleringer, J. R., Xu, X., et al. (2017). Using radiocarbon to constrain black and organic carbon aerosol sources in Salt Lake City. *Journal of Geophysical Research: Atmospheres*, *122*(18), 9843–9857. https://doi.org/10.1002/2017JD026519

Petzold, A., Ogren, J. A., Fiebig, M., Laj, P., Li, S.-M., Baltensperger, U., et al. (2013). Recommendations for reporting "black carbon" measurements. *Atmospheric Chemistry and Physics*, *13*(16), 8365–8379. https://doi.org/10.5194/acp-13-8365-2013

Pöschl, U. (2005). Atmospheric aerosols: Composition, transformation, climate and health effects. *Angewandte Chemie - International Edition*, *44*(46), 7520–7540. https://doi.org/10.1002/anie.200501122

Pósfai, M., Gelencsér, A., Simonics, R., Arató, K., Li, J., Hobbs, P. V., & Buseck, P. R. (2004). Atmospheric tar balls: Particles from biomass and biofuel burning. *Journal of Geophysical Research: Atmospheres*, *109*(D6), D06213. https://doi.org/10.1029/2003JD004169

Post, E., Bhatt, U. S., Bitz, C. M., Brodie, J. F., Fulton, T. L., Hebblewhite, M., et al. (2013). Ecological Consequences of Sea-Ice Decline. *Science*, *341*(6145), 519–524. https://doi.org/10.1126/science.1235225

Pozzoli, L., Dobricic, S., Russo, S., & Vignati, E. (2017). Impacts of large-scale atmospheric circulation changes in winter on black carbon transport and deposition to the Arctic.

Atmospheric Chemistry and Physics, *17*(19), 11803–11818. https://doi.org/10.5194/acp-17-11803-2017

Pugliese, S. C., Murphy, J. G., Vogel, F., & Worthy, D. (2017). Characterization of the δ13C signatures of anthropogenic CO2 emissions in the Greater Toronto Area, Canada. *Applied Geochemistry*, *83*, 171–180. https://doi.org/10.1016/j.apgeochem.2016.11.003

Qi, L., & Wang, S. (2019). Sources of black carbon in the atmosphere and in snow in the Arctic. *Science of The Total Environment*, *691*, 442–454. https://doi.org/10.1016/j.scitotenv.2019.07.073

Qi, L., Li, Q., Li, Y., & He, C. (2017a). Factors controlling black carbon distribution in the Arctic. *Atmospheric Chemistry and Physics*, *17*(2), 1037–1059. https://doi.org/10.5194/acp-17-1037-2017

Qi, L., Li, Q., Henze, D. K., Tseng, H. L., & He, C. (2017b). Sources of springtime surface black carbon in the Arctic: An adjoint analysis for April 2008. *Atmospheric Chemistry and Physics*, *17*(15), 9697–9716. https://doi.org/10.5194/acp-17-9697-2017

Randerson, J. T., Chen, Y., van der Werf, G. R., Rogers, B. M., & Morton, D. C. (2012). Global burned area and biomass burning emissions from small fires. *Journal of Geophysical Research: Biogeosciences*, *117*(G4), G04012. https://doi.org/10.1029/2012JG002128

Roiger, A., Thomas, J.-L., Schlager, H., Law, K. S., Kim, J., Schäfler, A., et al. (2015). Quantifying Emerging Local Anthropogenic Emissions in the Arctic Region: The ACCESS Aircraft Campaign Experiment. *Bulletin of the American Meteorological Society*, *96*(3), 441–460. https://doi.org/10.1175/BAMS-D-13-00169.1

Sang, X. F., Gensch, I., Laumer, W., Kammer, B., Chan, C. Y., Engling, G., et al. (2012). Stable Carbon Isotope Ratio Analysis of Anhydrosugars in Biomass Burning Aerosol Particles from Source Samples. *Environmental Science & Technology*, *46*(6), 3312–3318. https://doi.org/10.1021/es204094v

Santos, G. M., Southon, J. R., Griffin, S., Beaupre, S. R., & Druffel, E. R. M. (2007). Ultra small-mass AMS 14C sample preparation and analyses at KCCAMS/UCI Facility. *Nuclear Instruments and Methods in Physics Research Section B: Beam Interactions with Materials and Atoms*, *259*(1), 293–302. https://doi.org/10.1016/j.nimb.2007.01.172

Schulz, H., Zanatta, M., Bozem, H., Richard Leaitch, W., Herber, A. B., Burkart, J., et al. (2019). High Arctic aircraft measurements characterising black carbon vertical variability in spring and summer. *Atmospheric Chemistry and Physics*, *19*(4), 2361–2384. https://doi.org/10.5194/acp-19-2361-2019

Schwarz, J. P., Gao, R. S., Perring, A. E., Spackman, J. R., & Fahey, D. W. (2013). Black carbon aerosol size in snow. *Scientific Reports*, *3*(1), 1356. https://doi.org/10.1038/srep01356

Serreze, M. C., & Barry, R. G. (1988). Synoptic Activity in the Arctic Basin, 1979–85. *Journal of Climate*, *1*(12), 1276–1295. https://doi.org/10.1175/1520-0442(1988)001<1276:SAITAB>2.0.CO;2

Serreze, M. C., Box, J. E., Barry, R. G., & Walsh, J. E. (1993). Characteristics of Arctic synoptic activity, 1952-1989. *Meteorology and Atmospheric Physics*, *51*(3–4), 147–164. https://doi.org/10.1007/BF01030491

Sharma, S., Ishizawa, M., Chan, D., Lavoué, D., Andrews, E., Eleftheriadis, K., & Maksyutov, S.

(2013). 16-year simulation of arctic black carbon: Transport, source contribution, and sensitivity analysis on deposition. *Journal of Geophysical Research Atmospheres*, *118*(2), 943–964. https://doi.org/10.1029/2012JD017774

Sharma, Sangeeta, Andrews, E., Barrie, L. A., Ogren, J. A., & Lavoué, D. (2006). Variations and sources of the equivalent black carbon in the high Arctic revealed by long-term observations at Alert and Barrow: 1989-2003. *Journal of Geophysical Research Atmospheres*, *111*(14), 1989–2003. https://doi.org/10.1029/2005JD006581

Sharma, Sangeeta, Richard Leaitch, W., Huang, L., Veber, D., Kolonjari, F., Zhang, W., et al. (2017). An evaluation of three methods for measuring black carbon in Alert, Canada. *Atmospheric Chemistry and Physics*, *17*(24), 15225–15243. https://doi.org/10.5194/acp-17-15225-2017

Shaw, G. E., Stamnes, K., & Hu, Y. X. (1993). Arctic haze: Perturbation to the radiation field. *Meteorology and Atmospheric Physics*, *51*(3–4), 227–235. https://doi.org/10.1007/BF01030496

Shen, Z., Ming, Y., Horowitz, L. W., Ramaswamy, V., & Lin, M. (2017). On the seasonality of arctic black carbon. *Journal of Climate*, *30*(12), 4429–4441. https://doi.org/10.1175/JCLI-D-16-0580.1

Sobhani, N., Kulkarni, S., & Carmichael, G. R. (2018). Source sector and region contributions to black carbon and PM2.5 in the Arctic. *Atmospheric Chemistry and Physics*, *18*, 18123–18148. https://doi.org/10.5194/acp-18-18123-2018

Stein, A. F., Draxler, R. R., Rolph, G. D., Stunder, B. J. B., Cohen, M. D., & Ngan, F. (2015).

NOAA's HYSPLIT Atmospheric Transport and Dispersion Modeling System. *Bulletin of the American Meteorological Society, 96*(12), 2059–2077. https://doi.org/10.1175/BAMS-D-14-00110.1

Stephenson, S. R., Wang, W., Zender, C. S., Wang, H., Davis, S. J., & Rasch, P. J. (2018). Climatic Responses to Future Trans-Arctic Shipping. *Geophysical Research Letters*, *45*(18), 9898–9908. https://doi.org/10.1029/2018GL078969

Stohl, A., Andrews, E., Burkhart, J. F., Forster, C., Herber, A., Hoch, S. W., et al. (2006). Pan-Arctic enhancements of light absorbing aerosol concentrations due to North American boreal forest fires during summer 2004. *Journal of Geophysical Research Atmospheres*, *111*(22), 1–20. https://doi.org/10.1029/2006JD007216

Stohl, A., Berg, T., Burkhart, J. F., Fjæraa, A. M., Forster, C., Herber, A., et al. (2007). Arctic smoke – record high air pollution levels in the European Arctic due to agricultural fires in Eastern Europe in spring 2006. *Atmospheric Chemistry and Physics*, *7*(2), 511–534. https://doi.org/10.5194/acp-7-511-2007

Stohl, A., Klimont, Z., Eckhardt, S., Kupiainen, K., Shevchenko, V. P., Kopeikin, V. M., & Novigatsky, A. N. (2013). Black carbon in the Arctic: The underestimated role of gas flaring and residential combustion emissions. *Atmospheric Chemistry and Physics*, *13*(17), 8833–8855. https://doi.org/10.5194/acp-13-8833-2013

Stohl, A., Aamaas, B., Amann, M., Baker, L. H., Bellouin, N., Berntsen, T. K., et al. (2015). Evaluating the climate and air quality impacts of short-lived pollutants. *Atmospheric Chemistry and Physics*, *15*(18), 10529–10566. https://doi.org/10.5194/acp-15-10529-2015

Thomas, M. A., Devasthale, A., Tjernström, M., & Ekman, A. M. L. (2019). The Relation Between Aerosol Vertical Distribution and Temperature Inversions in the Arctic in Winter and Spring. *Geophysical Research Letters*, *46*(5), 2836–2845. https://doi.org/10.1029/2018GL081624

Walker, B. D., & Xu, X. (2019). An improved method for the sealed-tube zinc graphitization of microgram carbon samples and 14C AMS measurement. *Nuclear Instruments and Methods in Physics Research Section B: Beam Interactions with Materials and Atoms*, *438*, 58–65. https://doi.org/10.1016/j.nimb.2018.08.004

Wang, J. A., Sulla-Menashe, D., Woodcock, C. E., Sonnentag, O., Keeling, R. F., & Friedl, M. A. (2020). Extensive land cover change across Arctic–Boreal Northwestern North America from disturbance and climate forcing. *Global Change Biology*, *26*(2), 807–822. https://doi.org/10.1111/gcb.14804

Warneke, C., Froyd, K. D., Brioude, J., Bahreini, R., Brock, C. A., Cozic, J., et al. (2010). An important contribution to springtime Arctic aerosol from biomass burning in Russia. *Geophysical Research Letters*, *37*(1), n/a-n/a. https://doi.org/10.1029/2009GL041816

Weingartner, E., Burtscher, H., & Baltensperger, U. (1997). Hygroscopic properties of carbon and diesel soot particles. *Atmospheric Environment*, *31*(15), 2311–2327. https://doi.org/10.1016/S1352-2310(97)00023-X

Widory, D. (2006). Combustibles, fuels and their combustion products: A view through carbon isotopes. *Combustion Theory and Modelling*, *10*(5), 831–841. https://doi.org/10.1080/13647830600720264

Willis, M. D., Leaitch, W. R., & Abbatt, J. P. D. (2018). Processes Controlling the Composition and Abundance of Arctic Aerosol. *Reviews of Geophysics*, *56*(4), 621–671. https://doi.org/10.1029/2018RG000602

Willis, M. D., Bozem, H., Kunkel, D., Lee, A. K. Y., Schulz, H., Burkart, J., et al. (2019). Aircraft-based measurements of High Arctic springtime aerosol show evidence for vertically varying sources, transport and composition. *Atmospheric Chemistry and Physics*, *19*(1), 57–76. https://doi.org/10.5194/acp-19-57-2019

Winiger, P., Andersson, A., Yttri, K. E., Tunved, P., & Gustafsson, Ö. (2015). Isotope-Based Source Apportionment of EC Aerosol Particles during Winter High-Pollution Events at the Zeppelin Observatory, Svalbard. *Environmental Science & Technology*, *49*(19), 11959–11966. https://doi.org/10.1021/acs.est.5b02644

Winiger, P., Andersson, A., Eckhardt, S., Stohl, A., & Gustafsson, O. (2016). The sources of atmospheric black carbon at a European gateway to the Arctic. *Nature Communications*, *7*. https://doi.org/10.1038/ncomms12776

Winiger, P., Andersson, A., Eckhardt, S., Stohl, A., Semiletov, I. P., Dudarev, O. V., et al. (2017). Siberian Arctic black carbon sources constrained by model and observation. *Proceedings of the National Academy of Sciences*, *114*(7), E1054–E1061. https://doi.org/10.1073/pnas.1613401114

Winiger, P., Barrett, T. E., Sheesley, R. J., Huang, L., Sharma, S., Barrie, L. A., et al. (2019). Source apportionment of circum-Arctic atmospheric black carbon from isotopes and modeling. *Science Advances*, *5*(2), eaau8052. https://doi.org/10.1126/sciadv.aau8052

Woods, C., & Caballero, R. (2016). The role of moist intrusions in winter arctic warming and sea ice decline. *Journal of Climate*, *29*(12), 4473–4485. https://doi.org/10.1175/JCLI-D-15-0773.1

Xu, J. W., Martin, R. V., Morrow, A., Sharma, S., Huang, L., Richard Leaitch, W., et al. (2017). Source attribution of Arctic black carbon constrained by aircraft and surface measurements. *Atmospheric Chemistry and Physics*, *17*(19), 11971–11989. https://doi.org/10.5194/acp-17-11971-2017

Yttri, K. E., Lund Myhre, C., Eckhardt, S., Fiebig, M., Dye, C., Hirdman, D., et al. (2014). Quantifying black carbon from biomass burning by means of levoglucosan – a one-year time series at the Arctic observatory Zeppelin. *Atmospheric Chemistry and Physics*, *14*(12), 6427–6442. https://doi.org/10.5194/acp-14-6427-2014

Zhang, R., Khalizov, A. F., Pagels, J., Zhang, D., Xue, H., & McMurry, P. H. (2008). Variability in morphology, hygroscopicity, and optical properties of soot aerosols during atmospheric processing. *Proceedings of the National Academy of Sciences*, *105*(30), 10291–10296. https://doi.org/10.1073/pnas.0804860105

Zuberi, B. (2005). Hydrophilic properties of aged soot. *Geophysical Research Letters*, *32*(1), L01807. https://doi.org/10.1029/2004GL021496

3.6 Appendix

Table A3.1 Overview of samples analyzed for their isotopic composition. Please note that the Filter Sample ID refers to those listed in Table A3.4. The year of ^{14}C analysis was 2018.

UCIAMS#	Isotope Sample ID	Abbreviated Filter Sample ID	Sample Size	$\Delta^{14}C^1$	$\delta^{13}C^1$	f_{FF}	$\delta^{13}C_{FF}^2$	f_{gas}^2
			µg C	‰			‰	
PM								
200073	AL-lbHV-Mar.2014-EC	W-06 to W-09	15.9	-606.5 (23.4)	-27.4	0.61	-27.7 (1.6)	0.05 (0.15)
200074	AL-IbHV-April.2014-EC	W-10 to W-13	13.2	-593.6 (28.1)	-27.0	0.60	-26.9 (1.9)	0 (0.17)
200075	AL-lbHV-May.2014-EC	W-14, W-16	11.9	-675.3 (33.2)	-26.6	0.68	-26.4 (1.9)	0 (0.17)
200076	AL-lbHV-Jun.2014-EC	W-17, W-18	11.2	-509.9 (32.9)	-25.9	0.52	-24.9 (2.5)	0 (0.22)
200077	AL-lbHV-Jul.2014-EC	W-19, W-21	8.5	-387.7 (45.8)	-27.2	0.40	-27.5 (4.7)	0.04 (0.37)
200078	AL-lbHV-Aug.2014-EC	W-22 to W-24	18.9	-187.7 (21.0)	-25.6	0.20	-20.2 (5.6)	0 (0.46)
200079	AL-lbHV-Sept.2014-EC	W-26, W-27	5.0	-579.7 (89.7)	-27.6	0.59	-28.1 (5.9)	0.08 (0.46)
200081	AL-lbHV-Oct.2014-EC	W-28, W-29	17.0	-698.3 (22.8)	-27.0	0.70	-27.0 (1.3)	0 (0.13)
200082	AL-lbHV-Nov.2014-EC	W-31, W-32	18.6	-574.7 (19.3)	-28.3	0.58	-29.2 (1.6)	0.17 (0.15)
200083	AL-lbHV-Nov.2014-A-EC	W-31	14.6	-589.5 (25.1)	-28.3	0.60	-29.1 (1.8)	0.16 (0.16)
200084	AL-lbHV-Nov.2014-B-EC	W-32	12.3	-525.3 (29.9)	-28.3	0.53	-29.3 (2.4)	0.18 (0.20)
200085	AL-lbHV-Dec.2014-A-EC	W-33	10.6	-673.7 (37.6)	-27.1	0.68	-27.2 (2.2)	0.01 (0.18)
200086	AL-lbHV-Dec.2014-B-EC	W-34	12.1	-662.8 (32.5)	-27.1	0.67	-27.2 (1.9)	0.01 (0.17)
200088	AL-lbHV-Jan.2015-B-EC	W-38, W-39	18.6	-652.7 (20.1)	-26.7	0.66	-26.6 (1.3)	0 (0.13)
200089	AL-lbHV-Feb.2015-A-EC	W-41, W-42	15.9	-509.9 (22.3)	-27.4	0.52	-27.8 (2.0)	0.06 (0.17)
200090	AL-lbHV-Feb.2015-B-EC	W-43, W-45	14.1	-457.9 (25.7)	-27.4	0.47	-27.9 (2.5)	0.07 (0.20)
200091	AL-lbHV-Mar.2015-A-EC	W-46, W-47	19.5	-576.6 (18.2)	-27.4	0.58	-27.6 (1.5)	0.05 (0.14)
200092	AL-lbHV-Mar.2015-B-EC	W-48, W-50	15.0	-659.2 (25.5)	-27.4	0.67	-27.5 (1.6)	0.04 (0.14)
200093	AL-lbHV-Apr.2015-EC	W-51 to W-53	9.7	-470.5 (38.9)	-27.8	0.48	-28.6 (3.4)	0.12 (0.27)
200100	ALT-HV-May15-EC	19731-4 to 1973-7	9.0	-485.3 (42.0)	-26.9	0.49	-26.9 (3.4)	0 (0.27)
Snow								
200101	AlT-Oct-2014-		3.2	-106.2	-28.3	0.12	-37.2	0.78

	EC		(206.2)			(28.0)	(2.17)
200102	AlT-Dec-2014-EC	6.3	-460.2 (64.8)	-26.5	0.47	-26.0 (2.1)	0 (0.18)
200104	AlT-Jan-2015-EC	5.4	-173.3 (90.1)	-28.4	0.19	-34.6 (8.4)	0.58 (0.67)
200105	AlT-Feb-2015-EC	6.7	-391.7 (60.9)	-26.4	0.40	-25.5 (2.4)	0 (0.21)
200106	AlT-Mar-2015-EC	4.0	-190.3 (138.4)	-28.1	0.20	-32.3 (10.2)	0.41 (0.80)
200107	AlT-Apr-2015-EC	4.9	-380.4 (92.6)	-27.5	0.39	-28.2 (3.4)	0.09 (0.27)
200108	AlT-May-2015-EC	4.9	-398.9 (92.5)	-26.5	0.41	-25.9 (3.1)	0 (0.25)

[1]measurement uncertainty (1 sigma for $\Delta^{14}C$, 0.3‰ for $\delta^{13}C$), [2]propagated uncertainty (assuming $\delta^{13}C$ of biomass burning = -26‰, solid fossil fuels = -27‰, gaseous fossil fuels = -40‰)

Table A3.2 Geographical boundaries of BC source regions.

Sector	Latitude (°N)	Longitude (°E)
Arctic Ocean	75 – 90	-60 – -20
Greenland	60 – 75	-179 – 180
North America	40 – 75	-170 – -60
Russia	50 – 75	30 – 180, -179 – -170
Europe	40 – 75	-10 – 30
Asia	20 – 50	30 –150

Table A3.3 Process-specific blank quantification

Process	**Modern Carbon**		**Fossil Carbon**	
	µg C	±	µg C	±
OC/BC Separation	0.90	0.45	0.05	0.03
Combustion/Graphitization/AMS analysis	0.50	0.25	0.40	0.40
Total Blank	**1.40**	**0.70**	**0.45**	**0.43**

Table A3.4. Overview of samples analyzed for their TC, OC, and BC concentrations

Filter Sampling ID	Date Start	Date End	OC	BC[1]	TC	OC/BC	BC/TC
				ng C m^{-3}			%
PM							
AL_lbHV-140305W-06	3/5/2014	3/12/2014	344.6	60.1	404.7	5.7	0.15
AL_lbHV-140312W-07*	3/12/2014	3/19/2014	166.1	116.4	282.5	1.4	0.41
AL_lbHV-140319W-08	3/19/2014	3/26/2014	189.0	50.7	239.7	3.7	0.21
AL_lbHV-140326W-09	3/26/2014	4/2/2014	136.6	14.8	151.5	9.2	0.10
AL_lbHV-140402W-10	4/2/2014	4/9/2014	180.1	15.1	195.2	11.9	0.08
AL_lbHV-140409W-11	4/9/2014	4/16/2014	223.9	22.8	246.8	9.8	0.09
AL_lbHV-140416W-12	4/16/2014	4/23/2014	477.0	65.4	542.4	7.3	0.12
AL_lbHV-140423W-13	4/23/2014	4/30/2014	223.0	35.6	258.7	6.3	0.14
AL_lbHV-140507W-14	5/7/2014	5/21/2014	505.1	59.2	564.3	8.5	0.10
AL_lbHV-140521W-16	5/21/2014	6/4/2014	154.5	17.7	172.2	8.7	0.10
AL_lbHV-140604W-17	6/4/2014	6/18/2014	324.8	26.7	351.5	12.2	0.08
AL_lbHV-140618W-18	6/18/2014	7/2/2014	33.7	10.3	44.0	3.3	0.23
AL_lbHV-140702W-19	7/2/2014	7/16/2014	83.9	6.7	90.6	12.5	0.07
AL_lbHV-140716W-21	7/16/2014	7/30/2014	185.3	5.8	191.1	31.8	0.03
AL_lbHV-140730W-22*	7/30/2014	8/13/2014	267.9	44.5	312.4	6.0	0.14
AL_lbHV-140813W-23	8/13/2014	8/27/2014	156.3	10.3	166.6	15.1	0.06
AL_lbHV-140827W-24	8/27/2014	9/10/2014	152.8	15.3	168.1	10.0	0.09
AL_lbHV-140910W-26	9/10/2014	9/24/2014	77.1	13.3	90.4	5.8	0.15
AL_lbHV-140924W-27	9/24/2014	10/8/2014	83.0	18.0	101.0	4.6	0.18
AL_lbHV-141008W-28*	10/8/2014	10/22/2014	260.9	91.9	352.8	2.8	0.26
AL_lbHV-141022W-29	10/22/2014	11/5/2014	124.7	19.1	143.8	6.5	0.13
AL_lbHV-141105W-31	11/5/2014	11/19/2014	148.8	17.3	166.0	8.6	0.10
AL_lbHV-141119W-32	11/19/2014	12/3/2014	241.7	19.4	261.0	12.5	0.07
AL_lbHV-141203W-33	12/3/2014	12/17/2014	304.1	103.8	407.9	2.9	0.25
AL_lbHV-141217W-34	12/17/2014	12/31/2014	199.0	51.4	250.4	3.9	0.21
AL_lbHV-141231W-36	12/31/2014	1/14/2015	233.8	38.4	272.2	6.1	0.14
AL_lbHV-150114W-37	1/14/2015	1/21/2015	216.1	60.9	276.9	3.5	0.22
AL_lbHV-150121W-38	1/21/2015	1/29/2015	430.7	80.2	510.9	5.4	0.16
AL_lbHV-150129W-39	1/29/2015	2/4/2015	304.7	66.0	370.7	4.6	0.18
AL_lbHV-150204W-41	2/4/2015	2/11/2015	562.6	135.3	697.9	4.2	0.19
AL_lbHV-150211W-42	2/11/2015	2/18/2015	371.2	114.7	485.9	3.2	0.24
AL_lbHV-150218W-43	2/18/2015	2/25/2015	274.0	83.9	357.9	3.3	0.23
AL_lbHV-150225W-45	2/25/2015	3/4/2015	343.4	88.1	431.5	3.9	0.20
AL_lbHV-150304W-46	3/4/2015	3/11/2015	350.8	31.0	381.8	11.3	0.08
AL_lbHV-150311W-47	3/11/2015	3/18/2015	465.1	63.3	528.4	7.4	0.12
AL_lbHV-150318W-48	3/18/2015	3/25/2015	249.9	63.2	313.1	4.0	0.20

AL_lbHV-150325W-50	3/25/2015	4/1/2015	283.2	68.9	352.1	4.1	0.20
AL_lbHV-150401W-51	4/1/2015	4/8/2015	325.6	34.7	360.3	9.4	0.10
AL_lbHV-150408W-52	4/8/2015	4/15/2015	512.7	69.0	581.7	7.4	0.12
AL_lbHV-150415W-53	4/15/2015	4/22/2015	590.6	62.2	652.8	9.5	0.10
AL-IbHV-150422-19731-1	4/22/2015	4/29/2015	191.5	26.9	218.4	7.1	0.12
AL-IbHV-150429-19731-2	4/29/2015	5/7/2015	32.2	11.6	43.8	2.8	0.27
AL-IbHV-150507-19731-4	5/7/2015	5/13/2015	43.4	5.3	48.7	8.2	0.11
AL-IbHV-150513-19731-5	5/13/2015	5/20/2015	207.5	24.8	232.3	8.4	0.11
AL-IbHV-150520-19731-6	5/20/2015	5/27/2015	86.9	8.0	94.9	10.9	0.08
AL-IbHV-150527-19731-7	5/27/2015	6/3/2015	22.6	12.7	35.3	1.8	0.36
AL-IbHV-150603-19731-8	6/3/2015	6/10/2015	92.7	1.8	94.5	50.5	0.02
AL-IbHV-150610-19731-10	6/10/2015	6/24/2015	100.4	7.8	108.3	12.8	0.07
Snow							
AlT-Oct-2014-EC				8.2			
AlT-Dec-2014-EC				11.4			
AlT-Jan-2015-EC				32.9			
AlT-Feb-2015-EC		n.m		20.3		n.m	
AlT-Mar-2015-EC				8.1			
AlT-Apr-2015-EC				6.2			
AlT-May-2015-EC				13.8			

[1]BC snow units (μg C kg^{-1} snow), n.m. = not measured, *period of elevated BC concentration (≥2σ than seasonal average)

a) Mar2014

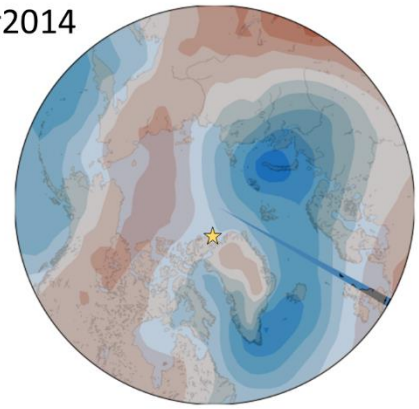

b) Apr2014

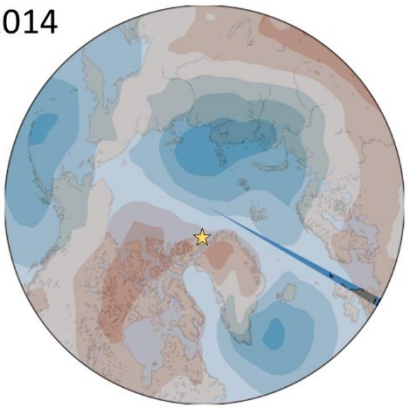

c) May2014

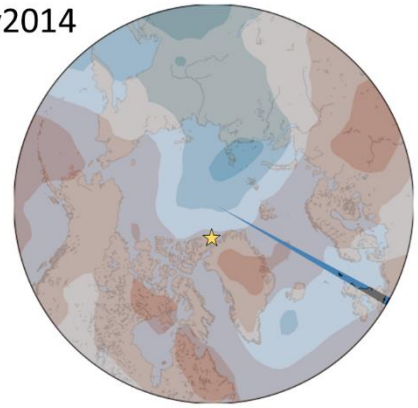

d) Jun2014

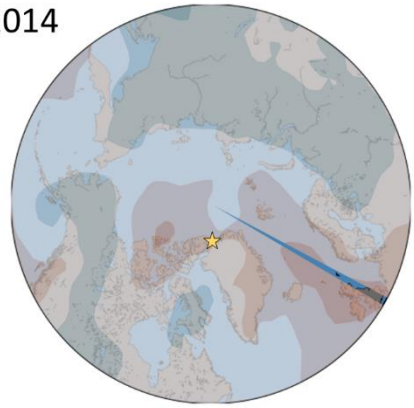

e) Jul2014

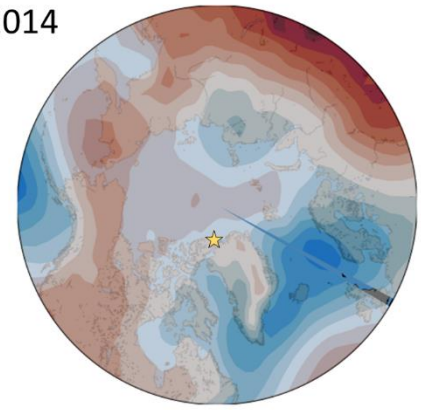

f) Aug2014

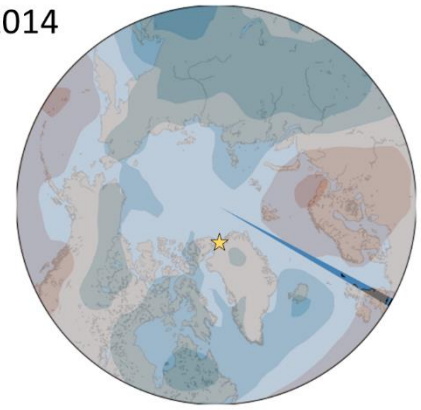

g) Sep2014

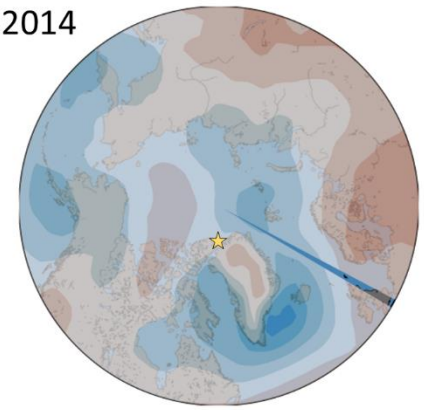

h) Oct2014

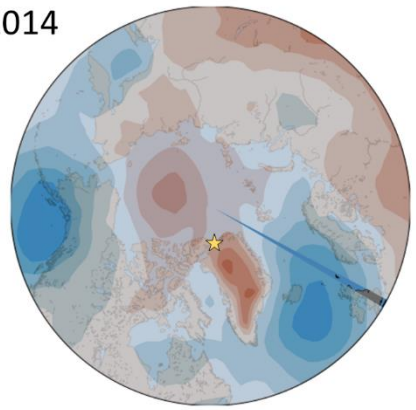

i) NovA2014

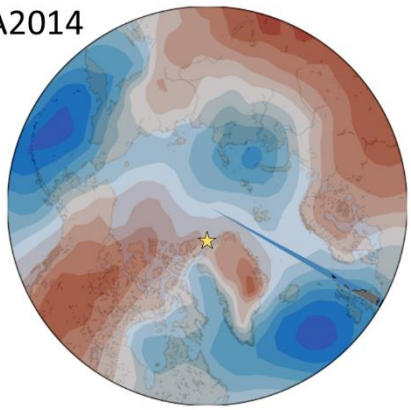

j) NovB2014

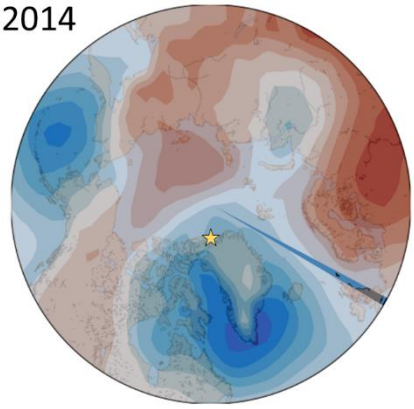

k) DecA2014

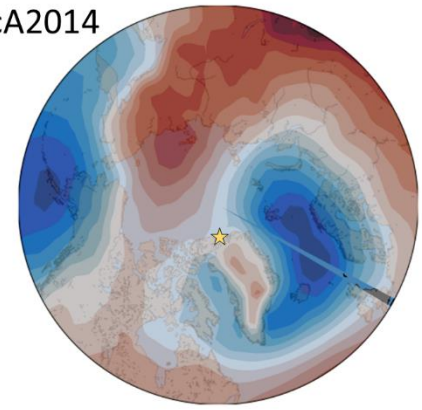

l) DecB2014

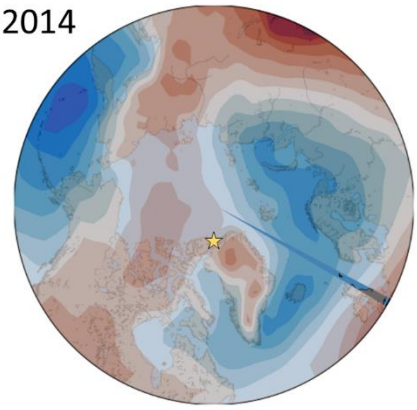

m) JanB2015

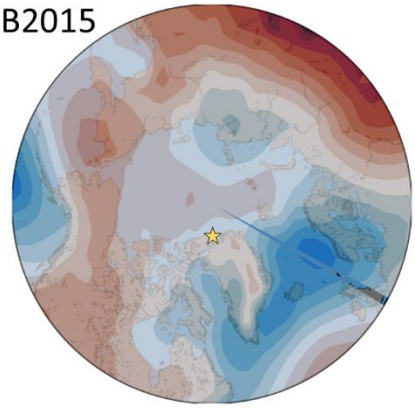

n) FebA2015

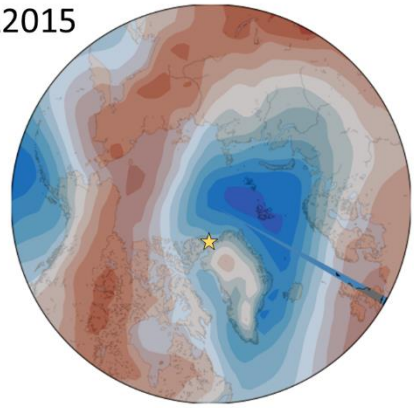

o) FebB2015

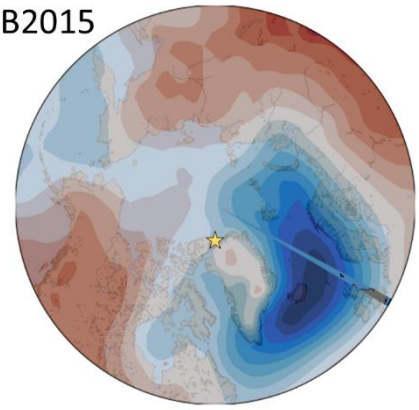

p) MarA2015

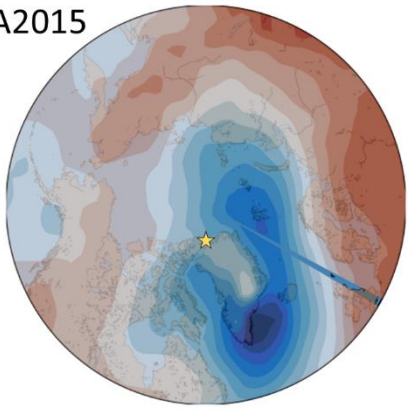

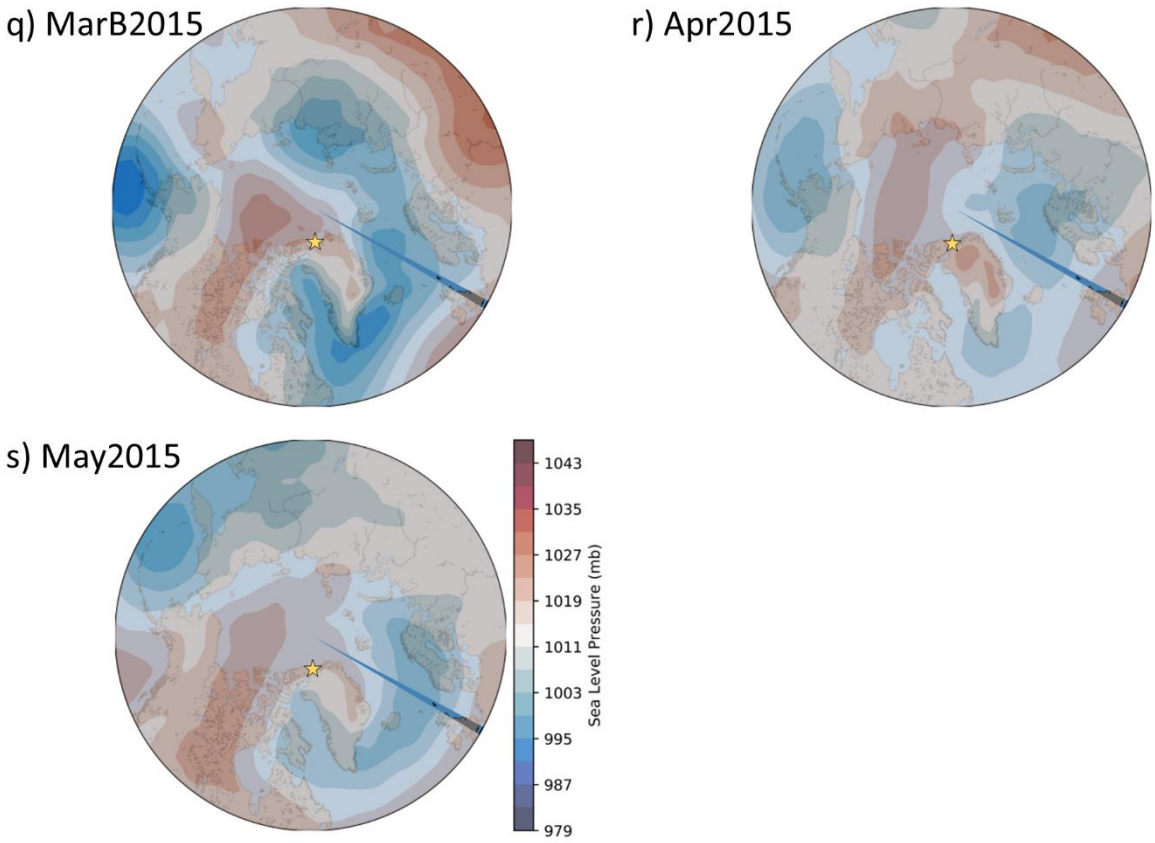

Figure A3.1 Monthly (a-s) mean sea level pressure from NCAR/NCEP reanalysis mean composites. Start and stop times follow those outlined in Tables A3.1 and A3.2.

a) Mar2014

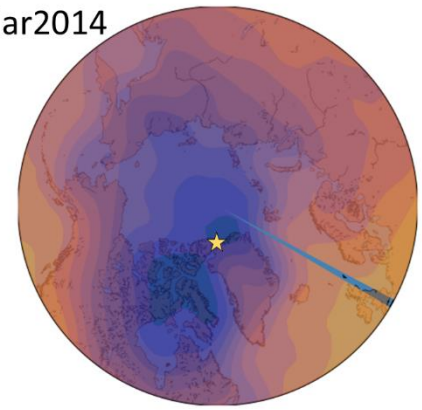

b) Apr2014

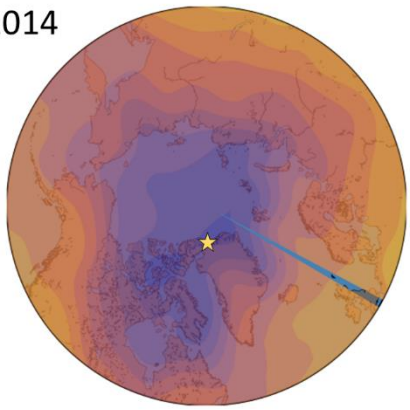

c) May2014

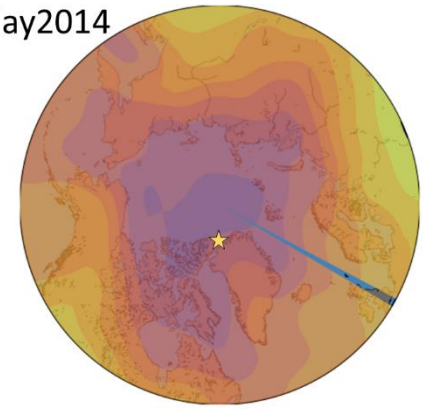

d) Jun2014

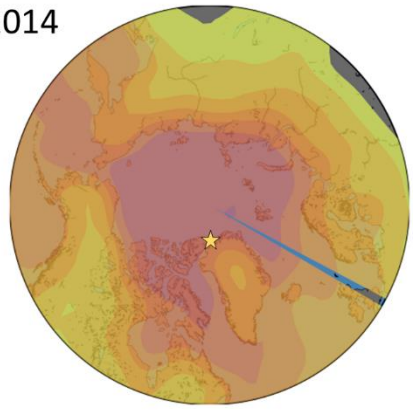

e) Jul2014

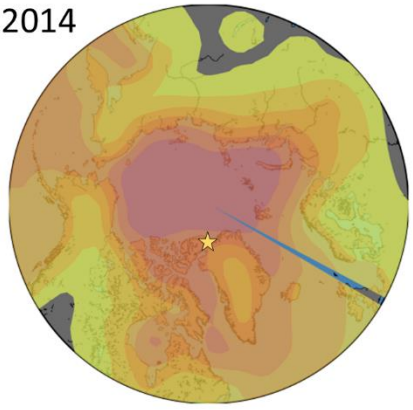

f) Aug2014

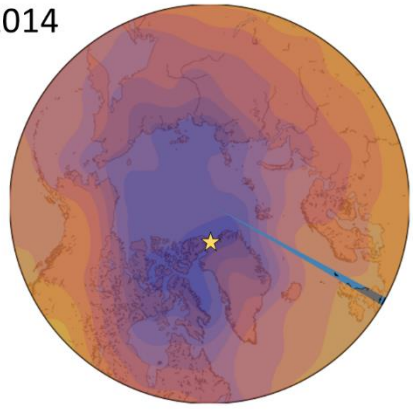

g) Sep2014

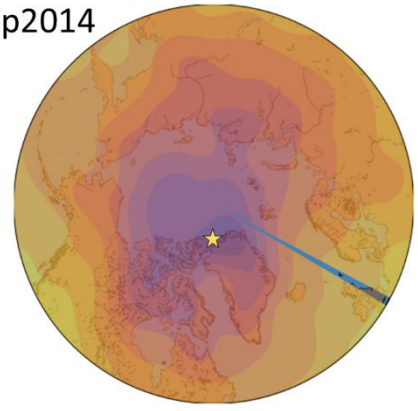

h) Oct2014

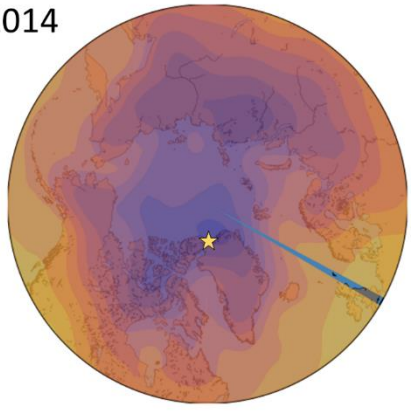

i) NovA2014

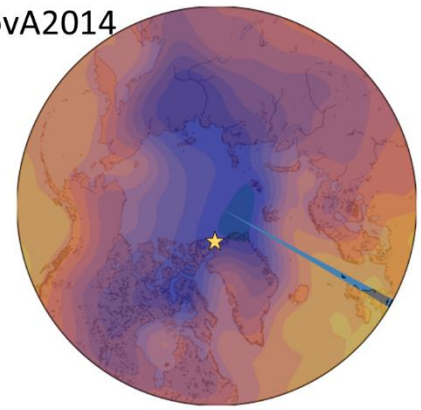

j) NovB2014

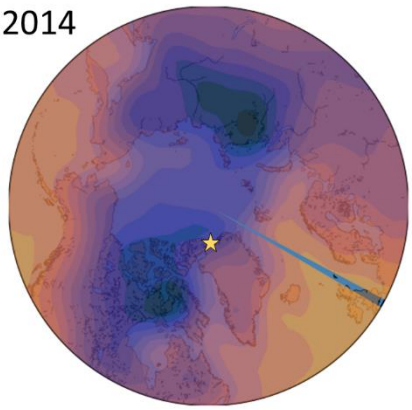

k) DecA2014

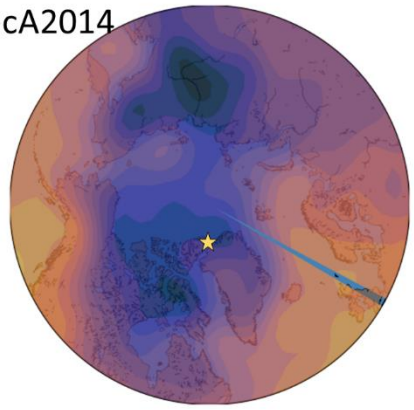

l) DecB2014

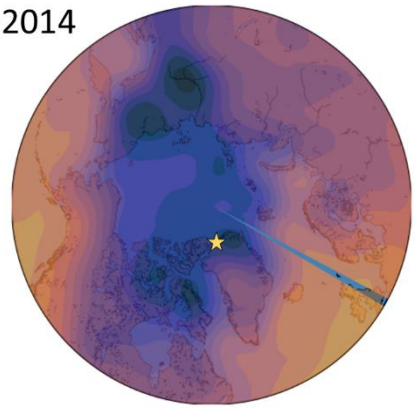

m) JanB2015

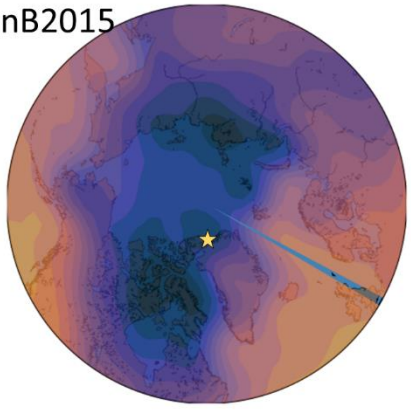

n) FebA2015

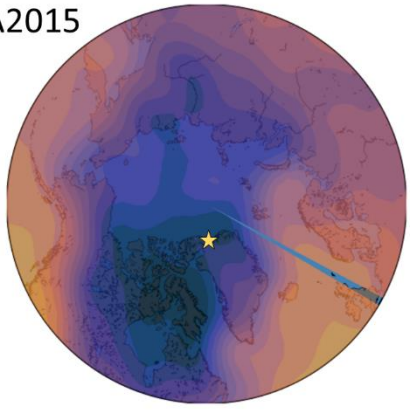

o) FebB2015

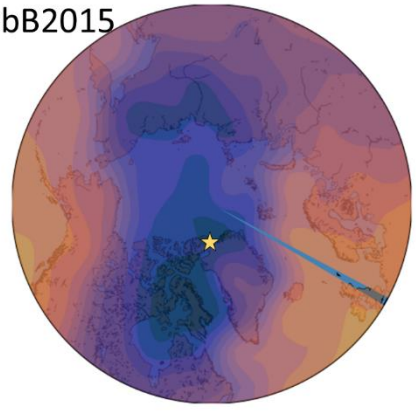

p) MarA2015

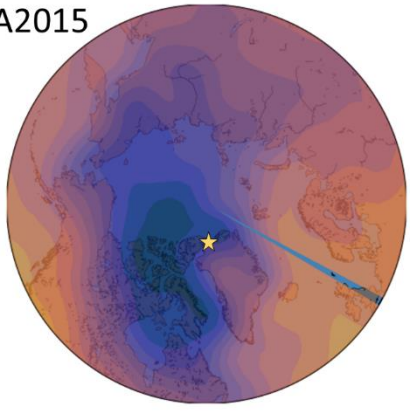

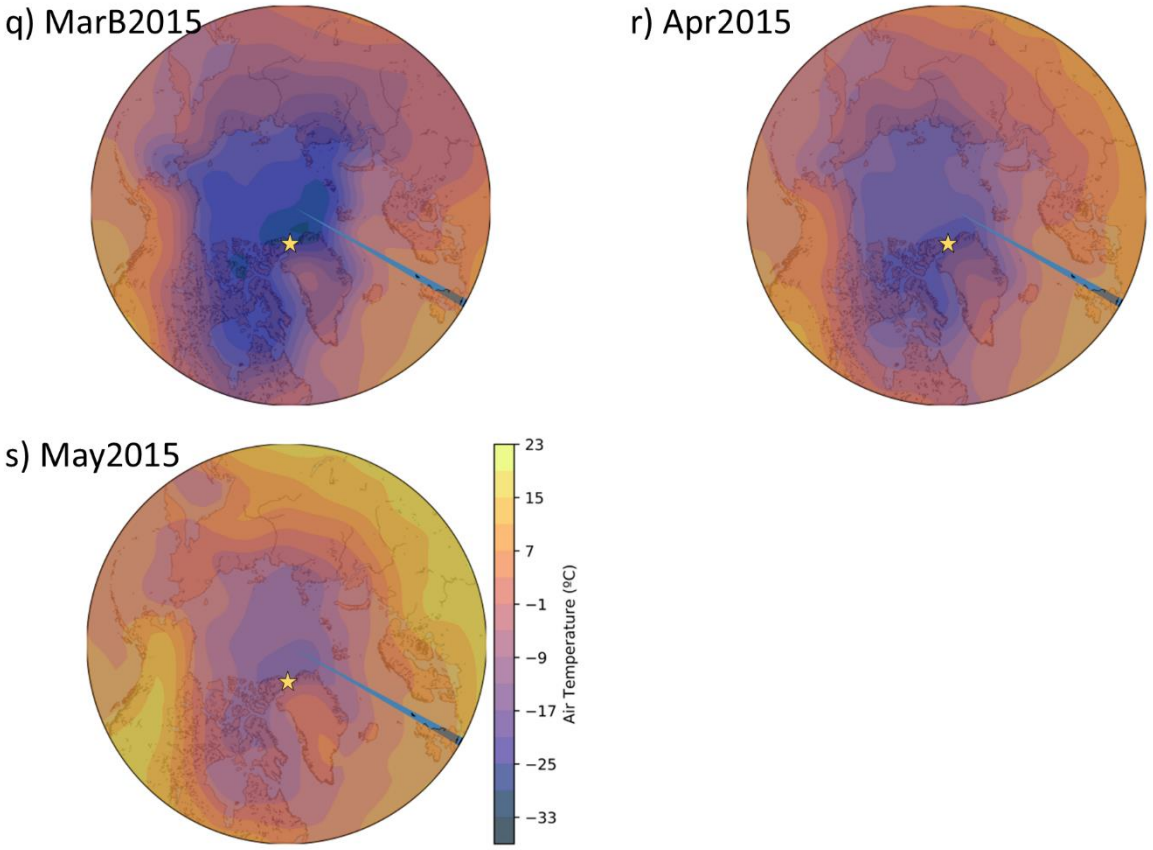

Figure A3.2 Monthly (a-s) and biweekly (i-q, with A refering to the first and B to the latter half of the month) mean air temperature from NCAR/NCEP reanalysis products. Specific dates averaged coincide with sample start and stop dates as noted in Table A3.1.

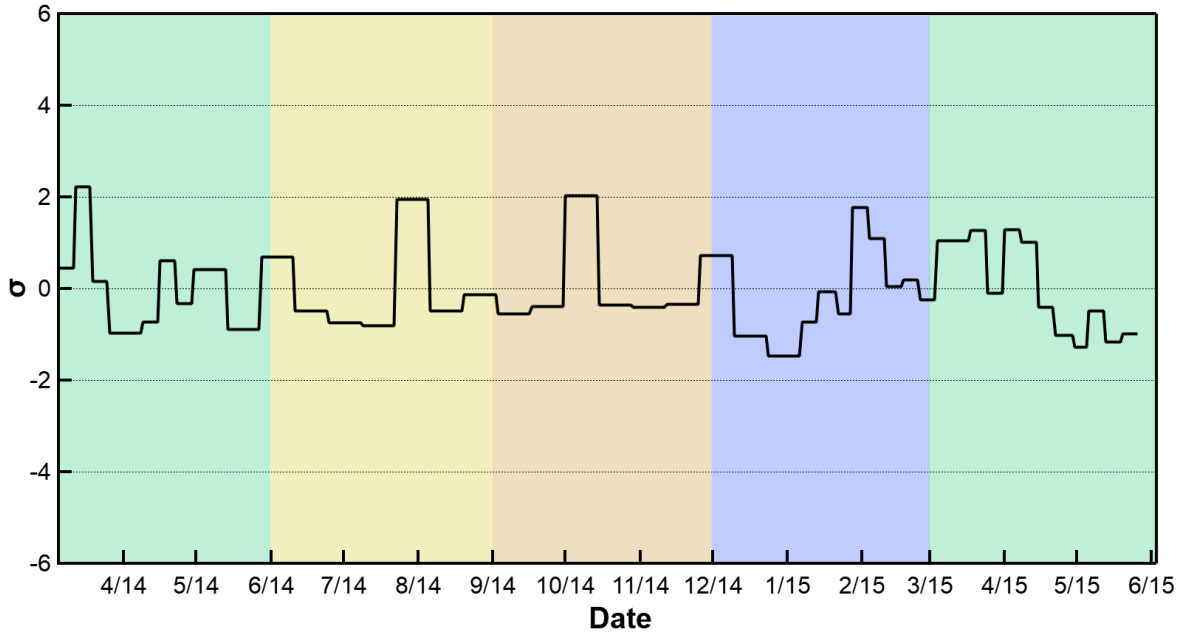

Figure A3.3 Time series showing difference between individual BC concentrations and seasonal averages calculated as respective seasonal standard deviations (Table 3.1). Background colors distinguish meteorological seasons, such as spring (green), summer (yellow), fall (brown), and winter (blue).

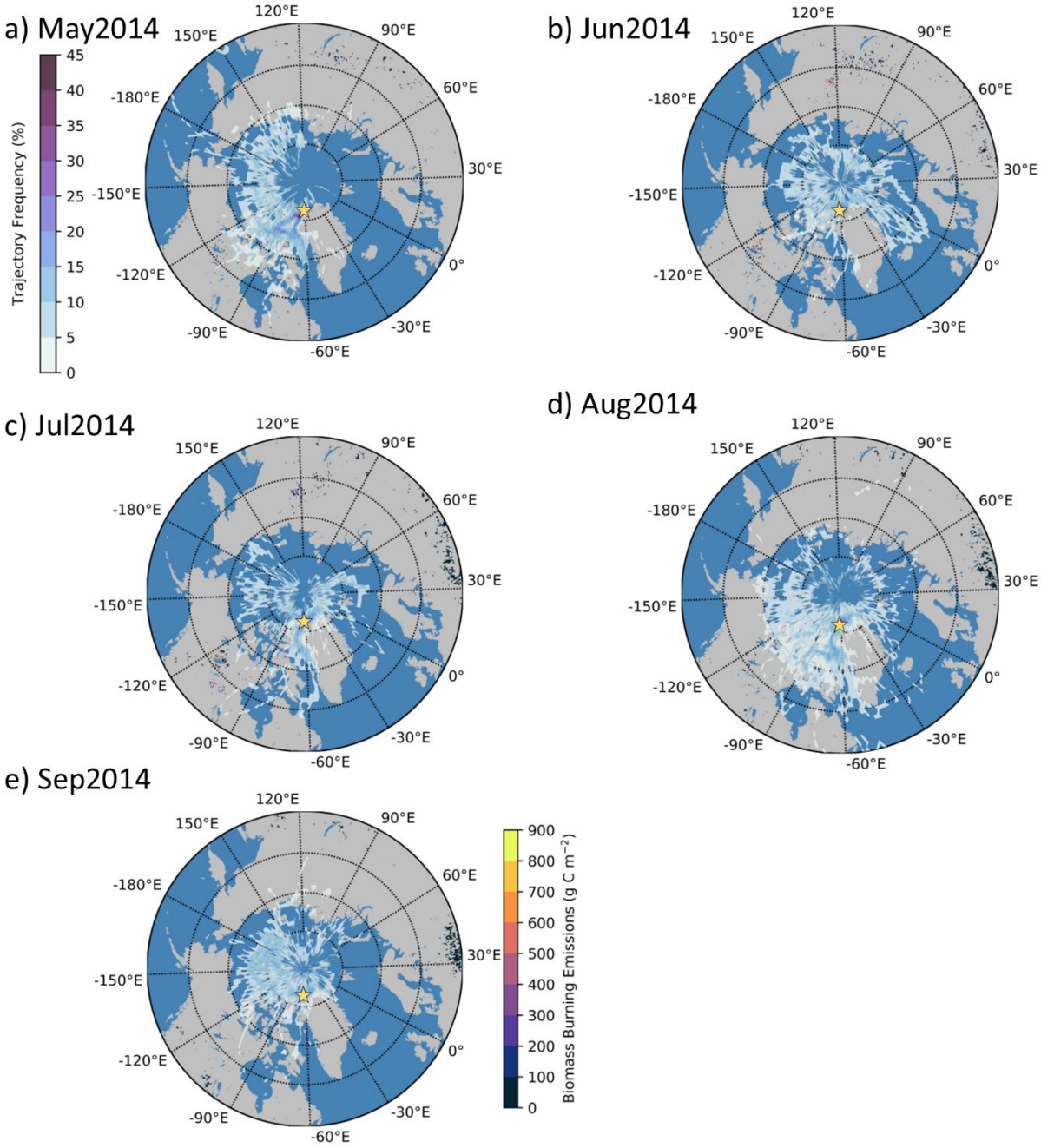

Figure A3.4 Monthly fire emissions from biomass burning during the fire season, from May (a) to September (e) 2014 and monthly back-trajectory frequency. Fire emissions taken from Global fire emissions database version 4 (Giglio et al., 2013; Randerson et al., 2012; van der Werf et al., 2017).

Chapter 4

Source apportionment of summertime organic aerosol in the marine boundary layer of the Pacific and Western Arctic Oceans

Adapted from:

B. T. Rodríguez, S. Kim, X. Xu, G. M. Santos, K. Park, C. E. Moffett, R. J. Sheesley, C. I. Czimczik. (In Prep.)

4.1 Introduction

Organic carbonaceous (OC) aerosol is a critical, short-lived climate forcer that has complex interactions with other climate-affecting components of the Earth system. OC influences climate directly by scattering solar radiation and indirectly due to its role in cloud condensation and precipitation (Fuzzi et al., 2015). The climatic impacts of OC aerosol are among the most uncertain because relevant emission/formation, aging, and removal mechanisms are highly variable and respective controlling factors are not well understood (Hodzic et al., 2016; Zhu et al., 2019).

Marine emissions are a major source of OC, yet their fluxes and radiative forcing remain poorly constrained (Gantt et al., 2012; Meskhidze et al., 2011; Myriokefalitakis et al., 2010). Estimates of marine OC emissions from global modelling studies range from 7 to 50 Tg $year^{-1}$ and are comparable to OC emissions from fossil fuels (Gantt et al., 2009; Ito & Kawamiya, 2010; Spracklen et al., 2008).

In marine environments, the OC burden varies with distance to the coast and latitude (Jimenez et al., 2009), and its origin from marine and terrestrial sources is poorly constrained by available measurements (Barrett & Sheesley, 2017). Coastal air masses contain marine and terrestrial OC aerosol, both primary and secondary in origin (i.e. bioaerosol and secondary particulate from biogenic volatile organic compounds) (Dall'Osto et al., 2017). In addition, anthropogenic emissions of OC aerosol contribute significantly to the aerosol burden of many coastal regions (Yu et al., 2018). Anthropogenic contributions to OC aerosol include co-emitted primary and secondary aerosol from fossil fuel combustion by ships, industry, and biofuel combustion by agricultural fires and residential cooking/heating. OC sources in heavily polluted and densely populated coastal regions are dominated by oxidized secondary OC from industrial and combustion-related volatile emissions (Jimenez et al., 2009; Nault et al., 2018).

Further offshore, marine emissions dominate. Primary marine OC emissions are modulated by wind-induced turbulent mechanisms that form sea spray aerosol (SSA), that is enhanced in organic matter in the sub-micron size range (Blanchard, 1964; Cavalli et al., 2004; Hoffman & Duce, 1974, 1976; O'Dowd & de Leeuw, 2007; O'Dowd et al., 2004a). This colloidal organic material is primarily composed of aggregated micro- and nanopolymers of polysaccharide and lignin-like molecules and highest in concentration within the sea surface microlayer (SML) (Aller et al., 2017; Alpert et al., 2015; Choi et al., 2019). Initial studies linked enhanced OC aerosol concentrations to biological activity (Cavalli et al., 2004; O'Dowd et al., 2004), i.e. exudation by phytoplankton (Ceburnis et al., 2011; Ovadnevaite et al., 2011; Russell et al., 2010). More recently, however, OC-rich, sub-micron marine aerosol was observed in remote marine regions regardless of biological productivity, suggesting that a larger organic pool is a major contributor to OC-enhanced primary marine aerosol (Bates et al., 2020; Quinn et al., 2014). This

pool contains surface-active organics that reduce surface tension and produce bubbles that emit bursts of primary marine aerosol when popped. This material is enhanced in refractory dissolved organic carbon (RDOC) that is decoupled from biological productivity (Kieber et al., 2016), but likely also contain exudates of living phytoplankton (Long et al. 2014).

The Arctic marine boundary layer is characterized by extremely low OC concentrations, particularly during summertime because OC is easily removed by wet deposition. For this reason, changes to the OC burden have large implications for the formation and subsequent microphysical properties of clouds. For example, elevated concentrations of ultra-fine particles (5-50 nm) have been measured in the Arctic boundary layer during pristine and stable conditions (Burkart et al., 2017a). These particles undergo slow condensational growth of semi-volatile organics (Burkart et al., 2017; Collins et al., 2017) before becoming a significant source of cloud condensation nuclei (CCN) in the High Arctic. CCN concentrations in the High Arctic are imperative to understanding the complex cloud-aerosol feedbacks associated with declining sea ice (Earle et al., 2011; Struthers et al., 2011; Willis et al., 2018). Studies also show an enhancement of CCN concentrations under low-wind conditions and when particle organic-to-sulfate ratio is high (Willis et al., 2016, 2017), which is contrary to observations from remote mid-latitude marine environments where CCN concentrations are greater under high-wind conditions due to enhanced SSA and sulfate emission through mechanical action (e.g. wave breaking and bubble bursting) (O'Dowd et al., 1997). These regional differences in OC burden and impact highlight the importance of factoring the environmental region as another modulator of ambient OC aerosol concentrations.

Analyses of the stable ($\delta^{13}C$) and radiocarbon ($\Delta^{14}C$) isotope ratios of OC aerosol provides insight to its terrestrial vs. marine and biogenic vs. fossil sources (Mackey et al., 2021;

Rodríguez et al., 2020). Stable isotope signatures reflect differences in carbon sources (mixing) and isotope fractionation during biogeochemical cycling. Plants of temperate and Arctic regions, as well as plants that were converted to fossil carbon reservoirs, use the C3 photosynthetic pathway; their bulk matter and VOC emissions $\delta^{13}C$ average -28±2‰ (Ceburnis et al., 2008; Kohn, 2010). Marine carbon pools, such as dissolved inorganic (DIC), particulate organic (POC), and dissolved organic (DOC) carbon, differ significantly in their $\delta^{13}C$ values. The $\delta^{13}C$ of DIC at the ocean surface globally is about 0-2‰ and is enriched relative to that of atmospheric CO_2 ($\delta^{13}CO_2$ ≈ -8.5‰) (White et al., 2015) due to kinetic fractionation favoring the dissolution of the heavier isotope. POC at the surface is produced by biological systems and has a $\delta^{13}C$ signature similar to primary producers and their exudates (-21 to -29‰) (Brown et al., 2014; Kwak et al., 2017). The large range in marine POC is due to variation in sea surface temperature, with lower $\delta^{13}C$ of POC observed at lower sea surface temperatures (Brown et al., 2014; Druffel et al., 1996; Griffith et al., 2012; Guo et al., 2004; Kwak et al., 2017; Kim et al., 2017; Lin et al., 2014; Zhang et al., 2012). DOC originates primarily from the microbial decomposition of POC and its $\delta^{13}C$ averages -21 to -22‰ at the surface (Druffel et al., 1992; Druffel et al., 2018; Zigah et al., 2017).

Radiocarbon measurements infer the "age" of carbon-bearing materials as well as differences in their carbon sources. Fossil carbon pools are devoid of ^{14}C (e.g., measurement result approaches $\Delta^{14}C$ = -1000‰, indistinguishable from background samples) due to a half-life of 5730 years ($\Delta^{14}C$ = -1000‰). The $\Delta^{14}C$ of terrestrial carbon pools as well as of marine DIC and DOC are similar to atmospheric CO_2, their ultimate carbon source. In 2020, the $\Delta^{14}C$ of pristine atmospheric CO_2 was about 0‰, following a 70-year decline of bomb ^{14}C in the atmosphere. In the late 1950s and early 1960s, thermo-nuclear weapons testing nearly doubled the atmospheric ^{14}C content ($\Delta^{14}C \geq 0$‰). Since then, the amount of ^{14}C in the atmosphere has been declining

due to mixing of atmospheric CO_2 with marine and terrestrial carbon pools, and by dilution with fossil fuel-derived CO_2 (Graven, 2015; Levin et al., 2010). DOC, in contrast, is significantly depleted in ^{14}C ($\Delta^{14}C$ < -150‰) because half of it is comprised of aged microbially-inaccessible RDOC and the other half is produced recently by phytoplankton (Bauer et al., 1998; Druffel et al., 2017; Griffith et al., 2012; Zigah et al., 2017). Together, these differences in carbon isotope ratios ($\delta^{13}C$, $\Delta^{14}C$) of terrestrial and marine sources allow the characterization of sources to bulk aerosol.

In this study, we characterized marine and terrestrial contributions to OC across the northern Pacific and the Western Arctic. Specifically, we combined measurements of (1) aerosol isotopic composition ($\delta^{13}C$, $\Delta^{14}C$) to apportion sources to marine OC and their variation with distance to coast, latitude, and air mass origin, and (2) concentrations of major ions and methanesulfonic acid (MSA) of ambient OC aerosol with (3) backward trajectory analyses of air masses and (4) observations of marine productivity (chlorophyll-induced fluorescence, $\Delta O_2/Ar$, and MSA) to understand contributions from marine RDOC, fresh biomass (terrestrial or marine), and fossil carbon sources. By providing data from a mobile platform, this work complements observations of marine air masses on land and advances our understanding of OC sources and climate impacts in the remote northern Pacific and western Arctic Ocean.

4.2 Methods

4.2.1 Sample collection

Aerosol total suspended particle (TSP, n=5) and particles with a diameter of 2.5 μm or less ($PM_{2.5}$, n=3) samples were collected onboard the R/V ARAON (Fig. 4.1), operated by the Korean Polar Research Institute, during the 2017 Arctic summer campaign from July 22 to August 19, 2017 (Table 4.1). Air volumes sampled ranged from 1509 to 5454 m^3, integrating 45-187

hours. The campaign began offshore at Busan, South Korea and ended in the Arctic Ocean (Fig. 4.2).

Samples were obtained with a volume-calibrated, high-volume aerosol sampler (Tisch Environmental, TE-PM10PLUS-BL) at a flow rate of 1,133 $L\,min^{-1}$ (40±4 CFM) on pre-combusted (450ºC, 4 hours) quartz fiber filters (2500 QAT-UP, Pallflex Tissuquartz, Pall, Port Washington, NY, USA). The loaded filter area was 393.75 cm^2. Samples were wrapped in pre-combusted aluminum foil, sealed in anti-static bags, and stored frozen (-20ºC) until analysis.

To prevent contamination from the boat (e.g., smokestack and cooking), the sampler was located on the bow and attached to a wind-sectoring system that automatically turned off the sampler during the following conditions: (1) wind speeds less than 5 m s^{-1}, (2) wind speeds greater than 18 m s^{-1}, and (3) wind direction between 90º and 270º relative to bow of the ship. All but one sample ("Ice Camp", see below) were captured while the boat was moving. Field blanks were obtained throughout the collection period and used to quantify background contamination by mounting 1/4 of pre-combusted filter, loosely wrapped in pre-combusted aluminum foil, on the inside of the sampler housing.

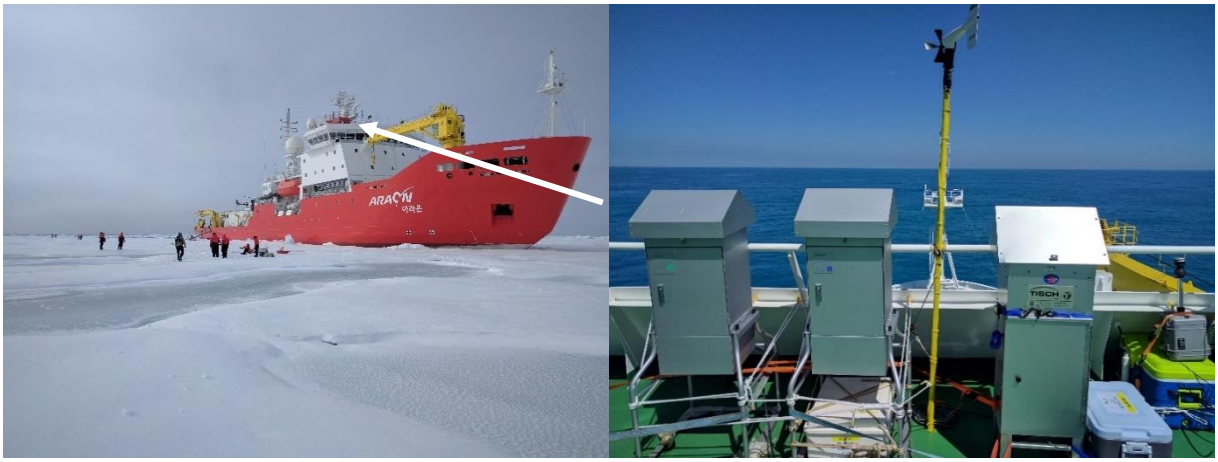

Figure 4.1 Picture of (left) R/V ARAON during ice camp activities and (right) high-volume sampling setup onboard the bridge deck. The white arrow points to the location of the sampler shown in (right).

Table 4.1 Overview of ambient aerosol samples collected onboard R/V ARAON

#	Fraction	Start time	Stop time	Sample volume	Start position	Stop position	Location	Marine Air[1]
		YYYYMMDD hhmm		m^3	ºN, ºE			%
1	$PM_{2.5}$	20170722 0618	20170724 0311	1510	35.059782500, 129.0581282	37.27540933, 133.272136	East Asia Coast	94.1
2	$PM_{2.5}$	20170724 0333	20170726 0336	2923	37.321109167, 133.3472968	41.8720895, 145.0678865	East Sea	58.4
3	$PM_{2.5}$	20170726 0407	20170730 2302	5454	41.881794833, 145.1996958	53.08332567, 171.6415087	Pacific Ocean	97.0
4	TSP	20170730 2346	20170803 1624	2715	53.083310000, 171.6415293	64.31915417, -165.7134878	Bering Sea	98.7
5	TSP	20170803 1649	20170806 2207	3055	64.319200833, -165.7133215	64.49334017, 166.5277122	Nome	73.5
6	TSP	20170806 2239	20170809 2208	3484	64.546774000, -166.77199	72.966017, -168.3506193	Bering Strait	80.8
7	TSP	20170809 2234	20170817 1707	3148	73.045185000, -168.3045378	75.41662483, 176.1900012	Ice Camp	100.0
8	TSP	20170819 2111	20170824 0345	4114	74.412642667, 173.0076982	75.50042233, -161.1236148	Chukchi Sea	93.7

[1]calculated as endpoints within PBL over ocean divided by total endpoints within the PBL

4.2.2 HYSPLIT backward trajectories

To distinguish marine and land air masses, we first estimated the origin of the air masses impacting each sample via the HYSPLIT backward trajectory model using daily files of archived 3-hr meteorological data from the Global Data Assimilation System (GDAS) with a 0.5º resolution grid (https://www.ready.noaa.gov/archives.php). Simulations were initialized every 6 hours and pre-cast for 240 hours before initialization with a time resolution of one hour.

Then, we calculated backward trajectory frequencies by counting the endpoints below the planetary boundary layer (PBL), as determined in GDAS meteorology data, in a 1×1º grid and divided each grid frequency by total number of endpoints within the PBL. Each trajectory endpoint was labeled as land or marine through comparison to the coastlines defined by the Global Self-consistent, Hierarchical, High-resolution Geography Database (GSHHG, http://www.soest.hawaii.edu/pwessel/gshhg/) in the intermediate resolution. The proportion of marine air masses impacting each sample was quantified by calculating the percentage of endpoints within the PBL present over the ocean over the total number of endpoints within the PBL.

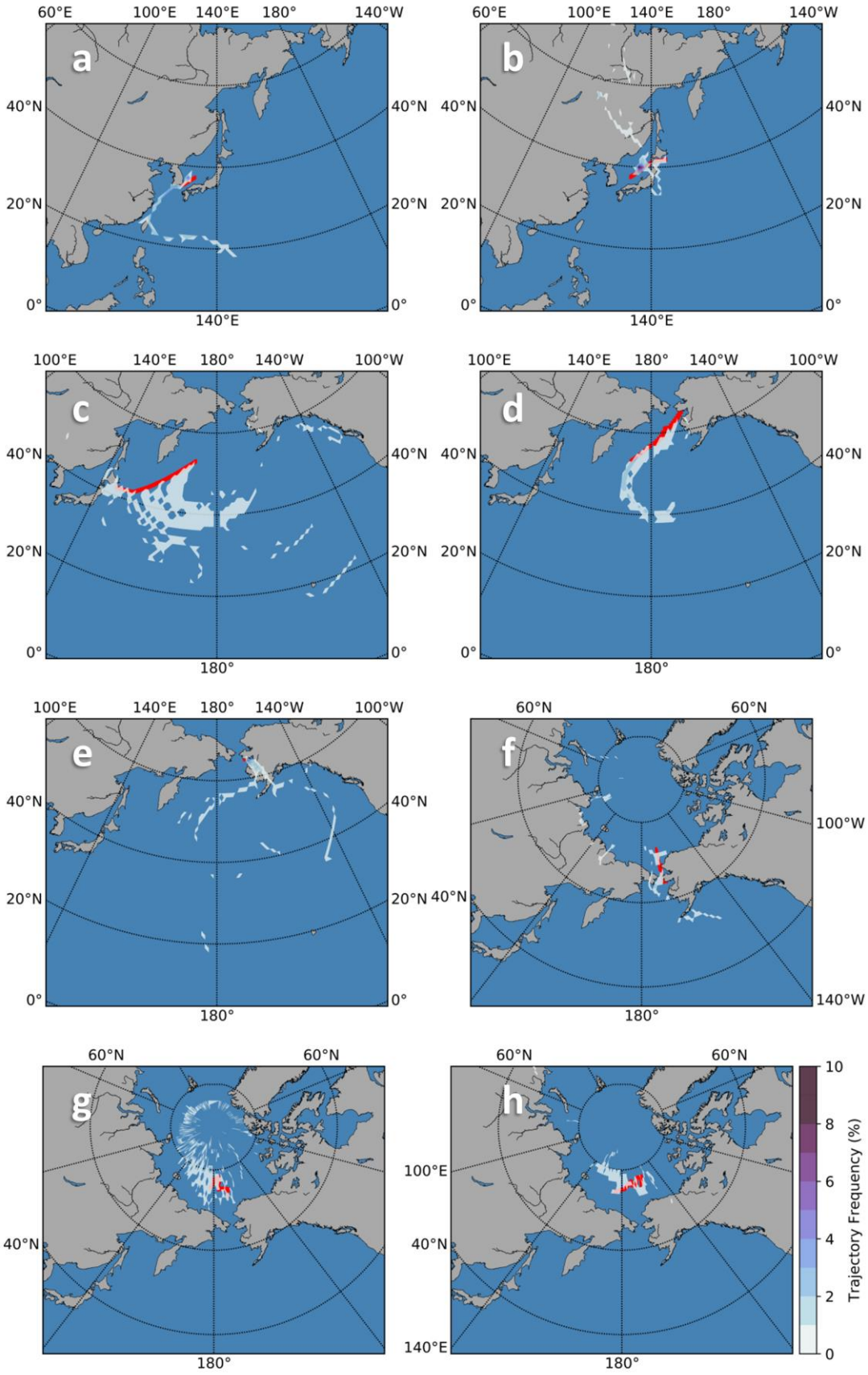
a
b
c
d
e
f
g
h
60°E
100°E
140°E
180°
140°W
100°W
60°N
40°N
20°N
0°
Trajectory Frequency (%)
0
2
4
6
8
10

Figure 4.2. Sampling locations onboard R/V ARAON during summer 2017. Samples were collected in the (a, b) East Sea, (c) Pacific Ocean, (d) Bering Sea, (e) offshore Nome, Alaska, (f) Bering Strait, (g) ice camp, and (h) Chukchi Sea. The boat trajectory is shown in red with corresponding backward air mass trajectory frequencies (color bar).

4.2.3 Isolation, quantification, and processing of isotopic fractions

Quantification of the mass of total carbon (TC), organic carbon (OC) and their respective aerosol carbon isotopic composition were attained at UC Irvine.

To quantify the concentration and stable carbon isotope composition of TC, two 1.5 cm^2 rectangular punches were cut out with a sample punch (SP-15, Sunset Laboratory, Portland, OR, USA), weighed into tin capsules (5×9 mm^2, 041077, Costech Analytical Technologies, Valencia, CA, USA) alongside field blanks and analytical standards, and measured using an elemental analyzer (Fisons NA-1500NC, Thermo, Waltham, MA, USA) coupled to an isotope-ratio mass spectrometer (IRMS, DeltaPlus XL, Thermo Fisher). Since the density of the filter material is variable, carbon mass is reported per volume air by multiplying TC mass per unit area by the loaded area and dividing by total volume collected. Stable carbon isotope results are reported in conventional delta notation relative to V-PDB for $\delta^{13}C$, with a measurement uncertainty of 0.2‰ (1 σ, from long-term measurements of secondary standards).

For TC-^{14}C analysis, 3-15 1.5 cm^2 punches were combusted in pre-combusted double-tubed quartz tubes with 70-80 mg CuO in a furnace (900ºC, 3 hrs). The evolved CO_2 was purified on a vacuum line and converted to graphite using a sealed-tube zinc reduction protocol for ultra-small samples (Walker & Xu, 2019) and measured alongside a suite of size-matched (14-152 µg C) and regular-sized (1 mg C) standards (i.e. carbonaceousmaterials with known $\Delta^{14}C$). Upon graphitization, $\Delta^{14}C$ was measured with Accelerator Mass Spectrometry (AMS) at UC Irvine's KCCAMS facility. The $\Delta^{14}C$ results of processing combustible-only standards, such as

^{14}C-free (coal) and modern carbon (oxalic acid 1 or OX1) were used in conjunction with field filter blanks to correct for contributions of extraneous carbon during sample collection and processing (Santos et al., 2007). The total extraneous carbon introduced by subjecting field filter blanks to combustion, graphitization, and AMS analysis for TC was 2.1±1.1 µg C. This value was used in a mass balance calculation to fix the TC $\Delta^{14}C$ results obtained.

OC concentrations were quantified with the Swiss_4S protocol on an OC/EC analyzer (Sunset Laboratory Inc.) as described in Mouteva et al. (2015) with the exception that only the "S1 OC peak" was collected as described in Zhang et al. (2012). Briefly, sample carbon was thermally evolved from one 1.5 cm^2 filter punch (n=2-6/sample) at 375ºC for 150 seconds under a pure oxygen flow (60 cc/min) and oxidized to CO_2 with MnO_2 at 870ºC. The CO_2 concentration was quantified by a non-dispersive infrared detector (NDIR, Sunset Laboratory Inc.). The instrument is calibrated with a series of volumetric injections of sucrose before sample analyses, and methane internal standard at the end of each run. Akin to TC, ambient concentrations are reported per unit volume of air sampled.

After CO_2 NDIR quantification, the CO_2 was purified on a vacuum line (Mouteva et al. 2015), quantified manometrically, sealed into a pre-combusted graphitization reaction tube, and converted to graphite as described for TC above. OC samples (n=3/sample) were analyzed alongside size-matched ^{14}C standards (OX1 and adipic acid, rather than coal). Adipic acid is ^{14}C free and its crystals are soluble in water, making this an ideal material to be used as fossil OC on filter for indirectly evaluation of the carbon introduced during OC isolation and isotopic sample processing (Mouteva et al. 2015). The same OC extraction scheme described above was used to isolate OC from OX1 and adipic acid aliquots. The total extraneous carbon introduced from OC isolation with Swiss_4S, graphitization, and AMS analysis for OC was 0.85±0.43 µg C. Similar-

ly, final OC $\Delta^{14}C$ values were mass balance corrected by this OC blank. $\Delta^{14}C$ data (in ‰) associated to TC and OC were corrected for isotopic fraction using online-$\delta^{13}C$ values quantified during the ^{14}C-AMS analysis.

4.2.4 Inorganic ions and MSA

Major anions and cations were extracted from filters (n=2/sample) with 20 mL of deionized water, sonicated for 15 min, and centrifuged for 5 min before analysis for cations and anions by ion chromatography (Dionex Aquion and ICS-2100, respectively) at Baylor University (Table A4. 2-A4.4). Sample concentrations for the water extracts were corrected for both field-blanks and water blanks. Ambient air concentrations were then calculated by dividing the mass per unit filter area by the volume of air passed through the filter. Non-sea-salt (NSS) sulfate and potassium concentrations were estimated by calculating the difference between the expected sea-salt contributions using the SO_4^{2-}/Na^+ and K^+/Na^+ ratios in seawater, 0.252 and 0.038 respectively, and measured concentrations.

4.2.5 Ancillary data

We obtained position and meteorological data from R/V ARAON throughout the observation period. Continuous chlorophyll-induced fluorescence measurements were taken with a 10-AU (Turner) Fluorimeter at 1-minute intervals. A membrane inlet mass spectrometer (MIMS) (Hiden 301) $\Delta O_2/Ar$ at one minute intervals at the sea surface as described in Park et al. (2019). $\Delta O_2/Ar$ measurements were available for the entire campaign (July 22 to August 25).

4.2.6 Dual-isotope source apportionment

Sources to OC aerosol were quantified with a 3-source mass-balance dual-isotope model (Phillips & Gregg, 2001). Three isotopically-distinct carbon pools were considered (Table 4.2)

and their respective uncertainty was propagated: (1) liquid fossils, a metric for marine shipping contributions, (2) fresh biomass, representative of organic carbon originating from newly-produced terrestrial and marine biomass, and (3) marine DOC (<0.7 μm diameter).

We chose liquid fossils as the dominant source of fossil OC, because marine traffic (that uses liquid fossil fuels) is the main anthropogenic influence within coastal and remote marine environments. However, coal combustion may also contribute so solid fossil fuels ($\delta^{13}C$=~-24.5±1‰, $\Delta^{14}C$=-1000‰) were also considered in Arctic coastal samples.

We combined contributions from newly produced terrestrial and marine biomass (terrestrial OC and marine POC) to represent another endmember to aerosol OC, because there is significant overlap in their $\delta^{13}C$ values. The overlap results from lower $\delta^{13}C$ values relative to incoming CO_2, incurred from isotopic fractionation during metabolic process of fixing CO_2 to organic matter, and temperature. Marine DIC was not considered an important source due to the enriched ($\delta^{13}C$=0-2‰) signature distinct from collected samples, though DIC is the source of carbon to young POC and DOC in the surface ocean.

Table 4.2. Observations and estimations of endmember isotopic signatures.

Sample #	Endmember	n	FM ^{14}C	$\Delta^{14}C$ ‰	±	n	$\delta^{13}C$ ‰	±	References
1-8	**Liquid Fossil**	10	0	-1000	5	10	-28.0	2.0	Widory, 2006
1-8	**Fresh Biomass**	10	1.015	7	2	40	-27.0	4.0	Kohn, 2010; Xu pers. comm
				Marine DOC					
1, 2	East/Japan Sea	19	0.776[1]	-230[1]	45[1]	3	-21.3	0.4	Kim et al., 2015
	Northeast Pacific Ocean	5	0.790	-215	47	5	-21.2	0.6	Bauer et al., 1998; Druffel et al., 1992, 2018; Druffel et al., 2019; Zigah et al., 2017
3	Northwest Pacific	3	0.714	-291	45[1]	3	-22.6	0.8[1]	Tanaka et al., 2010
4, 5, 6	Bering Sea/Strait	19	0.776[1]	-230[1]	45[1]	19	-21.7[1]	0.8[1]	

7, 8	Arctic	12	0.769	-238	29	8	-22.4	0.6	Benner et al., 2004; Druffel et al., 2017; Griffith et al., 2012

[1]Average±stdev values from (Bauer et al., 1998; Benner et al., 2004; Druffel et al., 2017; Druffel et al., 1992, 2018; Druffel et al., 2019; Griffith et al., 2012; Tanaka et al., 2010; Zigah et al., 2017)

Marine DOC was selected as a third potential source. Generally, DOC is significantly depleted in ^{14}C relative to atmospheric CO_2 values due to the existence of RDOC. Due to high-variability in marine end-member values, an average of previous isotopic ($\delta^{13}C$, $\Delta^{14}C$) measurements within corresponding ocean basins was used (Table 4.2). However, marine $DO^{14}C$ end-member values and ranges for the East Sea and Bering Sea/Strait regions had to be approximated due to a lack of observations in this region.

4.3 Results and discussion

4.3.1 Air mass origin

The backward trajectory frequency analysis indicates the sampling campaign captured a range of air masses, from continental outflow to coastal, remote, and within the Arctic polar dome (Fig. 4.2, Table 4.1). The air masses sampled at the beginning of the campaign (Fig 4.2a.) show strong continental outflow from the South Korean and Chinese coast. Sampling over the East Sea (Fig 4.2b) indicates strong local influences within the East Sea, coastal Japan, and inland Russia. Sampling over the eastern Pacific Ocean (Fig. 4.2c) captured air masses from the entire Northern Pacific. In the Bering Sea (Fig. 4.2d), air mass origin was confined to the Bering Sea and Northern Pacific. Offshore Nome (Fig. 4.2e) air masses indicated strong Alaskan coastal and north Pacific Ocean influences. In the Bering Strait (Fig. 4.2f), a mixture of air masses within the polar dome, Russian, and Alaskan coastal flow was sampled. The boat was then anchored to a sea ice floe (Fig. 4.2g), during which the boat drifted in the Chukchi Sea and air masses originated strictly within the polar dome. This sample is referred to as “Ice Camp” and used to characterize the signature of local emissions from our mobile sampling platform (including smoke-

stack and cooking emissions and mixing by helicopter activity). The final sample (Fig. 4.2h) collected over the Chukchi Sea, captured air masses within the polar dome that were also confined to the Chukchi and East Siberian Sea.

4.3.2 Carbonaceous aerosol concentrations and isotopes

OC concentrations in TSP ranged from 0.137 to 1.47 μg C m^{-3} (Table 4.3). On average, OC was 93±3% (avg±1σ) of TC mass. The highest OC concentrations were observed offshore of East Asia (1.5±0.1 μg C m^{-3}), in the East Sea (1.17±0.05 μg C m^{-3}), and offshore Nome (0.91±0.03 ng C m^{-3}). Incidentally, these samples also had the smallest contribution of marine air masses (Fig. 4.2a,b,e). This pattern also holds true for TC concentrations, wherein the same samples had the highest concentrations measured.

Table 4.3 Composition of bulk carbonaceous aerosol and aerosol fractions. Concentration and isotope data are average (1σ) for n>1 or average (measurement uncertainty; 2‰ for $\Delta^{14}C$, 0.2‰ for $\delta^{13}C$) for n=3, n=3, and n= 3 for TC and OC respectively.

#	Location	TC	OC	OC/ TC	TC $\delta^{13}C$	TC $\Delta^{14}C^1$	OC $\Delta^{14}C^1$	TC FM	OC FM
		μg C/m^3				‰			
1	East Asia Coast	1.7 (0.1)	1.5 (0.1)	0.88	-25.6	-710 (8)	-556 (9)	0.293 (0.008)	0.444 (0.009)
2	East Sea	1.26 (0.06)	1.17 (0.05)	0.93	-25.3	-124 (6)	-99 (2)	0.884 (0.006)	0.901 (0.002)
3	North Pacific Ocean	0.32 (0.06)	0.31 (0.06)	0.96	-23.0	-332 (8)	-259 (19)	0.674 (0.009)	0.741 (0.019)
4	Bering Sea	0.4 (0.1)	0.4 (0.1)	0.93	-24.6	-324 (9)	-283 (26)	0.681 (0.009)	0.717 (0.026)
5	Nome	0.95 (0.03)	0.91 (0.03)	0.96	-25.9	-213 (9)	-135 (0.7)	0.793 (0.009)	0.865 (0.001)
6	Bering Strait	0.329 (0.005)	0.309 (0.005)	0.94	-24.8	-245 (14)	-197 (22)	0.761 (0.014)	0.807 (0.006)
7	Ice Camp	0.22 (0.05)	0.21 (0.04)	0.92	-28.0	-733 (37)	-626 (5)	0.269 (0.037)	0.374 (0.005)

8	Chukchi Sea	0.147 (0.003)	0.137 (0.004)	0.93	-26.4	-285 (14)	-253 (4)	0.721 (0.014)	0.747 (0.004)

[1] TC year of measurement: 2018; OC year of measurement: 2019

Since OC accounted for the majority of TC, $\delta^{13}C$ values measured for TC were used as an estimate for $\delta^{13}C$ of OC. TC-$\delta^{13}C$ values ranged from -28.0 to -23.0‰ and averaged -25.4±1.4‰ (avg±1σ, n=8) (Table 4.3), which are typical values measured for surface POC measured in the north and central Pacific Ocean and Beaufort Sea (Druffel et al., 2017; Griffith et al., 2012). These values also overlap with typical $\delta^{13}C$ values of terrestrial C3-plants and liquid fossil and coal fuels (Fig. 4.3). Thus, $\delta^{13}C$ values alone cannot distinguish between these three endmembers. However, ^{14}C measurements can identify fossil contributions.

$\Delta^{14}C$ of TC ranged from -733 to -123‰ (average -370±226‰, n=8), while $\Delta^{14}C$ of OC ranged from -626 to -100‰ (average -301±190‰, n=8) (Table 4.3). On average, $\Delta^{14}C$ of TC was lower by 70±44‰ (avg±1σ) relative to that of OC (Fig. 4.3). The wide range of observed isotopic values, particularly $\Delta^{14}C$, high variability in air mass sources, and low field blanks suggest that the wind sectoring was effective in minimizing contamination from local sources (i.e. vessel smokestack and cooking emissions). As expected, the East Asia Coast sample, collected in a heavily traveled shipping area, has the lowest $\Delta^{14}C$.

4.3.3 OC source-apportionment

Marine DOC contributed from 18 to 90% to ambient OC (Fig. 4.4), with an average of 35±12%. The highest DOC contribution was estimated for the sample taken over the Pacific Ocean. This sample, along with Bering Sea sample had the highest marine air mass contributions (Table 4.4). In reality, surface DOC $\Delta^{14}C$ is highly variable in the Pacific Ocean, ranging from -163 to -275‰ (Bauer et al., 1998; Druffel et al., 1992; Zigah et al., 2017) (Table 4.2). The high

molecular weight DOC contains the youngest material (-24‰) while the low molecular weight DOC is the oldest (-304‰) and is older at depth (Zigah et al., 2017). To counteract this variability in $\Delta^{14}C$ of DOC, a large range of -230±45‰ was used for the DOC endmember in regions where no data exists. As a result, uncertainties ranged from 7 to 16% with an average of 12±4%. Nonetheless, overall depleted measured $\Delta\ ^{14}C$ suggests DOC is a significant contributor in all samples collected, particularly in remote marine boundary layer.

Table 4.4 Dual-isotope source apportionment of ambient OC aerosol

Sample #	Region	Fraction DOC	±	Fraction Liquid Fossil	±	Fraction Fresh Biomass	±
1	East Asia Coast	0.33	0.07	0.48	0.02	0.19	0.06
2	East Sea	0.30	0.14	0.03	0.03	0.66	0.11
3	Pacific Ocean	0.90	0.10	0.00	0.04	0.10	0.08
4	Bering Sea	0.47	0.09	0.17	0.02	0.34	0.07
5	Nome	0.22	0.16	0.09	0.04	0.69	0.12
6	Bering Strait	0.44	0.11	0.10	0.03	0.46	0.09
7	Ice Camp	0.00	0.14	0.65	0.04	0.42	0.11
8	Chukchi Sea	0.18	0.16	0.21	0.04	0.60	0.12

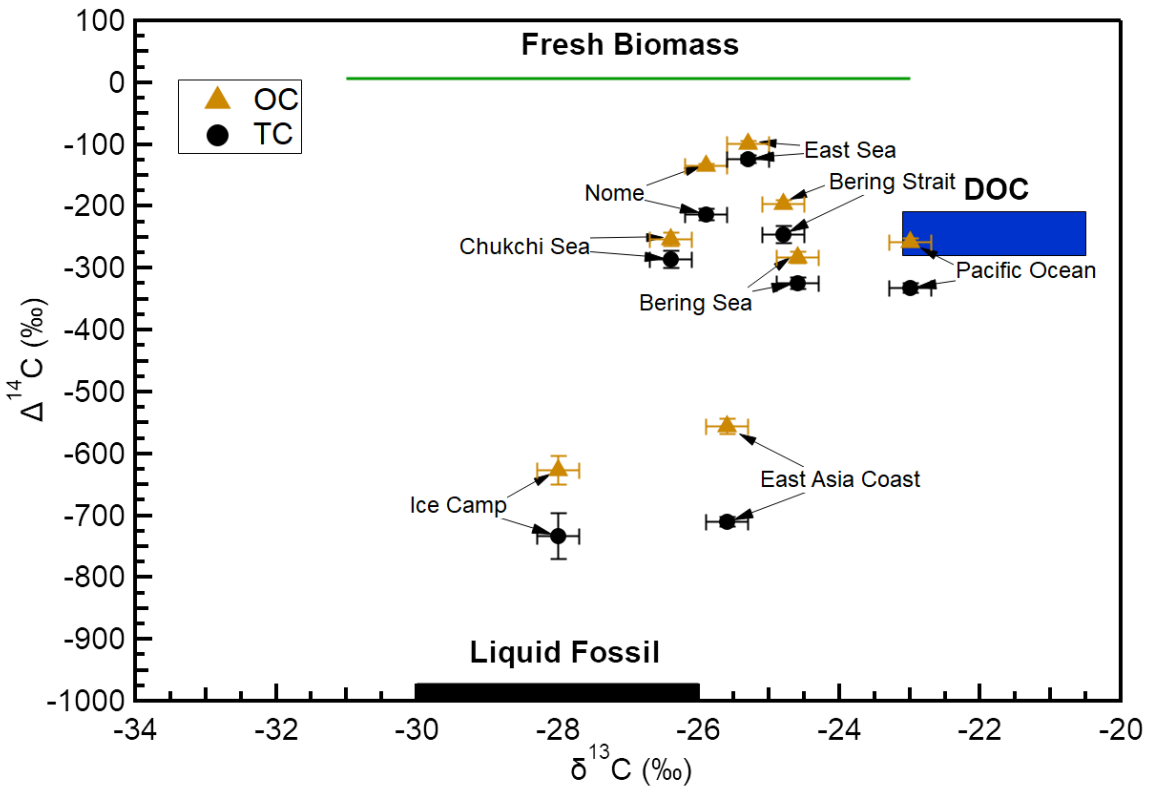

Figure 4.3 Stable ($\delta^{13}C$) and radiocarbon ($\Delta^{14}C$) values measured for TC (circle) and OC (triangle) of samples collected onboard R/V ARAON during the summer 2017 campaign to the Arctic. Plotted $\delta^{13}C$ values were measured for TC and inferred for OC due to the majority (93±3%) of TC being OC.

Riverine export of DOC is a globally significant source of DOC into the oceans (Fabre et al., 2020; Li et al., 2019; Raymond & Spencer, 2015). The samples obtained in the Bering Sea and Strait are heavily influenced by the Yukon-Kuskokwim delta in the Bering Strait. Riverine DOC export in midlatitude and tropical regions typically bring newly fixed carbon that is similar in ^{14}C content to atmospheric $^{14}CO_2$ (Raymond & Bauer, 2001). In the Arctic, however, thawing permafrost and glacier melt can contribute carbon from ancient carbon stores. For the Yukon river delta, exported DOC flux and age follow a seasonal pattern wherein the fluxes are greatest during spring and contain younger OC, largely from snowmelt and terrestrial primary production. Over summer and fall, DOC fluxes decline while the age of the carbon increases. This is attributed to DOC sources shifting from snowmelt and plant material to glacier melt and perma-

frost thaw (Aiken et al., 2014; Guo & Macdonald, 2006). DOC estimations in the Bering Sea and Bering Strait regions were 49±9% and 44±11% respectively and are possibly from this exported ^{14}C-depleted riverine DOC. This study, along with Beaupré et al. and Ceburnis et al. (2019; 2011) highlight the strength of carbon dual-isotopes to source apportion ambient OC aerosol and the significant source of refractory marine DOC to ambient boundary layer marine OC. Unfortunately, the greatest limitation to this approach is the lack of studies measuring DOC carbon isotopes in the western Pacific and Bering Sea/Strait regions and exploring the temporal variability of DO^{14}C in these regions. Future studies should particularly pay attention to the temporal variability of DO^{14}C and respective fluxes at the Yukon delta and other Arctic rivers near locations of declining permafrost (Mann et al., 2015; Wild et al., 2019). This has major implications for the carbon cycle and are very likely to increase in the future due to Arctic Amplification. Additionally, fluxes of atmospheric removal of RDOC should also be explored in future studies. RDOC is a major ocean carbon pool that has often been ignored as a significant source to atmospheric carbon, therefore its climate impact assessment and role in atmospheric processing remains incomplete.

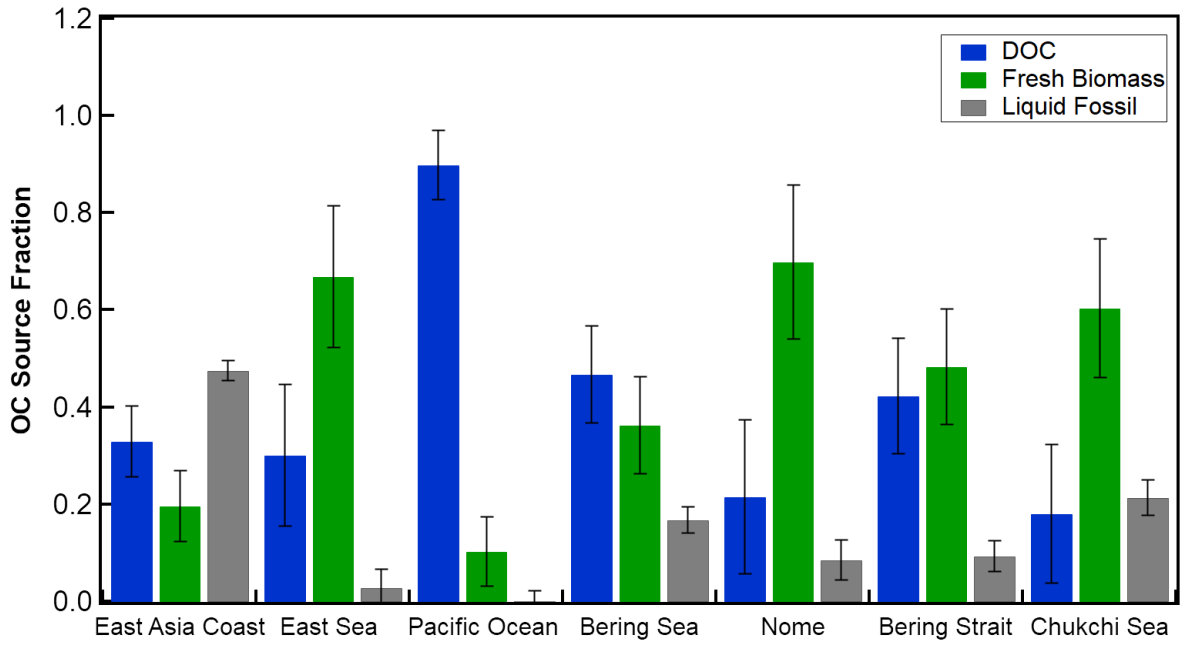

Figure 4.4 Source contribution to OC aerosol from marine dissolved organic carbon (DOC), fresh biomass, and liquid fossil based on dual-isotope (^{13}C, ^{14}C) mass balance.

Fresh biomass contributed 10-70% to ambient OC aerosol, with an average of 44±22%. It is important to note that fresh biomass is sourced from either newly fixed marine or terrestrial biomass. Therefore, further distinction between terrestrial and marine biomass must be approximated from fraction of terrestrial air mass contribution and proxies for biological productivity, such as chlorophyll-induced fluorescence, $\Delta O_2/Ar$ in respective oceans, and methanesulfonic acid concentrations in ambient aerosol (Tables A4.1, A4.4). Due to the large range for the endmember $\delta^{13}C$ value used to estimate fresh biomass (-31 to -23‰,Table 4.2), the uncertainties range from 5 to 12% with an average of 9±3%. The samples with the highest estimated fresh biomass contributions include Nome (70%), East Sea (67%), and the Chukchi Sea (60%). Coincidentally, the Nome and East Sea samples also had the highest terrestrial air mass contributions (Table 4.1), suggesting that the fresh biomass collected from these samples are of terrestrial origin. Elevated NSS-potassium ambient concentrations in the Nome, East Sea, and East Asia Coast sample (Fig. 4.5) further indicate that the fresh biomass particles collected originate from

biomass burning. Furthermore, elevated ambient nitrate concentrations in the Nome sample could also indicate an added anthropogenic fossil combustion source.

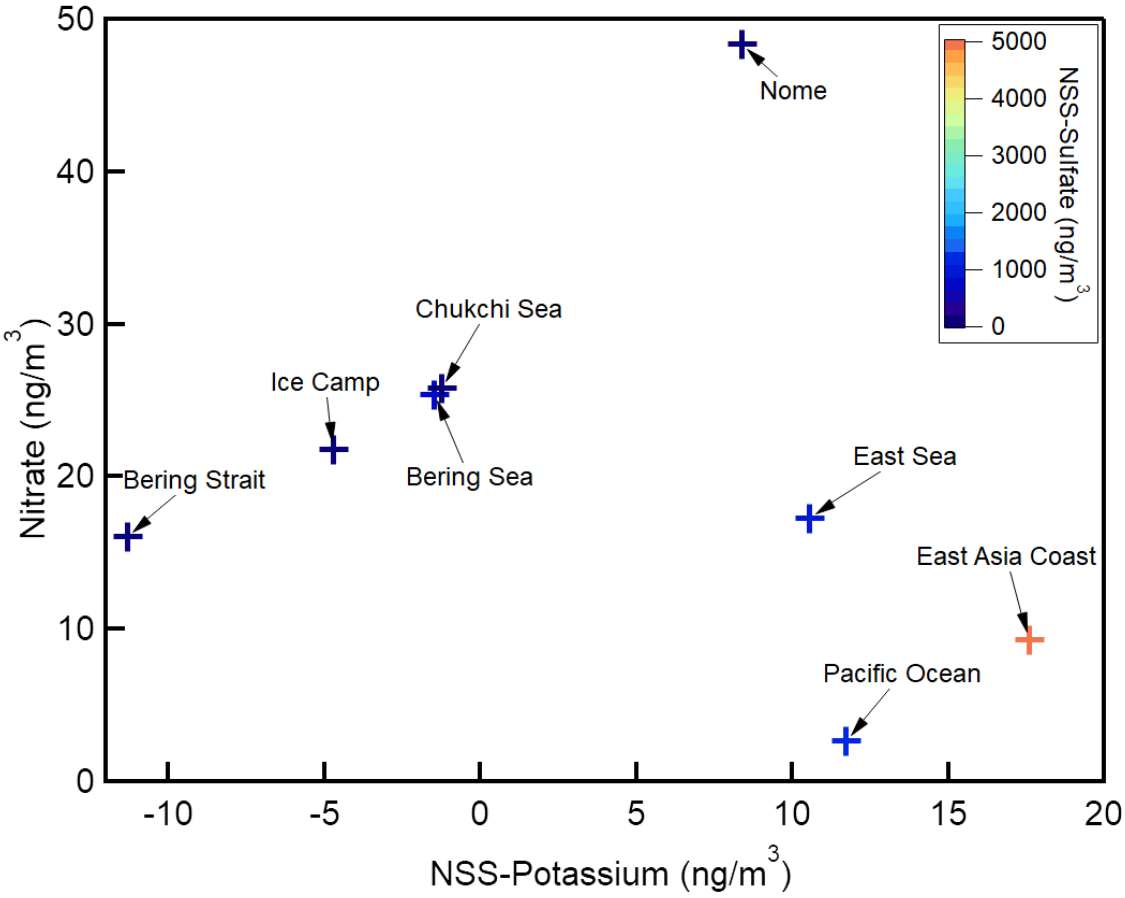

Figure 4.5 Particulate nitrate, potassium, and sulfate atmospheric concentrations.

Liquid fossil contributed 0 to 65% with an average of 22±23% to all samples. The two locations with the highest estimated fossil contributions were collected off the East Asia Coast (48%) and Ice Camp (65%). The sample taken off the East Asia Coast was expected to be high in fossil fuel contribution due to proximity to coastal marine traffic and terrestrial fossil fuel burning. The sample taken during the Ice Camp was also expected to be high in fossil fuel contribution, because the ship was attached to an ice floe during sampling. This meant that the winds often blew the smokestack towards the sampler. This was mostly mitigated by the wind-sectoring

system, as shown by low TC concentrations measured (0.22±0.05 µg C m^{-3}). However, the wind-sectoring system could not mitigate fossil exhaust from helicopter operations during the ice camp, and likely contributed to fossil contribution to the Ice Camp sample.

4.3.4 Marine biological influence

To further distinguish the marine from terrestrial biomass in the fresh biomass component, a multi-faceted approach, including ancillary in-situ measurements of biological productivity, was used to discuss the variation in contribution of marine biomass.

The highest contributions of fresh biomass were estimated for East Sea and Nome samples, 66±11% and 69±12%, respectively (Fig. 4.4). These samples also had the highest terrestrial influence according to back trajectory maps while chlorophyll-induced fluorescence (Fig. 5a) and active productivity (Fig. 5b) in these regions were low, which indicates a dominant terrestrial biomass source. Active productivity, and fluorescence also indicate high productivity in the Bering Strait sample, which contained an estimated 46±9% fresh biomass. This suggests that marine productivity was the major source to the fresh biomass in this sample. Interestingly, 60±12% of ambient aerosol obtained over the Chukchi Sea was estimated to be from fresh biomass. This was possibly due to some productivity that was observed in the marginal sea ice zone as shown in Fig. 4.6b.

In addition, MSA, a by-product of atmospheric dimethyl sulfide (DMS) oxidation, was highest in concentration in ambient aerosol collected over the Pacific Ocean and Bering Sea (Table A4.4), 110.3 and 137.5 ng m^{-3}, respectively. Fluorescence and productivity indicate active regions off the coast of Japan and near the Aleutian Islands. The high productivity in the Bering Strait indicates that the 48±9% estimated fresh biomass component originated from marine biomass. However, this was not reflected with elevated MSA concentrations possibly because the

sea surface temperatures (SSTs) declined considerably in the Bering Strait (Table A4.1). Lower MSA concentrations have been associated with cooler SSTs (Laing et al., 2013; Ye et al., 2015). In summary, marine biological productivity likely had the largest contribution to the fresh biomass component in remote and some coastal marine environments, such as the North Pacific, Bering Sea, Bering Strait, and Chukchi Sea. However, in coastal regions such as East Sea and Nome, a greater contribution from terrestrial combustion is likely.

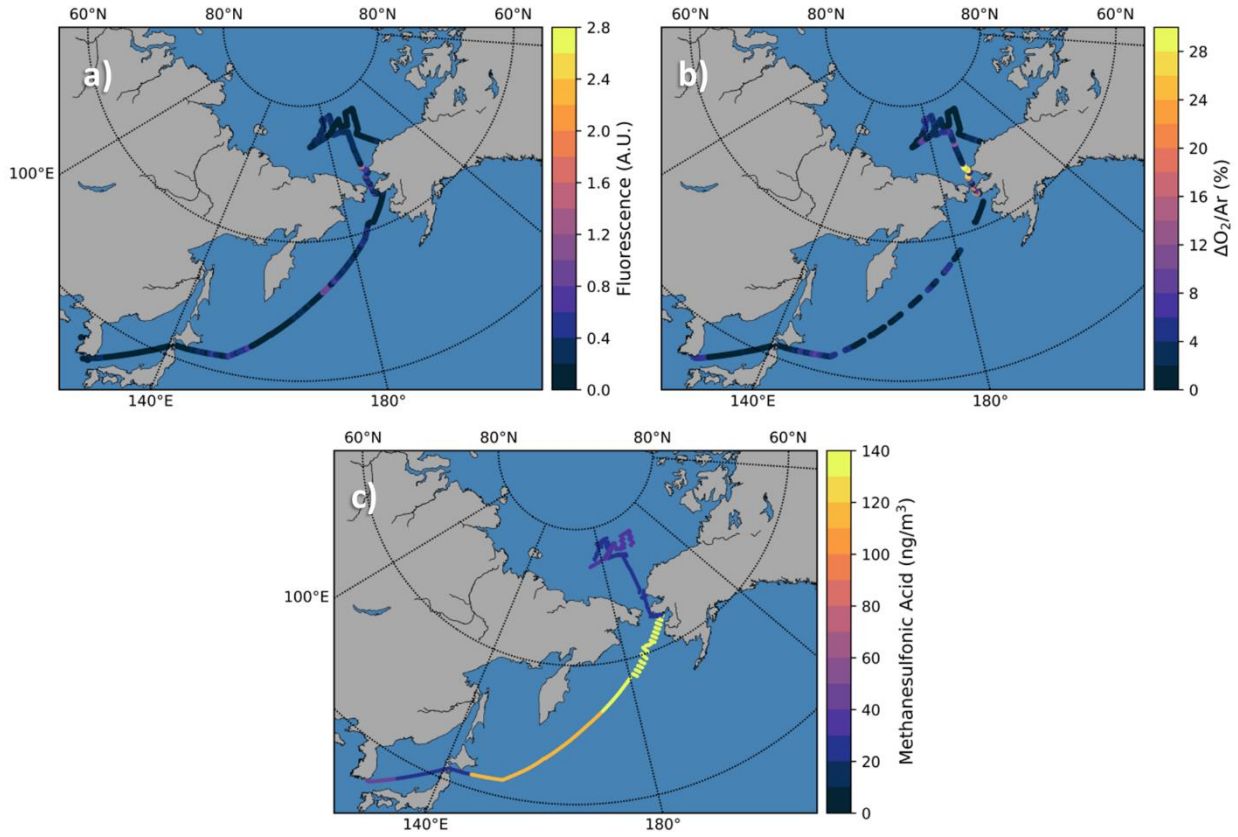

Figure 4.6. Measured indicators for active marine biological contribution to ambient OC aerosol. Surface fluorescence (a) was measured in situ. Net community productivity (b) is indicated by the ratio of the difference between photosynthetic and respiration dissolved O_2 to Argon ($\Delta O_2/Ar$). Methanesulfonic acid (MSA) (c) was measured in collected ambient aerosol.

4.4 Conclusions

In this study, ambient aerosols collected onboard the R/V ARAON from various coastal and remote marine regions were isotopically characterized ($\delta^{13}C$, $\Delta^{14}C$). Back trajectories along the ship route were calculated and the air mass origin within the boundary layer was characterized. Back trajectories originating from land varied significantly but averaged 13±15%. The highest terrestrial influences were observed at coastal regions, such as the East Sea, Nome, and Bering Strait. The lowest OC concentrations were observed over the Chukchi Sea (0.137 μg m^{-3}), and the highest over the East Asia Coast (1.47 μg m^{-3}). $\delta^{13}C$ of TC ranged from -28 to -23‰, while $\Delta^{14}C$ of TC ranged from -733 to -124‰. However, $\Delta^{14}C$ of OC was significantly higher compared to $\Delta^{14}C$ of TC (ranged from -626 to -99‰), but in general had lower $\Delta^{14}C$ values relative to atmospheric CO_2.

OC comprised of 88% to 96% of TC, therefore $\delta^{13}C$ values of TC were used to source apportion OC from three major sources with a dual-isotope, 3-source model: marine DOC, fossil carbon, and fresh biomass. Sources varied significantly across the regions of collection. DOC on average contributed 36±27% (avg±sd) and contributed most to OC collected over the Pacific Ocean (90±10%). This suggests that marine DOC significantly contributes to ambient aerosol in remote marine environments. OC collected over the Bering Sea and Strait are estimated to contain 49% and 44% RDOC respectively possibly due to exported riverine DOC from the Yukon delta and rivers from the Seward Peninsula. Liquid fossil contributed significantly to OC aerosol off the east Asia coast (48±2%), which was attributed to heavy marine traffic encountered. Fresh biomass contributed on average 43±22% (avg±sd) to OC and was highest for OC in the East Sea and Nome. Back trajectories also indicated that these samples had the highest terrestrial contributions, so they were likely sourced from terrestrial biomass combustion. Observed high active

productivity in the Bering Strait indicate that the 46% of the estimated fresh biomass contributions were sourced from marine productivity. Fresh biomass over the Pacific Ocean and Bering Sea, although not linked to high active productivity or chlorophyll-induced fluorescence, was linked to high MSA concentrations in OC (0.31 and 0.1 μg m^{-3} respectively).

4.5 References

Aiken, G. R., Spencer, R. G. M., Striegl, R. G., Schuster, P. F., & Raymond, P. A. (2014). Global Biogeochemical Cycles in the Yukon River basin. *Global Biogeochemical Cycles*, 525–537. https://doi.org/10.1002/2013GB004764.Received

Aller, J. Y., Radway, J. A. C., Kilthau, W. P., Bothe, D. W., Wilson, T. W., Vaillancourt, R. D., et al. (2017). Size-resolved characterization of the polysaccharidic and proteinaceous components of sea spray aerosol. *Atmospheric Environment*, *154*, 331–347. https://doi.org/10.1016/j.atmosenv.2017.01.053

Alpert, P. A., Kilthau, W. P., Bothe, D. W., Radway, J. A. C., Aller, J. Y., & Knopf, D. A. (2015). The influence of marine microbial activities on aerosol production: A laboratory mesocosm study. *Journal of Geophysical Research*, *120*(17), 8841–8860. https://doi.org/10.1002/2015JD023469

Barrett, T. E., & Sheesley, R. J. (2017). Year-round optical properties and source characterization of Arctic organic carbon aerosols on the North Slope Alaska. *Journal of Geophysical Research: Atmospheres*, *122*(17), 9319–9331. https://doi.org/10.1002/2016JD026194

Bates, T. S., Quinn, P. K., Coffman, D. J., Johnson, J. E., Upchurch, L., Saliba, G., et al. (2020). Variability in Marine Plankton Ecosystems Are Not Observed in Freshly Emitted Sea

Spray Aerosol Over the North Atlantic Ocean. *Geophysical Research Letters*, *47*(1). https://doi.org/10.1029/2019GL085938

Bauer, J. E., Druffel, E. R. M., Wolgast, D. M., Griffin, S., & Masiello, C. A. (1998). Distributions of dissolved organic and inorganic carbon and radiocarbon in the eastern North Pacific continental margin. *Deep-Sea Research Part II: Topical Studies in Oceanography*, *45*(4–5), 689–713. https://doi.org/10.1016/S0967-0645(97)00098-2

Beaupré, S. R., Kieber, D. J., Keene, W. C., Long, M. S., Maben, J. R., Lu, X., et al. (2019). Oceanic efflux of ancient marine dissolved organic carbon in primary marine aerosol. *Science Advances*, *5*(10), eaax6535. https://doi.org/10.1126/sciadv.aax6535

Benner, R., Benitez-Nelson, B., Kaiser, K., & Amon, R. M. W. (2004). Export of young terrigenous dissolved organic carbon from rivers to the Arctic Ocean. *Geophysical Research Letters*, *31*(5), 10–13. https://doi.org/10.1029/2003gl019251

Blanchard, D. C. (1964). Sea-to-Air Transport of Surface Active Material. *Science*, *146*(3642), 396–397.

Brown, K. A., McLaughlin, F., Tortell, P. D., Varela, D. E., Yamamoto-Kawai, M., Hunt, B., & Francois, R. (2014). Determination of particulate organic carbon sources to the surface mixed layer of the Canada Basin, Arctic Ocean. *Journal of Geophysical Research: Oceans*, *119*(2), 1084–1102. https://doi.org/10.1002/2013JC009197

Burkart, J., Hodshire, A. L., Mungall, E. L., Pierce, J. R., Collins, D. B., Ladino, L. A., et al. (2017). Organic Condensation and Particle Growth to CCN Sizes in the Summertime Marine Arctic Is Driven by Materials More Semivolatile Than at Continental Sites. *Geophysical Research Letters*, *44*(20), 10,725-10,734.

https://doi.org/10.1002/2017GL075671

Burkart, J., Willis, M. D., Bozem, H., Thomas, J. L., Law, K., Hoor, P., et al. (2017). Summertime observations of elevated levels of ultrafine particles in the high Arctic marine boundary layer. *Atmospheric Chemistry and Physics*, *17*(8), 5515–5535. https://doi.org/10.5194/acp-17-5515-2017

Cavalli, F., Facchini, M. C., Decesari, S., Mircea, M., Emblico, L., Fuzzi, S., et al. (2004). Advances in characterization of size-resolved organic matter in marine aerosol over the North Atlantic. *Journal of Geophysical Research*, *109*(D24), D24215. https://doi.org/10.1029/2004JD005137

Ceburnis, D., Garbaras, A., Szidat, S., Rinaldi, M., Fahrni, S., Perron, N., et al. (2011). Quantification of the carbonaceous matter origin in submicron marine aerosol by 13C and 14C isotope analysis. *Atmospheric Chemistry and Physics*, *11*(16), 8593–8606. https://doi.org/10.5194/acp-11-8593-2011

Ceburnis, D., O'Dowd, C. D., Jennings, G. S., Facchini, M. C., Emblico, L., Decesari, S., et al. (2008). Marine aerosol chemistry gradients: Elucidating primary and secondary processes and fluxes. *Geophysical Research Letters*, *35*(7), 1–5. https://doi.org/10.1029/2008GL033462

Choi, J. H., Jang, E., Yoon, Y. J., Park, J. Y., Kim, T. -W., Becagli, S., et al. (2019). Influence of Biogenic Organics on the Chemical Composition of Arctic Aerosols. *Global Biogeochemical Cycles*, *33*(10), 1238–1250. https://doi.org/10.1029/2019GB006226

Collins, D. B., Burkart, J., Chang, R. Y.-W., Lizotte, M., Boivin-Rioux, A., Blais, M., et al. (2017). Frequent Ultrafine Particle Formation and Growth in the Canadian Arctic Marine

Environment. *Atmospheric Chemistry and Physics*, *17*(21), 13119-13138. https://doi.org/10.5194/acp-17-13119-2017

Dall'Osto, M., Healy, R. M., Wenger, J. C., O'Dowd, C., Ovadnevaite, J., Ceburnis, D., et al. (2017). Distinct high molecular weight organic compound (HMW-OC) types in aerosol particles collected at a coastal urban site. *Atmospheric Environment*, *171*(September), 118–125. https://doi.org/10.1016/j.atmosenv.2017.10.007

Druffel, E., Griffin, S., Glynn, C. S., Benner, R., & Walker, B. D. (2017). Radiocarbon in dissolved organic and inorganic carbon of the Arctic Ocean. *Geophysical Research Letters*, *44*(5), 2369–2376. https://doi.org/10.1002/2016GL072138

Druffel, E. R. M., Williams, P. M., Bauer, J. E., & Ertel, J. R. (1992). Cycling of dissolved and particulate organic matter in the open ocean. *Journal of Geophysical Research*, *97*(C10), 15639. https://doi.org/10.1029/92JC01511

Druffel, E. R. M., Bauer, J. E., Williams, P. M., Griffin, S., & Wolgast, D. (1996). Seasonal variability of particulate organic radiocarbon in the northeast Pacific Ocean. *Journal of Geophysical Research: Oceans*, *101*(C9), 20543–20552. https://doi.org/10.1029/96JC01850

Druffel, E. R. M., Griffin, S., Wang, N., & Walker, B. D. (2018). Temporal Variability of Dissolved Organic Radiocarbon in the Deep North Pacific Ocean. *Radiocarbon*, *60*(4), 1115–1123. https://doi.org/10.1017/RDC.2018.39

Druffel, E. R. M., Griffin, S., Wang, N., Garcia, N. G., McNichol, A. P., Key, R. M., & Walker, B. D. (2019). Dissolved Organic Radiocarbon in the Central Pacific Ocean. *Geophysical Research Letters*, *46*(10), 5396–5403. https://doi.org/10.1029/2019GL083149

Earle, M. E., Liu, P. S. K., Strapp, J. W., Zelenyuk, A., Imre, D., McFarquhar, G. M., et al. (2011). Factors influencing the microphysics and radiative properties of liquid-dominated Arctic clouds: Insight from observations of aerosol and clouds during ISDAC. *Journal of Geophysical Research*, *116*(21), D00T09. https://doi.org/10.1029/2011JD015887

Fabre, C., Sauvage, S., Probst, J. L., & Sánchez-Pérez, J. M. (2020). Global-scale daily riverine DOC fluxes from lands to the oceans with a generic model. *Global and Planetary Change*, *194*(December 2019), 103294. https://doi.org/10.1016/j.gloplacha.2020.103294

Fuzzi, S., Baltensperger, U., Carslaw, K., Decesari, S., Denier Van Der Gon, H., Facchini, M. C., et al. (2015). Particulate matter, air quality and climate: Lessons learned and future needs. *Atmospheric Chemistry and Physics*, *15*(14), 8217–8299. https://doi.org/10.5194/acp-15-8217-2015

Gantt, B., Xu, J., Meskhidze, N., Zhang, Y., Nenes, A., Ghan, S. J., et al. (2012). Global distribution and climate forcing of marine organic aerosol-Part 2: Effects on cloud properties and radiative forcing. *Atmospheric Chemistry and Physics*, *12*(14), 6555–6563. https://doi.org/10.5194/acp-12-6555-2012

Gantt, Brett, Meskhidze, N., & Kamykowski, D. (2009). A new physically-based quantification of marine isoprene and primary organic aerosol emissions. *Atmospheric Chemistry and Physics*, *9*(14), 4915–4927. https://doi.org/10.5194/acp-9-4915-2009

Graven, H. D. (2015). Impact of fossil fuel emissions on atmospheric radiocarbon and various applications of radiocarbon over this century. *Proceedings of the National Academy of Sciences*, *112*(31), 9542–9545. https://doi.org/10.1073/pnas.1504467112

Griffith, D. R., McNichol, A. P., Xu, L., McLaughlin, F. A., MacDonald, R. W., Brown, K. A.,

& Eglinton, T. I. (2012). Carbon dynamics in the western Arctic Ocean: Insights from full-depth carbon isotope profiles of DIC, DOC, and POC. *Biogeosciences*, *9*(3), 1217–1224. https://doi.org/10.5194/bg-9-1217-2012

Guo, L., & Macdonald, R. W. (2006). Source and transport of terrigenous organic matter in the upper Yukon River: Evidence from isotope (δ13C, Δ 14C, and δ15N) composition of dissolved, colloidal, and particulate phases. *Global Biogeochemical Cycles*, *20*(2). https://doi.org/10.1029/2005GB002593

Guo, L., Tanaka, T., Wang, D., Tanaka, N., & Murata, A. (2004). Distributions, speciation and stable isotope composition of organic matter in the southeastern Bering Sea. *Marine Chemistry*, *91*(1–4), 211–226. https://doi.org/10.1016/j.marchem.2004.07.002

Hodzic, A., Kasibhatla, P. S., Jo, D. S., Cappa, C. D., Jimenez, J. L., Madronich, S., & Park, R. J. (2016). Rethinking the global secondary organic aerosol (SOA) budget: stronger production, faster removal, shorter lifetime. *Atmospheric Chemistry and Physics*, *16*(12), 7917–7941. https://doi.org/10.5194/acp-16-7917-2016

Hoffman, E. J., & Duce, R. A. (1974). The organic carbon content of marine aerosols collected on Bermuda. *Journal of Geophysical Research*, *79*(30), 4474–4477. https://doi.org/10.1029/jc079i030p04474

Hoffman, E. J., & Duce, R. A. (1976). Factors influencing the organic carbon content of marine aerosols: A laboratory study. *Journal of Geophysical Research*, *81*(21), 3667–3670. https://doi.org/10.1029/JC081i021p03667

Hyun Kwak, J., Han, E., Hwang, J., Kim, Y. I., Lee, C. Il, & Kang, C.-K. (2017). Flux and stable C and N isotope composition of sinking particles in the Ulleung Basin of the East/Japan

Sea. *Deep Sea Research Part II: Topical Studies in Oceanography*, *143*(April), 62–72. https://doi.org/10.1016/j.dsr2.2017.03.014

Ito, A., & Kawamiya, M. (2010). Potential impact of ocean ecosystem changes due to global warming on marine organic carbon aerosols. *Global Biogeochemical Cycles*, *24*(1), n/a-n/a. https://doi.org/10.1029/2009GB003559

Jimenez, J. L., Canagaratna, M. R., Donahue, N. M., Prevot, A. S. H., Zhang, Q., Kroll, J. H., et al. (2009). Evolution of organic aerosols in the atmosphere. *Science*, *326*(February), 1526–1529.

Kieber, D. J., Keene, W. C., Frossard, A. A., Long, M. S., Maben, J. R., Russell, L. M., et al. (2016). Refractory Dissolved Organic Carbon. *Geophysical Reserach Letters*, 2765–2772. https://doi.org/10.1002/2016GL068273.Received

Kim, M., Hwang, J., Rho, T., Lee, T., Kang, D.-J., Chang, K.-I., et al. (2017). Biogeochemical properties of sinking particles in the southwestern part of the East Sea (Japan Sea). *Journal of Marine Systems*, *167*, 33–42. https://doi.org/10.1016/j.jmarsys.2016.11.001

Kim, T. H., Kim, G., Lee, S. A., & Dittmar, T. (2015). Extraordinary slow degradation of dissolved organic carbon (DOC) in a cold marginal sea. *Scientific Reports*, *5*, 1–6. https://doi.org/10.1038/srep13808

Kohn, M. J. (2010). Carbon isotope compositions of terrestrial C3 plants as indicators of (paleo)ecology and (paleo)climate. *Proceedings of the National Academy of Sciences of the United States of America*, *107*(46), 19691–19695. https://doi.org/10.1073/pnas.1004933107

Laing, J. R., Hopke, P. K., Hopke, E. F., Husain, L., Dutkiewicz, V. A., Paatero, J., & Viisanen, Y. (2013). Long-term trends of biogenic sulfur aerosol and its relationship with sea surface temperature in Arctic Finland. *Journal of Geophysical Research Atmospheres*, *118*(20), 11,770-11,776. https://doi.org/10.1002/2013JD020384

Levin, I., Naegler, T., Kromer, B., Diehl, M., Francey, R., Gomez-Pelaez, A., et al. (2010). Observations and modelling of the global distribution and long-term trend of atmospheric 14CO2. *Tellus B: Chemical and Physical Meteorology*, *62*(1), 26–46. https://doi.org/10.1111/j.1600-0889.2009.00446.x

Li, M., Peng, C., Zhou, X., Yang, Y., Guo, Y., Shi, G., & Zhu, Q. (2019). Modeling Global Riverine DOC Flux Dynamics From 1951 to 2015. *Journal of Advances in Modeling Earth Systems*, *11*(2), 514–530. https://doi.org/10.1029/2018MS001363

Lin, F., Chen, M., Tong, J., Cao, J., Qiu, Y., & Zheng, M. (2014). Carbon and nitrogen isotopic composition of particulate organic matter and its biogeochemical implication in the Bering Sea. *Acta Oceanologica Sinica*, *33*(12), 40–47. https://doi.org/10.1007/s13131-014-0570-y

Mackey, K. R. M., Stragier, S., Robledo, L., Cat, L. A., Xu, X., Capps, S., et al. (2021). Seasonal variation of aerosol composition in Orange County, Southern California. *Atmospheric Environment*, *244*(January 2020), 117795. https://doi.org/10.1016/j.atmosenv.2020.117795

Mann, P. J., Eglinton, T. I., McIntyre, C. P., Zimov, N., Davydova, A., Vonk, J. E., et al. (2015). Utilization of ancient permafrost carbon in headwaters of Arctic fluvial networks. *Nature Communications*, *6*. https://doi.org/10.1038/ncomms8856

Meskhidze, N., Xu, J., Gantt, B., Zhang, Y., Nenes, A., Ghan, S. J., et al. (2011). Global distribution and climate forcing of marine organic aerosol: 1. Model improvements and evaluation. *Atmospheric Chemistry and Physics*, *11*(22), 11689–11705. https://doi.org/10.5194/acp-11-11689-2011

Mouteva, G. O., Fahrni, S. M., Santos, G. M., Randerson, J. T., Zhang, Y.-L., Szidat, S., & Czimczik, C. I. (2015). Accuracy and precision of ^{14}C-based source apportionment of organic and elemental carbon in aerosols using the Swiss_4S protocol. *Atmospheric Measurement Techniques*, *8*(9), 3729–3743. https://doi.org/10.5194/amt-8-3729-2015

Myriokefalitakis, S., Vignati, E., Tsigaridis, K., Papadimas, C., Sciare, J., Mihalopoulos, N., et al. (2010). Global Modeling of the Oceanic Source of Organic Aerosols. *Advances in Meteorology*, *2010*, 1–16. https://doi.org/10.1155/2010/939171

Nault, B. A., Campuzano-Jost, P., Day, D. A., Schroder, J. C., Anderson, B., Beyersdorf, A. J., et al. (2018). Secondary organic aerosol production from local emissions dominates the organic aerosol budget over Seoul, South Korea, during KORUS-AQ. *Atmospheric Chemistry and Physics*, *18*(24), 17769–17800. https://doi.org/10.5194/acp-18-17769-2018

O'Dowd, C. D., & de Leeuw, G. (2007). Marine aerosol production: a review of the current knowledge. *Philosophical Transactions of the Royal Society A: Mathematical, Physical and Engineering Sciences*, *365*(1856), 1753–1774. https://doi.org/10.1098/rsta.2007.2043

O'Dowd, C. D., Smith, M. H., Consterdine, I. E., & Lowe, J. A. (1997). Marine aerosol, sea-salt, and the marine sulphur cycle: A short review. *Atmospheric Environment*, *31*(1), 73–80. https://doi.org/10.1016/S1352-2310(96)00106-9

O'Dowd, C. D., Facchini, M. C., Cavalli, F., Ceburnis, D., Mircea, M., Decesari, S., et al. (2004). Biogenically driven organic contribution to marine aerosol. *Nature*, *431*(7009), 676–680. https://doi.org/10.1038/nature02959

Ovadnevaite, J., Ceburnis, D., Martucci, G., Bialek, J., Monahan, C., Rinaldi, M., et al. (2011). Primary marine organic aerosol: A dichotomy of low hygroscopicity and high CCN activity. *Geophysical Research Letters*, *38*(21), 1–5. https://doi.org/10.1029/2011GL048869

Park, K., Kim, I., Choi, J. O., Lee, Y., Jung, J., Ha, S. Y., et al. (2019). Unexpectedly high dimethyl sulfide concentration in high-latitude Arctic sea ice melt ponds. *Environmental Science: Processes and Impacts*, *21*(10), 1642–1649. https://doi.org/10.1039/c9em00195f

Phillips, D. L., & Gregg, J. W. (2001). Uncertainty in source partitioning using stable isotopes. *Oecologia*, *127*(2), 171–179. https://doi.org/10.1007/s004420000578

Quinn, P. K., Bates, T. S., Schulz, K. S., Coffman, D. J., Frossard, A. A., Russell, L. M., et al. (2014). Contribution of sea surface carbon pool to organic matter enrichment in sea spray aerosol. *Nature Geoscience*, *7*(3), 228–232. https://doi.org/10.1038/ngeo2092

Raymond, P. A., & Bauer, J. E. (2001). Use of 14 C and 13 C natural abundances for evaluating riverine, estuarine, and coastal DOC and POC sources and cycling: a review and synthesis. *Organic Geochemistry*, *32*(4), 469–485. https://doi.org/10.1016/S0146-6380(00)00190-X

Raymond, P. A., & Spencer, R. G. M. (2015). Riverine DOM. *Biogeochemistry of Marine Dissolved Organic Matter: Second Edition*, 509–533. https://doi.org/10.1016/B978-0-12-405940-5.00011-X

Rodríguez, B. T., Huang, L., Santos, G. M., Zhang, W., Vetro, V., Xu, X., et al. (2020). Seasonal cycle of isotope-based source apportionment of elemental carbon in airborne particulate matter and snow at Alert, Canada. *Journal of Geophysical Research: Atmospheres*, 1–15. https://doi.org/10.1029/2020jd033125

Russell, L. M., Hawkins, L. N., Frossard, A. A., Quinn, P. K., & Bates, T. S. (2010). Carbohydrate-like composition of submicron atmospheric particles and their production from ocean bubble bursting. *Proceedings of the National Academy of Sciences of the United States of America*, *107*(15), 6652–6657. https://doi.org/10.1073/pnas.0908905107

Santos, G. M., Southon, J. R., Griffin, S., Beaupre, S. R., & Druffel, E. R. M. (2007). Ultra small-mass AMS 14C sample preparation and analyses at KCCAMS/UCI Facility. *Nuclear Instruments and Methods in Physics Research Section B: Beam Interactions with Materials and Atoms*, *259*(1), 293–302. https://doi.org/10.1016/j.nimb.2007.01.172

Spracklen, D. V., Arnold, S. R., Sciare, J., Carslaw, K. S., & Pio, C. (2008). Globally significant oceanic source of organic carbon aerosol. *Geophysical Research Letters*, *35*(12). https://doi.org/10.1029/2008GL033359

Struthers, H., Ekman, A. M. L., Glantz, P., Iversen, T., Kirkevåg, A., Mårtensson, E. M., et al. (2011). The effect of sea ice loss on sea salt aerosol concentrations and the radiative balance in the Arctic. *Atmospheric Chemistry and Physics*, *11*(7), 3459–3477. https://doi.org/10.5194/acp-11-3459-2011

Tanaka, T., Otosaka, S., Wakita, M., Amano, H., & Togawa, O. (2010). Preliminary result of dissolved organic radiocarbon in the western North Pacific Ocean. *Nuclear Instruments and Methods in Physics Research, Section B: Beam Interactions with Materials and*

Atoms, *268*(7–8), 1219–1221. https://doi.org/10.1016/j.nimb.2009.10.137

Walker, B. D., & Xu, X. (2019). An improved method for the sealed-tube zinc graphitization of microgram carbon samples and 14C AMS measurement. *Nuclear Instruments and Methods in Physics Research Section B: Beam Interactions with Materials and Atoms*, *438*, 58–65. https://doi.org/10.1016/j.nimb.2018.08.004

White, J. W. C., Vaughn, B. H., & Michel, S. E. (2015). Stable Isotopic Composition of Atmospheric Carbon Dioxide (13C and 18O) from the NOAA ESRL Carbon Cycle Cooperative Global Air Sampling Network, 1990-2014, Version: 2015-10-26. University of Colorado, Institute of Arctic and Alpine Research (INSTAAR). Retrieved from ftp://aftp.cmdl.noaa.gov/data/trace_gases/co2c13/flask/

Widory, D. (2006). Combustibles, fuels and their combustion products: A view through carbon isotopes. *Combustion Theory and Modelling*, *10*(5), 831–841. https://doi.org/10.1080/13647830600720264

Wild, B., Andersson, A., Bröder, L., Vonk, J., Hugelius, G., McClelland, J. W., et al. (2019). Rivers across the Siberian Arctic unearth the patterns of carbon release from thawing permafrost. *Proceedings of the National Academy of Sciences of the United States of America*, *116*(21), 10280–10285. https://doi.org/10.1073/pnas.1811797116

Willis, M. D., Burkart, J., Thomas, J. L., Köllner, F., Schneider, J., Bozem, H., et al. (2016). Growth of nucleation mode particles in the summertime Arctic: a case study. *Atmospheric Chemistry and Physics*, *16*(12), 7663–7679. https://doi.org/10.5194/acp-16-7663-2016

Willis, M. D., Köllner, F., Burkart, J., Bozem, H., Thomas, J. L., Schneider, J., et al. (2017).

Evidence for marine biogenic influence on summertime Arctic aerosol. *Geophysical Research Letters*, *44*(12), 6460–6470. https://doi.org/10.1002/2017GL073359

Willis, M. D., Leaitch, W. R., & Abbatt, J. P. D. (2018). Processes Controlling the Composition and Abundance of Arctic Aerosol. *Reviews of Geophysics*, *56*(4), 621–671. https://doi.org/10.1029/2018RG000602

Ye, P., Xie, Z., Yu, J., & Kang, H. (2015). Spatial distribution of methanesulphonic acid in the Arctic aerosol collected during the Chinese Arctic Research Expedition. *Atmosphere*, *6*(5), 699–712. https://doi.org/10.3390/atmos6050699

Yu, M., Guo, Z., Wang, X., Eglinton, T. I., Yuan, Z., Xing, L., et al. (2018). Sources and radiocarbon ages of aerosol organic carbon along the east coast of China and implications for atmospheric fossil carbon contributions to China marginal seas. *Science of The Total Environment*, *619–620*(238), 957–965. https://doi.org/10.1016/j.scitotenv.2017.11.201

Zhang, R., Chen, M., Guo, L., Gao, Z., Ma, Q., Cao, J., et al. (2012). Variations in the isotopic composition of particulate organic carbon and their relation with carbon dynamics in the western Arctic Ocean. *Deep Sea Research Part II: Topical Studies in Oceanography*, *81–84*, 72–78. https://doi.org/10.1016/j.dsr2.2011.05.005

Zhang, Y. L., Perron, N., Ciobanu, V. G., Zotter, P., Minguillón, M. C., Wacker, L., et al. (2012). On the isolation of OC and EC and the optimal strategy of radiocarbon-based source apportionment of carbonaceous aerosols. *Atmospheric Chemistry and Physics*, *12*(22), 10841–10856. https://doi.org/10.5194/acp-12-10841-2012

Zhu, J., Penner, J. E., Yu, F., Sillman, S., Andreae, M. O., & Coe, H. (2019). Decrease in radiative forcing by organic aerosol nucleation, climate, and land use change. *Nature*

Communications, *10*(1), 423. https://doi.org/10.1038/s41467-019-08407-7

Zigah, P. K., McNichol, A. P., Xu, L., Johnson, C., Santinelli, C., Karl, D. M., & Repeta, D. J. (2017). Allochthonous sources and dynamic cycling of ocean dissolved organic carbon revealed by carbon isotopes. *Geophysical Research Letters*, *44*(5), 2407–2415. https://doi.org/10.1002/2016GL071348

4.6 Appendix

Table A4.1 Average (±1σ) ambient parameters

Sample	Location	Wind Speed	Air Temperature	Sea Surface T	Sea Surface Fluorescence	$\Delta O_2/Ar$
		$m \cdot s^{-1}$	°C			%

1	Korea/East Sea	5.2±3.0	n.m	24.9±2.2	0.15±0.09	3.3±2.6
2	East Sea	4.2±1.9	23.4±2.5	21.6±4.2	0.12±0.09	1.9±1.9
3	Pacific Ocean	8.7±2.0	16.6±4.0	12.7±2.4	0.32±0.25	2.9±2.1
4	Bering Sea	6.6±3.6	11.2±0.9	11.2±1.2	0.26±0.14	1.8±2.1
5	Nome	4.6±2.5	16.1±1.9	15.7±0.2	0.28±0.02	n.m
6	Bering Strait	7.5±4.4	6.6±3.4	8.7±2.3	0.43±0.34	13.7±13.4
7	Ice Camp	9.8±3.0	-0.7±0.8	-0.4±2.2	0.29±0.06	4.5±14.3
8	Chukchi Sea	3.8±2.0	-0.3±1.2	0.03±0.4	0.15±0.06	1.7±2.0

Table A4.2 Major seawater inorganic ions

Sample #	Sample Region	Cl^-	Na^+	Mg^{2+}	SO_4^{2-}	Ca^{2+}	K^+
				ng/m^3			
1	East Asia Coast	0.8	123.7	10.8	5020.2	8.9	22.3
2	East Sea	0.4	55.3	4.3	951.8	4.8	12.6
3	Pacific Ocean	1.5	168.9	14.6	1175.3	18.5	18.1
4	Bering Sea	22.8	349.8	34.5	781.2	9.7	11.8
5	Nome	1280.9	809.3	75.6	384.3	81.0	39.1
6	Bering Strait	2387.5	1440.3	134.9	384.3	34.1	43.4
7	Ice Camp	1113.6	671.6	66.7	238.6	35.0	20.8
8	Chukchi Sea	84.5	129.7	11.7	99.4	19.7	3.7

Table A4.3 Trace inorganic ions

Sample #	Sample Region	NO_3^-	NO_2^-	NH_4^+	F^-	Br^-	PO_4^{3-}
				ng/m^3			
1	East Asia Coast	9.3	11.4	1222.9	BDL	0.1	BDL
2	East Sea	17.3	4.8	386.6	BDL	0.3	BDL
3	Pacific Ocean	2.7	BDL	217.7	0.6	0.0	BDL

4	Bering Sea	25.4	1.3	30.4	BDL	BDL	BDL
5	Nome	48.4	2.9	BDL	BDL	0.8	BDL
6	Bering Strait	16.1	13.0	BDL	BDL	3.3	BDL
7	Ice Camp	21.8	BDL	BDL	0.4	0.4	49.3
8	Chukchi Sea	25.8	45.8	BDL	0.4	BDL	60.8

Table A4.4 Small organic acids

Sample #	Sample Region	Acetate	Formate	Malate	Oxalate	MSA
				ng/m^3		
1	East Asia Coast	1.6	5.3	49.1	20.2	46.6
2	East Sea	8.5	6.0	45.8	25.5	24.1
3	Pacific Ocean	BDL	BDL	1.2	BDL	110.3
4	Bering Sea	2.0	2.0	11.3	15.0	137.5
5	Nome	2.5	BDL	18.3	1.5	21.0
6	Bering Strait	0.4	1.8	6.5	11.0	26.6
7	Ice Camp	5.1	BDL	5.0	6.7	20.4
8	Chukchi Sea	27.5	1.1	5.7	BDL	33.8

Appendix 4A. Sunset trapping protocol

Created by: Gergana Mouteva

June, 2012

Updated by: Blanca Rodriguez January, 2019

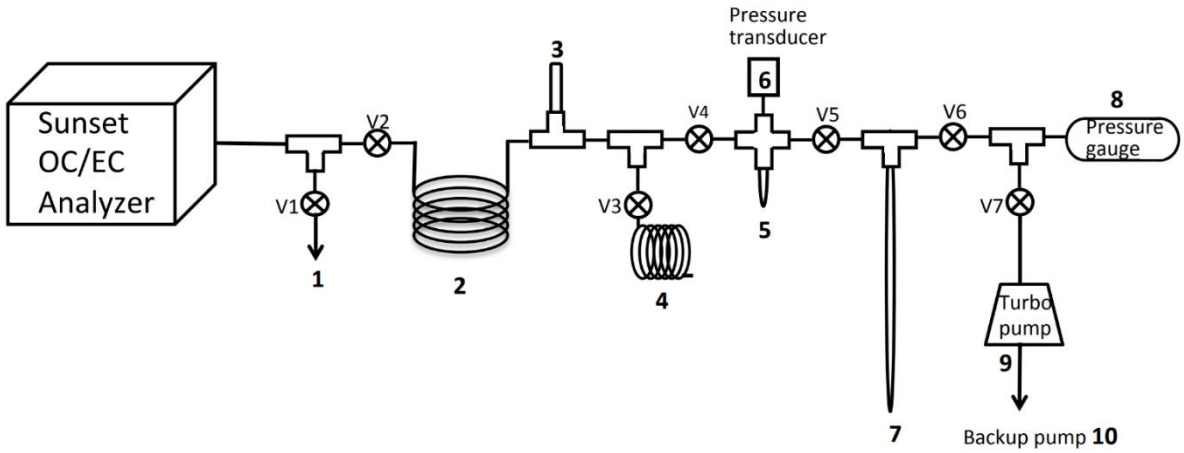

Materials:

- 2 1L stainless steel dewar flask
- Small yellow dewar
- Medium blue dewar
- 2 large adjustable stands
- 1 small adjustable stand
- ~2 inch tall block
- Tin mixing stick
- Liquid nitrogen
- Torch (gas/oxygen)
- Small forceps
- Sodium flare glasses
- Lighter or spark lighter
- Small graphitization vials (already loaded w/ reagents and prebaked - see details at appendix).

- Optional: 6 mm pyrex tube (empty) [at least 6” in length]
- Kimwipes
- Duster
- MilliQ water

Preparation:

Before starting clean out oven by clicking Actions → clean oven on the software. Running a blank through the trapping procedure is highly recommended before trapping real samples/standards. Prior to starting a procedure for trapping on the Sunset software make sure of the following:

- 1L dewar is full of liquid nitrogen (at least ½ full)
- Water trap is ready on other 1L dewar
- Vacuum line is open up to V2 (V4-V7 should be open), toggle V4-V7 valves before starting (NEVER TOGGLE V1, V2, OR V3, as they are open to room) AND Pirani gauge (8) reads 3e-4 or less
- Pressure transducer reading is at base level and stable (avoid touching the cable covered in aluminum foil as it will cause the reading to shift)
- V1 is open (it’s an exhaust (1)), V2 and V3 are closed
- File name, method, analyst, and filter size (1.00 for standards and blanks; 1.5 for samples) are filled out on the Sunset software
- File location is correct (all raw data should be written in C:/SunsetOCEC/rawdata/yyyy/mm/yyyymmdd.txt)
- Sunset is ready (front oven T < 75ºC, back oven T > 860ºC, PSIG ~0.14)
- Sample is inside the Sunset

Making a water trap:

In 1L dewar fill ¼ with fresh ethanol. Slowly add ground dry ice until bubbling stops. Keep adding dry ice until water trap has the consistency of a 7-Eleven slurpee. Mix with tin stick. To maintain, add dry ice once the consistency becomes too watery. Avoid putting in too much dry ice as it will over-thicken the mixture and put unnecessary strain on the stainless steel trap (2) when adding/removing water trap. Dewar should be ½ to ¾ full, if not, add more EtOh/dry ice.

Zeroing Sunset NDIR:

The Sunset NDIR should be zeroed out at the beginning of the day. To do this, start a temperature protocol. The instrument will first purge offline, then purge online before starting the protocol. After purging online, cancel the run. Extend the window with instrument parameters downward and click on "Zero NDIR". It takes about a minute or so.

Auto-zeroing flows:

The flowrates should also be zeroed at the beginning of the day too. Go to Actions → Auto-zero flows to do so.

Cleaning Filters:

To run blanks or standards, 1.5 cm^2 punches should be cleaned (pre-baked) in the Sunset before running them with a high-temperature protocol. You may do so by placing up to 6 (1.5 cm^2) quartz fiber filter punches on a flat quartz spoon and in the Sunset sample inlet. Select the "hero-clean.par" parameter file and start the temperature protocol. Run the protocol for at least 4 minutes or until CO_2 reading is zero.

OC Trapping Procedure:

All OC trapping should use the parameter file called: "OCCApture_Bern4s_475LONG_He4_650_gai_120s_rightTemps.par"

Trapping

Double check that all preparations are done. Start procedure by clicking "Start" on Sunset software. Software will first purge offline then online. Once purging online, submerge the trap with liquid nitrogen by placing the 1L dewar under it supported by a large adjustable stand. Close V4.

Once analyzing mode begins close V1. Wait for PSIG to reach at least 1 then open V2. PSIG will decrease to ~-8.7 and slowly rise, this is because the liquid nitrogen (LN) under vacuum con-

denses the output of the sunset and takes about 2 minutes to build positive pressure. Once PSIG ~1, open V3 to allow the output from the Sunset to go to exhaust. If you do not wait until the pressure is at least 1 you run the risk of sucking in atmospheric air-CO_2 and -H_2O into the trap (DO NOT DO THIS). PSIG should decline to ~0.4 afterward.

If not done already, put in a new small graphitization vial or 6 mm pyrex tube (7) by first closing V5 and V6 before removing old 6 mm tube (glass waste is under the bench) and replacing it with a new one. Open V6 slowly and evacuate tube. Once evacuated (Pirani gauge should read 3e-4 or less) open V5 and toggle both V5 and V6.

If you had opted to place the 6 mm pyrex tube (7) rather than a small graphitization vial, you can pre-bake the vial by using the torch set for sealing pyrex. Open the vial access to pump by opening V6 and V7, then proceed on "baking" the vial by moving the flame up and down a couple of times when this volume is being evacuated. Once the reading at the gauge reach baseline again, the vial should be ready to receive the CO_2 sample for storage.

Once the 475ºC step ends there is a 60 second step before flows switch to helium. Once either CO_2 reads 0 or at least 20 seconds before the switch over to helium, close V3. Wait until PSIG reaches 1. Close V2 and open V1 immediately.

Evacuating overpressurized oxygen in the trap (OC and EC)

The overpressurized oxygen in the trap will then be evacuated. Close V7 and open V4 to expand the oxygen up to V7. Mentally note down the transducer pressure max value (~300). Close V4 and open V7 slowly to evacuate the line from V4 onward. Once Pirani pressure gauge reads 5e-3 or below, close V7 and open V4 again. Repeat these steps of closing V7, opening V4, closing V4, opening V7 until the transducer pressure does not reach maximum value. **When opening**

any valve at this step, make sure the pump does not have direct access to the trap as it may break the turbo pump.

Once transducer does not reach maximum value, close V7 and open V4. You may **VERY SLOWLY** open V7 slightly (quarter turn max) and watch the turbo pump speed decline. Close V7 once the speed goes below 1400 Hz. Allow for pump to build speed up to 1500 Hz and open V7 slightly again. Repeat this until pump speed stops declining. Then you may open V7 completely and wait for vacuum to be restored (3e-4 or less). Toggle V4 and V7 valves.

Thaw CO_2 and move to measured volume (OC and EC)

Once vacuum is established again close V4 and switch out LN trap with water trap and wait about 1 minute. Close V5 and open V4. Toggle V4. Place small yellow dewar full of LN under the measured volume (5). This dewar should be supported by the second large adjustable stand and the block. Make sure the measured volume glass nub bottom tip is submerged in the LN and the LN is constantly being refilled to the brim. Wait at least 2 minutes, the pressure transducer reading should go down to or close to base value. Close V4 open V5 to pump away non-condensables. Once vacuum is established, toggle V5 and wait for vacuum again. Write down the base value for the pressure transducer. Close V5 and remove yellow dewar to allow frozen CO_2 to expand. Wait for CO_2 to expand, you may dip the bottom tip of the measured volume in room-temperature water to speed this process up. Write down the pressure transducer value. Look out for vapors inside of the measured volume or constantly decreasing values as this could be an indication of H_2O in the measured volume and will lead to incorrect carbon mass readings. Write it down if it does happen.

Manipulating the torch and sealing CO_2 in pyrex vial (OC and EC):

Start torch by opening the gas and using the lighter. Flame should be about 5 inches long before slowly adding oxygen. Add oxygen until blue tip is about 1 inch.

Place yellow dewar full of LN under the 6 mm pyrex tube (7). This should be supported by a small adjustable stand and a block. Make sure bottom tip of glass tube is submerged into LN. Close V6 and open V5 to allow expanded CO_2 to freeze in the 6 mm pyrex tube (7). Wait for pressure transducer to reach base value. Keep yellow dewar filled to the brim with LN. Toggle V5. Wait at least one minute to allow CO_2 to freeze. Close V5.

After torch is set up, if 6 mm pyrex tube is graphitization vial, mark the sealing height 5 cm from the bottom of the tube and label tube with sample name. Put on sodium flare glasses and open V6. Toggle V6. Once vacuum is established again flame the sides of the pyrex tube while avoiding touching the blue tip to any part of the glass until sides begin to collapse. Hold the bottom of the tube with forceps. Once glass plasticizes pull down with forceps gently. Lean tube to the side while focusing the flame (never the blue tip) on the collapsed part. Slowly pull the bottom tube away from the flame and place either on the bench (6 mm pyrex tube only) or in a sample holder (small graphitization vial). Don't touch either side of the tube, it's hot and cold.

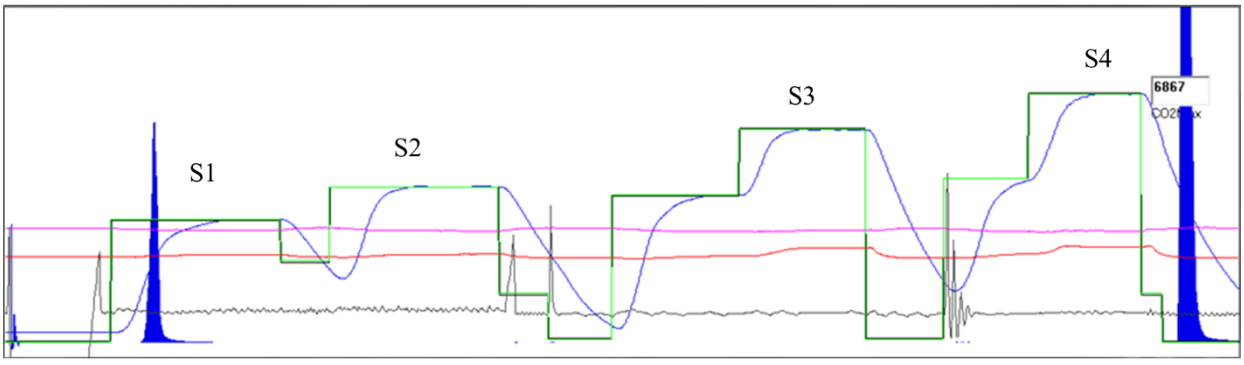

Open V5 and V4, toggle both. Remove water trap slowly and gently. Avoid putting too much stress on the trap. Allow leftover dry ice/EtOH to drip into the dewar. Pressure will build slowly as the trap thaws. The line is ready to trap again once vacuum is established again (~30-45 min).

Place water trap in the fume hood when finished and other dewars with LN upside down in fume hood to dry.

EC Trapping Procedure:

EC trapping procedure is mostly identical to the OC procedure with 4 main exceptions: (1) the protocol used should be the original Swiss_4S protocol (Bern4s_475_He4_650_gai_120s_rightTemps (optimized for new software).par), (2) the liquid nitrogen should be placed on the trap at the end of S3 once the temperature starts going down, (3) the trapping should begin as soon as S4 begins, and (4) EC capture requires a water extraction step to remove pyrolyzable OC.

Water Extraction:

Before capturing EC CO_2 on the vacuum line, charrable OC must be minimized. To do this, a 23 mm diameter circular QFF punch is taken and placed on a clean plastic filter holder between two sealing rings. The loaded side should face upwards and be sealed in the holder before attaching a luer-lock syringe and passing 20 mL of MQ water. The filter must then be very carefully placed on a clean aluminum foil that covers the filter like a "hut". Dry the filter at 60ºC for up to an hour. Once ready, you may carefully punch out 1.5 cm^2 for EC analysis. Be very wary of disturbing the loaded area with the tools and make sure to clean the tools with MQ water before and after use.

EC Capturing:

As mentioned earlier, the EC capturing method is mostly identical to the OC capture protocol except for the water extraction step and differing timing. Specifically, the liquid nitrogen should be applied to the trap at the end of S3 when the temperature begins decreasing. Close V1 as soon as S4 begins, which is when the instrument switches the carrier gas from helium to oxygen as shown below.

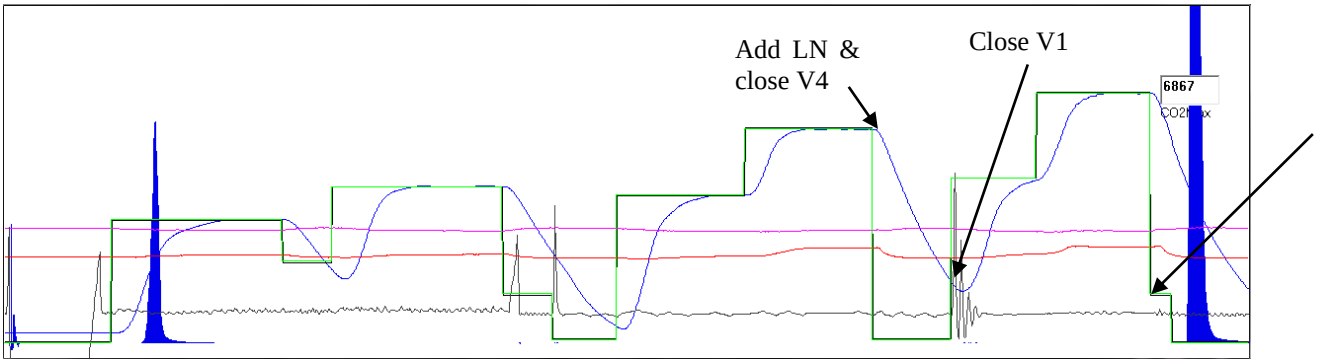

Once V1 is closed, wait till PSIG reaches 1 and open V2. This process is much faster, so be vigilant. The pressure will decrease but will rise much more quickly. Once PSIG reaches 1 again, open V3.

Once trapping is done, it is imperative that the Sunset not be in contact with the vacuum line by the time the calibration peak appears. As soon as S4 ends and the temperature begins to fall, close V3, wait for PSIG to reach 1 then close V2 and open V1 immediately.

Oxygen removal and CO_2 transfer afterward is identical to the OC procedure.

Small graphitization vial preparation:

Small graphitization vials are 6" length 6 mm diameter Pyrex tubes loaded with a 3 mm diameter inserts and two reagents: Zn and Fe. These are used to seal frozen CO_2 prior to graphitization (either through reactors or heat blocks in the Czimczik lab).

Tubing preparation:

Tube preparation begins by cutting a long Pyrex 6 mm diameter tube into 12” pieces. Mark the tube with a permanent marker at 6” intervals. Score the tube at 12” intervals. With your hands pushing away from the face, snap the long tube into 12” tubes. The cleaner the score, the cleaner the cut.

Using the gas/oxygen torch with a 1-2” inch blue tip (avoid touching the blue tip to the glass, and wear sodium flare glasses!), melt the glass into 2 6” inch tubes. To do this, hold the tube in front of the blue tip and rotate the tube to evenly distribute the heat. As the glass plasticizes, pull the two tubes apart slowly. The bottom of the tube should be relatively round, and the glass should be thickest at the bottom.

The sharp end of the tube should then be smoothed out. Place the other end of the tube in front of the blue tip and rotate the tube to evenly distribute the heat. Do this for about 4-6 seconds. Be wary as overdoing it will cause the end to collapse and not allow the 3 mm insert to fit. Check that the 3 mm insert still fits after conditioning the end. If it does not, dispose in glass waste.

Finally, to avoid the insert from touching the bottom of the tube, a small dimple at the bottom 1 cm is flamed in. To do this, position the tube sideways with the bottom of the tube in front of the blue tip. Move the tube up and down until you see the glass collapse and form a dimple (it will appear red). This dimple should be 1-2 cm above the inner tube bottom. If it’s too high, it will cause problems when sealing in the vacuum line.

These tubes should then be pre-baked at 550º C for 3 hours prior to loading reagents.

Loading reagents:

Each graphitization vial contains 10±1 mg of Zn in the outer tube and 5±0.5 of Fe in the 3 mm insert. The Zn may attach to the walls, so cover the outer tube with foil prior to adding the Zn. If too much Zn is added, the tube must go in hazardous waste.

Because the 3 mm insert touches the inner walls of the tube, which must be kept as clean as possible, do not touch the 3 mm insert with any un/gloved hand. Use tweezers to position the insert in a ¼" Swagelok nut sitting on a clean piece of foil on the balance and add the Fe to that while being very careful to minimize spoon to insert contact. Once done, pick up the insert and insert it into the 6 mm diameter at a 45º angle to avoid inserting it too fast and disturbing the Zn in the outer tube.

Pre-baking procedure:

Tubes must be conditioned before use at 300º C for 60 min. After conditioning, they must either be used the day of or stored in a vacuum line to avoid CO_2 adsorption to the pyrex walls.

Cleaning Filter Holders:

The following are needed for the cleaning procedure:

- Clean baked beaker
- Decon
- Boric Acid

Procedure:

- Disassemble all the filter holders and put them into the beaker,
- Add Decon (a few mls or read instructions) and fill with H2O MQ
- Sonicate for 30 min
- Pour out the solution and rinse thoroughly(!) with H2O MQ.
- Add some boric acid (H3BO3, probably from the PS store) ca. 0.5 g and fill up with H2O MQ.
- Sonicate again
- Rinse thoroughly, take holders out and let air dry on clean Al foil.
- You can make a tent with some foil to protect them from dust.

Note: When disposing from boric acid solution, use designated chemical waste containers. DO NOT POUR DOWN THE SINK.

Chapter 5

Conclusions and future research directions

The aim of my dissertation was to improve our understanding of sources to carbonaceous aerosol in the rapidly changing Arctic by measuring the carbonaceous content and isotopic composition of particulate matter and evaluating key environmental factors that modulate aerosol emissions and transport. My work involved evaluating innovative techniques, extensive field measurements, and subsequent rigorous laboratory analyses, which allowed me to quantify the relative contributions of different organic (OC) and black (BC) aerosol sources in diverse environments. These particles play a complex role in the climate system, via their role in light scattering and absorption, cloud nucleation, and the melting of ice- and snow-covered surfaces, and in air pollution and human health. The direct isotopic characterization of carbonaceous aerosol and subsequent source apportionment provided by this work contributes to an increasing body of knowledge that provides critical data for developing, evaluating, and monitoring effective measures for mitigating these critical air pollutants and short-lived climate forcers. Therefore, a major aim of this work was to provide a benchmark dataset to be used in validating future modelling efforts that improve our understanding of aerosol impacts on climate, air quality, and the carbon cycle. The following chapter summarizes the main scientific conclusions of this dissertation and provides a broader discussion of future research directions of carbon isotope-based aerosol source apportionment studies.

5.1 Summary of results

5.1.1 Evaluation of the ECT9 protocol for radiocarbon analysis of ultra-small samples (Chapter 2)

In Chapter 2 I evaluate the ECT9 technique for its ability to effectively separate OC from BC for subsequent ^{14}C analysis of these important aerosol fractions. The ECT9 method (formerly EnCan900) was developed to quantify the concentration and stable carbon isotopic composition ($\delta^{13}C$) of carbonaceous bulk aerosol and aerosol fractions across Canada (Chan et al., 2019; Huang et al., 2006). It is similar to other thermal-optical techniques used by global monitoring networks (NIOSH/IMPROVE) to quantify OC/BC concentrations (Chow et al., 2001) but does not use the optical measurements to correct for charring mass.

To evaluate the efficacy of the ECT9 protocol for ^{14}C analysis, I analyzed several pure and mixed ultra-small (<100 µg) ^{14}C standard materials to assess the extraneous carbon introduced through separation, graphitization, and ^{14}C quantification using a mass-balance approach (Santos et al., 2007). I show that this protocol incorporates 1.3±0.65 µg extraneous carbon and can separate pure standards when mixed, such as OC modern standard (adipic acid) and a BC fossil standard (coal, regal black). The analyses of OC/BC mixtures with drastically different ^{14}C contents was an important method-validation approach not previously done during the evaluation of other protocols (i.e. Swiss_4S, EUSAAR), which focused on the analysis of pure standard materials, aerosol standard materials, and, or intercomparisons of environmental samples (Mouteva et al., 2015; Szidat et al., 2013; Zenker et al., 2017).

Much like the NIOSH/IMPROVE thermal-optical protocols used in monitoring networks, the ECT9 protocol utilizes 100% He gas as carrier gas to evolve the OC and pyrolized organic carbon (POC) and carbonate carbon (CC) (i.e. POC+CC) steps and 2% O_2 in He, which are

prone to charring OC to BC (Zhang et al., 2012). This presents the biggest challenge to effectively separating OC and BC fractions for ^{14}C analysis. In my thesis, I show that the inclusion of an extended high-temperature thermal step to remove POC (870ºC for 600 seconds) prior to capturing BC minimizes charring to BC in the circumstances where the sampling material is relatively homogenous. With increasing sample complexity, such as a particulate matter standard (i.e. SRM1649a), however, the BC fraction contained significantly more ^{14}C compared to previous assessments. The increased ^{14}C content in SRM1649a as quantified by the ECT9 protocol and the SRM8785 (i.e. the resuspended version of SRM1649a) laser profiles suggests that thermally refractory OC can be charred and incorporated into BC, which is abated to a certain extent in the Swiss_4S protocol through pre-treatment with water to remove water-soluble organics (Zhang et al., 2012). Therefore, when reporting ^{14}C results with these techniques, the physical separation protocol and the inherent biases must be strongly considered.

The inherent differences in temperatures, how long the temperatures are sustained, and carrier gases in these ^{14}C-measuring thermal evolution protocols accentuates the importance evaluating each new protocol with a variety of simple and complex standards to understand how these factors affect method biases. Chapter 2 provides a comprehensive description of ECT9's procedural blank, evaluates the capacity to provide precise ^{14}C values to homogeneous and heterogeneous standards, and the inherent biases. The ECT9 protocol is a good alternative to Swiss_4S and works effectively in pristine environments such as the Arctic and the Amazon. This protocol was used in Chapter 3 of the dissertation and is expected to be used for future ^{14}C assessment of Canada's monitoring networks.

5.1.2 Understanding combustion sources and seasonality to BC in the High Arctic at Alert, Canada (Chapter 3)

BC is an important pollutant in the High Arctic through its direct radiative properties and indirect effects on clouds and air column temperatures (AMAP, 2015; Bond et al., 2013). While current modelling efforts have reasonably replicated the seasonal trends of surface BC and described the atmospheric processes involved in creating the seasonal trends, sources to this BC in particulate matter (PM) are not well characterized. This study utilizes the novel method for measuring ^{14}C in ultra-small (<15 μg C) samples (Walker & Xu, 2019) in conjunction with the ECT9 protocol described in Chapter 2 to assess the combustion sources to BC at the Alert, Canada monitoring station year-round.

I show that fossil fuel combustion is a major source to surface BC mass in particulate matter PM from fall to spring. Backward trajectories indicate that throughout this time, air masses were primarily transported from the Russian sector, though this analysis may underestimate long-range transport from Asia due to limited length of the trajectories (< 10 days). Backward trajectories also showed that North American boreal fires contributed significantly to the BC load at Alert during the summer and this was corroborated by ^{14}C data that also showed an increase in biomass burning contribution. In addition, enriched $\delta^{13}C$ results indicated the prevalence of solid/liquid fuels as a source for fossil BC over gaseous fuels throughout the year.

In Chapter 3 I also report the first year-round data set of ^{14}C of BC in snow collected near the PM sampling site at Alert. Increased ^{14}C content of BC in snow compared to PM measured at the same time, suggests snow contains a greater proportion of BC derived from biomass burning. Unfortunately, the snow collection protocol was not monthly rather than event based, so that some samples included only fresh snow and others consisted of aged snow or mixtures of fresh

and aged snow. As a result, the ^{14}C-difference between PM and snow was inconsistent, suggesting that incidences of increased dry deposition caused BC in collected snow to be similar to the ambient PM. I hypothesize that during time periods when BC in snow had a greater biomass burning component because biomass burning particles were removed from the upper atmosphere. The free troposphere is known to contain greater long-range transport sources from mid-latitudes (Freud et al., 2017; Xu et al., 2017). This suggests that the Alert monitoring station and other surface-observing stations that routinely measure PM, but not snow, may be underestimating the source of long-range transport by not measuring wet-deposited BC.

5.1.3 Quantifying source contributions to boundary layer OC aerosol at coastal, remote, and Arctic regions (Chapter 4)

BC is important for climate, air quality, and human health, but only constitutes 1-10% of carbonaceous aerosol mass. OC on the other hand, is also important for similar reasons, but much less is known about their impact on future climate. Source apportionment of OC in PM is challenging due to complex sources and atmospheric aging but are nonetheless important for establishing relevant sources to marine OC in coastal, remote, and Arctic regions. Characterizing these sources are incredibly important as significant increases to future shipping activity and shifts in marine and terrestrial productivity are expected in the Arctic. In Chapter 4, I quantify the contribution of fresh biomass, aged marine refractory dissolved organic carbon (RDOC), and fossil in OC with a dual-isotope ($\delta^{13}C$, ^{14}C) 3-source mass balance model. I show that RDOC contributes to PM throughout the East Sea, North Pacific, Bering Sea/Strait, and the Chukchi Sea (ranging from 18 to 90%) and is significantly higher in remote regions, such as the Pacific Ocean. Auxiliary measurements and back trajectories indicate that modern biomass in coastal regions, such as the East Sea and Nome, Alaska regions was comprised of terrestrial biomass

aerosol. Meanwhile, elevated productivity in the Bering Sea and Strait regions suggest a larger marine biomass contribution over terrestrial influence.

In this chapter, I highlight the need for in-depth isotopic characterization and concentration of surface marine RDOC and particulate organic matter (POM) to validate their contribution to atmospheric PM. In particular, the temporal variability of RDOC age from Arctic river delta (such as the Yukon–Kuskokwim) outflow and subsequent marine PM should be explored as a possible source of permafrost carbon to the ocean. This work would increase our understanding of RDOC origin, the shifting terrestrial carbon fluxes to the ocean and the atmosphere from permafrost thaw, and atmospheric degradation as an RDOC pathway loss. Additionally, the significant contribution of fresh biomass to marine PM found in this chapter accentuates the importance of exploring how increased marine OC aerosol flux from increased productivity would impact cloud properties and either modulate or enhance Arctic amplification.

5.2 Future research directions

5.2.1 Comprehensive evaluation of thermal-based isotopic analysis methods

The work in Chapter 2 highlights an opportunity to re-evaluate all thermal-based protocols that separate OC/BC prior to ^{14}C analysis with common standards. This includes protocols such as the NIOSH 5040, Swiss_4S, ECT9, EUSAAR_2, IMPROVE and all future protocols that will be used to interpret real samples. Previous evaluations (Currie et al., 2002; Klouda et al., 2005; Mouteva et al., 2015; Szidat et al., 2013; Zhang et al., 2012) have repeatedly shown that differences in carrier gas, temperature, and the length of temperature sustained will greatly impact the fraction of carbon that is isolated and consequently the isotopic composition. The chemical diversity of a real PM sample also adds a layer of complexity that cannot always be constrained across methodologies. However, by comparing the resulting isotopic composition of

complex standards (i.e. SRM1649a, SRM1649b, SRM8785, SRM8785) and real environmental samples from each protocol, a comprehensive evaluation of each protocol's biases can be created to bring regional datasets together. Future results of real complex samples should discuss their results in the context of this evaluation to gain a better understanding of the type of carbon fraction isolated.

Realistically, the multiple variables that dictate the fraction of carbon isolated by each thermal protocol make it impossible to recommend a single protocol. However, some considerations should be made before reporting any isotopic values utilizing these techniques. The most important is the extent of charring. Pyrolysis of OC will become incorporated as BC when isolated and can drastically alter the ^{14}C composition of the BC. No protocol is immune to this effect when analyzing unknowns with refractory organics. Future studies should take care to either intentionally adjust the variables (i.e. temperature, carrier gas etc.) to minimize the effect or preprocess samples to extract organics prior to capturing BC. Furthermore, transmittance data from the laser can be a valuable addition to future ^{14}C reporting as decreases in transmittance can be a quick indicator of charring. The usage of pure oxygen as carrier gas has been shown to encourage full oxidation of organics, which is why lower temperatures are typically used to evolve OC compared to methods using pure He. However, refractory organics can still resist complete oxidation even at lower temperatures. Extraction of these organics through chromatographic separation, may be used to further minimize this effect. For OC analysis, special attention should be placed to these methodology variables when attempting to identify sources to isolated OC in real samples as not all organics are necessarily included when isolated with all the protocols and consequent isotopic characterizations may not be representative of TOC.

5.2.2 Circum-Arctic isotopic characterization of BC in snow

BC continues to be an important short-lived climate forcer and air pollutant in the Arctic, particularly due to the changes in albedo incurred from its deposition on snow (AMAP, 2015; Bond et al., 2013). In Chapter 3 I show that wet-deposited BC can have significantly higher biomass combustion contribution than ambient PM collected at the same time, which indicates that networks are under-sampling biomass burning emissions and should be evaluated a greater scale. Isotopic composition alone cannot determine how biomass burning particles were preferably incorporated to snow over ambient aerosol, so future work investigating BC transport pathways should explore the relevant pathways for BC to incorporate into snow and where those air masses originate.

BC with organic/sulfate coatings, as seen in biomass burning particles or aged fossil combustion particles, can activate as cloud condensation nuclei (CCN) or are easily scavenged by existing liquid droplets due to their hygroscopic properties. Conversely, they are not effective ice-nucleating particles (INP) due to the dissimilarity to the hexagonal crystalline structure of ice (Kanji et al., 2017). However, the persistent existence of mixed-phase clouds ($-30^{o}C<T<0^{o}C$) in the Arctic throughout the year (de Boer et al., 2011; Coopman et al., 2018; Cox et al., 2014; Morrison et al., 2012) suggests that BC can still exist within snowing clouds in supercooled droplets. The contact freezing caused by collision between formed snow crystals and supercooled droplets, a process also known as riming, within and below the cloud is a likely BC pathway. However, the extent of this pathway is not known. The stark differences in ^{14}C between BC in snow and ambient PM suggests that weather systems transport BC in the free troposphere, which are known to include long-range transport, to the surface in the High Arctic. More measurements of are needed at the circum-Arctic scale to determine whether this is a systematic phe-

nomenon. This is a challenge since BC only accounts for 1-10% of the carbonaceous aerosol mass.

Future measurements should scrupulously quantify fresh snowfall amount to scale up BC concentrations in snow. This will be required to scale up these observations. Extensive air column measurements before, during, and after snowstorm systems of BC concentrations and meteorological conditions ought to capture the movement of BC within the air column during a snowstorm. To capture the process of BC inclusion, future work should focus on isolating snow particles in fresh snow with BC, an extremely challenging task given the extremely low concentrations of BC in snow, for scanning electron microscopy. This work in conjunction with state-of-the-art chemical transport models would considerably increase our understanding BC transport pathways and the role of meteorology in advancing those pathways. This would further enhance the representation of BC deposition and achieve more accurate representation of Arctic amplification in climate models. Analysis of their isotopic and elemental composition offers unique insights into their origin – information that is needed to quantify biomass burning and to develop and monitor effective air pollution measures.

5.2.3 Carbon isotopic characterization of marine aerosol in remote and Arctic regions

The Arctic is quickly changing, baseline data to capture this change with isotopic characterization is urgently needed. The results of Chapter 4 shows that marine emissions are important, but number of observations were severely limited due to exceedingly low concentrations and lack of replicates in the Arctic. Quantifying source apportionment of marine and terrestrial sources was extremely limited by lack of or severely limited surface observations of surface DOC and POM in the study regions. The work in Chapter 4 requires replication with full integration of aerosol observations with of marine DOC/POC observations at the same location. Addi-

tionally, exploring the chemical composition, such as the concentrations and isotopic composition of polysaccharides, aliphatic and aromatic compounds, of PM and marine POM/DOC could yield in-depth information about marine contributions to PM from specific carbon pools. Moreover, the role of surfactants concentrated at the surface microlayer has yet to be evaluated for its importance to contributing to OC, or how they may age and contribute to secondary organic aerosol (SOA).

Secondary marine aerosol is prevalent within the boundary layer and can have much longer lifetimes than POA due to their small size (<100 nm diameter). However, the sources to marine SOA have yet to be constrained in the Arctic by the corresponding carbon pool. Currently, sources to marine SOA are not well understood. If sample size allows, future work characterizing the isotopic composition of these SOA could yield powerful insights into the sources and formation pathways. Ultimately the results from this would better characterize SOA formation removal in chemical transport models that seek to describe the climatic impacts of SOA.

5.3 Concluding Remarks

The Arctic is currently experiencing unprecedented warming, which is leading to accelerated thaw of permafrost, loss of sea ice, and glacier retreat. Current climate models struggle to characterize future atmospheric short-lived climate forcer, such as BC and OC aerosol, fluxes, atmospheric burden, and their consequent climatic impact. This is because the emission pathways, atmospheric aging, deposition pathways, and aerosol-cloud interaction are still not well understood. This research improves unique methods for detecting sources to BC and OC and our understanding of those sources in context of the global C-cycle. Here, I have significantly optimized the technology that measures μg-C amounts of OC and BC to expand the study of carbonaceous aerosol fractions into clean air regions (i.e. the Arctic). However, more work is needed

to expand these observations to explore spatial and temporal variations in OC and BC fluxes by emission source from the ocean and land to and from the atmosphere to enhance future predictions of Arctic climate change.

5.4 References

AMAP. (2015). *AMAP assessment 2015: Black carbon and ozone as Arctic climate forcers*. *Arctic Monitoring and Assessment Programme (AMAP)*. Oslo, Norway. Retrieved from https://www.amap.no/documents/doc/amap-assessment-2015-black-carbon-and-ozone-as-arctic-climate-forcers/1299

de Boer, G., Morrison, H., Shupe, M. D., & Hildner, R. (2011). Evidence of liquid dependent ice nucleation in high-latitude stratiform clouds from surface remote sensors. *Geophysical Research Letters*, *38*, L01803. https://doi.org/10.1029/2010GL046016

Bond, T. C., Doherty, S. J., Fahey, D. W., Forster, P. M., Berntsen, T., Deangelo, B. J., et al. (2013). Bounding the role of black carbon in the climate system: A scientific assessment. *Journal of Geophysical Research Atmospheres*, *118*(11), 5380–5552. https://doi.org/10.1002/jgrd.50171

Chan, T. W., Huang, L., Banwait, K., Zhang, W., Ernst, D., Wang, X., et al. (2019). Intercomparison of elemental and organic carbon mass measurements from three North American national long-term monitoring networks at a co-located site. *Atmospheric Measurement Techniques*, *12*(8), 4543–4560. https://doi.org/10.5194/amt-12-4543-2019

Chow, J. C., Watson, J. G., Crow, D., Lowenthal, D. H., & Merrifield, T. (2001). Comparison of IMPROVE and NIOSH Carbon Measurements. *Aerosol Science and Technology*, *34*(1), 23–34. https://doi.org/10.1080/02786820119073

Coopman, Q., Garrett, T. J., Finch, D. P., & Riedi, J. (2018). High Sensitivity of Arctic Liquid

Clouds to Long-Range Anthropogenic Aerosol Transport. *Geophysical Research Letters*, *45*(1), 372–381. https://doi.org/10.1002/2017GL075795

Cox, C. J., Turner, D. D., Rowe, P. M., Shupe, M. D., & Walden, V. P. (2014). Cloud microphysical properties retrieved from downwelling infrared radiance measurements made at Eureka, Nunavut, Canada (2006-09). *Journal of Applied Meteorology and Climatology*, *53*(3), 772–791. https://doi.org/10.1175/JAMC-D-13-0113.1

Currie, L. A., Benner, B. A., Kessler, J. D., Klinedinst, D. B., Klouda, G. A., Marolf, J. V., et al. (2002). A critical evaluation of interlaboratory data on total, elemental, and isotopic carbon in the carbonaceous particle reference material, NIST SRM 1649a. *Journal of Research of the National Institute of Standards and Technology*, *107*(3), 279–298. https://doi.org/10.6028/jres.107.022

Freud, E., Krejci, R., Tunved, P., Leaitch, R., Nguyen, Q. T., Massling, A., et al. (2017). Pan-Arctic aerosol number size distributions: Seasonality and transport patterns. *Atmospheric Chemistry and Physics*, *17*(13), 8101–8128. https://doi.org/10.5194/acp-17-8101-2017

Huang, L., Brook, J. R., Zhang, W., Li, S. M., Graham, L., Ernst, D., et al. (2006). Stable isotope measurements of carbon fractions (OC/EC) in airborne particulate: A new dimension for source characterization and apportionment. *Atmospheric Environment*, *40*(15), 2690–2705. https://doi.org/10.1016/j.atmosenv.2005.11.062

Kanji, Z. A., Ladino, L. A., Wex, H., Boose, Y., Burkert-Kohn, M., Cziczo, D. J., & Krämer, M. (2017). Overview of Ice Nucleating Particles. *Meteorological Monographs*, *58*, 1.1-1.33. https://doi.org/10.1175/AMSMONOGRAPHS-D-16-0006.1

Klouda, G. A., Filliben, J. J., Parish, H. J., Chow, J. C., Watson, J. G., & Cary, R. A. (2005). Reference material 8785: Air particulate matter on filter media. *Aerosol Science and*

Technology, *39*(2), 173–183. https://doi.org/10.1080/027868290916453

Morrison, H., De Boer, G., Feingold, G., Harrington, J., Shupe, M. D., & Sulia, K. (2012). Resilience of persistent Arctic mixed-phase clouds. *Nature Geoscience*, *5*(1), 11–17. https://doi.org/10.1038/ngeo1332

Mouteva, G. O., Fahrni, S. M., Santos, G. M., Randerson, J. T., Zhang, Y.-L., Szidat, S., & Czimczik, C. I. (2015). Accuracy and precision of ^{14}C-based source apportionment of organic and elemental carbon in aerosols using the Swiss_4S protocol. *Atmospheric Measurement Techniques*, *8*(9), 3729–3743. https://doi.org/10.5194/amt-8-3729-2015

Santos, G. M., Southon, J. R., Griffin, S., Beaupre, S. R., & Druffel, E. R. M. (2007). Ultra small-mass AMS 14C sample preparation and analyses at KCCAMS/UCI Facility. *Nuclear Instruments and Methods in Physics Research Section B: Beam Interactions with Materials and Atoms*, *259*(1), 293–302. https://doi.org/10.1016/j.nimb.2007.01.172

Szidat, S., Bench, G., Bernardoni, V., Calzolai, G., Czimczik, C. I., Derendorp, L., et al. (2013). 14 C ANALYSIS OF CARBONACEOUS AEROSOLS : Exercise 2009. *Radiocarbon*, *55*(2), 1496–1509. https://doi.org/10.2458/azu_js_rc.55.16223

Walker, B. D., & Xu, X. (2019). An improved method for the sealed-tube zinc graphitization of microgram carbon samples and 14C AMS measurement. *Nuclear Instruments and Methods in Physics Research Section B: Beam Interactions with Materials and Atoms*, *438*, 58–65. https://doi.org/10.1016/j.nimb.2018.08.004

Xu, J. W., Martin, R. V., Morrow, A., Sharma, S., Huang, L., Richard Leaitch, W., et al. (2017). Source attribution of Arctic black carbon constrained by aircraft and surface measurements. *Atmospheric Chemistry and Physics*, *17*(19), 11971–11989. https://doi.org/10.5194/acp-17-11971-2017

Zenker, K., Vonwiller, M., Szidat, S., Calzolai, G., Giannoni, M., Bernardoni, V., et al. (2017). Evaluation and inter-comparison of oxygen-based OC-EC separation methods for radiocarbon analysis of ambient aerosol particle samples. *Atmosphere*, *8*(11). https://doi.org/10.3390/atmos8110226

Zhang, R., Chen, M., Guo, L., Gao, Z., Ma, Q., Cao, J., et al. (2012). Variations in the isotopic composition of particulate organic carbon and their relation with carbon dynamics in the western Arctic Ocean. *Deep Sea Research Part II: Topical Studies in Oceanography*, *81–84*, 72–78. https://doi.org/10.1016/j.dsr2.2011.05.005

Zhang, Y. L., Perron, N., Ciobanu, V. G., Zotter, P., Minguillón, M. C., Wacker, L., et al. (2012). On the isolation of OC and EC and the optimal strategy of radiocarbon-based source apportionment of carbonaceous aerosols. *Atmospheric Chemistry and Physics*, *12*(22), 10841–10856. https://doi.org/10.5194/acp-12-10841-2012